Untersuchungen über Aufbau und Auswirkungen von Spaltprodukten in schnellen Kernreaktoren

Investigations on the build-up and impacts of fission products in nuclear fast reactors

Diplomarbeit

von

Kilian Kern

zum Erwerb des akademischen Grades Diplom-Physiker
an der Fakultät für Physik des Karlsruher Instituts für Technologie

Referent: Prof. Dr. Thomas Müller
Korreferent: Dr. habil. Ron Dagan

Institut für Neutronenphysik und Reaktortechnik

2011

Erklärung

Hiermit erkläre ich, dass ich die vorliegende Diplomarbeit selbstständig und ohne unzulässige fremde Hilfsmittel angefertigt habe. Die verwendeten Literaturquellen sind im Literaturverzeichnis vollständig angegeben.

Karlsruhe, 29. April 2011

Als Diplomarbeit akzeptiert:

Karlsruhe, 29. April 2011

Contents

List of Figures

List of Tables

0   Zusammenfassung

Schnelle Kernreaktoren sind Gegenstand mehrerer laufender Forschungsprogramme, beispielsweise der EU-Projekte für schnelle Reaktoren sowie der internationalen Aktivitäten hinsichtlich Reaktoren der Generation IV. Ihr hartes Neutronenspektrum bietet wesentliche Vorteile hinsichtlich der Ausnutzung der Brennstoffressourcen und der Wirtschaftlichkeit eines geschlossenen Brennstoffkreislaufs, da es hohe Konversionsraten und Endabbrände ermöglicht. Das Neutronenspektrum hat jedoch erhebliche Auswirkungen auf den Aufbau einzelner Spaltproduktnuklide beim Betrieb eines Reaktors. Diese Auswirkungen liegen in den Sensitivitäten des Spaltprozesses gegenüber der Energie des einfallenden Neutrons und in Kernreaktionen zwischen Neutronen und Spaltprodukten, insbesondere (n, γ)-Reaktionen, begründet. Leider sind die experimentellen Daten über Spaltproduktausbeuten aus der Schnellspaltung im Vergleich mit Daten über thermische Spaltung eher begrenzt, woraus sich immer noch größere Unsicherheiten in den für Reaktorrechnungen verwendeten evaluierten Daten ergeben. Diese Arbeit setzt sich mit dem Aufbau von Spaltprodukten bei einem Uran-Plutonium-Brennstoffzyklus in einem natriumgekühlten schnellen Reaktor auseinander. Es sei an dieser Stelle erwähnt, dass Spaltproduktausbeuten aus der Spaltung verschiedener Nuklide grundsätzlich bedeutende Unterschiede aufweisen.

Die Arbeit besteht aus vier Teilen und befasst sich in hohem Maße mit der Modellbeschreibung von Spaltproduktausbeuten in Abhängigkeit von Targetkern und der Energie des einfallenden Neutrons. Das erste Kapitel gibt einen Überblick über die physikalischen Aspekte des Spaltprozesses sowie die bestehenden Verfahren zur seiner Beschreibung. Hierbei ist Anwendung rein theoretischer Modelle im Allgemeinen extrem aufwendig oder erfordert Vereinfachungen, die bisher keine quantitativ guten Übereinstimmungen mit den experimentellen Beobachtungen geliefert haben. Aus dieser Sicht sieht man sich veranlasst, auf der Systematik experimenteller Daten basierende empirische Modelle zu verwenden, deren Vorhersagekraft jedoch begrenzt ist. Weiterhin werden im ersten Kapitel die Facetten einer relativ einfachen, modernen und teilweise empirischen Beschreibung des Spaltprozesses eingehend beschrieben. Hierbei werden auch neue physikalische Erkenntnisse und originelle Ansätze diskutiert, die die Vorhersagekraft eines halbempirischen Spaltungsmodells deutlich verbessern. Diese sind in dem Spaltungsmodellcode GEF, der von K.-H. Schmidt und B. Jurado im EURATOM-Rahmenprogramm "European Facilities for Nuclear Data Measurements" (EFNUDAT) entwickelt wurde, umgesetzt. Die Weiterentwicklung des Codes wird von der Nuclear Energy Agency der OECD unterstützt. Auf diesen Code und seine Erweiterungen, die für einen umfassenderen Vergleich des Modells mit experimentellen Observablen sowie für dessen Anwendung in der Reaktorrechnung in dieser Arbeit entwickelt wurden, wird im zweiten Kapitel eingegangen.

Im dritten Kapitel werden die Ergebnisse aus Analysen experimenteller Daten, den Vorhersagen des Modells und den evaluierten Spaltproduktausbeuten der JEFF-3.1.1-Bibliothek präsentiert. Diese Analysen wurden für die Nuklide ^{235}U, ^{238}U, ^{239}Pu, ^{240}Pu, ^{241}Pu und ^{242}Pu durchgeführt. Hierbei wurden unter anderem die Eigenschaften der Massenverteilung

der Spaltproduktausbeuten in Abhängigkeit von der Neutronenenergie analysiert, was für weitere Entwicklungen einer Modellbeschreibung dieser Abhängigkeiten sicherlich interessant ist. Bei den Vergleichen von experimentellen Daten, Modell und Evaluierung stellte sich heraus, dass einerseits scheinbar bestimmte Defizite in den JEFF-3.1.1-Daten bestehen und andererseits der GEF-Code insbesondere hinsichtlich der einzelnen Spaltkanalanteile und der Anregungsenergie der Fragmente noch verbesserungsfähig ist.

Mehrere Argumente sprechen dafür, dass in den JEFF-3.1.1-Datensätzen für Schnellspaltung der Gerade-Ungerade-Effekt der Spaltproduktausbeuten in Abhängigkeit von der Protonenzahl nicht korrekt ist. Es wurde diesbezüglich eine erhebliche Abweichung zwischen dem relativ wichtigen evaluierten Datensatz für die Schnellspaltung des Targets ^{238}U und den in dieser Arbeit für das Neutronenflussspektrum des schnellen Reaktors berechneten Spaltproduktausbeuten beobachtet.

Das vierte Kapitel befasst sich mit den Reaktorrechnungen, die mit dem am KIT Campus Nord entwickelten modularen Code-System KANEXT durchgeführt wurden. Für die hieraus erhaltenen Spektren der Spaltreaktionsraten wurden mit der in dieser Arbeit entwickelten Erweiterung des GEF-Codes Spaltproduktausbeuten für Uran- und Plutoniumnuklide berechnet. Für die Abbrandrechnungen wurden sowohl die Spaltproduktausbeuten aus der KORFI4-Bibliothek von KANEXT sowie die in dieser Arbeit berechneten Spaltproduktausbeuten verwendet. Die Ergebnisse aus KANEXT für beide Fälle werden hinsichtlich der Reaktivität, der Nachzerfallswärme und der Mengen langfristig radioaktiver Spaltprodukte in abgebranntem Kernbrennstoff verglichen.

0 Abstract

Fast nuclear reactors are the subject of several ongoing research programs, e. g. the EU projects for fast reactors as well as the international activities with respect to Generation IV reactors. Their hard neutron spectrum offers significant advantages concerning the utilization of fuel resources and the economy of a closed fuel cycle, since it enables high conversion rates and final burn-up values. However, the neutron spectrum has important impacts on the build-up of single fission product nuclides during the operation of a reactor. These impacts are the result of sensitivities of the fission process to the incident neutron energy and of nuclear reactions between neutrons and fission products, in particular (n, γ) reactions. Unfortunately, experimental data on fission product yields from fast fission are rather limited compared to the data on thermal fission, with major uncertainties in the evaluated data applied to reactor calculations still resulting from this issue. This work deals with the generation of fission products in a uranium-plutonium fuel cycle in a sodium-cooled fast reactor (SFR). At this point, it should be mentioned that there are generally significant differences between the fission product yields from the fission of different target nuclides.

This work consists of four parts and is much focused on the modelling of fission product yields depending on the target nucleus and the incident neutron energy. The first chapter gives an overview of the physical aspects of the fission process as well as the existing approaches to its description. The application of purely theoretical models to this issue is generally very complicated or requires simplifications which have not returned good quantitative agreements with the experimental observations up to now. From this point of view, one feels compelled to use empirical models based on the systematics of experimental data, whose predictive power is however limited. Furthermore, the facets of a relatively simple, modern and partly empirical description of the fission process are described in detail in the first chapter. At that point, new physical findings and original approaches which considerably improve the predictive power of a semi-empirical fission model are also discussed. They are implemented in the fission model code GEF, which has been developed by K.-H. Schmidt and B. Jurado in the EURATOM Framework Programme "European Facilities for Nuclear Data Measurements" (EFNUDAT). Further development of the code is supported by the OECD Nuclear Energy Agency. This code and its extensions, which were developed in this work with the objective of a more thorough comparison of model results to experimental observables as well as the application to reactor calculations, are addressed in the second chapter.

In the third chapter, the results from analyses of experimental data, model predictions and evaluated fission yields data from the JEFF-3.1.1 library are presented. These analyses were carried out for the nuclides ^{235}U, ^{238}U, ^{239}Pu, ^{240}Pu, ^{241}Pu and ^{242}Pu. One issue analyzed at this point are the properties of the mass distribution of fission yields depending on the incident neutron energy. This is surely interesting in further developments of a model description of these dependencies. From the comparison of the experimental data, the model

and the evaluation it turned out that on the one hand, there seem to be some deficiencies in the JEFF-3.1.1 data and on the other hand, the GEF code is still improvable concerning the fractions of the distinct fission channels as well as the excitation energy of fission fragments.

There are several arguments that in the JEFF-3.1.1 fast fission data sets, the even-odd effect of fission product yields depending on the proton number is not correct. Concerning this issue, a significant deviation between the relatively important evaluated fast fission data set for the target ^{238}U and the yields calculated for the fast reactor neutron flux spectrum in this work has been observed.

The fourth chapter deals with the reactor calculations, which were performed with the modular code system KANEXT developed at KIT Campus Nord. For the fission reaction rate spectra obtained from KANEXT, fission product yields from the fission of uranium and plutonium nuclides were calculated by the extension of the GEF code developed in this work. In the burn-up calculations, fission yields from the KANEXT library KORFI4 as well as fission yields calculated in this work were applied. Concerning the reactivity, the decay heat and the amounts of long-term radioactive fission products, the results from both KANEXT calculations are compared to each other.

1 Description of the Fission Process

The modelling of fission product yields for important target nuclides in typical fast reactor spectra is one of the main objectives of this work. This chapter deals with the theoretical and empirical description of the nuclear fission process.

1.1 Introduction

At this point, a short introduction to the main features of the fission process will be given. Fission denotes the division of a heavy nucleus into two intermediate mass fragments. This exothermic process is generally inhibited by a so-called fission barrier, which can be explained by e. g. the well-known liquid drop model. This fission barrier is characterized by a saddle point of the potential energy in the space of deformation coordinates. If the nucleus is in its ground state, the barrier may be passed by tunneling, which is called spontaneous fission and plays a role especially in transuranic nuclides. However, fission may also be induced by bringing excitation energy into the nucleus, making the passage of the fission barrier much more probable. In nuclear reactors, this happens by neutron capture in which several MeV are released. The nucleus formed in this process is called "compound nucleus". Driven by the Coulomb repulsion of its protons, the nucleus becomes more and more elongated and finally ruptures into two highly excited fission fragments. The point in deformation space where the neck between the two nascent fragments ruptures is called "scission point". Subsequently, the fragments obtain a large amount of kinetic energy from the Coulomb repulsion. Since they are highly excited, they emit the so-called prompt neutrons and prompt gamma quanta. The neutrons are mostly emitted when the fragments have already been fully accelerated, and as long as this is possible, gamma emission is strongly suppressed. The residual nuclei emerging from this deexcitation process are called the fission products. It is observed that the variation of the compound nucleus excitation energy has an impact on the yields of different fission product nuclides, and these sensitivities are one indication that fission occurs via different modes competing with each other. This is a motivation for systematic investigations of the nuclear potential in deformation space to which this issue is related. It must be taken into account that shell effects, as explained by the nuclear shell model, play an important role in fission reactions at the compound nucleus excitation energies relevant for this work.

In this chapter, section 1.2 gives a review of most of the relevant work related to the description nuclear fission, which is a many-particle problem. The following sections 1.3 to 1.12 describe a modern and successful modelling of the fission fragment formation in a semi-empirical way. It is based on a macroscopic-microscopic approach including original descriptions of K.-H. Schmidt being used in his model code GEF [1], which is very advanced concerning some aspects. Sections 1.13 and 1.14 describe the models required for the calculation of fragment deexcitation, which determines the final fission product yield for a certain nuclide and, if existing, metastable state. For completeness, the characteristics of ternary fission reactions, i. e. fission into three fragments, are discussed in section 1.15.

1.2 Approaches to the Many-particle Problem

1.2.1 Microscopic Approaches

The most obvious and complete method for the description of the nuclear fission process is to solve the equations of motion for the individual nucleons. The Hamiltonian of a system of A nucleons in mutual interaction is given by (1). It becomes obvious that in the application to actinide nuclei with a mass number around $A \approx 240$, this large number of coupled equations needs to be solved. Additionally, the potential V_{ij} shows a complicated dependence on the relative coordinates $\vec{r}_j - \vec{r}_i$, momenta $\vec{p}_j - \vec{p}_i$, spins $\vec{s}$ and charge numbers q. Consequently, this approach cannot be applied directly because of the huge computational effort.

$$\mathcal{H} = \sum_{i=1}^{A} \frac{\vec{p}_i^2}{2m_i} + \frac{1}{2} \sum_{i=1}^{A} \sum_{j \neq i} V_{ij}(\vec{r}_j - \vec{r}_i, \vec{p}_j - \vec{p}_i, \vec{s}_i, \vec{s}_j, q_i, q_j) \tag{1}$$

The time-dependent Hartree-Fock method (TDHF), which was first introduced in the context of atomic physics, is an approximation to this problem. It assumes that the time-dependent nuclear wave function can be expressed by a Slater determinant (2), or a product of two Slater determinants, should the protons and neutrons be treated as distinguishable. This wave function is antisymmetric under the exchange of two particles and fulfills the Pauli exclusion principle.

$$\Psi(\vec{r}_1 \ldots \vec{r}_A, t) = \frac{1}{\sqrt{A!}} \begin{vmatrix} \varphi_1(\vec{r}_1, t) & \ldots & \varphi_A(\vec{r}_1, t) \\ \vdots & & \vdots \\ \varphi_1(\vec{r}_A, t) & \ldots & \varphi_A(\vec{r}_A, t) \end{vmatrix} \tag{2}$$

Hartree-Fock calculations generally correspond to the following scheme [2]:

- At the beginning, a mean potential is introduced.

- The Schrödinger equation is solved in this potential for the single particles.

- A new potential is calculated from the obtained wave function.

- The wave function is calculated in a recursion with the new potential until it converges.

Expressing the Hamiltonian by

$$\mathcal{H} \equiv \sum_{i=1}^{A} \left(h_0(\vec{r}_i) + w_i \right)$$

and the wave function by the one-body reduced density matrix $\rho(t)$, the matrix formulation of the TDHF equations is obtained from the von Neumann equation (3), in which $h(\rho(t))$ is given by (4).

$$i\hbar\frac{d\rho(t)}{dt} = [h(\rho(t)), \rho(t)] \tag{3}$$

$$
\begin{aligned}
h_{ij}(\rho) = \quad & h_0(\vec{r_i})\delta_{ij} + \textstyle\sum_{k=1}^A \sum_{l=1}^A \rho_{kl} \left[\int d\vec{r'} \int d\vec{r''} \; \varphi_i^\dagger(\vec{r'})\varphi_l^\dagger(\vec{r''})w(\vec{r'},\vec{r''})\varphi_j(\vec{r'})\varphi_k(\vec{r''}) \right. \\
& \left. - \int d\vec{r'} \int d\vec{r''}\varphi_i^\dagger(\vec{r'})\varphi_l^\dagger(\vec{r''})w(\vec{r'},\vec{r''})\varphi_j(\vec{r''})\varphi_k(\vec{r'}) \right]
\end{aligned}
\tag{4}
$$

However, the pairing forces between identical nucleons with orbitals time-reversed to each other are not yet included in this TDHF approximation. The approximation including them is the time-dependent Hartree-Fock-Bogoliubov method. The inclusion is done by making the substitutions

$$\rho(t) \rightarrow \begin{pmatrix} \rho(t) & \kappa(t) \\ -\kappa^\dagger(t) & 1 - \rho^\dagger(t) \end{pmatrix}$$

$$h(\rho(t)) \rightarrow \begin{pmatrix} h(\rho(t)) - \mu(t) & -\Delta(t) \\ \Delta^\dagger(t) & -h^\dagger(\rho(t)) + \mu(t) \end{pmatrix}$$

in (3), with $\mu(t)$ the chemical potential, $\kappa(t)$ the pairing tensor and $\Delta(t)$ the pairing potential [3].

The time-dependent Hartree-Fock-Bogoliubov equations are very hard to solve. First calculation results on the mass yields and kinetic energies of ^{238}U fission fragments based on this approach have been published by Goutte, Berger and Gogny in 2006. They agreed fairly well with experimental data [4].

1.2.2 Stochastic Approaches

Stochastic approaches have been developed in order to handle the enormous dimensions encountered in the microscopic description of the fission process. They have been applied to this problem from the late 1970s on. Compared to microscopic approaches, they provide better insight into collective fission dynamics [3]. Older stochastic approaches are based on the solution of Fokker-Planck equations, which is however only possible in special and mostly too simple cases. Newer approaches are based on the calculation of single random trajectories in phase space by the solution of dynamical Langevin equations. They have been applied since the 1990s and enable the solution of more complex problems. On the other hand, the calculation of a sufficient number of trajectories demands high computational efforts [5].

In applications of the Fokker-Planck equations, the total system is separated into two interacting subsystems of intrinsic nucleonic and carefully chosen collective degrees of freedom ξ_j and q_i. A weak coupling $V(\xi_j, q_i)$ between the two systems is assumed. The Hamiltonian has the form of (5), with π_j and p_i being the conjugate momenta of ξ_j and q_i.

$$\mathcal{H}(\xi_j, \pi_j, q_i, p_i) = \mathcal{H}_{intr}(\xi_i, \pi_i) + \mathcal{H}_{coll}(q_i, p_i) + V(\xi_j, q_i) \tag{5}$$

Several additional assumptions have to be introduced to derive the equation describing the fluctuations of the collective variables q_i. The relaxation time of collective degrees of freedom is assumed to be much longer than that of intrinsic ones, and an adiabatic collective motion is assumed. Some other assumptions are made with respect to the characteristics of $V(\xi_j, q_i)$. The time evolution of the density distribution $P(q_i, p_i, t)$ is then described by a classical Fokker-Planck equation (6), with the "collective potential energy" E_{pot} as well as the inertial (B_{ij}), friction (γ_{ij}) and diffusion tensors (D_{ij}) which are obtained from linear response theory. Between the diagonal elements of these tensors, the Einstein relation (7,8) holds, where T denotes the nuclear temperature and ω_l a local frequency.

$$
\begin{aligned}
\frac{\partial P(q_i, p_i, t)}{\partial t} = & \left\{ \sum_{m=1}^{N} \left[\sum_{j=1}^{N} -(B^{-1})_{mj} p_j \right] \frac{\partial}{\partial q_m} \right. \\
& + \sum_{j=1}^{N} \left[\sum_{l=1}^{N} \gamma_{ml}(B^{-1})_{lj} \right] \frac{\partial}{\partial p_m} p_j + \sum_{m=1}^{N} \left[\frac{\partial E_{pot}}{\partial q_m} \right. \\
& \left. + \sum_{j=1}^{N} \left(D_{mj} \frac{\partial}{\partial p_j} + \frac{1}{2} \sum_{l=1}^{N} \frac{\partial (B^{-1})_{jl}}{\partial q_m} p_l p_j \right) \right] \frac{\partial}{\partial p_m} \right\} \cdot P(q_i, p_i, t)
\end{aligned} \tag{6}
$$

$$D_{ll}(q_i, T) = \gamma_{ll}(q_i) \cdot \frac{\hbar \omega_l(q_i)}{2} \cdot \left| \coth \left(\frac{\hbar \omega_l(q_i)}{2T} \right) \right| \tag{7}$$

$$\omega_l(q_i) = \sqrt{\frac{1}{B_{ll}(q_i)} \cdot \frac{\delta^2 V(q_i)}{\delta q_l^2}} \tag{8}$$

From the solution of these equations, e. g. dynamical times, fission decay widths and variances of fission fragment yield distributions may be obtained. Moreover, these calculations showed the correlations of the trajectory in phase space before and after the saddle point to be very small, which justifies the sole consideration of the path between saddle and scission point in the modelling of the fission process [3].

A set of collective coordinates q_i with conjugate momenta p_i is also chosen in the application of the Langevin equations, which are coupled equations of the form (9). At this point, an approach of Ryabov et al. [6] is described.

$$
\begin{aligned}
\frac{dq_i}{dt} &= \mu_{ij} p_j \\
\frac{dp_i}{dt} &= -\frac{1}{2} p_j p_k \frac{\partial \mu_{jk}}{\partial q_i} + Q_i - \gamma_{ij} \mu_{jk} p_k + \theta_{ij} \xi_j(t)
\end{aligned} \tag{9}
$$

The indices i imply summation over all collective coordinates. Q_i is the driving force and $\gamma_{ij}(\vec{q})$ the friction tensor, which is related to the temperature T and the random force θ_{ij} by (10). T is determined from the Fermi gas formula

$$T = \sqrt{\frac{E_{intr}^*}{a(\vec{q})}}$$

with the intrinsic excitation energy E^*_{intr} and the deformation dependent level density parameter $a(\vec{q})$. The tensor of inertia is represented by μ_{ij} and the normalized random variable $\xi_j(t)$ is assumed to be white noise.

$$\sum_k \theta_{ik}\theta_{kj} = T\gamma_{ij} \tag{10}$$

In their calculations, Ryabov et al. used the three parameters of the $\{c, h, \alpha\}$ nuclear shape parameterization as collective coordinates.

From calculations based on the Langevin equations, insight into dynamical effects of the fission process has been obtained [4]. This is an important benefit from this approach, since it justifies a rather simple modelling of the fission process which will be discussed in sections 1.10 and 1.11.

1.2.3 Deterministic Approaches

The application of deterministic approaches is generally rather easy, and several models have been developed in the past. However, they provide a less complete description of the fission process than microscopic or stochastic approaches, and their results did not always agree well with experimental data. In fact, deterministic approaches can be very useful if they are based on physically well-founded approximations, which are found by more sophisticated models. The assumptions made in the past to establish deterministic approaches are, however, not always physically justified. Deterministic approaches often require additional inputs from empirical information. In the following, two rather successful examples will be discussed.

According to the transition state method, which was first applied by Nix and Swiatecki in 1965, statistical equilibrium is assumed at the saddle point [3]. At first, the normal modes of oscillation $\widetilde{q}_i$ about the saddle point shape are determined, and the probability densities of their coordinates and conjugate momenta are given by Gaussians (11,12), which depend on the nuclear temperature T as well as the eigenvalues $\widetilde{\kappa}_i$ and $\widetilde{B}_i$ of the stiffness and inertia tensors. With respect to the fission mode $\widetilde{q}_1$, the system is unstable, and the density is assumed as (13,14), corresponding to a slow fission velocity.

$$P(\widetilde{q}_i) = \sqrt{\frac{\widetilde{\kappa}_i}{\pi}} \cdot \sigma_i \cdot e^{-\widetilde{\kappa}_i \sigma_i^2 \widetilde{q}_i^{\,2}} \tag{11}$$

$$P(\widetilde{p}_i) = \frac{\sigma_i}{\sqrt{\pi \widetilde{B}_i}} \cdot e^{-\frac{\sigma_i^2 \widetilde{p}_i^{\,2}}{\widetilde{B}_i}} \tag{12}$$

$$\sigma_i^2 = \frac{1}{\hbar \omega_i} \tanh\left(\frac{\hbar \omega_i}{2T}\right) \qquad \omega_i = \sqrt{\frac{\widetilde{\kappa}_i}{\widetilde{q}_i}}$$

$$P(\widetilde{q}_1) = 1 \tag{13}$$

$$P(\widetilde{p}_1) = \frac{1}{2T\sqrt{\pi \widetilde{q}_1}} \cdot e^{-\frac{\widetilde{p}_1^{\,2}}{2T\widetilde{B}_1}} \tag{14}$$

The coordinates $\widetilde{q}_i$, $\widetilde{p}_i$ are then transformed into the system of the collective degrees of freedom q_i to be investigated, and the time evolution is obtained from classical mechanics by the solution of the Hamilton canonical equations. This approach requires some computational effort, especially if shell effects and dissipation are included. However, it correctly reproduces many features of the fission process, and is independent of the choice of a scission point configuration [3].

The random neck rupture model developed by Brosa in 1983 [3, 7] is one more frequently used deterministic approach. It explains the mass yield curves as the result of pre-scission

shapes with long and straight necks which may rupture by surface tension at random positions. The shape of the fissioning nucleus is assumed as rotationally symmetric and parameterized by (15), whereas due to boundary conditions $\frac{r_1}{r_2}$ and l are the only free parameters. For illustration, see Fig. 1. The point at which the neck ruptures is denoted by ζ_r. Finally, the mass yields for a specific fission channel are calculated via a Boltzmann factor (16), where the surface tension γ_0 is given by (17) and T is a function of the total excitation energy at scission.

$$
\rho(\zeta) = \left\{
\begin{array}{ll}
\sqrt{r_1^2 - \zeta^2} & -r_1 \leq \zeta \leq \zeta_1 \\
r + a^2 c \cdot \left[\cosh\left(\frac{\zeta - z + l - r_1}{a}\right) - 1\right] & \zeta_1 \leq \zeta \leq \zeta_2 \\
\sqrt{r_2^2 - (2l - r_1 - r_2 - \zeta)^2} & \zeta_2 \leq \zeta \leq 2l - r_1
\end{array}
\right. \tag{15}
$$

$$
Y(A) \propto \exp\left[-\frac{2\pi\gamma_0}{T}\left(\rho^2(\zeta_r(A)) - \rho^2(\zeta)\right)\right] \tag{16}
$$

$$
\gamma_0 = 0.9517\,\frac{\text{MeV}}{\text{fm}^2} \cdot \left[1 - 1.7828 \cdot \left(\frac{N_{CN} - Z_{CN}}{A_{CN}}\right)^2\right] \tag{17}
$$
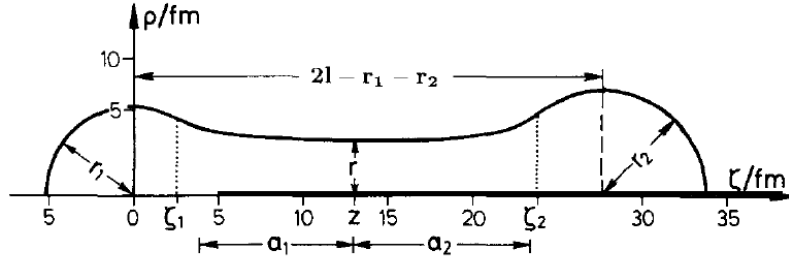
Figure 1: Flat-neck parameterization of Brosa's random neck rupture model [7].

The random neck rupture model is very different from other approaches, and also reproduces quite well the observed total kinetic energies of the distinct fission channels. However, the application of the model requires the determination of the scission point shape as well as, to some extent, empirical information [3, 7].

1.3   The Nuclear Potential

The task of describing the nuclear fission process motivates general investigations of the nuclear potential which determines nuclear deformation energies, nucleon binding energies and the Q values of nuclear reactions. It is especially interesting to investigate the characteristics of fission barriers. The nuclear potential can be calculated by the liquid drop model, which coarsely describes the nuclear potential neglecting almost all quantum-mechanical effects. These are included in the shell model, and are observed to cause deviations from the liquid drop potential, the so-called "shell corrections". Shells also have an important impact on the nuclear level density, and shell corrections are used for the empirical description of nuclear level density parameters. The shell corrections can be obtained using the Strutinsky method, which is a combination of the liquid drop model with the shell model.

1.3.1   Liquid Drop Model

The liquid drop model (LDM) is the oldest approach to the calculation of nuclear binding energies E_B as well as deformation energies. It treats the nucleus macroscopically as a charged liquid drop, taking into account the effects of the short-ranged strong interaction and the long-ranged Coulomb interaction. They are expressed by a formula consisting of a volume term, a surface term, a coulomb term and an asymmetry term. The first liquid drop formula was stated by Bethe and Weizsäcker in 1935. Advanced liquid drop formulae have been found e. g. by Myers and Swiatecki in the 1960s [3] or by Pearson in 2001 [8]. The description from Pearson (18) is presented here because it has been used for the derivation of the empirical formulae (42,43) to describe nuclear level density parameters [8]. Compared to the formula of Bethe and Weizsäcker, it contains an additional "surface-symmetry" term.

$$E_B(Z,A) = a_{vol} \cdot A + \underbrace{a_{sf} \cdot A^{\frac{2}{3}}}_{-E_s(0)} - \underbrace{\frac{1}{4\pi\varepsilon_0} \cdot \frac{3e^2}{5r_0} \cdot \frac{Z^2}{A^{\frac{1}{3}}}}_{E_c(0)} + \underbrace{\left(a_{sym} + \underbrace{a_{ss} \cdot A^{-\frac{1}{3}}}_{\text{new term}}\right) \cdot \frac{(A-2Z)^2}{A}}_{\text{asymmetry term}} \quad (18)$$

The values of the five fit parameters in (18) are listed below.

$$a_{vol} = 15.65\,\text{MeV} \quad a_{sf} = -17.63\,\text{MeV}$$

$$a_{sym} = -27.72\,\text{MeV} \quad a_{ss} = 25.60\,\text{MeV}$$

$$r_0 = 1.233\,\text{fm}$$

According to the LDM, all ground state nuclei are expected to be spherical. A quadrupole deformation a_{20} of the nucleus leads to an increase of its surface energy E_s and to a decrease of its Coulomb energy E_c, which behave like

$$E_s(a_{20}) = E_s(0) \cdot \left(1 + \frac{2}{5}a_{20}^2\right)$$

12

$$E_c(a_{20}) = E_c(0) \cdot \left(1 - \frac{1}{5}a_{20}^2\right)$$

whereas the shape $R(\Theta, \varphi)$ of the deformed nucleus is expressed by a spherical multipole expansion according to (19).

$$R(\Theta, \varphi) = R_0 \cdot \left[1 + \sum_{l,m} a_{lm}Y_{lm}(\Theta, \varphi)\right] \tag{19}$$

Thus, the nucleus will only be stable against spontaneous fission if the increase in surface energy is larger than the decrease in Coulomb energy, i. e.

$$E_c(0) < 2E_s(0)$$

which, according to the LDM, is the case if $\frac{Z^2}{A} < 50$. The fission barrier calculated by the LDM is single-humped as a function of deformation and, as a function of the nascent fragment mass, shows a minimum for symmetric splits of all nuclei with $\frac{Z^2}{A} > 19.8$. This value $\frac{Z^2}{A} = 19.8$ is called the "Businaro-Gallone point". The generally predicted spherical ground state shapes and the derived characterisics of the fission barrier contradict to experimental observations. The fermionic nature of nucleons is the only quantum-mechanical effect taken into account by the liquid drop model. It manifests itself in the so-called "asymmetry term" [10]. Since all other quantum-mechanical effects are neglected, the model is clearly insufficient for the description of the fission process [3].

1.3.2 Shell Model

The nuclear shell model was developed in 1949 by H. Jensen and M. Goeppert-Mayer. In the original model, nucleons were treated as non-interacting particles in an average potential consisting of a spherical central potential V_C and a spin-orbit interaction V_{LS}. The single-particle levels ε_ν are obtained from the solution of the Schrödinger equation with the Hamiltonian being

$$\mathcal{H} = -\frac{\hbar^2}{2m}\Delta + V_C(r) + V_{LS}(r) \cdot \frac{\left\langle \vec{L} \cdot \vec{S} \right\rangle}{\hbar^2}$$

In 1955 a deformed central potential $V_C(r, \Theta)$ was introduced by Nilsson. With this approach, the potential energy of non-magic nuclei was found to reach a minimum in a deformed shape, and deformed ground state shapes could be explained.

Although the shell model considers the quantum-mechanical effects neglected by the LDM, its accuracy with respect to nuclear potential calculations is limited. The errors originate from the neglect of residual interactions between the nucleons and the limited precision of the average potential. They lead to a systematic distortion of the result for the total energy, which is expressed as

$$U = \sum_\nu 2n_\nu \varepsilon_\nu$$

in case of an even-even nucleus, with the occupation numbers n_ν. Thus, the shell model itself could not compete with liquid drop potential calculations. However, it was able to explain the observed magic numbers (2, 8, 20, 28, 50, 82, 126) of protons and neutrons in atomic nuclei [3, 10].

1.3.3 Strutinsky Method

Nevertheless, there is a method of combining the LDM with the shell model that exploits the specific advantages of both models. It was proposed by Strutinsky in 1966 and is also called "macroscopic-microscopic approach" or "shell correction method". The method consists of adding a shell correction δU and a pairing correction δP to the liquid drop potential:

$$E = E_{LDM} + \delta U + \delta P$$

The shell correction is then expressed by the chemical potential μ and the single-particle levels ε_ν obtained from the shell model, with μ being determined by the number of particles N in (21). For the blurring parameter, $\gamma = 10\,\text{MeV}$ is a suitable value.

$$\delta U = \sum_\nu 2n_\nu\varepsilon_\nu - \frac{2}{\sqrt{\pi}\gamma} \int_{-\infty}^{\mu} d\varepsilon\, \varepsilon \cdot \sum_\nu e^{\frac{(\varepsilon-\varepsilon_\nu)^2}{\gamma^2}} \tag{20}$$

$$N = \frac{2}{\sqrt{\pi}\gamma} \int_{-\infty}^{\mu} d\varepsilon \sum_\nu e^{\frac{(\varepsilon-\varepsilon_\nu)^2}{\gamma^2}} \tag{21}$$

This method of adding a small shell correction δU to the dominating liquid drop potential E_{LDM} suppresses the systematic errors originating from the approximations made in the shell model. It thus leads to more precise results for the nuclear potential [3]. Finally, the effects from proton and neutron pairing are included by the pairing correction δP, which can be approximately calculated [5, 11] as

$$\delta P \approx \begin{cases} -\frac{1}{4}\Delta^2 \cdot g(\varepsilon_F) & \text{for even } Z, N \\ -\frac{1}{4}\Delta^2 \cdot g(\varepsilon_F) + \Delta & \text{for odd } A \\ -\frac{1}{4}\Delta^2 \cdot g(\varepsilon_F) + 2\Delta & \text{for odd } Z, N \end{cases} \tag{22}$$

with the average pairing gap $\Delta = \frac{12\,\text{MeV}}{\sqrt{A}}$ and $g(\varepsilon_F)$ being the single-particle level density at the Fermi energy, which is related by (23) to the Fermi gas level density parameter a (39).

$$g(\varepsilon_F) = \frac{6}{\pi^2} \cdot a \tag{23}$$

1.4 Properties of the Nuclear Potential Landscape

1.4.1 Macroscopic-microscopic Calculations

The macroscopic-microscopic approach presented in the last paragraph enables a realistic calculation of the potential landscape in deformation space. From the observation of different fission modes whose weights vary with the excitation energy of the compound nucleus, one may already expect several paths leading over distinct saddle points in this landscape between the ground state and the scission point. This issue was investigated by P. Möller et al. [12] who made extensive nuclear potential calculations in the 1990s using the macroscopic-microscopic approach. The results from these calculations are useful for the determination of fission barrier characteristics, which are required to predict the fractions of these so-called "fission channels", resonance effects in subbarrier fission and variances of mass yield distributions.
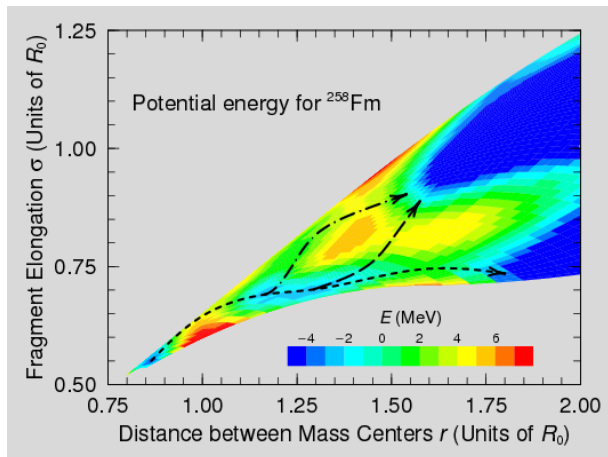
Figure 2: Two-dimensional potential energy landscape for ^{258}Fm, from [12].

When calculating the nuclear potential landscape, one has to be aware that the nuclear potential depends on the exact shape of the fissioning nucleus and even on the proton and neutron distribution. The most simple way is to vary two coordinates, e. g. the mass quadrupole momentum and the neck diameter, keeping other coordinates fixed. This method may already show different fission paths and saddle points in the potential landscape, as shown in Fig. 2. However, this simplification will generally distort the results and thus also the heights and deformation coordinates of saddle points. Contrary to what one would expect, it is not possible either to obtain the correct fission paths and saddle points if the potential is minimized with respect to the other coordinates. Indeed, it is necessary to describe the shape of the fissioning nucleus by at least five coordinates. This implies that the calculation of nuclear potential energy landscapes requires considerable computational efforts. As illustrated in Fig. 2, there are usually two barriers between the ground state

and the scission point with a minimum in between, the so-called isomeric well. The most precise way of investigating the heights of saddle points along the fission path in a five-dimensional deformation space is to apply a "flooding method" starting at the ground state deformation and looking at which level the isomeric well or the scission point "become wet".
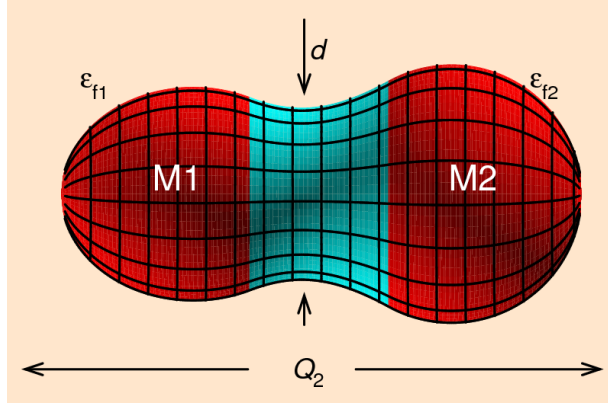
Figure 3: Deformation coordinates used by Möller et al. [12]

The deformation coordinates used by Möller et al. are the quadrupole momentum, the mass asymmetry, the deformations of the two fragments and the neck diameter, as shown in Fig. 3. The ratios of proton and neutron numbers were assumed to be identical for both fragments. Charge polarization could be included in future investigations as a sixth dimension.

Möller et al. found that multiple fission paths are found for most nuclei. These paths lead over different saddle points in the potential energy landscape, with the one leading to symmetric fission being between one and two MeV higher than the one leading to asymmetric fission for most actinide nuclei. Due to low separating ridges between the symmetric and asymmetric fission valleys behind the outer saddle point, later transitions between them cannot generally be excluded by nuclear potential calculations. Fig. 2 nicely shows the different fission paths leading over one common inner barrier, through the isomeric well and over specific outer barriers, leading to compact or elongated scission configurations. The short-dashed line probably corresponds to the so-called "standard 1" channel, the long-dashed line might be the "standard 2" and the dash-dotted line might be the "superlong" channel. This issue will be discussed in the following sections.

1.4.2 Cayley Tree

The Cayley tree from Brosa et al. [7] shown in Fig. 4 gives a detailed description of the structure of fission paths in the potential energy landscape. The weights of the illustrated "superasymmetric" and "supershort" channels are generally very small. The mass-asymmetric standard channels are the most important for fissioning nuclei with $A > 227$, and sometimes there is even significant contribution from the standard 3 channel, which is not shown here. A shortcoming in Fig. 4 is that the superlong barrier is in fact less elongated than illustrated.

Thus, on its way to fission, a nucleus with a deformed ground state will generally pass the inner barrier towards the isomeric well. It then may pass several outer barriers, mainly the standard and superlong barriers. According to [7], there is a bifurcation between the distinct standard channels after the standard barrier, followed by separate secondary barriers. It is still a subject of debate whether the standard 1 and standard 2 channels have different outer saddle points or there is a common outer saddle with a bifurcation behind [5]. Finally, the fractions of the specific fission channels are related to the penetrabilities of their paths in deformation space.
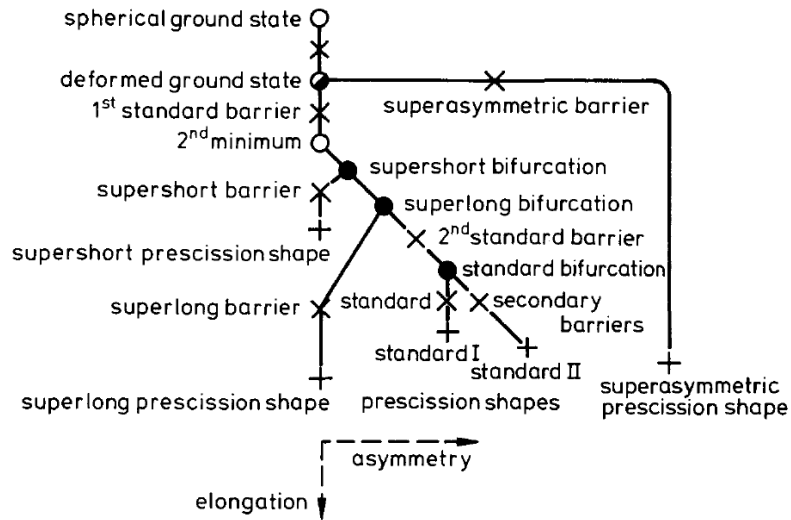
Figure 4: Cayley tree of fission paths, from [7].

1.5 Multichannel Theory
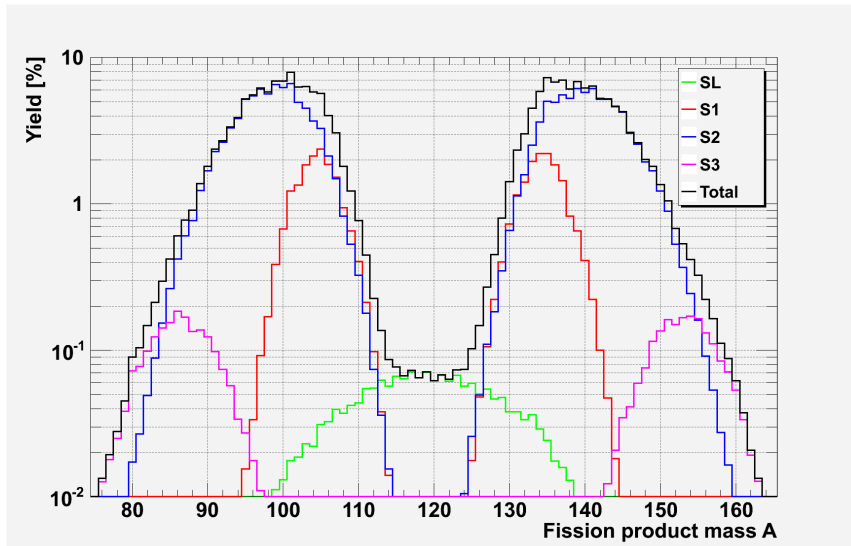
Figure 5: Contributions of single fission channels to the post-neutron mass distribution of $^{241}Pu(n_{th}, f)$, obtained from a calculation with GEF 2010/5.

The different fission channels predicted by nuclear potential calculations manifest themselves in several fission observables and their correlations. From the current point of view, there is experimental evidence for the existence of one mass-symmetric and three mass-asymmetric fission channels, which can be distinguished experimentally with respect to the proton and neutron number distributions of fragment yields, kinetic energies as well as the numbers of prompt neutrons and gammas emitted. Each of them contributes to the total fission product yields, as shown in Fig. 5. The mass-asymmetric fission channels are attributed to shell effects in the nascent fragments.

The multichannel theory was already introduced by Turkevich and Niday in 1951 [3], whereas the current explanation of the "superlong", "standard 1" and "standard 2" channels was stated by Wilkins, Steinberg and Chasman in 1976 [13].

1.5.1 Superlong Channel

The superlong (SL) channel is the dominating fission channel of most nuclei with masses $A < 227$. In the case of the heavier nuclei relevant for reactor applications, its fraction is very small at low excitation energy, but strongly energy dependent. This channel is characterized by a wide mass distribution, an extraordinary low total kinetic energy (TKE) and a high prompt neutron multiplicity.

18

The SL channel is attributed to the liquid-drop potential, which favors symmetric fission of heavy nuclei above the Businaro-Gallone point ($\frac{Z^2}{A} > 19.8$). However, for masses $A > 227$ strong shell effects are not too far from symmetry (see Fig. 7), leading to lower outer saddle points for asymmetric mass splits. In the scission configuration both fragments are strongly elongated, causing a high excitation energy gain when they relax into their ground state deformation. Small shell effects appearing in symmetric splits may modulate specific nuclide yields from this channel as well as its total fraction, but are too weak to generate a fission channel [25].

1.5.2 Standard 1 Channel

In most nuclei, the standard 1 (S1) channel corresponds to an asymmetric mass split. It is characterized by a high TKE of the fission fragments and a strong charge polarization, manifesting itself in an extraordinary high $\frac{N}{Z}$ ratio in the heavy fragment. As shown by Fig. 6, the neutron emission from the heavy fragment is low, but rather high from the light fragment. A dip in the prompt gamma multiplicity is observed for the heavy fragments from this channel (see Fig. 10), indicating that their spin is low. The width of the S1 mass distribution is small.

This fission channel is generally attributed to the influence of the $Z = 50$ and $N = 82$ shells, which favors the formation of a heavy fragment close to the doubly magic ^{132}Sn. This fragment is close to spherical at its formation as well as in its ground state, which explains its low prompt gamma multiplicity (see section 1.14 for details) and its low excitation energy, manifesting itself in the low neutron multiplicity. The light fragment, on the other hand, is deformed at its formation and exhibits higher excitation energy and spin. The distance between saddle and scission point is rather short for this channel.

The S1 channel is the reason for the short spontaneous fission half lives in the heavy fermium region, where both fragments are close to ^{132}Sn. There it leads to symmetric splits, competing with the SL channel. Even in this case, the S1 and SL channels can be distinguished by their mass widths and total kinetic energies. Among uranium and plutonium isotopes, the S1 fraction is observed to be higher for heavy isotopes, where the $\frac{N}{Z}$ ratio is closer to that of ^{132}Sn.

It was found experimentally that the mean proton number of the heavy fragment from the S1 channel stays rather constant at $\overline{Z_{S1,h}} \approx 52.5$ for different fissioning nuclei, whereas the neutron number varies [14]. The number is observed to decrease slightly for an increasing neutron number of the fissioning nucleus. K.-H. Schmidt [1, 15] found that these slight variations can be described by the empirical formula (24).

$$\overline{Z_{S1,h}} = \frac{70}{3} \cdot \frac{Z_{CN}^{1.3}}{A_{CN}} + 16.5 \tag{24}$$

1.5.3 Standard 2 Channel

The standard 2 (S2) channel is the dominating fission channel for most nuclei with a mass $A > 227$. Its average mass split is more asymmetric than that of the S1 channel. The channel is characterized by an intermediate TKE and a $\frac{N}{Z}$ ratio closer to that of the compound nucleus. The mean numbers of neutrons emitted from each fragment are intermediate and comparable to each other. The mass distribution of the S2 channel is significantly broader than that of the S1 channel.

Wilkins, Steinberg and Chasman found that this channel is attributed to a $N = 88$ neutron shell with a deformation of $\beta \approx 0.65$ in the heavy fragment. Thus, both nascent fragments are assumed to be moderately deformed, which is in accordance with the observed excitation energies. The saddle-to-scission distance is somewhat longer than for the S1 channel.

However, although this channel is attributed to a neutron shell only, $\overline{Z_{S2,h}}$ is also observed to remain rather constant at $\overline{Z_{S2,h}} \approx 55$. This was a surprising result of fission experiments with many exotic nuclei performed at GSI Darmstadt [16], especially since the existence of a proton shell in the heavy fragment could not be confirmed by theoretical calculations. The nearly constant $\overline{Z_{S2,h}}$ is possibly caused by more complex dynamical effects.

Similarly, the systematics of $\overline{Z_{S2,h}}$ are described by the following formula [1, 15]:

$$\overline{Z_{S2,h}} = \frac{65}{3} \cdot \frac{Z_{CN}^{1.3}}{A_{CN}} + 21.4 \tag{25}$$

1.5.4 Standard 3 Channel

For many nuclei heavier than uranium, there is evidence for another fission channel with even more asymmetric mass splits. It shows up at light fragment masses between $82 \leq \overline{A_{S3,l}} \leq 86$, its distribution width being comparable to that of the S1 channel. In contrary to the S1 and S2 channels, the mean heavy fragment mass is found to vary strongly for fissioning systems. It should be noted that the term "standard 3" (S3) is used by some sources to denote even other physically different fission channels. In this work it denotes the standard 3 channel as described by Mulgin, Okolovich and Zhdanova [17].

The varying mean heavy fragment masses indicate that in this channel the light fragment is stabilized by a shell. Mulgin, Okolovich and Zhdanova attribute it to a close-to-sphere neutron shell $N = 52$ and predict a higher TKE than for the S2 channel at the same split asymmetry due to this spherical shell. However, according to experimental results of Siegler et al. [18] the TKE of the S3 channel is several MeV lower. Due to its small fraction and the coverage by the S2 channel, the S3 channel is hard to observe and not well understood.

1.6 Fission Barrier Transmission

For the determination of fission probabilities and the weights of the distinct fission channels, transmission coefficients of the fission barrier need to be calculated. According to the theory of Bohr and Wheeler, this can be done using the quantum mechanical penetrability of the barrier. This penetrability can be calculated by the following approaches [3]:

- WKB (Wentzel-Kramers-Brillouin) approximation

- Hill-Wheeler approach

The WKB approximation is a general approach to the calculation of quantum mechanical penetrabilities as well as wave functions and their energy eigenvalues in an arbitrary potential $V(x)$. There are, however, some limitations on the applicability of this approximation. Since the WKB approximation is based on the expansion of the wave function in powers of $\hbar$ (26,27), the second term in (27) needs to be small, which cannot assumed to be valid if E is close to the top of the fission barrier.

$$\Psi(x,t) = A(x)e^{\frac{i}{\hbar}(S(x)-Et)} \tag{26}$$

$$S'^2(x) = 2m(E - V(x)) + \hbar^2 \left[\frac{3}{4}\frac{S''(x)^2}{S'(x)^2} - \frac{1}{2}\frac{S'''(x)}{S'(x)} \right] \tag{27}$$

The barrier transmission is reduced to a one-dimensional problem by introducing the deformation parameter η and the inertia of the system $B(\eta)$, which has the unit of a mass. For the penetrability, the WKB approximation yields (28), where $\eta_{1,2}$ are defined by $V(\eta_{1,2}) = E$.

$$P_F(E) = \exp\left[-\frac{2}{\hbar} \int_{\eta_1}^{\eta_2} d\eta \ \sqrt{2B(\eta)\left(V(\eta) - E\right)} \right] \tag{28}$$

Due to the mentioned limits of applicability of the WKB method, except for spontaneous fission transmission coefficients are usually calculated using the Hill-Wheeler penetrability. It expresses the penetrability exactly, assuming $V(\eta)$ to be an inverted parabola and $B(\eta)$ to be constant. According to potential energy calculations, this approximation is justified for the fission barriers of actinide nuclei [19]. The Hill-Wheeler approach yields (29), where ω_F denotes the frequency of the harmonic oscillator described by the inverted fission barrier.

$$P_F(E) = \frac{1}{1 + \exp\left[\frac{2\pi(E_F-E)}{\hbar\omega_F}\right]} \tag{29}$$

The fission transmission coefficients are determined according to (30) by the folding of the penetrability (28,29) with the density of transition states ρ_F on top of the barrier, where ε_c denotes the beginning of the continuum. Above the fission barrier ($E > E_F$) they are essentially determined by the level density, whereas the barrier height and curvature is important for tunneling ($E < E_F$).

$$T_F(E, J^\pi) = \sum_i P_F(E - \varepsilon_i) + \int_{\varepsilon_c}^{\infty} d\varepsilon \; \rho_F(\varepsilon, J^\pi) \cdot P_F(E - \varepsilon) \tag{30}$$

It has to be taken into account that the fission barrier is usually double-humped with a deep minimum in between. If the excitation energy E is higher than the lower one of two barriers A and B, the total transmission coefficient is given by (31).

$$T_F(E, J^\pi) = \frac{T_A(E, J^\pi) \cdot T_B(E, J^\pi)}{T_A(E, J^\pi) + T_B(E, J^\pi)} \tag{31}$$

At lower energies, there are resonances in $T_F(E, J^\pi)$ originating from the double-humped barrier, which show up in sub-barrier fission cross-sections. The WKB approximation, which is valid at energies sufficiently lower than the lower barrier, yields for the total penetrability:

$$P_F(E) = \frac{P_A P_B}{4} \left[\left(\frac{P_A + P_B}{4} \right)^2 \sin^2(\varphi) + \cos^2(\varphi) \right]^{-1} \tag{32}$$

$$\varphi(E) = \frac{1}{\hbar} \int_{\eta_1}^{\eta_2} d\eta \; \sqrt{2B(\eta)\,(E - V(\eta))} \tag{33}$$

In the potential well between the barriers, so-called "class II states" of the compound nucleus exist, which determine the resonances of $T_F(E, J^\pi)$. At this point, the nucleus may decay to lower excitation states in the well. Assuming the well as a harmonic oscillator potential, the resonances are located at energies given by (34), where E_{II}^0 is the minimum of the potential well and ω_{II} the circular eigenfrequency of the oscillator.

$$E_n = E_{II}^0 + \hbar\omega_{II} \cdot \left(n + \frac{1}{2} \right) \tag{34}$$

If there is a decay to a lower class II state, the nucleus may still fission by tunneling through the outer barrier, or it may decay back to the ground state by gamma emission. For the nuclei ^{236}U and ^{238}U, both ways of decay have been observed. For nuclei with higher Z, the decay via isomeric fission strongly dominates, indicating that the ratio $\frac{T_A(E,J^\pi)}{T_B(E,J^\pi)}$ is much smaller. According to calculations based on the Hill-Wheeler approach, the decay constants for class II states are given by (35,36) and the one for spontaneous fission by (37) [3], with $E_{II} = E_{II}^0 + \frac{1}{2}\hbar\omega_{II}$.

$$\lambda_{if} \approx 3.61 \cdot 10^{20} \text{s}^{-1} \cdot \exp\left[-\frac{2\pi}{\hbar\omega_B}(E_B - E_{II}) \right] \tag{35}$$

$$\lambda_\gamma \approx 10^{14} \text{s}^{-1} \cdot \exp\left[-\frac{2\pi}{\hbar\omega_A}(E_A - E_{II}) \right] \tag{36}$$

$$\lambda_{sf} \approx 3.61 \cdot 10^{20} \text{s}^{-1} \cdot \exp\left[-2\pi \left(\frac{E_A}{\hbar\omega_A} + \frac{E_B}{\hbar\omega_B} \right) \right] \tag{37}$$

The results obtained from (35,36) using RIPL-3 parameters [20] are compared to literature values from [21] in Table 1. Due to resonance effects, the ratio $\frac{\lambda_{if}}{\lambda_\gamma}$ may be in fact lower than the calculation. However, the results show the limited precision of the calculation.

Nuclide	Literature Values				Calculated	
	E_{II} [MeV]	J^π	$T_{\frac{1}{2}}$ [ns]	$\frac{\lambda_{if}}{\lambda_\gamma}$	$T_{\frac{1}{2}}$ [ns]	$\frac{\lambda_{if}}{\lambda_\gamma}$ (upper limit)
^{236}U	2.750 ± 0.003	0^+	120 ± 2	0.149 ± 0.069	20.4	1.26
^{238}U	2.5579 ± 0.0005	0^+	280 ± 6	0.0267 ± 0.0041	46.1	$2.45 \cdot 10^3$

Table 1: Decay data of class II states from literature [21] and calculations based on RIPL-3 [20] barrier parameters.

In the modelling of fission product yields, the transmission coefficients are required to determine the weights of the distinct fission channels, which are obtained from the values calculated by (31) for the several outer barriers. For elements up to uranium, the weights are probably mainly determined by the outer barriers, since the ratios $\frac{T_A(E,J^\pi)}{T_B(E,J^\pi)}$ are large [19]. For heavier elements, the outer barriers are lower [20], and the inner barrier may have an impact. Another constraint is that the state density $\rho_F(E, J^\pi)$ depends on shell corrections on top of the fission barrier, which are generally unknown [19]. Thus, in the determination of fission channel weights and their sensitivities to the excitation energy of the system, some assumptions need to be made. To obtain good results, one will need to include experimental information, as provided in section 3.2. It should also be noted that, according to experimental observations, the fractions of fission channels are subject to slight fluctuations in the resonances of the fission cross-section [22].

1.7 The Nuclear Level Density

As shown in the last section, the nuclear level density at the saddle point is needed for the calculation of fission barrier transmission coefficients. Furthermore, the nuclear level density is required for the description of the division of intrinsic excitation energy between the nascent fragments and for the application of the Weisskopf-Ewing and Hauser-Feshbach formalisms to fission fragment deexcitation.

An early approach to an analytical expression of the level density was based on the description of the nucleus as a Fermi gas of non-interacting particles. Due to shell effects and pairing correlations between the nucleons, this description is not valid at low excitation energies. Nevertheless, the Fermi gas level density, which is given by (38), has been frequently used for the description of the nuclear fission process [23]. For a Fermi gas, the level density parameter a does not depend on the excitation energy E. According to [11], a is given by an empirical formula (39) depending on the nuclear mass and surface area, where B_s is the surface area enhancement factor due to deformation.

$$\omega(E) = \frac{\sqrt{\pi}}{12} \cdot \frac{e^{2\sqrt{aE}}}{E^{\frac{5}{4}} \cdot a^{\frac{1}{4}}} \tag{38}$$

$$a = 0.073 \frac{1}{\text{MeV}} \cdot A + 0.095 \frac{1}{\text{MeV}} \cdot B_s \cdot A^{\frac{2}{3}} \tag{39}$$

For the entropy and the temperature (expressed in units of energy) of the system, it holds

$$S(E) = \ln \omega(E) \qquad T(E) = \left(\frac{dS}{dE}\right)^{-1}$$

which yields

$$T(E) = \left(\sqrt{\frac{a}{E}} - \frac{5}{4E}\right)^{-1} \tag{40}$$

for the Fermi gas temperature [24]. However, according to recent findings, the temperature of medium-mass nuclei is observed to be constant at excitation energies up to $E = 20\,\text{MeV}$. Furthermore, this holds for all masses at least up to excitation energies of about 7MeV [23].

Thus, the constant temperature description is appropriate for the description of nuclear fission in the typical neutron spectra of critical fast reactors. It corresponds to an exponential level density

$$\omega(E) = \frac{1}{T} \cdot e^{\frac{E-E_0}{T}} \tag{41}$$

and a linear increase of the entropy with the excitation energy of the system. The constant temperature is explained as the result of a superfluid phase transition in the nucleus, with the excitation energy breaking Cooper pairs of protons and neutrons [23]. Experimental evidence for this nucleon pairing are the enhanced transfer of neutron pairs in peripheral

nuclear collisions and the asymmetry independent even-odd effect of proton number dependent fission yields.

The systematics of the backshift E_0 and the temperature T in (41) have been thoroughly investigated by Till von Egidy et al. [8, 9]. The parameters were found to be well described by empirical formulae (42,43) depending on the mass number A, the shell correction W, W', its derivative $\frac{dW(Z,N)}{dA}$ and the deuteron pairing energy P_d, which are given by

$$W(Z,N) = [m(Z,N) - m_{LDM}(Z,N)] \cdot c^2$$

$$W' = \begin{cases} W - \frac{1}{2}P_d & \text{for even } Z,\ N \\ W & \text{for odd } A \\ W + \frac{1}{2}P_d & \text{for odd } Z,\ N \end{cases}$$

$$\frac{dW(Z,N)}{dA} = \frac{1}{4} \cdot [W(Z+1, N+1) - W(Z-1, N-1)]$$

$$P_d = \frac{1}{2} \cdot (-1)^{Z+1} \cdot [m(Z+1, N+1) - 2m(Z,N) + m(Z-1, N-1)] \cdot c^2$$

and inserted into

$$T = \frac{1}{A^{\frac{2}{3}}} \left(17.45\,\text{MeV} - 0.51 \cdot W'(Z,N) + 0.051 \frac{1}{\text{MeV}} \cdot W'^2(Z,N) \right) \tag{42}$$

$$E_0 = \begin{cases} -1.24\,\text{MeV} - \frac{1}{2}P_d + 0.33 \cdot \frac{dW(Z,N)}{dA} & \text{for even Z, N} \\ -1.33\,\text{MeV} - \frac{1}{2}P_d + 0.90 \cdot \frac{dW(Z,N)}{dA} & \text{for even Z, odd N} \\ -1.33\,\text{MeV} + \frac{1}{2}P_d - 0.90 \cdot \frac{dW(Z,N)}{dA} & \text{for odd Z, even N} \\ -1.22\,\text{MeV} + \frac{1}{2}P_d + 0.33 \cdot \frac{dW(Z,N)}{dA} & \text{for odd Z, N} \end{cases} \tag{43}$$

Apart from shell effects, the intrinsic nuclear temperature (42), which is the average energy per excited nucleon, is found to be proportional to $A^{-\frac{2}{3}}$, i. e. to the reciprocal of the nuclear surface area. This shows that the number of excited nucleons is proportional to the surface of the nucleus. Another important finding of von Egidy et al. [8, 9] is that enhancement factors to the level density, e. g. for rotation, are not required. The relation between (41) and the state density depending on excitation energy, spin and parity is generally expressed by (44,45).

$$\rho(E, J^\pi) = \frac{1}{2} \cdot \omega(E) \cdot f(J) \tag{44}$$

$$f(J) = e^{\frac{J^2}{2\sigma^2}} - e^{\frac{(J+1)^2}{2\sigma^2}} \tag{45}$$

In the constant temperature model, the spin-cutoff factor σ in (45) is calculated by (46).

$$\sigma = 0.98 \cdot A^{0.29} \tag{46}$$

1.8 The Separability Principle

In the macroscopic-microscopic approach to the fission process, the separability principle [4] is very valuable. According to this principle, the microscopic properties of a fissioning nucleus are already determined by those of the nascent fragments. These microscopic properties are the shell correction energy and the intrinsic nuclear temperatures of the nascent fragments, which are determined by their masses and shell corrections, according to (42). This principle is applicable as soon as the fissioning system has reached a point not far beyond the outer saddle point. For this, there is experimental and theoretical evidence.

Above all, the theoretical evidence originates from two-center shell model calculations which were first performed by Mosel and Schmitt [4]. They found that the influence of fragment shells reaches far into the potential energy landscape. However, another requirement for the applicability of the separability principle is the early preformation of fission fragments. The results of Mosel and Schmitt suggest that the fragments are already strongly preformed when the nuclear shape is necked in to 40%. Calculations based on the Langevin equation of motion show the large inertia of the mass division, which prevents significant changes of fragment masses during the saddle-to-scission time. On the other hand, the inertia of the $\frac{N}{Z}$ degree of freedom is found to be small. In Schmidt's approach, this quantity is thus assumed to be determined at the scission point, which, combined with an empirical shift, gives quite good results. For details, see sections 1.11 and 3.6.

The experimentally observed fragment mass distributions, which are clearly related to shells in the fragments, are another indication for the impact of nascent fragment shells on the potential energy landscape at least up to the outer saddle points. Assuming that the mass split is determined at the outer saddle already, the widths of the experimentally observed fragment mass distributions are better reproduced than with the approach of Wilkins, Steinberg and Chasman [13], in which the potential at the scission point is assumed to be decisive. Finally, the outer fission barrier characteristics derived from experimental fragment mass distributions are in satisfactory agreement with the theoretical predictions of the separability principle, where the macroscopic deformation energy of the nascent fragments and their shell corrections are included.

The applicability of the separability principle makes the macroscopic-microscopic approach particularly strong in its application to the fission process. This is especially due to the fact that different degrees of freedom can be assumed to freeze out at different stages of the fission process, and that the knowledge of inertia and friction tensors is not required.

Finally, there is an important benefit from the separability principle: The predicted individual, constant temperatures of nascent fragments give an explanation for the observed flow of excitation energy between them, which is explained in section 1.9.

1.9 Excitation Energies

For the calculation of fission fragment deexcitation, kinetic energies and even-odd effects in nuclide yields, it is necessary to know the fragment excitation energies. The excitation energy of a fission fragment generally originates from the following three sources:

- The excitation energy brought into the compound nucleus by the incident particle.

- Part of the energy release up to the scission point.

- The fragment deformation induced by Coulomb forces and shell effects during the fission process, which converts into excitation energy when the fragment relaxes to its ground-state deformation after scission.

The energy release up to the scission point is given by (47), which originates from the work of M. Asghar and R. W. Hasse (1984) [1, 25]. It describes the potential energy difference between the SL outer saddle and the scission point as a linear function of $\frac{Z^2}{\sqrt[3]{A}}$. If the compound nucleus excitation energy E_{CN}^* is lower than the SL barrier, the energy release is reduced due to tunneling.

$$
E_{sc} = 0.08\,\text{MeV} \cdot \frac{Z_{CN}^2}{\sqrt[3]{A_{CN}}} - 93\,\text{MeV} - \begin{cases} E_{F,SL} - E_{CN}^* & E_{CN}^* < E_{F,SL} \\ 0 & E_{CN}^* \geq E_{F,SL} \end{cases} \tag{47}
$$

Indeed, there are clear indications for an excitation energy increase with the proton number Z_{CN} of the compound nucleus. These are e. g. the increasing prompt neutron multiplicities. As a consequence, the number of delayed neutrons decreases since they are emitted promptly already. The decreasing even-odd effect in proton number dependent fission yields with increasing Z_{CN} is also related to the increase of E_{sc}, which will be explained in section 1.12.

To take into account the physical effects determining the division of the excitation energy of the fissioning nucleus between the two fragments, one needs to distinguish between intrinsic and collective excitation energy. Intrinsic excitation energy is stored in single-particle and quasiparticle excitations, whereas collective excitation energy is stored in the collective degrees of freedom of the system, i. e. as rotational or vibrational energy. Additionally, E_{sc} also partly ends up in kinetic energy of the fission fragments.

The total intrinsic and collective excitation energy is given by (48,49). According to Schmidt's model, in an even-even nucleus the compound nucleus excitation energy above the barrier ends up in collective excitations if it is lower than the pairing gap, otherwise it ends up in intrinsic excitation energy. The compound nucleus excitation energy is not assumed to contribute to the kinetic energy release.

$$
E_{intr}^* = 0.45 \cdot E_{sc} + \begin{cases} E_{CN}^* - E_F & \text{even-even CN, } E_{CN}^* - E_F \geq 2\Delta \\ E_{CN}^* - E_F & \text{odd-A or odd-odd CN, } E_{CN}^* - E_F \geq 0 \\ 0 & E_{CN}^* - E_F < 0 \end{cases} \tag{48}
$$

$$E^*_{coll} = 0.3 \cdot E_{sc} + \begin{cases} E^*_{CN} - E_F & \text{even-even CN, } 0 \le E^*_{CN} - E_F < 2\Delta \\ 0 & \text{otherwise} \end{cases} \qquad (49)$$

From the nascent fragment temperature difference predicted by the separability principle, a flow of intrinsic excitation energy is expected during the descent from the saddle to the scission point. According to the Fermi gas temperature formula (40), at high excitation energies it holds $E \approx aT^2$, where a is more or less proportional to the mass number (39). Thus, assuming the final fragment temperatures to be equal, the Fermi gas model predicts a division of the excitation energy proportional to the fragment masses:

$$\frac{E^*_{light}}{E^*_{heavy}} = \frac{A_{light}}{A_{heavy}}$$

Up to now, in the modelling of fragment excitation energies such a division has generally been assumed [23], as it is also done in the fission model of TALYS 1.2 [19]. However, several experiments have shown that in low-energy fission the increase of the compound nucleus excitation energy E^*_{CN} ends up in the excitation energy of heavy fragments only, as shown by Fig. 6. As found by Schmidt [23], this is caused by the superfluid phase transition in the nascent fragments which causes their temperatures to stay constant, but maximizes the entropy of the system. The heavier fragment, which usually has the lower temperature (42), attracts all of the additional intrinsic excitation energy.
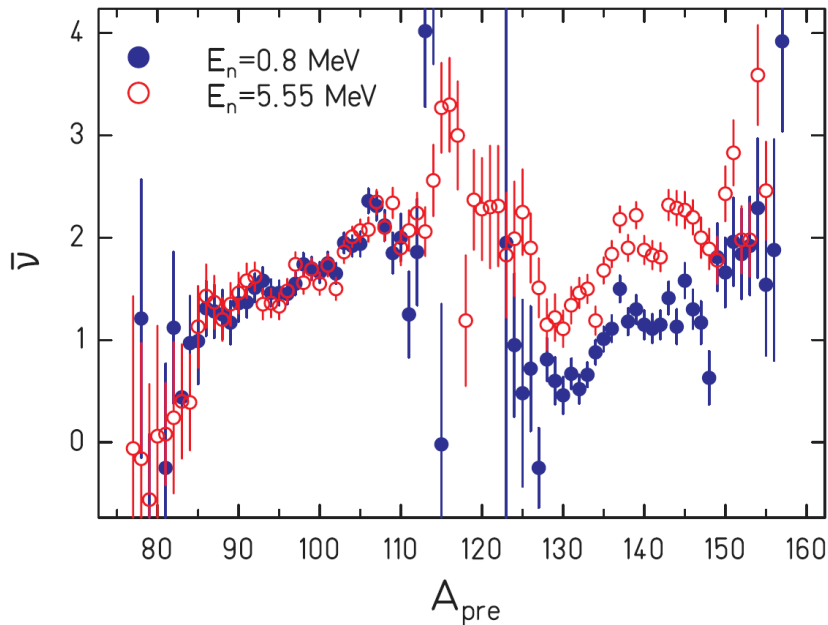
Figure 6: Mass-dependent mean neutron multiplicities of $^{237}Np(n,f)$ at 0.8 MeV and 5.55 MeV incident neutron energy, from [23].

However, one has to take into account that, if the temperature difference is too small, the system does not have enough time to shift the entire intrinsic excitation energy before scission. There are indications for this from the observed even-odd effects in the yields, see section 1.12. In Schmidt's model, the intrinsic excitation energy ending up in the light fragment is thus given by a constant depending on the nascent fragment temperatures, with the remainder ending up in the heavy fragment. The collective excitation energy is generally assumed to be distributed equally between both fragments. Finally, the total fragment excitation energies are given by (50,51). There is still a necessity and possibility to improve this description by a more detailed physical modelling.

$$E^*_{light} = E_{def,light} + \frac{E^*_{coll}}{2} + \begin{cases} \frac{T_{light} \cdot T_{heavy}}{\left| T_{heavy} - T_{light} \right|} & \frac{T_{light} \cdot T_{heavy}}{\left| T_{heavy} - T_{light} \right|} < \frac{E^*_{intr}}{2} \\ \frac{E^*_{intr}}{2} & \text{otherwise} \end{cases} \tag{50}$$

$$E^*_{heavy} = E_{def,heavy} + \frac{E^*_{coll}}{2} + \begin{cases} E^*_{intr} - \frac{T_{light} \cdot T_{heavy}}{\left| T_{heavy} - T_{light} \right|} & \frac{T_{light} \cdot T_{heavy}}{\left| T_{heavy} - T_{light} \right|} < \frac{E^*_{intr}}{2} \\ \frac{E^*_{intr}}{2} & \text{otherwise} \end{cases} \tag{51}$$

In this work, Schmidt's model was found to give a wrong reproduction of the experimentally observed even-odd effect in the mean kinetic energies of fission fragments depending on their proton number. Indeed, there is an even-odd effect in the $\overline{TXE}(Z)$, resulting in a staggering of the mean kinetic energies which is significantly smaller than it is expected from the staggering of the Q value. Lang et al. [26] explain this as the result of proton pair breaking. According to their explanation, even-Z fragments from even-Z compound nuclei may either originate from a superfluid fission process in which all protons stay paired or a proton pair may be broken on the fission path. If a proton pair is broken, the required energy is taken from the pre-scission kinetic energy of the system, leading to an enhancement of the mean total excitation energy of splits into two even-Z fragments. The results from benchmarking the model are given in sections 3.4 and 3.5.

1.10 Mass Distributions

The mass distributions of fission fragment yields are well described by a superposition of several Gaussians which is illustrated in Fig. 5. Besides calculating the fractions of the distinct fission channels, the modelling of these distributions includes the determination of the central values and widths of the Gaussians.

Regarding the central values, one needs to consider the empirical finding that for different systems, the yields of heavy fragments from the S1 and S2 channels are located at rather constant Z values, which are given by (24,25). The corresponding central mass values can be obtained from these values $\overline{Z_{ch}}$ using a scission-point model which is described in section 1.11. With this model, the $\overline{Z}(A)$ values are calculated, and used in a recursion (52,53).

$$\overline{A_1} = \frac{A_{CN}}{Z_{CN}} \cdot \overline{Z_{ch}} \tag{52}$$

$$\overline{A_{i+1}} = \frac{A_{CN}}{Z_{CN}} \cdot \left[\overline{Z_{ch}} - \left(\overline{Z}([\overline{A_i} + \frac{1}{2}]) - Z_{ucd}([\overline{A_i} + \frac{1}{2}]) \right) \right] \tag{53}$$

Since, as mentioned before, calculations based on the Langevin equation of motion show the large inertia of the mass-asymmetry degree of freedom in the fission process [4], the pre-neutron mass distribution of fragment yields must be strongly influenced by the potential energy at the fission barrier as a function of mass asymmetry. Indeed, the mass asymmetry of a nuclear fission process can be assumed to be determined not far beyond the outer saddle point along the fission path. According to the liquid drop model, the barrier height as a function of the nascent fragment mass is represented by a wide parabola [27], which explains the large width of the superlong channel in the mass yield distribution. The asymmetric fission channels are related to rather narrow valleys on top of this macroscopic potential, which are caused by shell effects. If these valleys are close to symmetry, they have a lower minimum than the macroscopic potential, which leads to preferentially asymmetric mass splits. The curvature of the macroscopic potential also influences the height of the saddle points attributed to the asymmetric channels. This is illustrated by Fig. 7.

The curvature of the macroscopic potential as a function of mass asymmetry $\frac{d^2V}{d\eta^2}$ has been investigated by several authors. According to Schmidt [1, 15], the experimentally observed transition to symmetric fission of neutron deficient light actinides is best reproduced by a monotonic increase of $\frac{d^2V}{d\eta^2}$ with the fissility parameter $\frac{Z_{CN}^2}{A_{CN}}$. The curvature as a function of mass asymmetry η (54) is expressed by (55) for the SL channel. For a given nascent fragment mass, the potential energy at the fission barrier is then calculated by (56,57).

$$\eta = \frac{4}{A_{CN}} \cdot \left(A - \frac{A_{CN}}{2} \right) \tag{54}$$

$$\frac{d^2V}{d\eta^2} = 2.59 \cdot 10^{-6} \, \text{MeV} \cdot \left(\frac{Z_{CN}^2}{A_{CN}} \right)^{4.58} \tag{55}$$

30
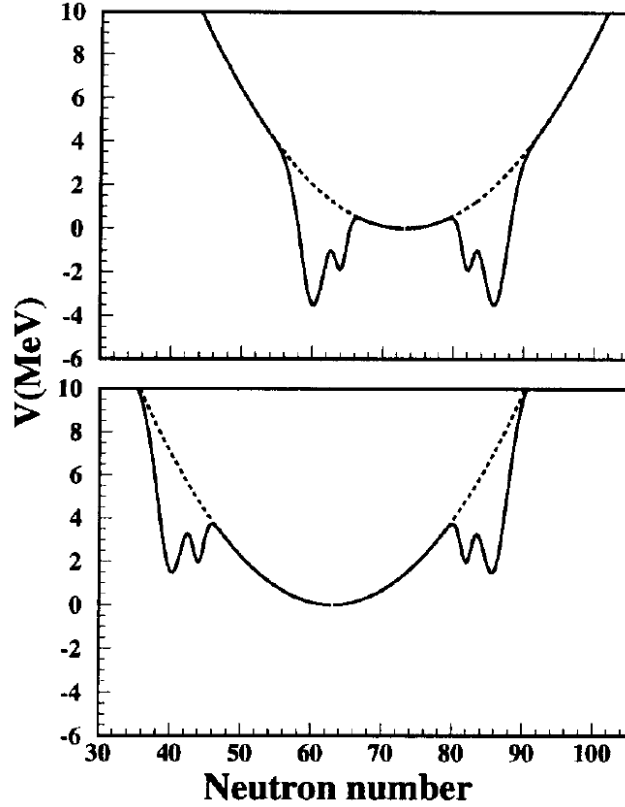
Figure 7: Potential energy at the fission barrier as a function of the fragment neutron number for the compound nuclei ^{238}U (upper part) and ^{208}Pb (lower part), from [27].

$$V(A) = C \cdot \left(A - \frac{A_{CN}}{2} \right)^2 \tag{56}$$

$$C = \frac{8}{A_{CN}^2} \cdot \frac{d^2 V}{d\eta^2} \tag{57}$$

For the width of the mass yield distribution, which is related to the potential curvature as well as the excitation energy of the system, there is a statistical description. The nascent fragment mass, which is a collective degree of freedom of the system, can be considered as the coordinate of a harmonic oscillator whose potential is described by (56). The width of the distribution is then determined by the wave functions of the harmonic oscillator states. In a canonical ensemble of particles, the occupation of these harmonic oscillator states is described by a Boltzmann distribution characterized by a collective temperature T_{coll}. According to Bohr's transition state principle, at the saddle point thermal equilibrium is assumed between all degrees of freedom. Thus, the collective temperature T_{coll} is assumed to be equal to the intrinsic temperature at the saddle point [5].

31

With the circular eigenfrequency ω of the oscillator, in the canonical ensemble the width σ of the mass distribution is given by (58), which is obtained from folding the probability distribution of all states with the Boltzmann distribution. The frequency ω itself may be calculated by a stochastic approach using the Einstein relation (8). In the limits of a very high or very low collective temperature, the width is given by (59).

$$\sigma^2 = \frac{\hbar\omega}{2C} \cdot \coth\left(\frac{\hbar\omega}{2T_{coll}}\right) \tag{58}$$

$$\sigma^2 = \begin{cases} \frac{\hbar\omega}{2C} & T_{coll} \ll \hbar\omega \\ \frac{T_{coll}}{2C} & T_{coll} \gg \hbar\omega \end{cases} \tag{59}$$

As it is shown by these equations, the width depends on T_{coll}, but not directly on the excitation energy of the system. However, they have been derived assuming a canonical ensemble of nucleons, whereas a nucleus is a mesoscopic system, and the excitation energy for a certain degree of freedom is limited. In fact, a nucleus is better described as a microcanonical ensemble, where the occupation of states does not correspond to a Boltzmann distribution and is truncated at the total excitation energy of the system. This is assumed to cause the broadening of the width of the mass yield distribution with increasing excitation energy, whereas the collective temperature T_{coll} can, following Bohr's transition state principle, assumed to be constant at excitation energies relevant in fast reactor neutron spectra [15, 23, 25].

The treatment of the mass width, which was described for the SL channel here, is performed for the asymmetric channels analogously. Their potential curvatures can be described empirically e. g. by (60,61) [1].

$$C_{S1} = 0.4 \, \text{MeV} \cdot \frac{A_{CN}^2}{Z_{CN}^2} \tag{60}$$

$$C_{S2} = 0.13 \, \text{MeV} \cdot \frac{A_{CN}^2}{Z_{CN}^2} \tag{61}$$

It must be taken into account that these channels are related to shell effects which wash out when the excitation energy is increased, leading to a decrease of the potential curvature. In this work, the curvature decrease, which is included in GEF 2010/5c and newer versions, was found to be necessary to give a good description of the experimentally observed widths of fast fission mass yields given in section 3.2, however the description of variances by the code is still empirical.

With this description, the observation that the mass width $\sigma_{A,S1}$ of the S1 channel hardly increases with the excitation energy of the system can be understood as the result of the high curvature C_{S1}. This corresponds to a high zero-point oscillation energy and large distances between the energy levels. Hence, the high curvature results in a strong population of the oscillator ground state, corresponding to a small and rather constant width of the mass distribution.

32

1.11 Charge Distributions

Since the $\frac{N}{Z}$ degree of freedom of the nascent fragments has been shown to have a small inertia, this value is expected to be determined close to the scission point. With respect to the charge polarization, the system is expected to closely follow the bottom of the potential valley. On the other hand, due to its large inertia, the mass division is fixed well before the scission point. Thus, the mean proton number can be obtained from a scission-point model according to which the potential is minimized with respect to the proton numbers of the two fragments. In this scission-point model, the nascent fragment mass numbers are given, and their deformations are known from e. g. the observed post-scission excitation energies. The potential is expressed by the sum of the fragment deformation energy and the Coulomb energy, which depends on the distance between the centers of the two fragments. Fig. 8 illustrates the assumed scission point configuration which is rotationally symmetric about the fission axis. Unlike the deformations, the so-called tip distance d in the space between the fragments is not known from the observed excitation energies. It needs to be determined empirically from the observed nuclide yield distribution itself.
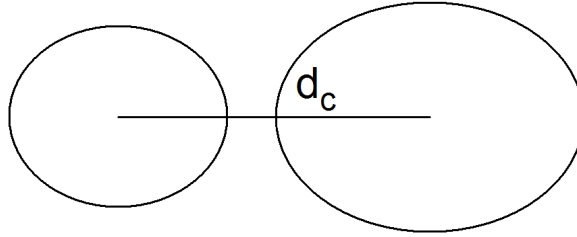
Figure 8: Sketch of the assumed scission point configuration.

The potential energy of this configuration is given by (62,63), where the distance between the fragment centers is given by (64). The fragment mass numbers A_{light}, A_{heavy}, their quadrupole deformations β_{light}, β_{heavy} and the tip distance d are used as input [25].

$$V = E_{LDM}(Z_{light}, A_{light}, \beta_{light}) + E_{LDM}(Z_{heavy}, A_{heavy}, \beta_{heavy}) + E_c(Z_{light}, Z_{heavy}, d_c) \quad (62)$$

$$E_c(Z_{light}, Z_{heavy}, d_c) = \frac{1}{4\pi\varepsilon_0} \cdot \frac{Z_{light}Z_{heavy}e^2}{d_c} \quad (63)$$

$$d_c = r_0 \cdot \left[\sqrt[3]{A_{light}} \cdot \left(1 + \frac{2}{3}\beta_{light}\right) + \sqrt[3]{A_{heavy}} \cdot \left(1 + \frac{2}{3}\beta_{heavy}\right) \right] + d \quad (64)$$

It has already been observed by Wilkins, Steinberg and Chasman [13] that the $\overline{Z_{scp}}(A)$ values obtained from this model tend to be too low for the light and too high for the heavy

fragments if a short tip distance $d \approx 1 \, \text{fm}$ is assumed. To solve this problem, they proposed to use a longer tip distance. As it is shown by Fig. 9, an increase of the tip distance mainly affects the charge polarization of very asymmetric splits. However, even for $d = 10 \, \text{fm}$, which is almost the sum of the long half axes, no good results are obtained in the region of the S1 channel. Thus, a good description of the charge polarization is obviously not obtained from a mere variation of the tip distance.

It must be noted that in this scission point model the impact of shell effects is neglected. Above all, one may expect a strong impact of the ^{132}Sn shell closure on the charge polarization of fragments from the S1 channel. These facts show the limitations of the scission-point model based on liquid drop potential calculations.

In fact, a good empirical description can be obtained if an additional shift is applied to the $\overline{Z_{scp}}(A)$ values obtained from the scission point model. The mean isobaric proton number $\overline{Z}(A)$ of light fragments is shifted to higher values, with the $\overline{Z}(A)$ of the complementary heavy fragments being decreased. At $A = \frac{A_{CN}}{2}$, a smooth transition of $\overline{Z}(A)$ is reached by the overlap of the "light" and "heavy" Gaussians. The procedure is expressed by (65) and included in GEF 2010/5c [1]. As it is shown by the figures in section 3.6 (which show post-neutron values) and in the final EFNUDAT report on GEF [25], the results from this description are satisfactory.

$$\overline{Z}(A) = \begin{cases} \overline{Z_{scp}}(A) + 0.37 & \text{light fragments} \\ \overline{Z_{scp}}(A) - 0.37 & \text{heavy fragments} \end{cases} \tag{65}$$

The width of the isobaric proton number distribution in the yields can be described analogously to the width of the mass yield distribution in section 1.10. In this case, the potential curvature C is given by (66).

$$C = \frac{1}{2} \cdot [V(Z_{light} + 1, Z_{heavy} - 1) - 2V(Z_{light}, Z_{heavy}) + V(Z_{light} - 1, Z_{heavy} + 1)] \tag{66}$$

Up to here, the pre-neutron nuclide yield distribution has been described in the following way:

- For a single channel, the mass distribution is described by two Gaussians whose central values add up to the compound nucleus mass number.

- For a specific channel and mass, the isobaric proton number distribution is given by a Gaussian which is centered at the value $\overline{Z}(A)$ obtained from the model described in this section.

- The entire pre-neutron nuclide yield distribution is a superposition of the different fission channels, whose fractions are obtained according to section 1.6.

34
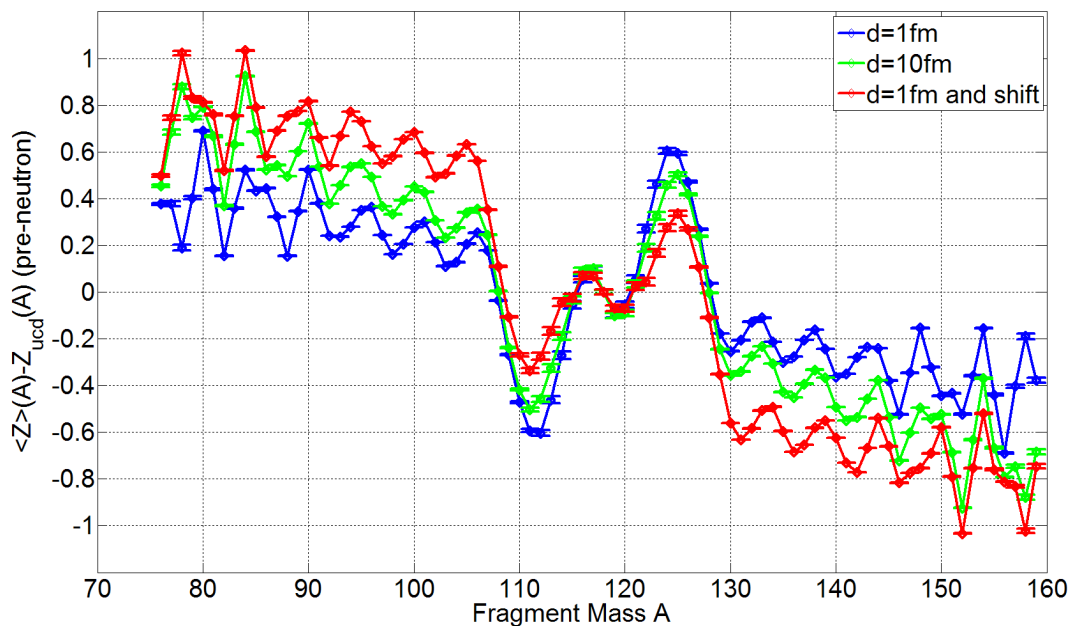
Figure 9: Pre-neutron charge polarization of $^{235}U(n_{th}, f)$ calculated by GEF 2010/5c for $d = 1$ fm, $d = 10$ fm and with inclusion of the shift.

1.12   Even-odd Effect

In fact, although the pre-neutron fragment yield distributions are on the average well described by several Gaussian functions, even-odd modulations of these distributions have to be taken into account. In the proton number dependent yield distributions, the following effects are observed:

- In even-Z fissioning systems, the production of even-Z fragments is generally enhanced regardless of the split asymmetry. However, the enhancement is found to increase with asymmetry.

- In odd-Z fissioning systems, the production of even-Z light fragments and odd-Z heavy fragments is observed to increase with split asymmetry. In rather symmetric splits, no even-odd effect is observed.

- The effect is particularly strong in the fission of e. g. thorium nuclei, and it decreases with increasing proton number of the fissioning nucleus.

- The effect is found to wash out when the excitation energy of the compound nucleus increases.

In the analysis of fission yields, the even-odd effect is generally expressed by the quantity

$$\delta = \frac{Y_{even} - Y_{odd}}{Y_{even} + Y_{odd}} \tag{67}$$

which can be calculated globally over all yields Y_i or locally around a certain proton or neutron number X_i. The latter is done using the Tracy [28] formula (68), which expresses the even-odd deviations of the yields Y_i to Y_{i+3} from a Gaussian distribution. The values obtained from (67) and (68) are related by (69).

$$\Delta_i = \frac{1}{8} \cdot (-1)^{X_i+1} \cdot [\ln Y_{i+3} - \ln Y_i - 3 \cdot (\ln Y_{i+2} - \ln Y_{i+1})] \tag{68}$$

$$\delta_i = \frac{e^{2\Delta_i} - 1}{e^{2\Delta_i} + 1} \tag{69}$$

There have been early attempts to explain this effect via the conservation of proton pairs during the fission process, which however were inconsistent and could e. g. not explain the even-odd effect in odd-Z fissioning systems. Recently, a consistent and physically well-founded description [29], which is connected to the energy sorting mechanism described in section 1.9, has been found by Schmidt.

According to Schmidt, one needs to distinguish between the even-odd effect originating from pairing correlations and the asymmetry-driven even-odd effect. Both effects depend on the intrinsic excitation energy at the scission point. The proton even-odd effect from pairing correlations is quite well described by the exponential function

$$\delta_p = e^{-\frac{E_{intr}^*}{4.5\,\mathrm{MeV}}}$$

which takes account of the increase of pair breaking when E_{intr}^* increases.

The asymmetry-driven even-odd effect, on the other hand, is related to the energy sorting process. From the physical point of view, a complete energy sorting between the nascent fragments must include the formation of a fully paired hot fragment (which is usually the light one), since this leads to a higher entropy. This also explains the observed even-odd effect in systems with an odd proton or neutron number. The transfer of a nucleon through the neck of the fissioning nucleus leading to the formation of an even hot fragment is considered as the final step of the energy sorting process. The transfer of a proton is possible during the time frame before the Coulomb barrier is established, whereas the transfer of a neutron is possible until neck rupture. Thus, there will be an asymmetry-driven even-odd effect in the yields if the energy sorting is completed within this time frame. The speed of this energy sorting is assumed to be proportional to the temperature difference between the nascent fragments.

In the proton number dependent fragment yields of odd-Z nuclei, there is only the asymmetry-driven even-odd effect, starting at a certain threshold asymmetry of the split. This indicates

that the system does not always have enough time to finish the energy sorting before the Coulomb barrier is established. K.-H. Schmidt found that the threshold for the occurrence of the asymmetry-driven proton even-odd effect [25] is

$$\frac{|T_{light} - T_{heavy}|}{E^*_{intr}} > 0.035 \tag{70}$$

which also provides new insight into the dynamical times of the fission process. The stochastic nature of the excitation energy and the duration of the energy sorting leads to a gradual increase of the even-odd effect with asymmetry. The interplay of pairing correlations δ_{pair} with the asymmetry-driven even-odd effect δ_{asym} can be described by the empirical relation (71) [1].

$$\delta = \delta_{pair} + (0.7 - \delta_{pair}) \cdot \delta_{asym} \tag{71}$$

The even-odd effect in neutron number dependent fragment yields is described analogously. Since the transfer of neutrons is still possible after the establishment of the Coulomb barrier, the threshold value expressed by (70) is expected to be lower with respect to the neutron even-odd effect. Unfortunately, direct experimental information on the neutron number dependent yield distribution before evaporation is not available. Thus, the neutron even-odd effect in the pre-neutron yields is unknown. However, this effect has an impact on the mean number of prompt neutrons, and is thus a source of uncertainty. This uncertainty is illustrated in the following table, which lists the $\overline{\nu_p}$ values obtained from GEF 2010/5c without and with a maximum neutron even-odd effect.

Reaction	$\overline{\nu_p}$	
	$\delta_n = 0$	$\delta_n = 1$
$^{235}U(n_{th}, f)$	2.27	2.05
$^{239}Pu(n_{th}, f)$	3.18	2.97

In the post-evaporation neutron number dependent yields, a global even-odd effect of $\delta_n \approx 0.05$ is usually observed, which may be a hint on the pre-evaporation distribution. Unfortunately, the models for fragment excitation energies, spins and deexcitation are not yet precise enough to enable the unfolding of post-neutron fission yields.

1.13   Treatment of Fission Fragment Deexcitation

1.13.1   Bohr Independence Hypothesis

In 1936, Bohr formulated his so-called Bohr Independence Hypothesis, indicating that the formation and subsequent decay processes of a compound nucleus are independent [30]. This implies that the compound nucleus is assumed to reach statistical equilibrium in the time frame between its formation and decay. Because of this, the decay of the compound nucleus is expected to be completely determined by its excitation energy, parity and angular momentum.

However, Bohr's hypothesis could not be verified at the time it was formulated, as good experimental data about the reaction cross sections were not available. From the theoretical point of view, one expects the establishment of thermal equilibrium to be less probable at higher excitation energies, as the average lifetime of the compound nucleus decreases. Furthermore, the hypothesis can obviously not be applied if the average excitation energy of a single nucleon is higher than its binding energy.

The first experimental proof of the Bohr Independence Hypothesis was the experiment of Ghoshal in 1950, where the probabilities of decay reactions of the compound nucleus ^{64}Zn formed by $\alpha +^{60}Ni$ and $p +^{63}Cu$ were observed to agree within the error limits. The excitation energy was up to $E \approx 40$ MeV. In later experiments it was found that for an excitation energy $E < 20$ MeV an equilibrated compound nucleus is formed in over 90% of the cases. For $E = 60$ MeV, the probability is approximately 30% [30]. This means that Bohr's hypothesis is applicable at the excitation energy of fragments from nuclear fission, which is mostly below 20 MeV.

1.13.2   Weisskopf-Ewing Formalism

In 1940, Weisskopf and Ewing made use of Bohr's hypothesis when they formulated a theory about compound nucleus reactions, applicable to reactions to the continuum. Their theory provides relations between the cross-sections, the decay widths and the nuclear level densities. It is applicable to decay reactions to the continuum and below the excitation energy range of pre-equilibrium decays. The spin of the compound nucleus is neglected.

Following Bohr's hypothesis, the cross-section $\sigma_{\alpha\alpha'}$ of the formation α of a compound nucleus and its subsequent decay α' can be written as

$$\sigma_{\alpha\alpha'}(E, E')\, dE' = \sigma_{c\alpha}(E) \cdot P_{\alpha'}(E, E')\, dE' \tag{72}$$

where E denotes the compound nucleus excitation energy, E' the energy of the emitted particle and $\sigma_{c\alpha}$ the compound nucleus formation cross-section. The probability $P_{\alpha'}(E, E')\, dE'$ is expressed by the ratio of the decay width $\widetilde{\Gamma}_{\alpha'}(E, E')\, dE'$ to the integrals over all possible decays α'' of the compound nucleus:

$$P_{\alpha'}(E, E') \, dE' = \frac{\widetilde{\Gamma}_{\alpha'}(E, E') \, dE'}{\sum_{\alpha''} \int_0^{E-Q''} \widetilde{\Gamma}_{\alpha''}(E, E'') \, dE''} \tag{73}$$

The explicit expression for $\widetilde{\Gamma}_{\alpha'}(E, E')$ can be derived from the principle of detailed balance, which states that if two systems a and b with state densities ρ_a and ρ_b are in statistical equilibrium, the depopulation of states of system a by transitions to b equals their population by the time-reversed process. This is expressed by

$$\rho_a \Gamma_{ab} = \rho_b \Gamma_{ba} \tag{74}$$

As the spin dependence is neglected in the Weisskopf-Ewing theory, the level density ω coincides with the state density ρ. The principle of detailed balance is now exploited making the following substitutions

$$\rho_a = \omega_a = \omega_{CN}(E)$$
$$\rho_b = \omega_b = \omega_{\alpha'}(U') \cdot \omega_c(E')$$
$$\Gamma_{ab} = \widetilde{\Gamma}_{\alpha'}(E, E') \, dE'$$
$$\Gamma_{ba} = \frac{v' \sigma_{c\alpha'}(E')}{V}$$

which lead to the equation

$$\omega_{CN}(E) \cdot \widetilde{\Gamma}_{\alpha'}(E, E') \, dE' = \omega_{\alpha'}(U') \cdot \omega_c(E') \cdot \frac{v' \sigma_{c\alpha'}(E')}{V} \tag{75}$$

with the velocity of the emitted particle v', the laboratory volume V and the residual nucleus excitation energy $U' = E - E' - B$, which is E minus the kinetic and binding energy of the outgoing particle. The level density of system b needs to be expressed by the product $\omega_{\alpha'}(U') \cdot \omega_c(E')$ of the residual nucleus level density and the density of continuum states in channel α'. The density of continuum states is

$$\omega_c(E') = g_{\alpha'} \cdot \frac{4\pi p'^2 V}{h^3} \frac{dp'}{dE'} \, dE' = g_{\alpha'} \cdot \frac{8\pi \mu_{\alpha'} E' V}{h^3 v'} \, dE' \tag{76}$$

where $g_{\alpha'} = 2i_{\alpha'} + 1$ is the emitted particle spin degradation, $\mu_{\alpha'}$ its reduced mass and p' its momentum. The final result is

$$\widetilde{\Gamma}_{\alpha'}(E, E') \, dE' = \frac{(2i_{\alpha'} + 1)\mu_{\alpha'}}{\pi^2 \hbar^3} \frac{1}{\omega_{CN}(E)} \cdot \sigma_{c\alpha'}(E') \cdot \omega_{\alpha'}(U') \cdot E' \, dE' \tag{77}$$

Inserting (77) into (73) returns

$$P_{\alpha'}(E, E') \, dE' = \frac{g_{\alpha'} \mu_{\alpha'} \sigma_{c\alpha'}(E') \omega_{\alpha'}(U') E' \, dE'}{\sum_{\alpha''} g_{\alpha''} \mu_{\alpha''} \int_0^{E-Q''} \sigma_{c\alpha''}(E'') \omega_{\alpha''}(U'') E'' \, dE''} \tag{78}$$

and (78) into (72)

$$\sigma_{\alpha\alpha'}(E, E')\ dE' = \sigma_{c\alpha}(E) \cdot \frac{g_{\alpha'}\mu_{\alpha'}\sigma_{c\alpha'}(E')\omega_{\alpha'}(U')E'\ dE'}{\sum_{\alpha''} g_{\alpha''}\mu_{\alpha''} \int_0^{E-Q''} \sigma_{c\alpha''}(E'')\omega_{\alpha''}(U'')E''\ dE''} \qquad (79)$$

which is the Weisskopf-Ewing formula.

For the description of the prompt neutron evaporation process, (77) is useful. The neutron spin $i_n = \frac{1}{2}$ and its reduced mass μ_n as well as the level densities and the inverse reaction cross section $\sigma_{c\alpha'}$ are required as input. In the relevant energy range, the level density is best described by the exponential constant temperature level density (41) which leads to a roughly Maxwellian shape of the neutron emission spectrum.

From the theoretical point of view, the inverse reaction cross section $\sigma_{c\alpha'}$ is available from several optical models. For this application, the models of D. Wilmore, P. E. Hodgson (1964) and A. J. Koning, J. P. Delaroche (2003) are the most appropriate [31].

There is also the Dostrovsky parameterization (1959) which simply relates the neutron reaction cross-section $\sigma_{cn}(E)$ to the mass number A of the target nucleus:

$$\sigma_{cn}(E) = \pi r_0^2 \cdot \left(\sqrt[3]{A} + 1 \right)^2 \cdot \alpha \cdot \left(1 + \frac{\beta}{E} \right)$$

$$\alpha = 0.76 + \frac{2.2}{\sqrt[3]{A}}$$

$$\beta = \frac{1}{\alpha}(2.12A^{-\frac{2}{3}} - 0.05)$$

$$r_0 = 1.233\,\text{fm}$$

This is a rather coarse description, but it has the advantage that the integral decay width

$$\begin{aligned}
\Gamma_n(E) \quad &= \hbar \cdot \int_0^{E-Q'} \widetilde{\Gamma}_n(E, E')\ dE' \\
&= \frac{(2i_n+1)\mu_n}{\pi^2\hbar^2} \frac{1}{\omega_{CN}(E)} \cdot \int_0^{E-Q'} dE'\ \sigma_{cn}(E') \cdot \omega_n(U') \cdot E'
\end{aligned} \qquad (80)$$

as well as the neutron emission spectrum can be calculated analytically [30].

1.13.3 Hauser-Feshbach Formalism

The Hauser-Feshbach theory was formulated in 1952 by Walter Hauser and Herman Feshbach. It enables a more precise calculation of the various reaction cross sections, as the theory includes the effects resulting from spins, orbital angular momenta and their laws of conservation. For the description of the competition between neutron and gamma emission in the deexcitation of a nucleus, this theory should be applied [5]. It also enables the calculation of compound nucleus decay widths from the continuum to discrete states. Therefore it has been widely used since the early days of experimental nuclear physics.

The angular momenta are denoted by

- $\vec{i}$, the spin of the projectile

- $\vec{I}$, the spin of the target nucleus

- $\vec{j} = \vec{i} + \vec{I}$, the combined spin of the reacting particles

- $\vec{l}$, the orbital angular momentum between the projectile and the target nucleus

- $\vec{J} = \vec{j} + \vec{l}$, the spin of the compound nucleus

- $\vec{i'}$, $\vec{I'}$ and $\vec{l'}$ analogously for the emission process

In the Hauser-Feshbach theory, the compound nucleus formation cross-section for a particular value of J is expressed by

$$\sigma_{c\alpha}^{J}(E) = \pi\lambda_{\alpha}^{2} \cdot \sum_{jl} \frac{2J+1}{(2i+1)(2I+1)} \cdot T_{\alpha l j}^{J}(E) \tag{81}$$

where the $T_{\alpha l j}^{J}(E)$ are the transmission coefficients for a certain angular momentum l, combined reacting particles spin j and compound nucleus spin J. λ_{α} is the reduced de Broglie wavelength of the incident particle, expressed by $\lambda_{\alpha} = \frac{\hbar}{\sqrt{2\mu_{\alpha}E_{\alpha}}}$ in the non-relativistic and $\lambda_{\alpha} = \frac{c\hbar}{E_{\alpha}}$ in the ultrarelativistic case. The formation cross section for all J is thus

$$\sigma_{c\alpha}(E) = \pi\lambda_{\alpha}^{2} \cdot \sum_{Jjl} \frac{2J+1}{(2i+1)(2I+1)} \cdot T_{\alpha l j}^{J}(E) \tag{82}$$

The Hauser-Feshbach analogon to the Weisskopf-Ewing decay probability (73) is

$$P_{\alpha'}^{J}(E, E') = \frac{\sum_{j'l'} T_{\alpha'j'l'}^{J}(E') \sum_{I'} \rho_{\alpha'}(U', I')}{\sum_{\alpha''j''l''} \int_{0}^{E-Q''} dE'' \, T_{\alpha''j''l''}^{J}(E'') \sum_{I''} \rho_{\alpha''}(U'', I'')} \tag{83}$$

and the Hauser-Feshbach formula, which is the analogon to (79)

$$\sigma_{\alpha\alpha'}(E, E') = \pi\lambda_{\alpha}^{2} \cdot \sum_{Jjl} \frac{2J+1}{(2i+1)(2I+1)} \cdot T_{\alpha j l}^{J}(E)$$

$$\cdot \frac{\sum_{j'l'} T_{\alpha'j'l'}^{J}(E') \sum_{I'} \rho_{\alpha'}(U', I')}{\sum_{\alpha''j''l''} \int_{0}^{E-Q''} dE'' \, T_{\alpha''j''l''}^{J}(E'') \sum_{I''} \rho_{\alpha''}(U'', I'')} \tag{84}$$

For Hauser-Feshbach calculations, one needs to know the transmission coefficients $T_{\alpha j l}^{J}(E)$. These can be obtained from an optical model.

The Hauser-Feshbach decay width to a discrete state is

$$\Gamma_{\alpha'l'j'}^{J}(E) = \frac{1}{2\pi} \frac{T_{\alpha'l'j'}^{J}(E')}{\rho_{CN}(E, J)} \tag{85}$$

and the analogon to (80)

$$
\begin{aligned}
\Gamma_{\alpha'}^J(E) &= \frac{1}{2\pi}\frac{1}{\rho_{CN}(E,J)}\int_0^{E-Q'} dE' \ \sum_{l'j'I'} T_{\alpha'l'j'}^J(E')\rho_{\alpha'}(U',I') \\
&= \frac{2i'_{\alpha'}+1}{2\pi^2(2J+1)}\frac{1}{\rho_{CN}(E,J)}\cdot\int_0^{E-Q'} dE' \ \frac{\sigma_{c\alpha'}^J(E')}{\lambda_{\alpha'}^2}\sum_{I'}(2I'+1)\rho_{\alpha'}(U',I')
\end{aligned}
\tag{86}
$$

with the relation

$$
\sum_{l'j'} T_{\alpha'l'j'}^J(E') = \frac{(2i'_{\alpha'}+1)(2I'+1)}{2J+1}\frac{\sigma_{c\alpha'}^J(E')}{\pi\lambda_{\alpha'}^2}
$$

The Weisskopf-Ewing theory can be derived from the Hauser-Feshbach theory if the level density is assumed to be spin independent and spin-orbit forces are neglected [30].

1.14   Population of Metastable States

Many nuclei and also many fission products have one or two excitation states with a relatively long lifetime of at least about one second. The lifetime of an excited state is long if low-multipole gamma emission or even any single gamma emission is forbidden by the conservation of angular momentum or parity [10]. Because of this long lifetime, alpha or beta emission and even spontaneous fission may compete with the transition to lower excitation states. These so-called "metastable states" may have higher energy than many other states of the same nucleus, but are usually located below the continuum. Compared to its ground state, a metastable nucleus shows different decay characteristics and also some differences in the various cross-sections. The declaration of an excitation state as metastable is rather subjective [31].

As the Hauser-Feshbach theory enables the calculation of decay widths from the continuum to discrete states, it can predict the population of metastable states by the deexcitation of highly excited nuclei. However, the Hauser-Feshbach theory requires the spin J of the initial state to be known.

From the 1970s on, several experiments have been performed with the objective to obtain information about fragment spins. These experiments can be classified into measurements of mass-dependent prompt gamma multiplicities and measurements of isomeric ratios of the produced fission fragments. Mass-dependent gamma multiplicities of ^{252}Cf spontaneous fission fragments, for instance, have been measured thoroughly in the experiment of R. Schmid-Fabian in 1988 [3]. In other experiments, isomeric ratios have been measured at least for some isotopes of bromide, yttrium, tin, antimony, tellurium, iodine, xenon and caesium.

Based on experimental results, Vandenbosch and Huizenga as well as Nifenecker et al. have formulated fragment deexcitation models [3]. According to Nifenecker et al., at first neutron emission takes most excitation energy. Gamma emission starts at an excitation energy

42

around $E^* \approx 4\,\text{MeV}$ and a spin around $J \approx 6\hbar$ with a dipole transition of 1.5 to 2 MeV. The further decay along the yrast line, i. e. where the excitation energy is completely bound in rotational energy, is dominated by electric quadrupole (E2) transitions. Indeed, the use of such deexcitation models in order to reconstruct the initial spin from measured isomeric ratios requires assumptions with respect to e. g. level densities and initial excitation energies, thus there is some uncertainty in the reconstructed J values. Moreover, the gamma multiplicity should not be associated to the initial spin too closely.
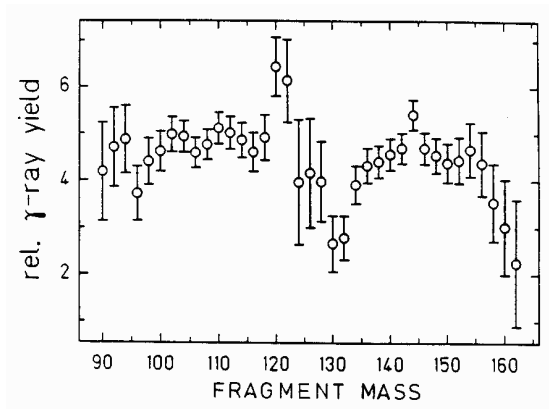
Figure 10: Mean gamma multiplicity as a function of fragment mass for spontaneous fission of ^{252}Cf, from [3].

As shown by Fig. 10, the experimental observations are that the mass-dependent gamma multiplicity shows a structure with a mean value of ≈ 4, a dip around $A = 132$ and a hump around the complementary fragment. The fragment spins were found to be oriented perpendicular to the fission axis. From measurements of isomeric ratios it is known that their sensitivities to the incident neutron energy strongly depend on the proton and neutron number of the fragment. Additionally, these measurements have shown an even-odd effect in the fragment spins, with even-Z fragments having about $4\hbar$ lower spins than odd-Z fragments [32].

All these facts point out that the formation of fragment spins is a rather complex process. If one wants to model the ratios of isomers produced in nuclear fission, this issue still requires considerable theoretical efforts. The above mentioned even-odd effect of fragment spins is not yet understood. However, at this point it should be mentioned that the model of Zielinska-Pfabé and Dietrich [33] explains the dip in the fragment spins around $A = 132$ at least qualitatively.

Zielinska-Pfabé and Dietrich generalized a model of J. O. Rasmussen et al. (1969) to the case of two deformed fission fragments [33]. They developed a description of the potential energy near the scission point depending on fragment deformations, their orientations and

their center-of-mass distance. The population of so-called bending modes is then calculated via a quantum-mechanical and statistical approach. The final angular momenta are then predicted from the values of the above mentioned observables. This model requires information about fragment deformations and the strength of coupling between different degrees of freedom of the bending modes. From comparison with experiment, Zielinska-Pfabé and Dietrich concluded that there is a large coupling between those degrees of freedom. The model reproduces an increasing fragment spin with increasing fragment deformation, which explains the dip in the gamma multiplicity around $A = 132$. However, the model does certainly not reflect the whole truth since it assumes bending modes as the only source of angular momenta. There is also a more recent alternative model from Mikhailov and Quentin [34, 35] according to which fragment spins are determined by the quantum-mechanical uncertainty relation between fragment orientation angles and angular momenta. They claim that bending modes are the dominant source of angular momentum only if one fragment is nearly spherical and that their theory is supported by experimental observations of prompt gamma angular distributions.

1.15 Ternary Fission

The emission of a light charged third fragment in the fission process was discovered in 1946. This phenomenon is important for reactor technology, as the light charged particle is mostly an alpha particle or a triton. It contributes to the build-up of fission gases in the fuel rods, with the tritium also being a beta emitter of 12.3 years half life. Ternary fission generally occurs once every few hundred fission events.

From the energy distributions and angular correlations of ternary fission fragments it was concluded that the light particle is emitted from the space between the two heavier fragments close to the scission time. The light particle is mostly emitted perpendicular to the heavier fragments, hence it cannot originate from evaporation. However, about 3% of the light particles are emitted along the axis of the heavier fragments. Regarding the kinetic energy, it is observed that the total kinetic energy of ternary fission fragments is only slightly lower than that of binary fragments. The kinetic energy distribution of the light charged particle is roughly a Gaussian with a mean value between 10 and 20 MeV, mainly depending on its N and Z and hardly on N and Z of the compound nucleus. The mass yield distributions of ternary fission fragments indicate that, compared to binary fission, light charged particles are mostly emitted at the expense of the lighter fission fragment. Among the very light fragments, enhanced yields of even-Z and, less pronounced, even-N fragments are observed for even-Z as well as for odd-Z compound nuclei.

The fraction of ternary fission reactions is around 0.2% for uranium and plutonium isotopes. It is generally observed that, compared to thermal neutron induced fission, this fraction is enhanced by about 25% in spontaneous fission of the same nucleus. Above the fission barrier, the ternary fission probability is rather insensitive to the incident neutron energy. Rajagopalan and Thomas found that it increases by $1.9\% \pm 0.6\%$ per MeV of neu-

tron energy. However, an important sensitivity is that the probability was found to increase linearly with $\frac{Z^2}{A}$ of the compound nucleus.

In the 1980s, several theories were formulated which explained ternary fission as two simultaneous ruptures of the neck between the nascent fragments. Furthermore, the approach of Halpern (1971) gives a coarse quantitative description of the relative light charged particle yields [3]. According to Halpern, the yields decrease exponentially with the average "energy cost" E_c of the production of a certain light charged particle, which is written as

$$E_c = B + \Delta V + K$$

where B is the binding energy of the light charged particle to its "mother" fragment (i. e. the light fragment), K is its average initial kinetic energy and ΔV is the Coulomb potential difference between the binary and ternary configuration.

Some sources like Bowman et al. (1962) claim that a small fraction of prompt neutrons is also emitted as ternary fragments, commonly called "scission neutrons" [3]. They concluded this from the observation of a neutron flux component that was uncorrelated with the charged fragment directions. However, there have been contradictory results about the fraction of this component [3]. Weisskopf-Ewing evaporation calculations performed with the GEF code in this work also indicate that the vast majority of prompt neutrons must be emitted by the fully accelerated fission fragments. The scission neutrons are still a subject of debate [25].

Light Charged Particle	Relative Yield [%]	
	^{235}U	^{239}Pu
^{1}H	0.91	1.67
^{2}H	0.45	0.55
^{3}H	5.76	5.80
^{4}He	90.60	89.50
^{6}He	1.42	1.67
^{8}He		0.03
^{7}Li		0.06
^{8}Li	0.04	
^{9}Li	0.02	0.05
^{8}Be	0.04	
^{9}Be	0.02	0.05
^{10}Be	0.28	0.43
^{11}Be		0.03
^{12}Be	0.01	0.02
^{9}B	0.02	
^{10}B	0.28	
^{12}B	0.01	
^{8}C		0.03
^{14}C	0.08	0.12
^{15}C	0.01	
^{21}Ne	0.05	
Ternary Fraction [%]	0.188 ± 0.008	0.245 ± 0.012

Table 2: Yields of light charged particles for $^{235}U(n_{th}, f)$ and $^{239}Pu(n_{th}, f)$ from the JEFF-3.1.1 library [36].

2 Simulation Codes for Fission

This chapter gives an overview of the code applications concerning the modelling of the nuclear fission process in this work. The basic properties of the GEF code [1] from K.-H. Schmidt are discussed. Furthermore, a documentation of the extension of the code developed in this work for the calculation of fission product yields in a fast reactor spectrum will be given. The potentials and challenges of fission yield modelling based on GEF are also discussed. The TALYS code which also contains a fission model and has been used for the evaluation of cross-section data from the TENDL-2009 library applied in this work is presented as well. There are several other fission model codes which cannot be addressed here.

2.1 GEF

2.1.1 Basics of the Code

The GEF ("general fission") code [1], which is being developed by K.-H. Schmidt and B. Jurado, is a semi-empirical fission model code. It calculates fission product yields from neutron-induced first-chance (n, f) and spontaneous fission reactions of a wide range of heavy nuclei. The code is applicable to incident neutron energies up to at least $E_n \approx 10\,\mathrm{MeV}$, but since multi-chance fission is not yet implemented in it, the total fission yields can only be calculated directly up to $E_n \approx 6\,\mathrm{MeV}$. From version 2011/1 on, the calculation of isomeric ratios is included.

The code uses the multichannel theory presented in section 1.5, representing the pre-neutron yield distribution by a superposition of several Gaussians, whereas their central values and variances are still described on a mainly empirical level. In GEF 2010/5c, the S3 channel has been implemented to reproduce the mass yields from spontaneous fission of ^{252}Cf [5].

The main specific strengths of the code emerge from the application of the separability principle, the quite realistic calculation of excitation energies and the well-founded description of the even-odd effect in the yields. The additional calculation of fragment spins allows the application of very advanced models based on the Hauser-Feshbach formalism to fragment deexcitation. All these issues are crucial for a good modelling of fission yields. Additionally, the computational effort of the code is relatively low.

As pointed out by the name of the code, another strategy of its developers is to increase its predictive power by finding a general description of the fission yield characteristics of many different nuclei. Besides the relations (24,25), an empirical description of the relative heights of channel specific outer saddle points has been obtained in this way. In GEF 2010/5c, the depths of the valleys on top of the liquid drop barrier (56) (see Fig. 7) related to the S1 and S2 channels are given by (87,88).

$$D_{S1} = 3.1 \,\text{MeV} \cdot \left(1 - 0.065 \cdot \left| 82 - \frac{50}{Z_{CN}} \cdot N_{CN} \right| \right) \tag{87}$$

$$D_{S2} = 4.0 \,\text{MeV} \tag{88}$$

The absolute height E_F of the lowest outer fission barrier is calculated by the analytical formula (89) based on the Thomas-Fermi model from Myers and Swiatecki [37], with the ground state shell correction $W(Z, A)$. The heights of the other outer barriers are then obtained using (56,87,88).

$$E_F = \begin{cases} \frac{Z^2}{\sqrt[3]{A}} \cdot \frac{1}{X} \cdot F(X) - W(Z, A) & \frac{Z^2}{A} < 35.85 \\ \frac{Z^2}{\sqrt[3]{A}} \cdot \frac{1}{X} \cdot F(X) - W(Z, A) - 0.5 \,\text{MeV} \cdot \left(\frac{Z^2}{A} - 35.85 \right) & \frac{Z^2}{A} \geq 35.85 \end{cases} \tag{89}$$

$$F(X) = \begin{cases} -0.124136 \,\text{MeV} \cdot X + 4.834797 \,\text{MeV} & 30 \leq X \leq 34.15 \\ 1.99749 \cdot 10^{-4} \,\text{MeV} \cdot (48.5428 - X)^3 & 34.15 \leq X \leq 48.5428 \end{cases}$$

$$X = \frac{Z^2}{A} \cdot \left[1 - \left(\frac{Z}{75} + \frac{5}{6} \right) \cdot \frac{(A - 2Z)^2}{A^2} \right]^{-1}$$

$$W(Z, A) = [m(Z, A) - m_{LDM}(Z, A)] \cdot c^2$$

The parameter Δ_{SL} denotes a correction of less than 1 MeV which is added to the absolute outer saddle height $E_{F,calc}$ of the SL channel calculated as described above, i. e. $E_F = E_{F,calc} + \Delta_{SL}$. It may be entered manually to adjust to the peak-to-valley ratio of the observed mass yield curves. This correction is related to small shell effects influencing the fraction and outer saddle height of the SL channel. In GEF, transmission coefficients of the outer barriers are calculated by the Hill-Wheeler approach (30) and used for the calculation of fission channel fractions, whereas (31) is neglected. According to the findings in section 1.6, this seems to be a reasonable simplification at least for light actinides up to uranium. One should keep in mind that the simplification may not be suitable for higher elements, where the outer barriers are significantly lower than the inner ones.

Fragment excitation energies are calculated according to the procedure in section 1.9. For the SL channel, nascent fragment deformations $\beta_{SL}(Z)$ depending on the proton number are determined by a scission point model with a tip distance of $d = 1 \,\text{fm}$. In this model, the liquid drop potential of the scission point configuration is minimized with respect to the fragment deformations. For the asymmetric channels, the deformations of light fragments are empirically described by

$$\beta_{light}(Z) = 0.0225 \cdot (Z - 28) + 0.25$$

and those of heavy fragments by

$$\beta_{heavy}(Z) = 0.0325 \cdot (Z - 50) + 0.2$$

whereas heavy fragments from the S1 channel and light fragments from the S3 channel are assumed to be spherical. The excitation energies originating from fragment relaxation are calculated by the liquid drop model.

To the evaporation of prompt neutrons, the Weisskopf-Ewing formalism (77) with a constant inverse reaction cross-section is applied.

Finally, a high predictive power of the code is expected in the coarse weights of fission channels, the fragment excitation energies and the proton even-odd effect in the yields. On the other hand, the predictive power with respect to other aspects such as the behaviour of charge polarization with an increasing excitation energy or the neutron even-odd effect in pre-evaporation fission yields is still questionable. These limitations are mainly due to the lack of experimental insight needed to adjust a semi-empirical model. The benchmarking of the code in chapter 3 gives some impressions of the accuracy of the code.

2.1.2 Developments in this Work

The code developments in this work had three objectives:

- Extension of the GEF code to enable investigations of the characteristics of fragment kinetic energies and prompt neutron emission.

- Implementation of an improved model for fission fragment deexcitation.

- Creation of a code based on GEF for the calculation of fission product yields in a fast neutron spectrum.

At first, extensions of the original GEF code were developed which enable the output of kinetic energies, prompt neutron spectra $\chi(E)$ and multiplicities $\overline{\nu_p}(A_{pre})$ depending on the pre-neutron fragment mass. The output of the total kinetic energy, which had not yet been implemented, was included using the relation (90).

$$TKE = Q + E^*_{CN} - E^*_{light} - E^*_{heavy} \tag{90}$$

For the calculation of the Q value, the atomic mass values from [38] were used. Histograms of the obtained TKE values for the different fission channels were added to the output. With the TKE as input, the code was then extended to calculate the momenta of fission fragments in the laboratory system, in which the compound nucleus is assumed to be at rest. Neutron emission is assumed to be isotropic in the fragment inertial system. The velocities of emitted neutrons are folded with the velocity of the mother nucleus in the laboratory system, and the impact of neutron emission on the fission fragment momenta is also considered. All this is done in a relativistic calculation.

At first, the momenta of the fully accelerated fragments in the laboratory system are calculated by momentum conservation, from which one obtains (91) for the fragment momenta. In this equation, E denotes the total relativistic energy given by (92).

$$p = \frac{1}{2Ec} \cdot \sqrt{E^4 + (m_1^4 + m_2^4) \cdot c^8 - 2E^2 \cdot (m_1^2 + m_2^2) \cdot c^4 - 2m_1^2 m_2^2 c^8} \tag{91}$$

$$E = (m_1 + m_2) \cdot c^2 + TKE \tag{92}$$

In the following, the index f denotes the fission fragment that is subject to the calculation, c its complementary fragment and d the residual nucleus after the emission of one neutron. The initial momentum p_f of the fragment is calculated by the application of (91,92) with $m_1 = m_f + \frac{E_f^*}{c^2}$ and $m_2 = m_c + \frac{E_c^*}{c^2}$, whereas m_f and m_c are taken from the mass table [38]. The momentum p is related to the boost β and the Lorentz factor γ by (93,94).

$$\beta = \frac{p}{\sqrt{p^2 + m^2 c^2}} \tag{93}$$

$$\gamma = \frac{1}{\sqrt{1 - \beta^2}} \tag{94}$$

In the second step, the momentum p_n' of an emitted neutron in the inertial system of the emitting fragment is calculated by the same procedure, using the masses $m_1 = m_n$ and $m_2 = m_d + \frac{E_f^* - S_n - E_n''}{c^2}$, with the neutron mass m_n and its separation energy S_n. The kinetic energy E_n'' of the neutron in the inertial system of the residual nucleus is obtained from the evaporation model and is nearly identical to the total kinetic energy in the fragment inertial system, so $TKE = E_n''$ is applied.

In the third step, the angle Θ' between the emission direction and the direction of fragment motion, as seen from the fragment inertial system, is chosen. This is done by chosing the value of $\cos(\Theta')$ using evenly distributed random numbers from the interval $[-1, 1]$, which corresponds to the mentioned isotropic emission.

The kinetic energy E_n of the neutron in the laboratory system is then calculated by (95).

$$E_n = \gamma_f \gamma_n' m_n c^2 - \beta_f \gamma_f p_n' c \cdot \cos(\Theta') - m_n c^2 \tag{95}$$

In the final step, the momentum p_d of the residual nucleus in the laboratory system is calculated by (96). In the fragment inertial system, its momentum p_d' is equal to that of the emitted neutron, $p_d' = p_n'$.

$$\begin{aligned} p_d = \quad & \left[\beta_f^2 \gamma_f^2 \gamma_d'^2 m_d^2 c^2 + 2\beta_f \gamma_f^2 \gamma_d' p_d' m_d c \cdot \cos(\Theta') \right. \\ & \left. + \gamma_f^2 p_d'^2 \cdot \cos^2(\Theta') + p_d'^2 \cdot (1 - \cos^2(\Theta')) \right]^{\frac{1}{2}} \end{aligned} \tag{96}$$

After this, the emission of another neutron can be calculated. In this way, the $\chi(E)$ spectrum as well as the pre- and post-neutron kinetic energies of fission fragments are obtained.

The calculated $\chi(E)$ spectra of $^{235}U(n_{th}, f)$ and $^{239}Pu(n_{th}, f)$ have mean values of $\overline{E} \approx 2.0\,\mathrm{MeV}$, showing that most neutrons are indeed emitted from the fully accelerated fission fragments. In Figs. 13 and 14, they are compared to evaluated data from the JEFF-3.1.1 library.

To improve the description of neutron emission, a new deexcitation model based on the Weisskopf-Ewing formalism was implemented. In the new model, the neutron emission spectrum is calculated by (77) using the Dostrovsky parameterization for the inverse cross-section $\sigma_{cn}(E')$ as described in section 1.13.2. To simplify the modelling of neutron and gamma competition in the deexcitation, gamma emission is neglected if the excitation energy E^* is higher than the neutron separation energy S_n of the mother nucleus plus the energy E_g of the lowest excited state of the daughter nucleus. If E^* is below this threshold, a pure gamma deexcitation is assumed. The energy gap E_g is estimated by the pairing gap $\Delta = \frac{12\,\mathrm{MeV}}{\sqrt{A}}$ of the nucleus, i. e.

$$ E_g = \begin{cases} 2\Delta & \text{even } Z,\ N \\ \Delta & \text{odd } A \\ 0 & \text{odd } Z,\ N \end{cases} $$
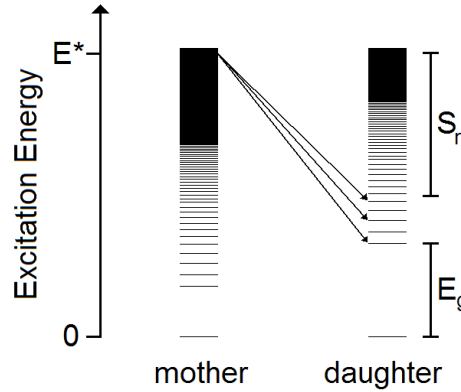
Figure 11: Possible neutron decays according to the model in GEF EXT.

For the calculation of fission product yields in a fast neutron spectrum, a code called GEF EXT ("extension") was developed, which is based on the code of GEF 2010/5c. In GEF EXT, the fragment deexcitation model from GEF 2010/5c has been replaced by the new one described above. As shown in Figs. 13 and 14, calculations of the prompt neutron spectrum $\chi(E)$ showed that the new model agrees better with the JEFF-3.1.1 data than the model in GEF 2010/5c. This is due to the usage of the Dostrovsky inverse cross-section

in the new model, whereas in GEF 2010/5c a constant inverse cross-section is used. However, a remaining problem is that the new model tends to overestimate the prompt neutron multiplicity $\overline{\nu_p}$. The higher mean value of the $\chi(E)$ spectrum from GEF 2010/5c probably causes the better agreement with the observed $\overline{\nu_p}$ values. Because of the good reproduction of the evaluated JEFF-3.1.1 spectrum, the usage of von Egidy's [8, 9] level density parameters (42,43) as well as the Dostrovsky inverse cross-section in (77) can be recommended. The fact that, according to section 3.5, the experimental kinetic energies are satisfactory reproduced for the majority of fission events of several nuclides shows that there are no large deviations between the calculated and the real TXE. The calculated mean prompt neutron multiplicity $\overline{\nu_p}$, which nevertheless is too high, points out that the description of gamma competition in the deexcitation model needs to be improved.

The GEF EXT code includes the calculation of multi-chance fission reactions, i. e. emission of one or more neutrons from the compound nucleus with a subsequent fission process. These reactions become important at incident neutron energies $E_n \geq 6$ MeV which are higher than the fission barrier of the target nucleus. In evaluated data libraries, separate cross-sections are available for the different fission chances. The probabilities for the multi-chance fission reactions (n, f), (n, nf) and $(n, 2nf)$, which play a role in fast reactor spectra, have been obtained from the cross-sections in the JEFF-3.1.1, ENDF/B-VII.0 and JENDL-4.0 evaluated data libraries. These libraries have been created by European, American and Japanese nuclear data projects and are publicly available at the OECD NEA database, from which they can be retrieved by the Janis software [39]. They contain data in the ENDF-6 format [40] in which the first, second and third chance fission cross-sections have the numbers MT=19, MT=20 and MT=21. These cross-sections have been retrieved and processed by Janis 3.1 [39], and their ratios are applied in the GEF EXT code.

In the modelling of multi-chance fission by GEF EXT, the formation of an equilibrated compound nucleus by neutron capture is assumed, and the neutron emission by the compound nucleus in (n, nf) reactions is calculated using the Weisskopf-Ewing formalism. Additionally, the fission probability of the residual nucleus after neutron emission has to be taken into account. This probability has also been estimated using the ratios of evaluated incident neutron or gamma fission cross-sections (MT=18) to the total inelastic reaction cross-sections (MT=3), taking incident neutron data from the JEFF-3.1.1 and incident gamma data from the TENDL-2009 library (see section 2.2 for explanation). Incident gamma data were used to estimate the fission probability of the residual nuclei ^{239}Pu, ^{240}Pu and ^{242}Pu, whose neutron separation energies are higher than or close to their fission barrier. For the residual nuclei ^{235}U, ^{238}U and ^{241}Pu, incident neutron cross-sections were applied. The only alternative library containing the required incident gamma cross-sections is ENDF/B-VII.0, in which there is an error in the ratio between both cross-sections at low energy. For third chance fission reactions $(n, 2nf)$, it is reasonable to set the excitation energy of the fissioning nucleus to a constant value slightly above the fission barrier. The procedure is illustrated in Fig. 12.
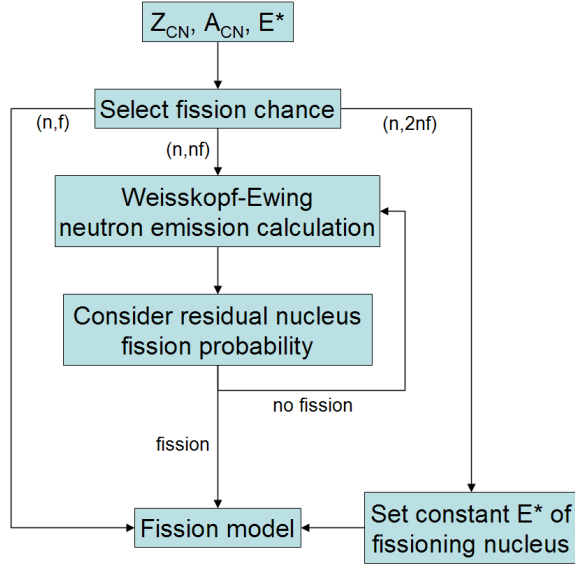
Figure 12: Inclusion of multi-chance fission in GEF EXT.

In the output of GEF EXT, specific fission yields for metastable states are given. For the different fissioning nuclei, the isomeric ratios have been taken from evaluated fission yield data files and sets listed in Table 3. For the fissioning nucleus ^{238}Pu, evaluated data on $^{237}Pu(n,f)$ are not available and the set $^{239}Pu(n,f)$ T from JEFF-3.1.1 was used. It is not clear whether it makes sense to apply the isomeric ratios from these files to second or third chance fission reactions. However, to the vast majority of the dominating first chance fission events, the evaluated data are applied exactly as intended. Details concerning the application of evaluated fission yield data sets are discussed in sections 3.1 and 4.6.

Fissioning Nucleus	Data Set	Fissioning Nucleus	Data Set
^{234}U	JEFF-3.1.1, $^{233}U(n,f)$ T	^{238}Pu	JEFF-3.1.1, $^{239}Pu(n,f)$ T
^{235}U	JEFF-3.1.1, $^{234}U(n,f)$ F	^{239}Pu	JEFF-3.1.1, $^{238}Pu(n,f)$ T
^{236}U	JEFF-3.1.1, $^{235}U(n,f)$ T	^{240}Pu	JEFF-3.1.1, $^{239}Pu(n,f)$ T
^{237}U	JEFF-3.1.1, $^{236}U(n,f)$ F	^{241}Pu	JEFF-3.1.1, $^{240}Pu(n,f)$ F
^{238}U	ENDF/B-VII.0, $^{237}U(n,f)$ F	^{242}Pu	JEFF-3.1.1, $^{241}Pu(n,f)$ T
^{239}U	JEFF-3.1.1, $^{238}U(n,f)$ F	^{243}Pu	JEFF-3.1.1, $^{242}Pu(n,f)$ F

Table 3: Sources of the isomeric ratios in the output of GEF EXT.

The SL shell effect parameters Δ_{SL} have been taken from GEF 2010/5c. Two of them have been added to better reproduce experimental and evaluated data and are listed below.

Fissioning Nucleus	Δ_{SL} in GEF EXT [MeV]
^{239}U	-0.1
^{242}Pu	-0.57

The code GEF EXT takes the fission reaction rate spectrum (101) as input, from which it calculates weighted fission product yields for the target nuclei ^{235}U, ^{238}U, ^{239}Pu, ^{240}Pu, ^{241}Pu and ^{242}Pu.
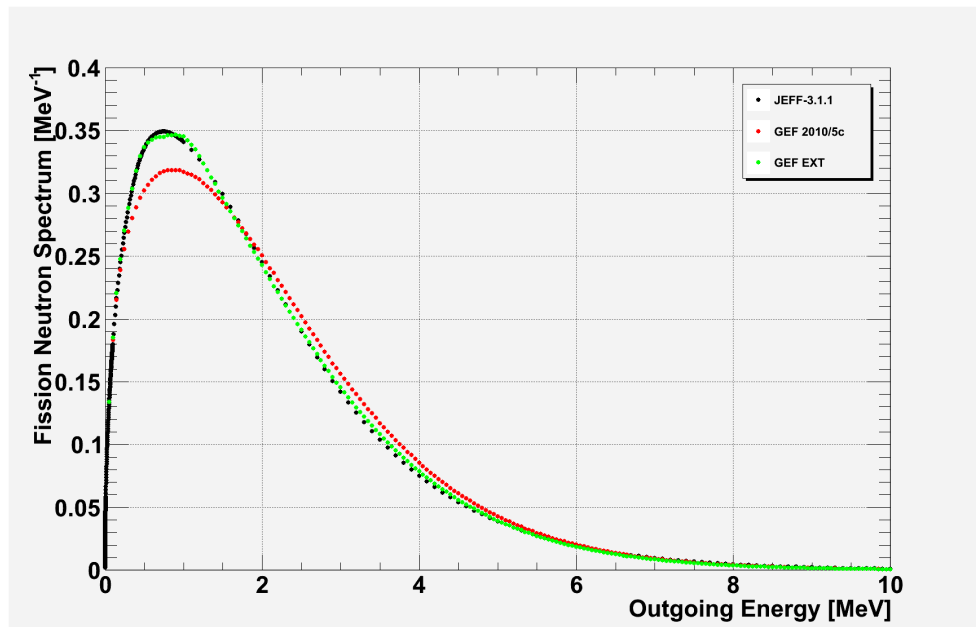
Figure 13: Prompt neutron spectra of $^{235}U(n_{th}, f)$ from GEF 2010/5c, GEF EXT and JEFF-3.1.1 evaluated data.
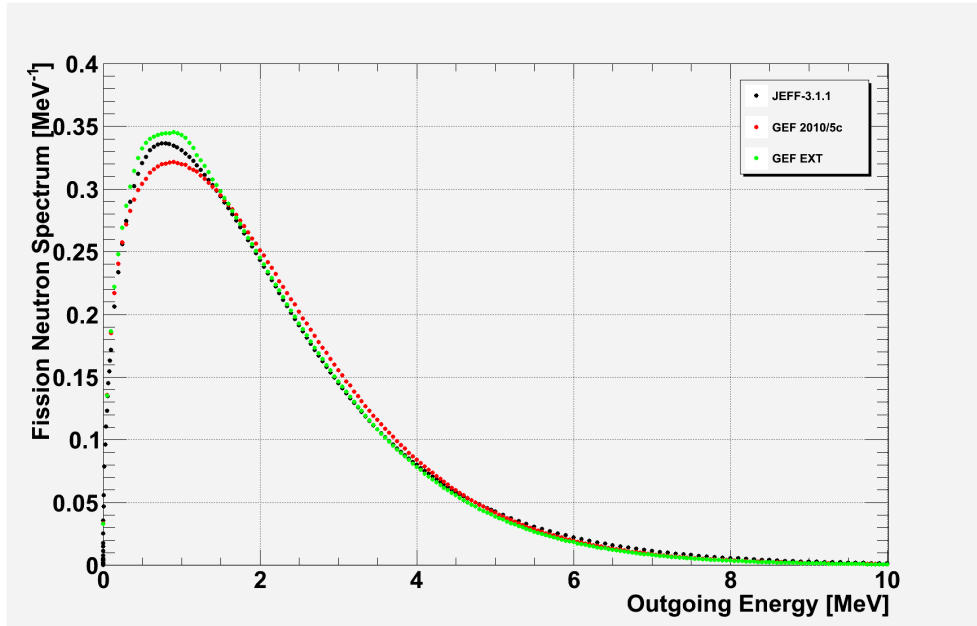
Figure 14: Prompt neutron spectra of $^{239}Pu(n_{th}, f)$ from GEF 2010/5c, GEF EXT and JEFF-3.1.1 evaluated data.

2.1.3 Potentials and Challenges for Future Work

The model description of the fission process described in this work certainly enables interesting applications in the evaluation of nuclear data. Above all, it could serve to improve the even-odd effects of fission yields in evaluated nuclear data files, and unmeasured isomeric ratios could be completed by the results from GEF 2011/1 and newer versions. A consistent model of the fission process and all its observables can be expected to have a higher predictive power than the models applied to fission yield evaluation so far. Schmidt's approach enables a gradual transition from an empirical towards a more theoretical description with good quantitative results. This makes it possible to create evaluated fission yield data files with more neutron energy interpolation points than in the existing libraries, and model calculations may be performed for the neutron spectrum of a specific reactor.

Nevertheless, the precision of the model still should be improved, as the results in chapter 3 show. Significant progress may be achieved by adjusting it better to the experimental data. However, several major challenges are remaining:

- To find out how to adjust the model parameters of the neutron even-odd effect in the yields, insight into the pre-neutron fragment yield distribution needs to be obtained.

- The physics behind the formation of fragment spins, which are important to fragment deexcitation and the population of metastable states, are not yet well understood.

- The physics behind the shift of the channel specific mean pre-neutron fragment masses with the excitation energy of the system are not yet clear due to the lack of experimental data on fast fission.

- If multi-chance fission is to be included, information on the competition of fission, neutron and gamma emission of the excited nucleus is required, which in general needs to be obtained from a model. Regarding the ratios of evaluated neutron-induced multi-chance fission cross-sections (e. g. MT=19, MT=20) used in the GEF EXT code, there are still major deviations between the different libraries mentioned in section 2.1.2. Concerning incident gamma cross-sections, there are surely large uncertainties and few alternatives to TENDL-2009.

2.2 Other Related Activities

At this point a brief description of the TALYS code used in the creation of the TENDL evaluated data libraries, which were also applied in this work, will be given.

The TALYS code is a modern nuclear reactions simulation code being developed by A. Koning, S. Hilaire and M. Duijvestijn at NRG Petten, Netherlands, and at CEA Bruyeres-le-Chatel, France. It offers a variety of possible applications and has been used for the creation of the TALYS Evaluated Nuclear Data Libraries (TENDL). As mentioned in section 2.1.2, incident gamma cross-section data from the TENDL-2009 library are used in the GEF EXT code. The TALYS code is rather focused on the calculation of cross-sections, but is also able to calculate fission product yields from fission at excitation energies up to 28 MeV [41].

TALYS contains an elaborate model for the calculation of fission transmission coefficients, which is based on spin and parity dependent state densities connected with the Hill-Wheeler or the WKB penetrability. The transmission coefficients enter a Hauser-Feshbach calculation which returns the corresponding fission cross-section. All the effects to be expected from a multi-humped fission barrier are included. However, the distinct fission channel fractions may not be precisely predicted by a purely theoretical model. The problem is that unknown physical quantities, such as shell corrections on top of the fission barriers which influence the level density, are required for the calculation. Fission barrier parameters from several external sources can be applied in TALYS.

The distribution of pre-neutron mass yields is calculated by an advanced version of the multi-modal random neck-rupture model of Brosa (see section 1.2.3), which is based on the pre-scission shape obtained from calculated potential energy surfaces. The isobaric proton number distribution of the yields is obtained from the scission-point model of Wilkins et al. [19], similar to GEF.

Compared to GEF, the TALYS 1.2 fission model can be considered to be less advanced

with respect to the calculation of fragment excitation energies, even-odd effects and prompt neutron evaporation. However, the other features of the code enable interesting applications in the modelling of the competition between fission, neutron emission and gamma emission. This is useful in the description of multi-chance fission, as discussed in section 2.1.2.

3 Analysis of Evaluated and Experimental Data

This chapter deals with various analyses of fission product yields from experiments, evaluated data and model calculations with the GEF 2010/5c and GEF EXT codes. The kinetic energies of fission fragments calculated by the codes are also compared to experimental values from a number of sources. The analysis is performed for the uranium and plutonium nuclides relevant in the U/Pu fuel cycle. The objective of this chapter is to draw conclusions on the quality of the model codes and the JEFF-3.1.1 evaluated data library.

3.1 About Evaluated Fission Yields Data

For the application in reactor calculations, evaluated fission product yields data are publicly available from the European JEFF, the American ENDF/B, the Japanese JENDL and other nuclear data projects. In this work, the fission yield data from the JEFF-3.1.1 library [36], which was released in January 2009, have been analyzed.

The current way of including the neutron energy dependence of fission yields on evaluated data libraries is to use multiple fission yield data sets attributed to different incident neutron energies as interpolation points. In the libraries of the three projects mentioned above, there are data sets for thermal (T), fast (F) and high energetic (H) neutrons. The following table lists the energy ranges to which the different sets of JEFF-3.1.1 are to be applied [36, 40].

Data Set	E_n Lower Limit	E_n Upper Limit
T	thermal	400 keV
F	400 keV	14 MeV
H	14 MeV	20 MeV

This way of describing the energy dependence has been established because of the fact that reliable fission yields could not yet be calculated using theoretical models and that the experimental data on fast fission are mostly incomplete. The energy $E_n = 14$ MeV, which has been investigated more thoroughly by experiments, is an exception [15]. It makes sense to create a specific data set for this energy, which is the average energy of fusion neutrons from $^2H + {}^3H \rightarrow {}^4He + n$. Thus, the experimental yields at this energy have been evaluated using correlations and covariances of the yields, and are applied to high energetic fission above $E_n = 14$ MeV [42]. The available data sets for thermal fission can be considered as the most reliable evaluated data, since most experiments have been performed at thermal energy. The yields in the fast fission data sets have been evaluated from measurements in fast reactor spectra and fission neutron spectra [43]. Due to the scarce experimental information, which is rather limited to mass distributions in this case, the isobaric nuclide yield distributions in these data sets cannot be expected to be very precise.

Evaluated fission yields data for reactor calculations need to include all important nuclides and isomers, which implies the necessity to estimate unknown nuclide yields. Additionally,

many isomeric ratios are still unknown, which results in uncertainties in the calculated decay heat during the first minutes after reactor shutdown. The isomeric ratios in the JEFF-3.1.1 data have been completed by a simple model of Madland and England for the calculation of isomeric ratios which takes the spin values of the ground and isomeric states as input. However, the predictive power of this model is limited [43]. Unmeasured nuclide yields have been estimated from the value of a fit function consisting of five Gaussians, representing the SL, S1 and S2 channels. The fit was applied to the mass yield distribution, whereas the isobaric nuclide yields distribution, including the even-odd effects, was taken from the empirical "Z_p" model developed by Wahl. Further adjustments have been applied to fulfill the conservation of charge and nucleon number, the symmetry of the elemental yields distribution and the normation of the sum of all yields except light charged particles to 2. The methods applied in the evaluation of the JEFF-3.1.1 fission yields are completely described in the PhD thesis of R. Mills, University of Birmingham (1995) [42].

In the JEFF-3.1.1 fission yields database there are "parent independent" (MT=454) and "parent cumulative" (MT=459) yields. The parent independent yield of a nuclide expresses its amount produced in the fission process only. On the other hand, the cumulative yield of a nuclide expresses its production in the fission process plus its integral production by the radioactive decay of its mother nuclides which have been produced in the fission process simultaneously. In the JEFF-3.1.1 evaluation, they have been calculated from the independent yields including delayed neutron emission and considering nuclides with half lives of more than 1000 years as stable [42]. Cumulative yields are useful for several purposes:

- They enable easy calculations of the integral delayed neutron and decay energy release.

- They facilitate the lumping of nuclides in reactor burn-up calculations.

- They indicate the equilibrium production rate of a nuclide in a reactor if reactions of neutrons with its parents can be neglected.

However, for the calculation of time-dependent decay heat, radiotoxicity etc. the independent yields (MT=454) should generally be applied [42].

To get an impression of their accuracy, the model codes GEF 2010/5c and GEF EXT are firstly compared to experimental and the most reliable evaluated data. Secondly, some conclusions on the quality of less reliable evaluated fission yields data, i. e. especially the fast fission yields data, can be drawn from the comparison to the model results. Some minor deficiencies of the evaluated data are spotted in the following analyses already.

3.2 Analysis of Mass Yield Distributions

In order to enable a systematic accumulation of all nuclear data from international experiments, the EXFOR library has been established. In this library, each experiment has an entry number and the data are stored in a standardized format. In this work, an analysis of experimental fast fission mass yield distributions from the EXFOR library was performed. A superposition of Gaussians was fitted to the distributions, commonly described by the function

$$
\begin{aligned}
y(A) = \quad & h_{SL} \cdot \left(e^{-\frac{(A-\overline{A_{SL,l}})^2}{2\sigma_{SL}^2}} + e^{-\frac{(A-\overline{A_{SL,h}})^2}{2\sigma_{SL}^2}} \right) + h_{S1} \cdot \left(e^{-\frac{(A-\overline{A_{S1,l}})^2}{2\sigma_{S1}^2}} + e^{-\frac{(A-\overline{A_{S1,h}})^2}{2\sigma_{S1}^2}} \right) \\
+ & h_{S2} \cdot \left(e^{-\frac{(A-\overline{A_{S2,l}})^2}{2\sigma_{S2}^2}} + e^{-\frac{(A-\overline{A_{S2,h}})^2}{2\sigma_{S2}^2}} \right) + h_{S3} \cdot \left(e^{-\frac{(A-\overline{A_{S3,l}})^2}{2\sigma_{S3}^2}} + e^{-\frac{(A-\overline{A_{S3,h}})^2}{2\sigma_{S3}^2}} \right)
\end{aligned}
$$

which includes the SL, S1, S2 and S3 channels and contains 16 parameters. According to the model description of GEF 2010/5, $\overline{A_{SL,l}}$ and $\overline{A_{SL,h}}$ do not exactly coincide in the pre-neutron distribution already. The fits were either performed to the pre-neutron mass yield distribution or half of the post-neutron mass yield distribution only, so there was no necessity to additionally introduce separate widths σ_i for both fragments. Since A is an integer, the integral

$$
Y(A) = \int_{A-\frac{1}{2}}^{A+\frac{1}{2}} dA' \, y(A')
$$

was used to fit the data. The fits were performed with ROOT 5.24/00 [44].

The several Gaussians were fitted by the following procedure: A first fit was performed with the curves of the S1 and S2 channels only. After that, the parameters of this first fit were fixed and the SL curve was fitted. Since the width and the central mass values of the SL curve could not be determined from the fits, they were taken from GEF 2010/5. The obtained height h_{SL} of this curve was also fixed and the S3 curve was fitted as a last step. With this procedure, the results became more stable, and the deviations around the central masses of the SL and S3 channels were significantly reduced.

The covariance matrix of fit parameters V_{par} was read out from ROOT 5.24/00, and the errors of the specific channel yields analyzed in this work were obtained by calculating their covariance matrix V_Y (97). Covariances of parameters of the SL and S3 channels with previously fixed parameters were assumed to be zero, as well as the errors of parameters taken from the model.

$$
V_Y = \begin{pmatrix} \frac{\partial Y_{SL}}{\partial h_{SL}} & \cdots & \frac{\partial Y_{SL}}{\partial \sigma_{S3}} \\ \vdots & \ddots & \vdots \\ \frac{\partial Y_{S3}}{\partial h_{SL}} & \cdots & \frac{\partial Y_{S3}}{\partial \sigma_{S3}} \end{pmatrix} \cdot V_{par} \cdot \begin{pmatrix} \frac{\partial Y_{SL}}{\partial h_{SL}} & \cdots & \frac{\partial Y_{SL}}{\partial \sigma_{S3}} \\ \vdots & \ddots & \vdots \\ \frac{\partial Y_{S3}}{\partial h_{SL}} & \cdots & \frac{\partial Y_{S3}}{\partial \sigma_{S3}} \end{pmatrix}^T \tag{97}
$$

All fits were performed with the χ^2 method. The errors were taken from the data in the case of ^{238}U. In the other cases they were estimated iteratively from the expected χ^2 value and assumed to be statistical.

For the numerous diagrams obtained from the analysis, see appendix B.

3.2.1 ^{235}U

In the case of uranium isotopes, there is a big data stock about fast fission. The mass distributions from fast fission of ^{235}U were measured by the Fiziko-Energeticheskii Institut in Obninsk, Russia, at the end of the 1960s and are available for 17 energies between $E_n = 120\,\text{keV}$ and $E_n = 6.06\,\text{MeV}$ [45, 46]. These sources provide data on the pre-neutron emission mass distribution in the range $118 \leq A \leq 157$. They were obtained from coincidence measurements with silicon detectors.

The results from this work agree rather well with the channel fractions and mass variances of Straede et al. [47]. They used more or less the same fit method as this work, taking the width of the SL channel from a model. There is another source [48] with more deviating values, maybe because they analyzed the fragment distributions in mass and TKE. This procedure may give more stable results since the information on the TKE is included, but it is difficult to define a reasonable fit function $TKE(A)$ for the mass-dependent TKE distribution, which is not well described by a Gaussian. Reliable results were obtained for the yield of the SL channel. The S3 channel was not found to contribute significantly to the mass distributions of $^{235}U(n,f)$.

In the diagrams we see that the experimental and modelled fractions of the S1 and S2 channels (Figs. B.1, B.2) more or less agree in the low energy range, but the decrease of Y_{S1} with increasing neutron energy is not reproduced. The fraction of the SL channel (Fig. B.3) fits quite well at least below 4 MeV. It was calculated with the recommended SL shell effect $\Delta_{SL} = 0.3\,\text{MeV}$. In this case, the mass widths (Figs. B.4, B.5) predicted by GEF 2010/5c tend to be too wide, but the energy dependence of the S2 width is well reproduced.

Here it is particularly interesting to have a closer look at the mean fragment masses. The mean pre-neutron mass of heavy fragments from the S2 channel (Fig. B.7) was found to decrease significantly with increasing neutron energy. The energy dependence of the mean fragment mass from the S1 channel (Fig. B.6) is less pronounced. This effect has also been observed by Vives et al. [49] in $^{238}U(n,f)$. They attribute it to the washing out of shell effects when the excitation energy increases. However, they have not investigated experimentally whether the shift of $\overline{A_{S2,h}}$ is caused by a shift in the mean proton or neutron number. The effect is not yet included in GEF 2010/5c. Surprisingly, the mean heavy fragment mass $\overline{A_{S1,h}}$ predicted by the code is about 1.4 mass units higher.

3.2.2 ^{238}U

For ^{238}U, there is a good work from Vives et al. [49] in which all masses and total kinetic energies have been measured at 15 incident neutron energies between $E_n = 1.2$ MeV and $E_n = 5.8$ MeV. The kinetic energies, mass widths and fission channel fractions have been analyzed in it, and the latter two are also shown in the diagrams. However, Vives et al. obtained their values from fits to the distribution in mass and TKE. This analysis gives an impression of the agreement between the results from analyses of mass and mass-TKE distributions. Furthermore, the fractions of the SL channel (Fig. B.10) are obtained using the SL mass widths and central values from GEF 2010/5.

The fraction Y_{SL} of the SL channel was calculated with the SL shell effect $\Delta_{SL} = -0.1$ MeV to fit the data point at $E_n = 2.5$ MeV. It turned out that it increases less steeply than predicted by GEF 2010/5c. The mass width of the S1 channel (Fig. B.11) predicted by GEF 2010/5c generally seems to increase too steeply, whereas the agreement of the S2 width (Fig. B.12) is not too bad in this case. In the low energy region, the variation of the S1 and S2 channel fractions (Figs. B.8, B.9) is only weakly reproduced. The results from this work generally deviate more or less from Vives et al. [49], possibly because of the different evaluation methods. The uncertainties of the data given in the source may be too low and the real mass distributions cannot be expected to be exactly Gaussian.

3.2.3 ^{239}Pu

Data on the mass distributions of fission fragments from plutonium isotopes are available from coincidence experiments at the Fiziko-Energeticheskii Institut in Obninsk, Russia, and radiochemical experiments of the European Institute for Transuranium Elements in Leopoldshafen, Germany, which were performed with test samples irradiated in the Rapsodie SFR at CEA Cadarache, France. The data on ^{239}Pu have been taken from [50, 51, 52], with [50, 51] containing pre-neutron mass yields in the ranges $80 \leq A \leq 120$ and $120 \leq A \leq 160$ respectively, whereas [52] contains cumulative decay chain yields, i. e. mass yields after prompt and delayed neutron emission, in the range $125 \leq A \leq 152$.

For the fraction Y_{SL} of the SL channel, no significant values were found for all plutonium isotopes. The fraction of the S1 channel (Fig. B.13) predicted by GEF 2010/5c is around 50% too low, which is a general problem with the plutonium isotopes. The S2 mass width (Fig. B.16) is well reproduced except the point of [51], whereas the agreement for the S1 width (Fig. B.15) is also less good. However, the quantities extracted by the analysis are subject to large uncertainties in the case of plutonium isotopes. The model calculation was performed with the recommended SL shell effect $\Delta_{SL} = -0.1$ MeV. The post-neutron quantities evaluated from [52] are given separately in the table below.

post-neutron quantities, $E_n = 1.0\,\text{MeV}$		
	[52]	GEF EXT
σ_{S1}, heavy	2.46 ± 0.08	3.43
σ_{S2}, heavy	5.49 ± 0.07	5.40
$\overline{A_{S1,h}}$	133.7 ± 0.1	133.9
$\overline{A_{S2,h}}$	140.0 ± 0.2	139.4

The existence of the S3 channel could be shown for the targets ^{239}Pu, ^{241}Pu and ^{242}Pu. In Tables 4, 5 and 6, results from fits with an S3 fraction Y_{S3} greater than its uncertainty are listed. The S3 fraction is generally observed to be small even at high excitation energies, and its mass distribution appears to be more narrow than that of the S1 channel. In the case of $^{239}Pu(n, f)$, the S3 channel was found to be located around a pre-neutron mass of $\overline{A_{S3,l}} \approx 82$ in the light fragment, corresponding to a heavy fragment of $\overline{A_{S3,h}} \approx 158$.

Neutron Energy [MeV]	Y_{S3}	$\overline{A_{S3}}$	σ_A, S3	Data Source
0.72	$(1.8 \pm 1.3) \cdot 10^{-3}$	81.6 ± 0.5	1.25 ± 0.52	[50]
1.72	$(3.1 \pm 1.4) \cdot 10^{-3}$	81.7 ± 1.4	2.10 ± 1.06	[50]
2.72	$(2.6 \pm 1.7) \cdot 10^{-3}$	82.0 ± 1.6	1.97 ± 1.30	[50]
5.45	$(3.4 \pm 2.0) \cdot 10^{-3}$	157.7 ± 1.1	1.80 ± 1.23	[51]

Table 4: Characteristics of the S3 channel in $^{239}Pu(n, f)$ evaluated in this work.

3.2.4 ^{240}Pu

Complete data on the mass yields of $^{240}Pu(n, f)$ are scarce and could only be taken from [52], which contains cumulative chain yields in the range $125 \leq A \leq 152$. Due to the limited mass range, the characteristics of the SL and S3 channels could not be determined. The results for the S1 and S2 channels are given in the table and compared to the model codes. The model calculations were performed with the recommended SL shell effect $\Delta_{SL} = -0.35\,\text{MeV}$.

post-neutron quantities, $E_n = 1.0\,\text{MeV}$		
	[52]	GEF EXT
Y_{S1}	0.315 ± 0.027	0.137
Y_{S2}	0.678 ± 0.028	0.841
σ_{S1}, heavy	2.52 ± 0.14	3.25
σ_{S2}, heavy	5.45 ± 0.10	5.16
$\overline{A_{S1,h}}$	133.8 ± 0.1	134.1
$\overline{A_{S2,h}}$	140.0 ± 0.2	139.7

3.2.5 ^{241}Pu

For the fast fission of ^{241}Pu, there are cumulative chain yields from [52], yields after prompt neutron emission from [53] and pre-neutron yields from [54]. In the diagrams we see that GEF 2010/5c reproduces the increase of the S1 channel fraction Y_{S1} (Fig. B.17) when the neutron number of the fissioning nucleus increases, but the values of Y_{S1} are too low. In this case, Y_{S1} is clearly found to decrease with increasing excitation energy of the system. Although [53] contains post-neutron data, the light fragments of the S3 channel were found at slightly higher masses than in the case of ^{239}Pu. The values obtained from pre-neutron data and post-neutron data on heavy fragments [52, 54] are listed in the following two tables. The widths of the post-neutron mass distributions of light fragments evaluated from [53] are shown in Figs. B.19 and B.20. The width of the S1 channel calculated by GEF EXT is in good agreement with the data, whereas for the S2 channel it deviates surprisingly much to lower values. The values of [54] are found to agree well with GEF 2010/5c. The SL shell effect parameter was set to $\Delta_{SL} = -0.57$ MeV in the calculation to best reproduce the peak-to-valley ratio of $^{241}Pu(n_{th}, f)$ in JEFF-3.1.1.

post-neutron quantities, $E_n = 1.0$ MeV		
	[52]	GEF EXT
σ_{S1}, heavy	2.66 ± 0.18	3.40
σ_{S2}, heavy	5.41 ± 0.16	5.34
$\overline{A_{S1,h}}$	134.1 ± 0.2	134.2
$\overline{A_{S2,h}}$	140.6 ± 0.4	139.9

pre-neutron quantities, $E_n = 2.74$ MeV		
	[54]	GEF 2010/5c
σ_{S1}	3.61 ± 0.25	3.62
σ_{S2}	6.66 ± 0.08	6.46
$\overline{A_{S1,h}}$	135.3 ± 0.3	135.1
$\overline{A_{S2,h}}$	141.4 ± 0.2	141.4

Neutron Energy [MeV]	Y_{S3}	$\overline{A_{S3}}$	σ_A, S3	Data Source
0.3	$(3.1 \pm 2.0) \cdot 10^{-3}$	84.9 ± 1.0	2.29 ± 0.81	[53]
1.6	$(3.2 \pm 2.5) \cdot 10^{-3}$	83.8 ± 1.5	2.79 ± 1.20	[53]
2.74	$(2.3 \pm 1.6) \cdot 10^{-3}$	159.1 ± 2.6	2.97 ± 1.99	[54]
5	$(1.7 \pm 1.5) \cdot 10^{-3}$	85.1 ± 2.6	1.70 ± 2.52	[53]

Table 5: Characteristics of the S3 channel in $^{241}Pu(n, f)$ evaluated in this work.

3.2.6 ^{242}Pu

For this nucleus, cumulative chain yields from [52] and pre-neutron mass yields from [54] are available. A large discrepancy is observed between the S2 mass widths (Fig. B.24) evaluated from [54] and calculated by GEF 2010/5c. If we have a look at Fig. B.12, we find that the mass width of the S2 channel might indeed stay rather constant up to 2 MeV above the fission barrier, which is located at $E_n \approx 1\,\mathrm{MeV}$ in this case, however, the discrepancy is surprisingly large. The characteristics of the S3 channel have also been extracted from [54]. The calculations with GEF 2010/5c were performed using the recommended SL shell effect $\Delta_{SL} = -0.3\,\mathrm{MeV}$. The post-neutron quantities evaluated from [52] are listed in the table below.

post-neutron quantities, $E_n = 1.0\,\mathrm{MeV}$		
	[52]	GEF EXT
σ_{S1}, heavy	2.59 ± 0.25	3.18
σ_{S2}, heavy	5.52 ± 0.17	5.04
$\overline{A_{S1,h}}$	134.3 ± 0.2	134.5
$\overline{A_{S2,h}}$	140.7 ± 0.4	140.3

Neutron Energy [MeV]	Y_{S3}	$\overline{A_{S3}}$	σ_A, S3	Data Source
1.2	$(2.9 \pm 1.3) \cdot 10^{-3}$	159.8 ± 1.8	2.99 ± 1.45	[54]
3.37	$(2.0 \pm 1.6) \cdot 10^{-3}$	158.5 ± 1.3	1.56 ± 2.60	[54]

Table 6: Characteristics of the S3 channel in $^{242}Pu(n,f)$ evaluated in this work.

3.3 Even-odd Effect

In this work, an analysis of the proton even-odd effect in experimental fission yields data has been performed. The results are compared to the predictions of GEF 2010/5c and to the results from the analysis of JEFF-3.1.1 data. The analysis of the proton even-odd effect in fission product yields requires reliable experimental data on their proton number distribution. The currently most reliable sources for this purpose are spectrometric experiments performed at the Lohengrin [26, 55] and Cosi-Fan-Tutte [56] spectrometers of the Institut Laue-Langevin in Grenoble, France. The cited experiments provide data on the proton number distribution of light fragment yields from $^{235}U(n_{th}, f)$, $^{239}Pu(n_{th}, f)$ and $^{241}Pu(n_{th}, f)$. They are compared to evaluated JEFF-3.1.1 data and results from model calculations with the GEF 2010/5c code. The analysis of the global even-odd effect has been performed using (67) and that of the local even-odd effect using (68,69) from section 1.12.

The local even-odd effect is shown in the following diagrams. Due to the non-linearity of (68), the superposition of different fission channels may lead to negative local values of the even-odd effect especially at the inner tails of the distribution.

3.3.1 ^{235}U
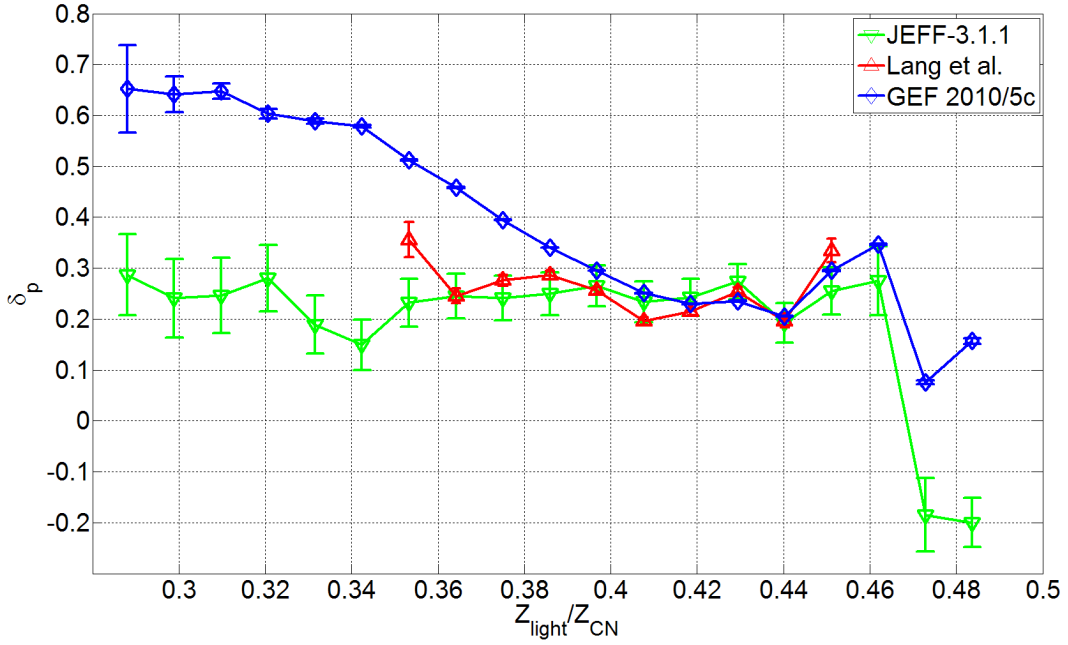
Figure 15: Local proton even-odd effect δ_p of $^{235}U(n_{th}, f)$ fission fragment yields. Experimental data taken from [26].

In the case of ^{235}U, the local proton even-odd effects from evaluated data, experiment and model calculation show a good agreement except for highly asymmetric splits, where the experiment and the model show an increase of the local even-odd effect. Although according to Table 8 the $\overline{TXE}$ of the S2 channel is well reproduced, the local even-odd effect from the model starts to increase at less asymmetric splits already, showing the uncertainties of the description. However, the rather constant behaviour shown by JEFF-3.1.1 at high asymmetry contradicts to the theory and is probably a deficiency of the evaluated data. This is also the case for ^{239}Pu and ^{241}Pu.

Values of the global proton even-odd effect:

Source	δ_p
JEFF-3.1.1	0.242 ± 0.018
Lang et al. [26]	0.237 ± 0.005
GEF 2010/5c	0.265

3.3.2 ^{239}Pu
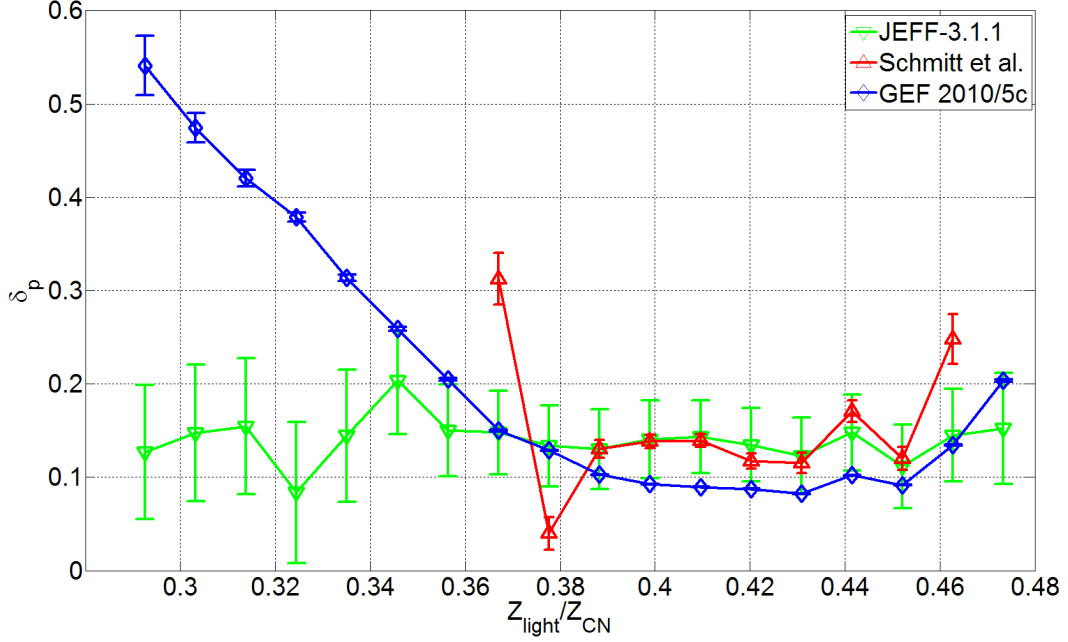
Figure 16: Local proton even-odd effect δ_p of $^{239}Pu(n_{th}, f)$ fission fragment yields. Experimental data taken from [55].

Experimental and evaluated data show a good agreement in the case of ^{239}Pu. There are some deviations at high asymmetry and close to symmetry. These could be caused by incompletely measured elemental yields in the tails of the distribution, as [55] provides data on the nuclide yield distribution of fragments with masses $86 \leq A \leq 109$ only. In this case, the values obtained from GEF 2010/5c are noticably lower than the ones obtained from experiment. According to the findings in section 3.5, the calculated total excitation energies should not deviate much. The deviation could result from various other uncertainties in the model.

Values of the global proton even-odd effect:

Source	δ_p
JEFF-3.1.1	0.133 ± 0.018
Schmitt et al. [55]	0.134 ± 0.006
GEF 2010/5c	0.097

3.3.3 ^{241}Pu
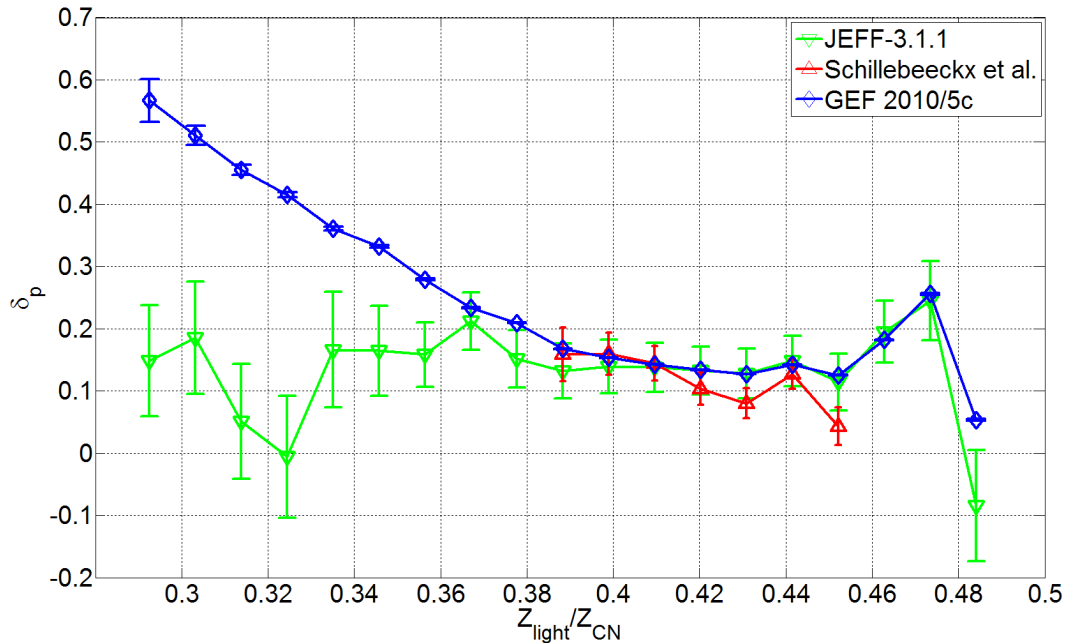
Figure 17: Local proton even-odd effect δ_p of $^{241}Pu(n_{th}, f)$ fission fragment yields. Experimental data taken from [56].

In this case there is a very good agreement between the model and JEFF-3.1.1 except for $\frac{Z_{light}}{Z_{CN}} < 0.36$. The experimental values, which have been obtained from the Cosi-Fan-Tutte spectrometer, systematically deviate to lower values. The global even-odd effect from experiment is lower than in the case of ^{239}Pu, whereas following the theory it should be comparable since the intrinsic excitation energies at scission are expected to be similar. Anyway, the evaluated data on this nucleus are subject to larger uncertainties than in the case of ^{235}U.

Values of the global proton even-odd effect:

Source	δ_p
JEFF-3.1.1	0.137 ± 0.018
Schillebeeckx et al. [56]	0.100 ± 0.015
GEF 2010/5c	0.146

3.4 Neutron Multiplicities

Due to the fact that charged particle emission from the fragments can be excluded and that the fraction of ternary fission is very small, the charge-split dependent mean prompt neutron multiplicity $\overline{\nu_p}(Z_{light})$ of the reaction can be determined from the post-neutron nuclide yields. However, this is only possible with evaluated data and model calculations, where the yields are complete. It is done using the relation

$$\overline{\nu_p}(Z_{light}) = N_{CN} - \overline{N}(Z_{light}) - \overline{N}(Z_{CN} - Z_{light})$$

from which the diagrams in this section were obtained, with $\overline{N}(Z)$ being the mean neutron number of fragments with proton number Z. The model calculations were carried out with GEF 2010/5c and the extended version of it called GEF EXT used to calculate the yields for the burn-up application in this work. The two codes have some differences in their evaporation models. For details, see section 2.1.2. Here, the results for the thermal fission of ^{235}U, ^{239}Pu and ^{241}Pu are compared.

The global $\overline{\nu_p}$ is not always well predicted by the codes. It is especially overestimated by GEF EXT, which however better represents the prompt neutron $\chi(E)$ spectrum, as shown by Figs. 13 and 14. The gamma competition in its deexcitation model seems to be underestimated. Another general difficulty is the precise modelling of the corresponding excitation energies. Concerning Table 7, it must be mentioned that the JEFF-3.1.1 $\overline{\nu_p}$ values have not been calculated from the yields, but taken from the evaluated $\overline{\nu_p}(E)$, which is available as MT=456.

Target	$\overline{\nu_p}$		
	JEFF-3.1.1	GEF 2010/5c	GEF EXT
^{235}U	2.42	2.26	2.77
^{239}Pu	2.87	3.18	3.65
^{241}Pu	2.92	3.17	3.65

Table 7: Calculated and JEFF-3.1.1 global prompt neutron multiplicities for thermal neutron induced fission. JEFF-3.1.1 values taken from MT=456.

The models more or less represent the qualitative trends of $\overline{\nu_p}(Z_{light})$. There also seem to be some deficiencies in the JEFF-3.1.1 fission yields, since the decrease of $\overline{\nu_p}(Z_{light})$ at symmetry in the case of ^{241}Pu contradicts to the expected high excitation energy. See Fig. 20.

The even-odd structure in the $\overline{\nu_p}(Z_{light})$ from both model codes is not found back in JEFF-3.1.1. In an investigation on this effect, it turned out that the even-odd structure originates from the level density backshifts and pairing gaps used to describe the competition between neutron and gamma emission in the evaporation model. One should be aware that

the observed proton even-odd effect in the spins of heavy fragments [32] is not included and expected to increase the competition of gamma emission from odd-Z fragments [5]. Additionally, only a slight proton even-odd staggering has been experimentally observed in the kinetic energies of light fragments. The staggering in the results from GEF 2010/5c is much more pronounced, i. e. the relative excitation energy of even-Z fragments is underestimated. For these reasons, the real $\overline{\nu_p}(Z_{light})$ is expected to be rather smooth. This can be considered as a weak point of the model codes. The details will be discussed in the next section.
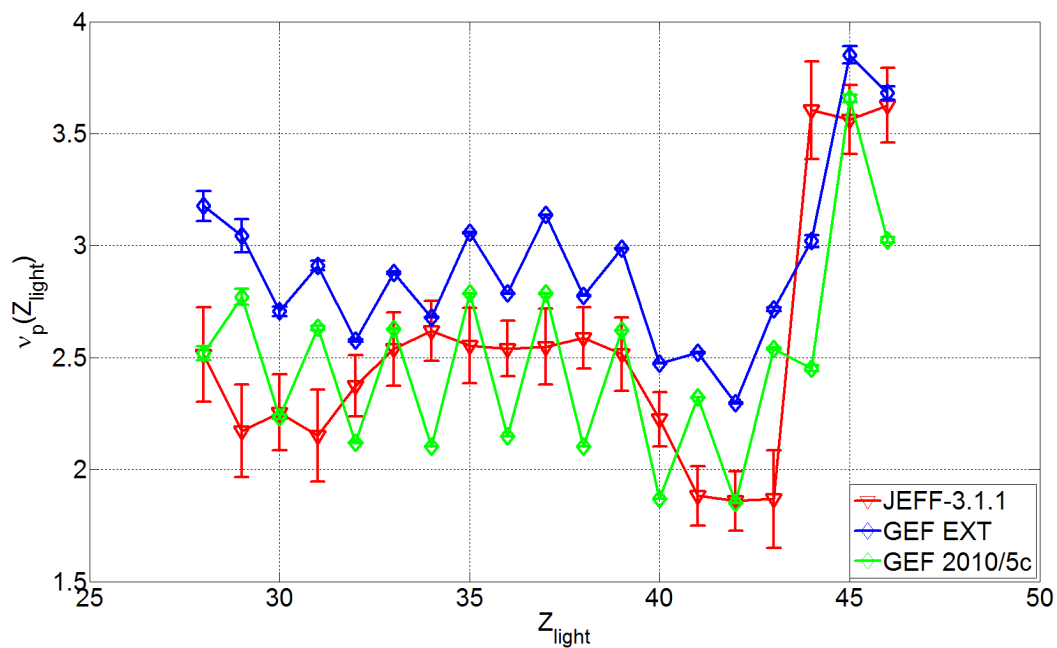
Figure 18: Charge split dependent neutron multiplicity of $^{235}U(n_{th}, f)$ from the models and JEFF-3.1.1 fission yields.
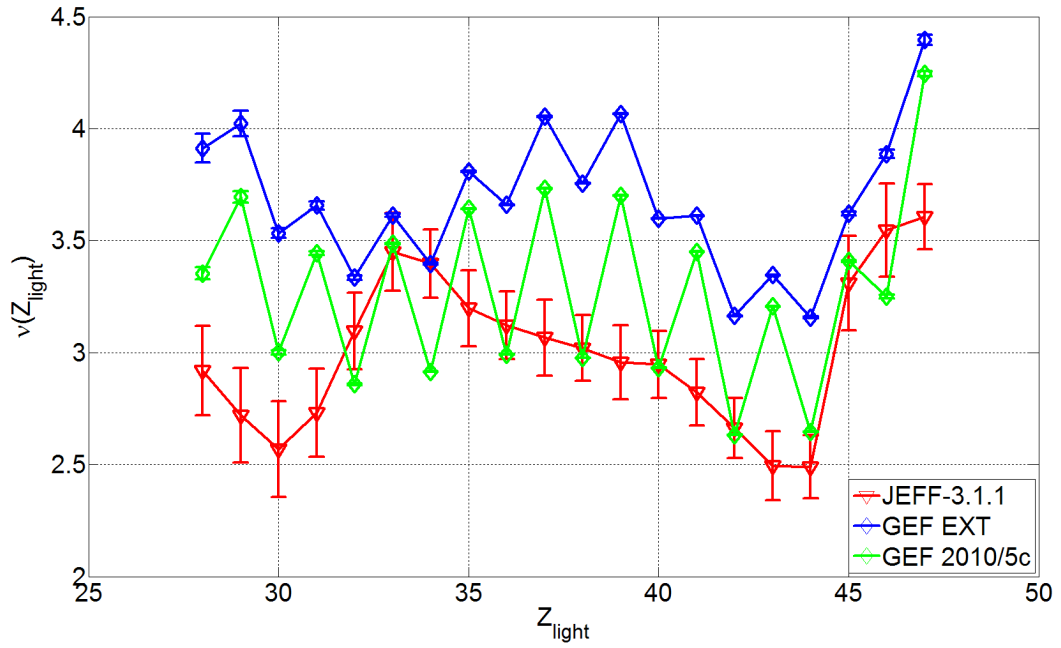
Figure 19: Charge split dependent neutron multiplicity of $^{239}Pu(n_{th}, f)$ from the models and JEFF-3.1.1 fission yields.
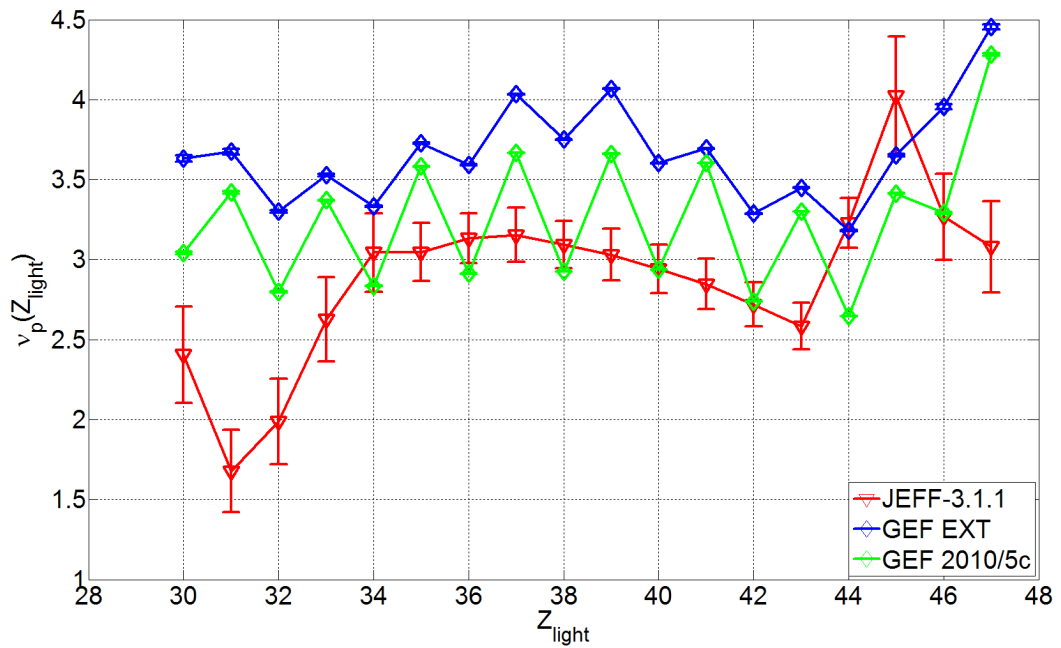
Figure 20: Charge split dependent neutron multiplicity of $^{241}Pu(n_{th}, f)$ from the models and JEFF-3.1.1 fission yields.

3.5 Kinetic Energies

The kinetic energies of fission fragments give some information on their initial excitation energies. For this reason, it is interesting to compare the kinetic energies from the model code to experimental data. The proton number dependent mean kinetic energies $\overline{E_{kin}}(Z)$ of fragments from $^{235}U(n_{th}, f)$, $^{239}Pu(n_{th}, f)$ and $^{241}Pu(n_{th}, f)$ have been measured in the experiments of [26, 55, 56]. The GEF 2010/5c model code was extended to calculate the mean pre- and post-neutron $\overline{E_{kin}}(Z)$. The neutron emission was observed to lower the kinetic energy of light fragments by 1.0 to 1.5 MeV, which is the result of the decreasing nuclear mass.

In the results from GEF 2010/5c on the post-neutron and pre-neutron $\overline{E_{kin}}(Z)$, a strong even-odd structure by 1.5 to 2 MeV is observed which clearly originates from the contribution of the proton pairing energy to the Q value. It becomes evident that the structure in the post-neutron $\overline{E_{kin}}(Z)$ cannot originate from the rather small variations in the calculated prompt neutron multiplicity. The even-odd structure in the experimental data is much smaller, so there is indeed a problem with the calculated excitation energies. As mentioned before, there is obviously an even-odd effect in the fragment excitation energies, with the TXE of splits into even-Z fragments being enhanced. An explanation of this effect from [26] has been mentioned in section 1.9.

The kinetic energies which have been measured by the spectrometric experiments at ILL Grenoble [26, 55, 56] give an impression of the precision of the calculated TXE. [26] and probably also [55] contain reconstructed pre-neutron kinetic energies, whereas in [56] they are declared as post-neutron data. One should keep in mind that the ratios of the S1 and S2 channel fractions are badly reproduced by the model in case of the plutonium isotopes.

Another option is to compare the channel specific mean TKE to experimental data. For this, see Table 8. A general observation is that the difference in $\overline{TKE}$ between the S1 and S2 channels calculated by GEF 2010/5c is too small. The deviation of the values for the SL channel is surprisingly large, since the $\overline{\nu_p}$ of symmetric splits is not badly reproduced by the model. However, the experimentally observed increase of the channel specific $\overline{TKE}$ with an increasing neutron energy is not reproduced. Unfortunately, mass or charge dependent mean kinetic energy values do not provide good information on this effect because it is hidden by the variations of the S1 and S2 channel fractions. The decrease in the $\overline{TKE}$ predicted by GEF 2010/5c must be due to the vanishing of even-odd effects or to the broadening of the channel specific pre-neutron nuclide yield distributions when the neutron energy increases. There may be a mechanism making the incident neutron energy partly end up in kinetic energy, but this will have to be investigated more carefully. In the model, the incident neutron energy is assumed to end up in intrinsic or collective excitation energy only.

Reaction	Channel	Neutron Energy [MeV]	$\overline{TKE}$ (pre-neutron) [MeV]		Source
			Experimental	GEF 2010/5c	
$^{235}U(n,f)$	SL	thermal	157 ± 7	164.12	[22]
	S1		187 ± 1	177.68	
	S2		167 ± 1	167.04	
$^{238}U(n,f)$	SL	1.6	143.1 ± 6.9	168.78	[49]
	S1		180.2 ± 0.2	182.15	
	S2		164.99 ± 0.07	170.32	
	SL	2.5	151.8 ± 6.8	168.92	
	S1		180.86 ± 0.13	181.27	
	S2		165.5 ± 0.04	169.45	
	SL	5.8	154.4 ± 3.4	168.57	
	S1		181.92 ± 0.20	180.15	
	S2		166.63 ± 0.05	168.36	
$^{237}Np(n,f)$	SL	5.5	160.9 ± 0.2	172.02	[18]
	S1		186.0 ± 0.1	184.27	
	S2		170.0 ± 0.1	172.50	
$^{239}Pu(n,f)$	S1	thermal	190.4 ± 0.2	186.03	[57]
	S2		174.2 ± 0.3	174.37	

Table 8: Channel specific mean TKE from GEF 2010/5c and experiments. Note that [18] does not explicitly declare the values as pre-neutron data.
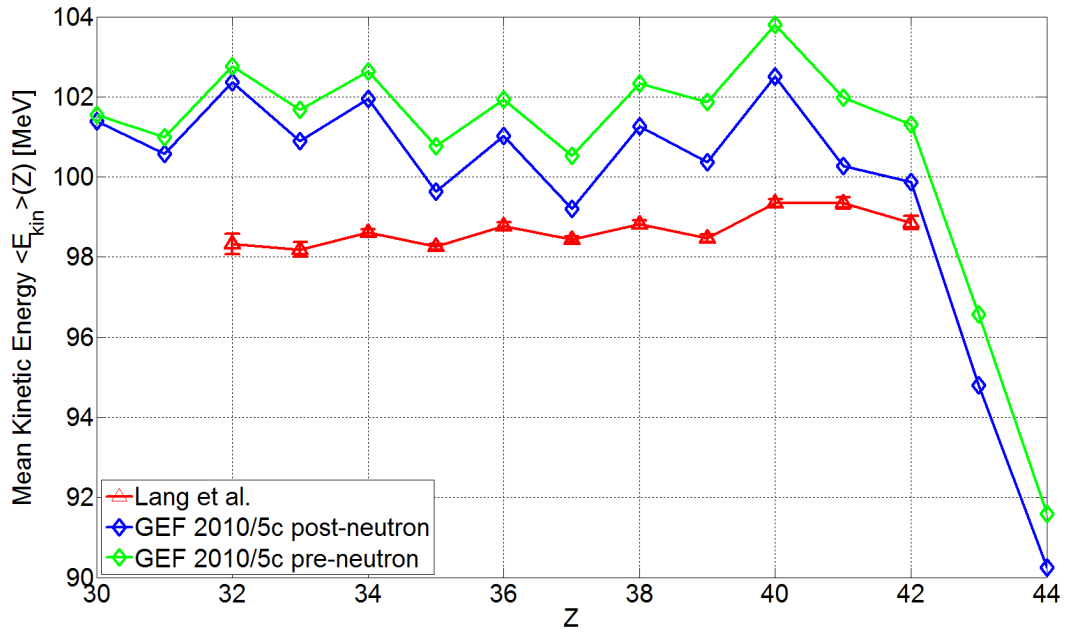
Figure 21: Charge dependent mean kinetic energies of $^{235}U(n_{th}, f)$ from GEF 2010/5c. Experimental data taken from [26].
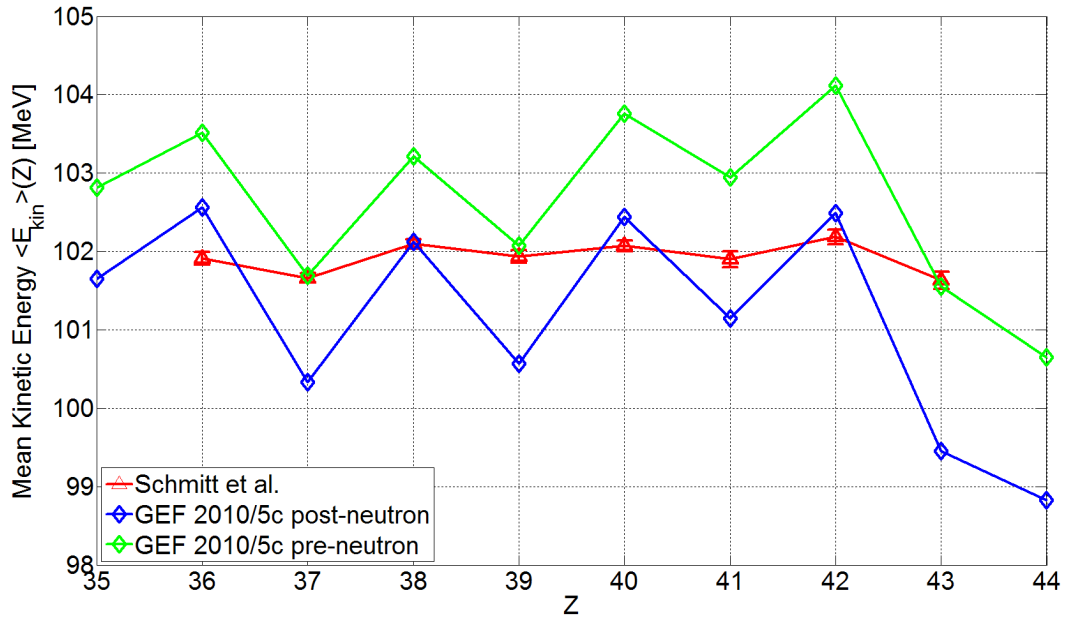
Figure 22: Charge dependent mean kinetic energies of $^{239}Pu(n_{th}, f)$ from GEF 2010/5c. Experimental data taken from [55].
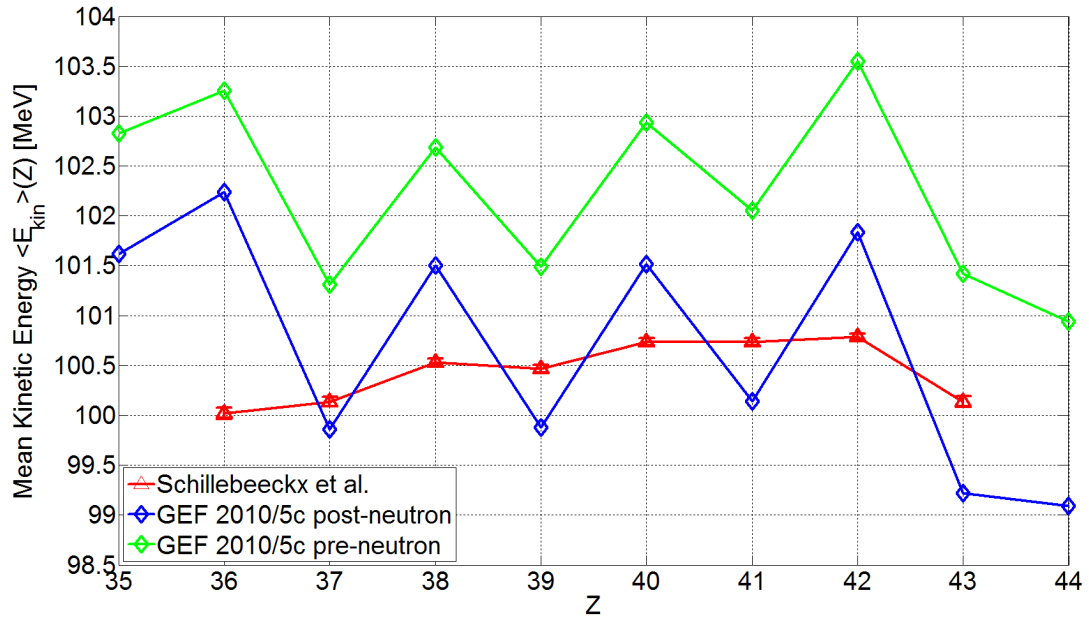
Figure 23: Charge dependent mean kinetic energies of $^{241}Pu(n_{th}, f)$ from GEF 2010/5c. Experimental data taken from [56].

3.6 Charge Polarization

The charge polarization of fission fragments is usually expressed by the deviation of the mean proton number $\overline{Z}(A)$ for a specific mass A from the proton number Z_{ucd} expected from unchanged charge density. However, there is no direct experimental information on $\overline{Z}(A)$ before neutron emission. The graphics in this section represent the $\overline{Z}(A)$ of the deexcited fission products. JEFF-3.1.1 evaluated data are compared to the experiments [26, 55, 56] and to the results of GEF EXT. It becomes apparent that there are still some deviations related to the $\overline{\nu_p}$ predicted by this code. In all of the following diagrams, oscillations of the mass-dependent charge polarization are observed. They are largely the consequence of the proton even-odd effect in the yields.

The calculated $\overline{Z}(A)$ values of ^{235}U fission products agrees rather well with the experimental and evaluated data. The deviations of the model in the ranges $90 \leq A \leq 105$ and $145 \leq A \leq 155$ seem to be caused by a too high, respectively too low neutron multiplicity, which becomes obvious from the horizontal shift in the oscillations. In the diagram of ^{239}Pu there are larger deviations than in ^{235}U in the regions of high yields. They are obviously the result of a too high prompt neutron multiplicity predicted by the code, which was shown in section 3.4. Concerning ^{241}Pu, there is also a large deviation for the light fragment, where the neutron multiplicity is apparently too high. In this case, there are also large

uncertainties in the evaluated fission yields data.
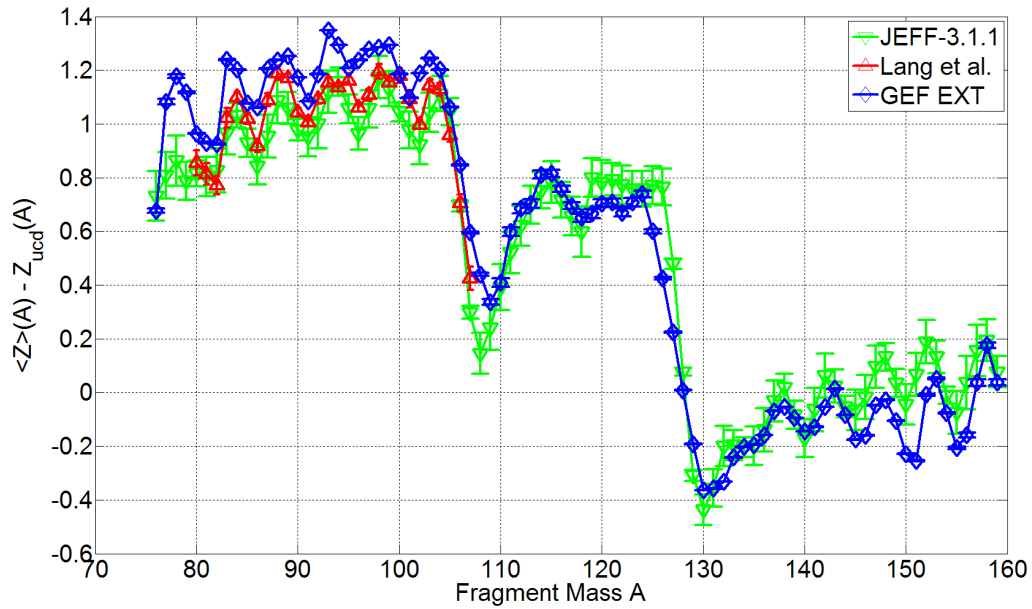
Figure 24: Charge polarization calculated from $^{235}U(n_{th}, f)$ post-neutron nuclide yields. Experimental data taken from [26].
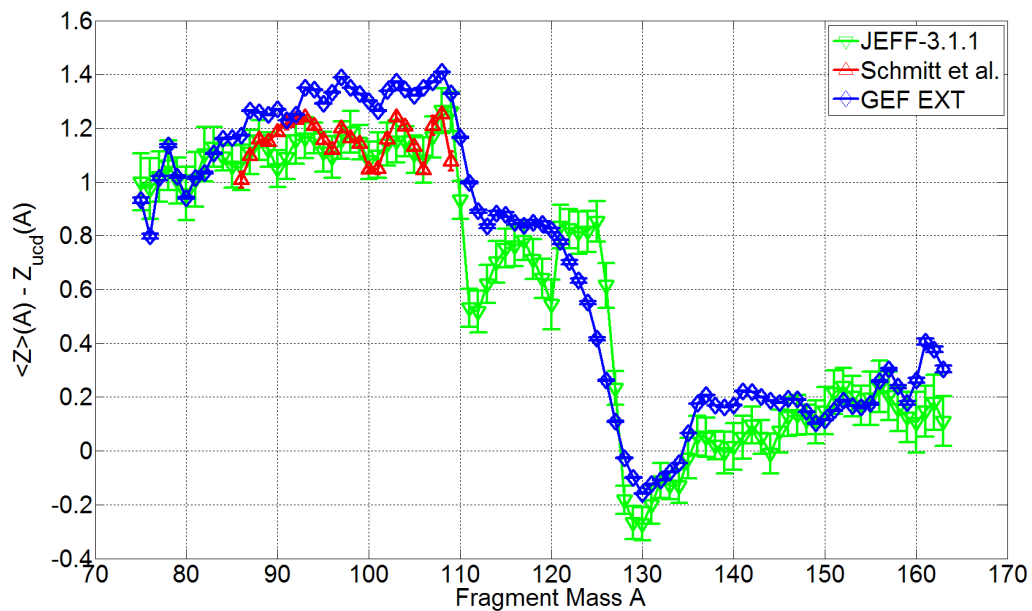
Figure 25: Charge polarization calculated from $^{239}Pu(n_{th}, f)$ post-neutron nuclide yields. Experimental data taken from [55].
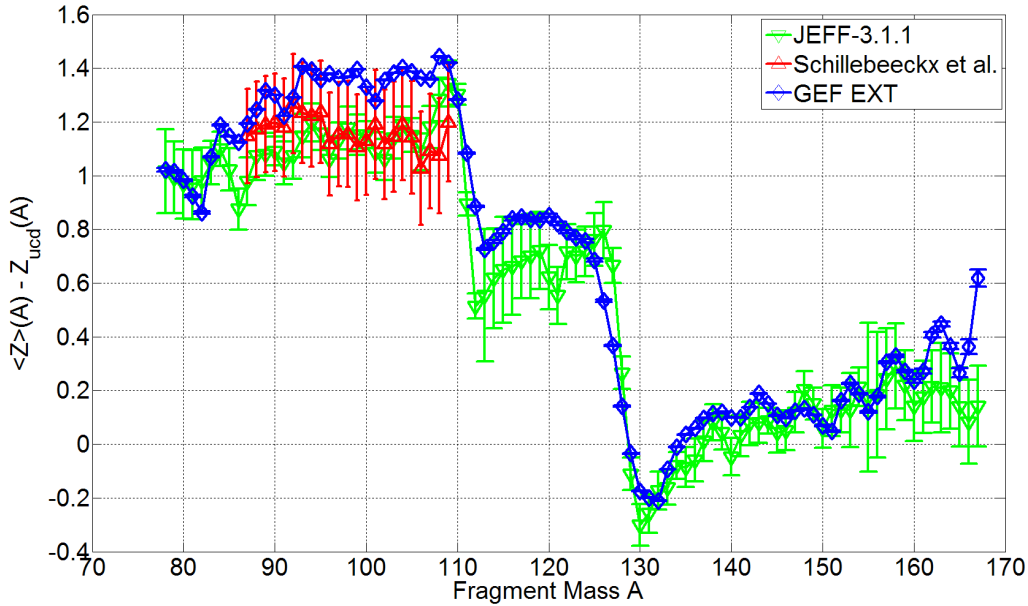
Figure 26: Charge polarization calculated from $^{241}Pu(n_{th}, f)$ post-neutron nuclide yields. Experimental data taken from [56].

3.7   Conclusion

From the analysis performed in this chapter, several conclusions can be drawn regarding the quality of fission yields from the JEFF-3.1.1 evaluation and model calculations. It has become clear that further improvements should be applied to GEF 2010/5c and the GEF EXT based on it. The fractions of the distinct fission channels are the first important issue. Although GEF 2010/5c is good at predicting the number of humps in the mass yields distribution for a wide range of nuclei, there may be large deviations from the experimentally observed ratio $\frac{Y_{S1}}{Y_{S2}}$ of the weights of the S1 and S2 channels, and its energy dependence is not well reproduced. The energy dependence of the SL channel fraction Y_{SL} is satisfactory at least in the fission of ^{235}U, whereas the calculation requires the shell effect Δ_{SL} in the height of its outer barrier to be adjusted empirically. Empirical information may be generally necessary to improve the modelled fractions of fission channels.

The neutron energy dependence of the S1 channel mass width predicted by GEF 2010/5c generally appears to be a little too steep, whereas for the S2 channel it is mostly in good agreement. There are some offsets of the calculated widths from the experimental ones, which should be reduced. The general description of mass widths in GEF is still being developed.

As it was shown in sections 3.4 and 3.5, it is also very important to improve the calculation

of excitation and deformation energies at the scission point, which have a crucial impact on neutron evaporation and even-odd effects in the yields. One issue which should be included in the model is the even-odd effect in the mean TXE of fission fragments depending on their proton number. The evaporation model of GEF EXT, which reproduces the $\chi(E)$ spectrum better than GEF 2010/5c needs to be improved with respect to gamma competition. A correct description of neutron emission could lead to considerably improved values of the post-neutron $\overline{Z}(A)$.

The even-odd effect in the proton number dependent fission yields is satisfactory reproduced, although there are some deviations from the fine structure in the local even-odd effect, see also [29]. Its physically well-founded description in GEF 2010/5c can be expected to give more reliable results than the empirical "Z_p" model developed by Wahl. The application of the latter model in the evaluation of JEFF-3.1.1 fission yields has obviously led to deficiencies with respect to the even-odd effects. These deficiencies are striking in the fast fission data set for e. g. ^{238}U, where the global even-odd effect in the elemental yields is only $\delta_p = 0.055 \pm 0.018$ and obviously strongly underestimated, see section 4.6. This is further confirmed by a $^{238}U(\gamma, f)$ photofission experiment [58], where an even-odd effect of $\delta_p = 0.200$ was observed even at a mean compound nucleus excitation energy of $\overline{E_{CN}^*} = 8.3\,\mathrm{MeV}$.

Another weak point in the JEFF-3.1.1 data is that the mass distributions of plutonium fission fragments are better represented including the S3 channel, which was not correctly considered in the evaluation. The findings in this work are that the mass distribution of the S3 channel is more narrow than that of the S1 channel. The connection of this channel to a $N = 52$ shell in the light fragment could not be confirmed unambiguously.

The shift of the channel specific mean fragment masses and $\overline{TKE}$ when the neutron energy is varied are two more observations to deserve further investigations and, if necessary, an inclusion in the model.

4 Application

In this chapter, the reactor burn-up calculations in this work and their results are discussed. The application is mainly focused on a SFR design being described in section 4.1, whereas the impacts of fission products concerning several important aspects of reactor physics are investigated. The GEF EXT code has been applied to reactor calculations. Concerning issues sensitive to the fission yields data, results from this application are presented.

4.1 Fast Reactor Design

In this work, burn-up calculations were performed for a recent design proposal of a sodium cooled fast reactor in an international project [59]. In this section, a short description of this lattice design is presented.

The fuel pins are arranged in a compact, hexagonal lattice. Their cladding has an inner radius of $r_i = 0.351$ cm and an outer radius of $r_o = 0.404$ cm and consists of chrome steel with a composition as given in Table 9.

Steel Composition	
Element	Proportion [at%]
Fe	74.11
Cr	13.36
Ni	9.36
Si	1.27
Mn	1.14
Mo	0.76

Table 9: Steel composition of the cladding.

80.9% of the inner volume is filled with MOX produced from depleted uranium and typical LWR plutonium. The length specific total amount of heavy metals is 3.051 $\frac{g}{cm}$. Their composition in fresh fuel is given in Table 10.

Element	U		Pu		Am	
Proportion [at%]	81.64		18.00		0.36	
Isotope Vector [at%]	^{235}U	0.25	^{238}Pu	2.00	^{241}Am	100.00
	^{238}U	99.75	^{239}Pu	54.00		
			^{240}Pu	26.00		
			^{241}Pu	10.00		
			^{242}Pu	8.00		

Table 10: Heavy metal composition of the fresh fuel in the SFR design.

The volume ratio of coolant and fuel pins is $\frac{V_c}{V_f} = 0.5448$. In the calculation, the core is assumed to be infinitely high, and the problem is reduced to two dimensions. Thus, the area of the Wigner-Seitz cell is

$$A_{cell} = \pi \cdot r_o^2 \cdot \left(1 + \frac{V_c}{V_f}\right) = 0.7921 \text{ cm}^2$$

and the lattice pitch p is

$$p = \sqrt{\frac{2A_{cell}}{\sqrt{3}}} = 0.9564 \text{ cm}$$

The lattice of the core design is illustrated in Fig. 27, which shows part of a fuel assembly. Additionally, the structure material of fuel assemblies and the space between them is taken into account. Burn-up calculations were performed with a homogenized zone, representing a core design with an infinite number of identical fuel assemblies. This will be discussed in the next section.
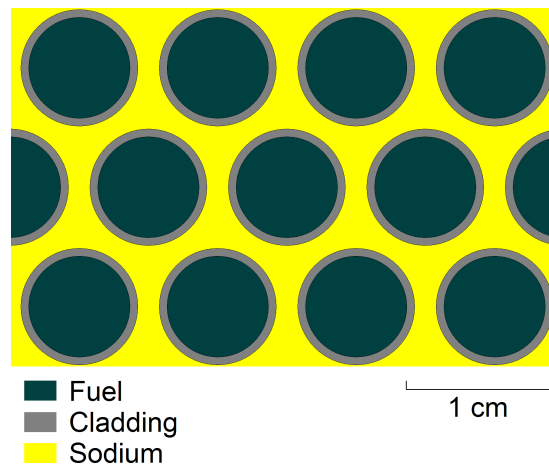
Figure 27: SFR lattice design for the burn-up applications in this work.

4.2   Reactor Burn-up Calculations

The reactor burn-up calculations were performed with the modular code system KANEXT [60], developed in the past four decades at the research center of Karlsruhe. Good descriptions of the available options and of input specifications may be found in references [61, 62]. These calculation procedures are frequently re-validated to assure a certain level of confidence. An important validation effort is the simulation of the reactor experiment ICE in the Nuclear Power Plant Obrigheim in the 1970s. The KANEXT validation is described in detail in reference [62], whereas in [63] comparable good agreement is observed for simulations with burn-up options of the advanced Monte Carlo code MCNPX [64]. The simulation tool KANEXT contains several libraries for dedicated purposes, see e. g. [65]. The handling of fission product yields is based on the principles of the original ORIGEN code [66]. In KANEXT the external code KORIGEN [67] applies a slightly extended ORIGEN format, whereas for the KANEXT module BURNUP the data is additionally reordered to improve the data access [68].

For a reactor pin-cell calculation, the unit cell of the lattice design is cylindrized, keeping its area fixed. This cylindrization reduces the two-dimensional problem to a one-dimensional one. The neutron fluence at the border of the cell is assumed to be zero, i. e. the neutron flux $\phi(r, E)$ there must be stationary with respect to r [69]:

$$\left. \frac{d\phi(r, E)}{dr} \right|_{r=r_{cell}} = 0$$
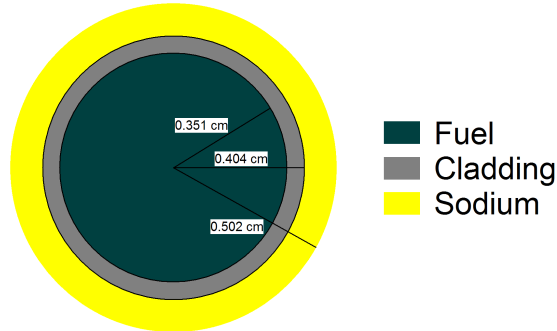
Figure 28: Cylindric unit cell of the SFR lattice design.

In contrary to a LWR, in the SFR the neutron flux $\phi(r, E)$ is separable into a space- and an energy-dependent factor according to (98) [61].

$$\phi(r, E) = R(r) \cdot \varphi(E) \tag{98}$$

This approximation can be made in SFR calculations, since there the mean free paths of neutrons are long in terms of the lattice pitch. Because of the latter, in an infinite and

homogeneous core the space-dependent factor $R(r)$ can also be considered as a constant. With these approximations, all the materials in the SFR can be homogenized to a mixture for which reactor calculations are performed in zero space dimensions. In this work, a burn-up calculation has been performed for a PWR as well. The additional simplifications applied to the SFR are not applicable there, and the calculation was performed in one space dimension for a pin-cell as it is illustrated by Fig. 28 for the SFR.

As explained in some more detail in the references [61, 62], the KANEXT module BURNUP [68] needs three special libraries. The applied files are:

- KORFI4.NDLITE, the standard library for light elements

- KORFI4.NDACT, the standard library for actinides

- KORFI4.NDFPS, the standard library for fission products

The latter library contains fission product yields for different types of reactors. On this burn-up library, the yields are stored as constants which are applied to all incident neutron energies. In KANEXT, the dependence of fission yields on the incident neutron energy is not yet taken into account by multiple interpolation points using the fission reaction rate spectrum as input, as it could be done with the JEFF-3.1.1 library. Instead, the energy dependence is taken into account by using weighted fission yields for the neutron spectrum of the specific reactor type.

In sections 4.7 to 4.9, results from the use of a new library KORFIN_GEF.NDFPS created [70] from the yields calculated from the fission reaction rate spectra by the GEF EXT code are presented.

The burn-up calculations were performed using 350 energy groups for the SFR and 69 energy groups for the PWR, under the application of the GRUCAL multi-group libraries G350P5JEFF311D and G69P5JEFF31LWR respectively.

4.3 Burn-up Behaviour of Heavy Metals

Nuclide	BOC		EOC		Change of Amount	
	$\left[\frac{\text{mol}}{\text{cm}}\right]$	[at%]	$\left[\frac{\text{mol}}{\text{cm}}\right]$	[at%]	$\left[\frac{\text{mol}}{\text{cm}}\right]$	[%]
^{234}U			$5.388 \cdot 10^{-7}$	0.005	$+5.388 \cdot 10^{-7}$	
^{235}U	$2.612 \cdot 10^{-5}$	0.204	$1.116 \cdot 10^{-5}$	0.096	$-1.496 \cdot 10^{-5}$	-57.28
^{236}U			$3.218 \cdot 10^{-6}$	0.028	$+3.218 \cdot 10^{-6}$	
^{238}U	$1.042 \cdot 10^{-2}$	81.43	$9.284 \cdot 10^{-3}$	80.18	$-1.139 \cdot 10^{-3}$	-10.93
^{237}Np			$4.263 \cdot 10^{-6}$	0.037	$+4.263 \cdot 10^{-6}$	
^{239}Np			$4.573 \cdot 10^{-6}$	0.039	$+4.573 \cdot 10^{-6}$	
^{238}Pu	$4.609 \cdot 10^{-5}$	0.360	$3.576 \cdot 10^{-5}$	0.309	$-1.034 \cdot 10^{-5}$	-22.43
^{239}Pu	$1.244 \cdot 10^{-3}$	9.72	$1.230 \cdot 10^{-3}$	10.62	$-1.439 \cdot 10^{-5}$	-1.16
^{240}Pu	$5.992 \cdot 10^{-4}$	4.68	$6.315 \cdot 10^{-4}$	5.45	$+3.230 \cdot 10^{-5}$	$+5.39$
^{241}Pu	$2.305 \cdot 10^{-4}$	1.80	$1.360 \cdot 10^{-4}$	1.17	$-9.441 \cdot 10^{-5}$	-40.97
^{242}Pu	$1.844 \cdot 10^{-4}$	1.44	$1.706 \cdot 10^{-4}$	1.47	$-1.378 \cdot 10^{-5}$	-7.47
^{241}Am	$4.609 \cdot 10^{-5}$	0.360	$3.269 \cdot 10^{-5}$	0.282	$-1.340 \cdot 10^{-5}$	-29.07
^{242m}Am			$8.166 \cdot 10^{-7}$	0.007	$+8.166 \cdot 10^{-7}$	
^{243}Am			$2.203 \cdot 10^{-5}$	0.190	$+2.203 \cdot 10^{-5}$	
^{242}Cm			$5.337 \cdot 10^{-6}$	0.046	$+5.337 \cdot 10^{-6}$	
^{243}Cm			$4.437 \cdot 10^{-7}$	0.004	$+4.437 \cdot 10^{-7}$	
^{244}Cm			$5.786 \cdot 10^{-6}$	0.050	$+5.786 \cdot 10^{-6}$	
^{245}Cm			$4.769 \cdot 10^{-7}$	0.004	$+4.769 \cdot 10^{-7}$	
Total	$1.280 \cdot 10^{-2}$	100.00	$1.158 \cdot 10^{-2}$	100.00	$-1.221 \cdot 10^{-3}$	-9.54

Table 11: Heavy metal contents of the fuel of the SFR design. EOC values calculated for a burn-up of 80.1 $\frac{\text{GWd}}{\text{t}_{\text{hm}}}$.

For the SFR, KANEXT burn-up calculations have been performed with a constant linear power rating of 335 $\frac{W}{\text{cm}}$ and a duration of 729.6 days. After this time, the fuel has reached a burn-up of 80.1 $\frac{\text{GWd}}{\text{t}_{\text{hm}}}$.

In exploratory burn-up calculations, the inclusion of reactions of neutrons with fission products was found to have only marginal impacts on the time evolution of the heavy metal inventory. Changes in the nuclide composition of the actinides have been investigated in a burn-up calculation including the multi-group cross-sections of 228 fission products and 26 actinide nuclides from ^{233}U to ^{246}Cm, using the KORFI4 fission yield library. The results are given in Table 11.

As to be inferred from this table, at 80.1 $\frac{\text{GWd}}{\text{t}_{\text{hm}}}$ burn-up 9.54% of the initial heavy metal has been fissioned. The total loss of heavy metal is greater than the loss of ^{238}U, which shows that in this homogeneous SFR design more heavy metal is fissioned than ^{238}U converted.

This is underlined by the macroscopic one-group cross-sections in Tables 12, 13, according to which the uranium conversion rate expressed by

$$CR = \frac{\overline{\Sigma_{c,^{238}U}}}{\overline{\Sigma_{f,total}}}$$

is $CR = 0.789$ at BOC and $CR = 0.813$ at EOC. The amounts of the fissile materials ^{235}U and ^{241}Pu which are not or not directly made up by the conversion process $^{238}U(n,\gamma) \rightarrow {}^{239}U \xrightarrow{\beta^-} {}^{239}Np \xrightarrow{\beta^-} {}^{239}Pu$ strongly decrease. The change of the plutonium isotope vector is noticeable.

4.4   Neutron Flux Spectrum

The neutron flux spectrum of the SFR roughly extends over the energy range $50\,\mathrm{eV} \leq E \leq 10\,\mathrm{MeV}$ and is shaped by many resonance effects. It reaches a maximum at a neutron energy of $E \approx 150\,\mathrm{keV}$. The dip located at $E = 2.84\,\mathrm{keV}$ is related to the first resonance in the capture cross-section of ^{23}Na. In Fig. 29, the flux integrals over the 350 energy groups from KANEXT are shown, and their sum is normalized to one.

The effects related to burn-up turn out to have only a small influence on the neutron flux spectrum. To investigate this issue, the flux spectrum has been calculated for the begin of the cycle (BOC) as well as for the end of the cycle (EOC) in two burn-up calculations with and without fission products. When discussing the observed specific impacts of fission products on the EOC flux spectrum, it has to be taken into account whether their effects on burn-up have been included. In the calculations, the reactions between neutrons and fission products were once included when calculating the burn-up as well as the EOC flux spectrum and once completely omitted. The burn-up of actinides and the build-up of fission products were found to influence the neutron flux spectrum differently in different energy ranges. In general, the burn-up leads to a slight softening of the spectrum. The most probable reason for this is the decrease of fissile nuclide concentrations, which leads to lower macroscopic fission and capture cross-sections in the low-energy range and enlarges the lifetime of low-energetic neutrons. There may be another effect from the change of the fission rate fractions of single nuclides (see Table 12), which all have a characteristic $\chi(E)$ spectrum. The detailed observations are listed below.

Energy Range	Observation
below ^{23}Na resonance (2.84 keV)	flux increases with burn-up, but reduction by fission products
^{23}Na resonance (2.84 keV) to 150 keV	flux increases with burn-up, supported by fission products
150 keV to 425 keV	flux decreases with burn-up, no impact of fission products
above 425 keV	flux decreases with burn-up, supported by fission products
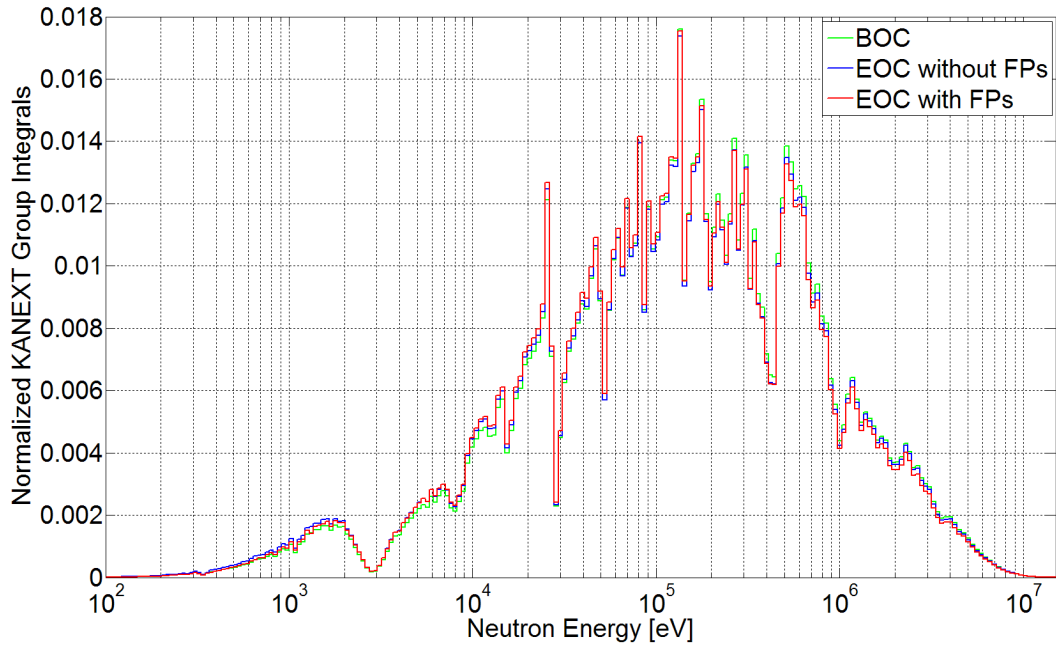
Figure 29: Neutron flux spectrum of the SFR expressed by the 350 KANEXT group integrals.

4.5 Fission Reaction Rates

The relative contribution of single target nuclides to the total fission reaction rate can be determined using macroscopic one-group cross-sections. Microscopic one-group cross-sections $\overline{\sigma}$ are obtained from weighting the energy-dependent cross-section $\sigma(E)$ of a single atom with the neutron flux spectrum $\varphi(E)$, according to (99). Because of the validity of (98), microscopic one-group cross-sections are space independent in a SFR zone.

$$\overline{\sigma} = \frac{\int_0^\infty dE \ \sigma(E) \cdot \varphi(E)}{\int_0^\infty dE \ \varphi(E)} \tag{99}$$

Nevertheless, the macroscopic cross-sections $\overline{\Sigma}(\vec{r})$, which are related to the atom density $N(\vec{r})$ per unit volume by (100), are space dependent in any heterogeneous reactor design. In this work, they are always given for the homogenized zone as applied in the burn-up calculation.

$$\overline{\Sigma}(\vec{r}) = N(\vec{r}) \cdot \overline{\sigma} \tag{100}$$

At this point, the softening of the flux spectrum with burn-up manifests itself in an slight increase of the microscopic one-group fission cross-sections $\overline{\sigma_f}$ of thermally fissile nuclides. On the other hand, the fission cross-sections of non-thermally fissile nuclides decrease. It

turns out that ^{238}Pu also is a rather good fissile material in the SFR spectrum, having a microscopic one-group fission cross-section of more than 1.2 barns, whereas its one-group radiative capture cross-section is only 0.525 barns at BOC and 0.544 barns at EOC. The total macroscopic fission cross-section of the mixture decreases with burn-up. All results concerning fission cross-sections are given in Table 12.

Nuclide	Macroscopic one-group fission cross-sections				$\overline{\sigma_f}$ [barn]	
	BOC		EOC		BOC	EOC
	$\overline{\Sigma_f}\left[\frac{1}{\text{cm}}\right]$	%	$\overline{\Sigma_f}\left[\frac{1}{\text{cm}}\right]$	%		
^{234}U			$1.27\cdot10^{-7}$	0.01	0.326	0.309
^{235}U	$3.73\cdot10^{-5}$	1.33	$1.62\cdot10^{-5}$	0.64	1.876	1.913
^{236}U			$2.47\cdot10^{-7}$	0.01	0.108	0.101
^{238}U	$3.64\cdot10^{-4}$	13.04	$3.01\cdot10^{-4}$	12.05	$4.59\cdot10^{-2}$	$4.27\cdot10^{-2}$
^{237}Np			$1.02\cdot10^{-6}$	0.04	0.336	0.317
^{239}Np			$1.57\cdot10^{-6}$	0.06	0.474	0.450
^{238}Pu	$4.39\cdot10^{-5}$	1.57	$3.38\cdot10^{-5}$	1.34	1.254	1.245
^{239}Pu	$1.68\cdot10^{-3}$	60.19	$1.67\cdot10^{-3}$	66.11	1.775	1.783
^{240}Pu	$1.80\cdot10^{-4}$	6.44	$1.81\cdot10^{-4}$	7.21	0.395	0.377
^{241}Pu	$4.37\cdot10^{-4}$	15.64	$2.63\cdot10^{-4}$	10.40	2.492	2.539
^{242}Pu	$3.97\cdot10^{-5}$	1.42	$3.47\cdot10^{-5}$	1.38	0.283	0.268
^{241}Am	$1.00\cdot10^{-5}$	0.36	$6.71\cdot10^{-6}$	0.27	0.286	0.270
^{242m}Am			$1.97\cdot10^{-6}$	0.08	3.111	3.172
^{243}Am			$3.32\cdot10^{-6}$	0.13	0.210	0.198
^{242}Cm			$2.55\cdot10^{-6}$	0.10	0.645	0.627
^{243}Cm			$1.10\cdot10^{-6}$	0.04	3.197	3.251
^{244}Cm			$1.84\cdot10^{-6}$	0.07	0.438	0.416
^{245}Cm			$9.99\cdot10^{-7}$	0.04	2.694	2.745
All	$2.79\cdot10^{-3}$	100.00	$2.52\cdot10^{-3}$	100.00		

Table 12: Macroscopic and microscopic one-group fission cross-sections at BOC and at a burn-up of 80.1 $\frac{\text{GWd}}{\text{t}_{\text{hm}}}$.

The fission reaction rate spectra $f(E)$ of uranium and plutonium target nuclides, which are obtained by (101), have also been investigated. They have no space dependence in the SFR due to the validity of (98).

$$f(E) = \frac{\sigma_f(E)\cdot\varphi(E)}{\int_0^\infty dE\ \sigma_f(E)\cdot\varphi(E)} \tag{101}$$

The reaction spectrum of ^{238}U, which exhibits a clear threshold behaviour and fissions at relatively high incident neutron energies, is shown in Fig. 30 in terms of the normalized integrals over the 350 KANEXT energy groups (top) as well as per unit energy in 40 keV bins and a linear scale (bottom). It turns out that the fission reaction rate spectra of fissile

nuclides are very much concentrated at low energy and in the epithermal range. For the spectra of more nuclides, see appendix C.
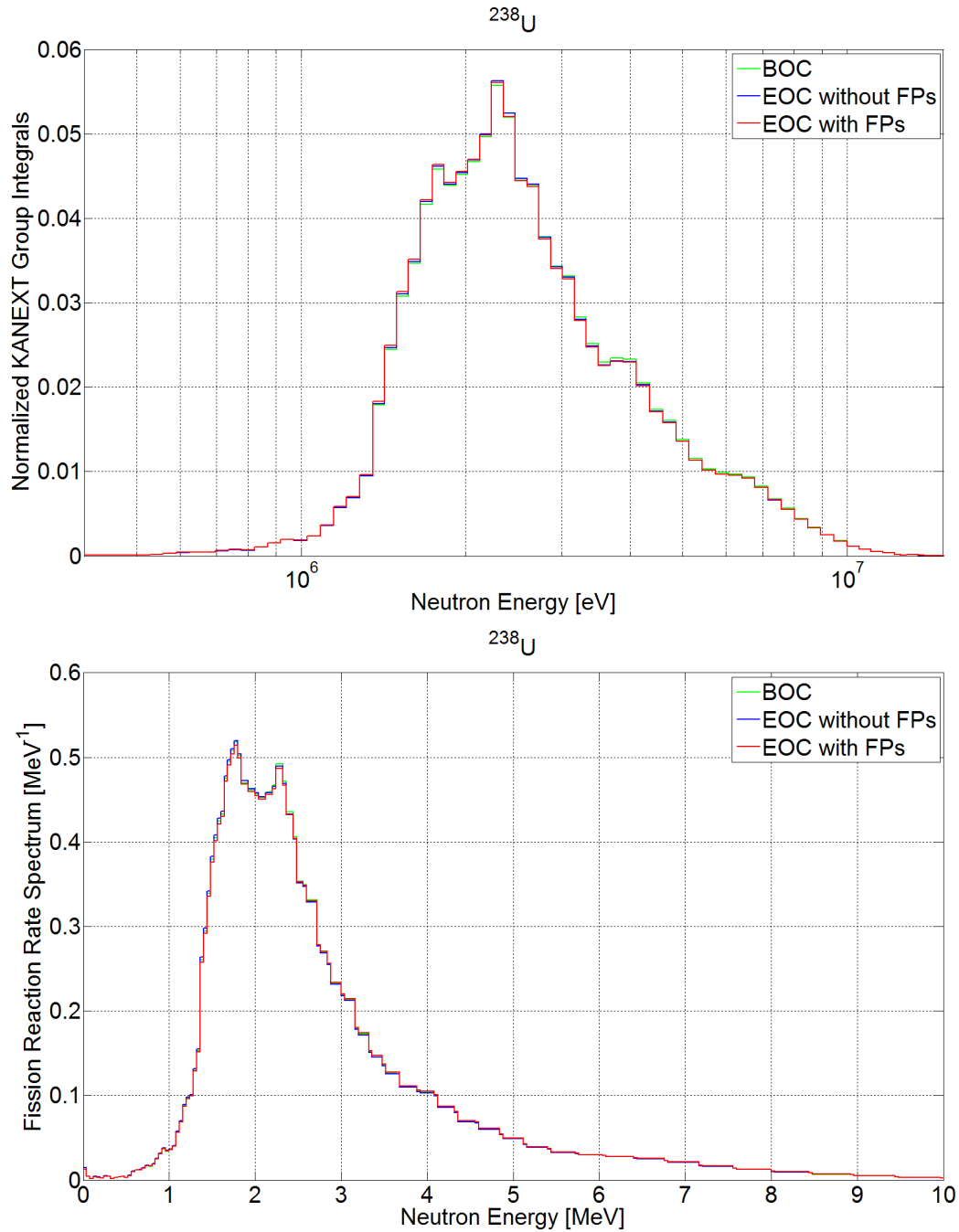
Figure 30: Fission reaction rate spectrum of $^{238}U(n,f)$ resulting from the SFR flux spectrum in group integrals (top) and in linear scale per unit energy (bottom).

4.6   Compilation of Fission Yields

With the code GEF EXT developed in this work, weighted fission product yields were calculated for the BOC reaction spectra as displayed in section 4.5, which only slightly differ from the EOC spectra. The calculation was performed for the targets ^{235}U, ^{238}U, ^{239}Pu, ^{240}Pu, ^{241}Pu and ^{242}Pu which are supported by the code and the results have been stored in ENDF-6 format. From the obtained yields, a preliminary KANEXT burn-up library KORFIN_GEF.NDFPS containing fission yields for 19 nuclides was created by [70], whereas missing nuclides were completed by the yields from the lowest available energy set of JEFF-3.1.1 [36]. The JEFF-3.1.1 data are not quite consistently applied in this way, but since the thermal (T) data set is only available for fissile nuclides whose fission reaction rate spectra are found to be concentrated below 400 keV in section 4.5, no large effects are expected from this. For the creation of this library, parent independent fission yields (MT=454) were used. The new library was tested in a burn-up calculation. Results from this calculation are given in sections 4.7 to 4.9.

The yields calculated by GEF EXT have been compared to JEFF-3.1.1. They may be found in appendix D. It turned out that the proton even-odd effects predicted by GEF EXT are also in sharp contrast to the fast fission data sets (F) of JEFF-3.1.1. Especially, the JEFF-3.1.1 data set $^{238}U(n,f)$ F which is to be applied to almost the entire $^{238}U(n,f)$ reaction spectrum, strongly deviates from the proton number dependent yields calculated by GEF EXT, see Fig. 31. This result shows that in the fast fission of ^{238}U in a SFR, a significant even-odd effect is expected by the model, which also points out that there are probably deficiencies in the JEFF-3.1.1 [36] evaluation.
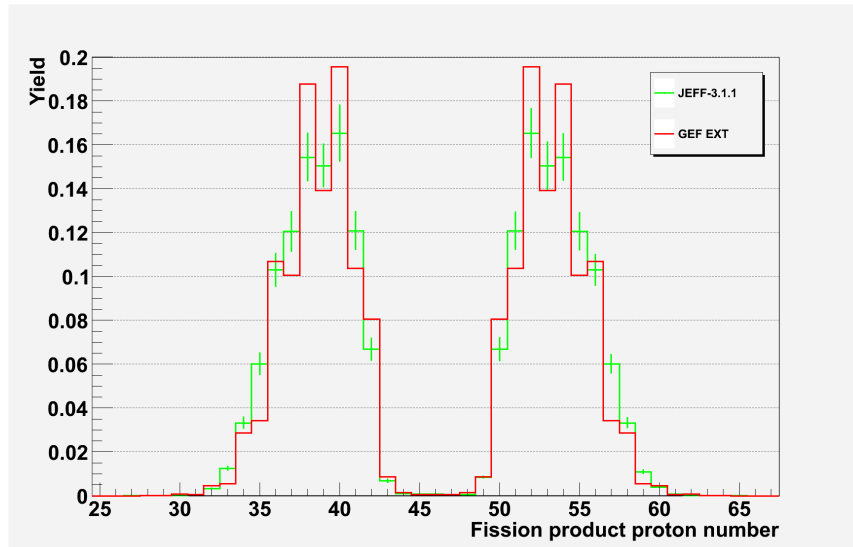
Figure 31: Proton number dependent fission yields (linear scale) for $^{238}U(n,f)$ from the (F) data set in JEFF-3.1.1 and calculated with GEF EXT.

4.7 Neutron Absorption of Fission Products

The most important impacts of the presence of fission products in the reactor are related to their neutron capture reactions. It was found that neutron capture of fission products significantly influences the build-up of several nuclides in the SFR. Compared to a light water reactor, the effect is however less pronounced, as indicated by the results in section 4.9. In the neutron spectrum of the SFR, the macroscopic and microscopic one-group capture cross-sections are very different from those in a LWR. As a result, the absorption fractions of single fission product nuclides are also very different, which is shown by the tables 4.1 and 4.2 in [61]. Table D.1 in appendix D lists the absorption fractions of the top 100 fission product nuclides in the SFR. It has been calculated for the final burn-up of $80.1 \frac{\text{GWd}}{\text{t}_{\text{hm}}}$ using the yields from the KORFI4 and KORFIN_GEF libraries. The results roughly agree with the values for a burn-up of $30 \frac{\text{GWd}}{\text{t}_{\text{hm}}}$ in [61]. It must be noted that the nuclide ^{135}Xe, which is the strongest absorbing fission product in LWRs [61], is not even among the top 100 in the SFR. In fact, all of the important absorbers in the SFR are stable or have half lives of at least several weeks. Thus, the reactivity of a SFR only changes very slowly after shutdown, and there is no effect similar to the xenon-effect in light water reactors.

Fission products were found to have an important impact on the reactivity of the SFR. Table 13 shows the macroscopic capture cross-sections of the homogenized cell. At the end of the cycle, fission products make up around 11% of the total macroscopic capture cross-section, which considerably reduces the reactivity, as shown by Fig. 32. Table D.1 shows that a few nuclides have an important impact on absorption. The k_∞ eigenvalue of the SFR design calculated with the KORFIN_GEF yields is somewhat higher than with KORFI4. It turns out that fission yields related to the build-up of important nuclides as listed in Table D.1 need to be precisely determined to reduce the uncertainty of the reactivity.

Material	Macroscopic one-group capture cross-sections					
	BOC		EOC			
			KORFI4		KORFIN_GEF	
	$\overline{\Sigma_c} \left[\frac{1}{\text{cm}}\right]$	%	$\overline{\Sigma_c} \left[\frac{1}{\text{cm}}\right]$	%	$\overline{\Sigma_c} \left[\frac{1}{\text{cm}}\right]$	%
^{238}U	$2.20 \cdot 10^{-3}$	64.01	$2.05 \cdot 10^{-3}$	54.76	$2.05 \cdot 10^{-3}$	55.26
Other Actinides	$9.14 \cdot 10^{-4}$	26.63	$9.37 \cdot 10^{-4}$	25.03	$9.40 \cdot 10^{-4}$	25.30
Fission Products	0	0.00	$4.30 \cdot 10^{-4}$	11.47	$3.94 \cdot 10^{-4}$	10.62
Cladding	$2.87 \cdot 10^{-4}$	8.36	$2.94 \cdot 10^{-4}$	7.85	$2.94 \cdot 10^{-4}$	7.93
Oxygen	$2.01 \cdot 10^{-5}$	0.59	$1.84 \cdot 10^{-5}$	0.49	$1.84 \cdot 10^{-5}$	0.50
Coolant	$1.42 \cdot 10^{-5}$	0.41	$1.47 \cdot 10^{-5}$	0.39	$1.48 \cdot 10^{-5}$	0.40
Total	$3.43 \cdot 10^{-3}$	100.00	$3.74 \cdot 10^{-3}$	100.00	$3.72 \cdot 10^{-3}$	100.00

Table 13: Contributions to the macroscopic radiative capture cross-section of the homogenized cell. EOC values calculated for a burn-up of $80.1 \frac{\text{GWd}}{\text{t}_{\text{hm}}}$ using the KORFI4 and KORFIN_GEF fission yield libraries.
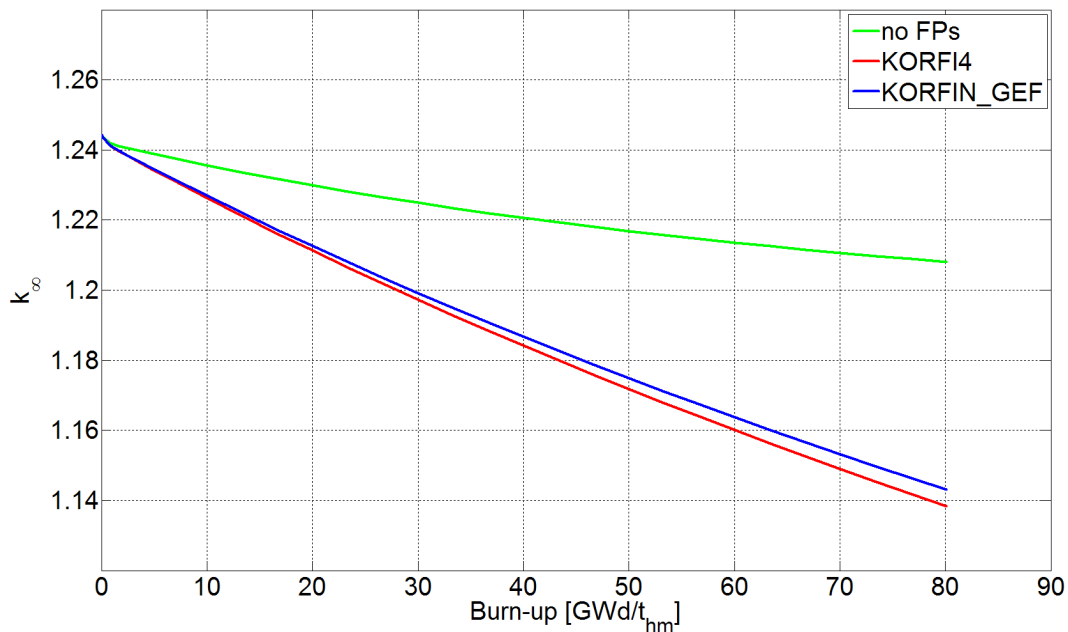
Figure 32: k_∞ eigenvalues of the SFR design as a function of burn-up for KORFI4 and KORFIN_GEF yields and without fission products.

4.8 Decay Heat

After the reactor has been shut down, the heat generation from the decay of radioactive nuclides in the core is remaining. To calculate the time evolution of this thermal power, the KORINT module is applied, which generates an input to the external code KORIGEN [67] from the nuclide densities obtained in the burn-up calculation.

Calculations of the thermal decay power were performed for the nuclide densities in the SFR at the end of the cycle, i. e. after 729.6 days of operation. The densities were obtained from burn-up calculations with the fission yields from the KORFI4 and KORFIN_GEF libraries as input. Figs. 33 and 34 show the time evolution of the thermal decay power within the first 30 minutes and the first 24 hours after shutdown. The deviation between the results is astonishingly small. It turns out that decay power does not only originate from fission products, but also from the actinides. Among these, the decay of ^{239}Np plays a major role during the first days.

The thermal decay power of fission products obtained with the KORFI4 yields starts at $20.1\frac{W}{cm}$, which is 6.0% of the $335\frac{W}{cm}$ initial power before shutdown. With the KORFIN_GEF yields, the initial decay power is somewhat lower with a value of $18.6\frac{W}{cm}$, i. e. 5.5%.
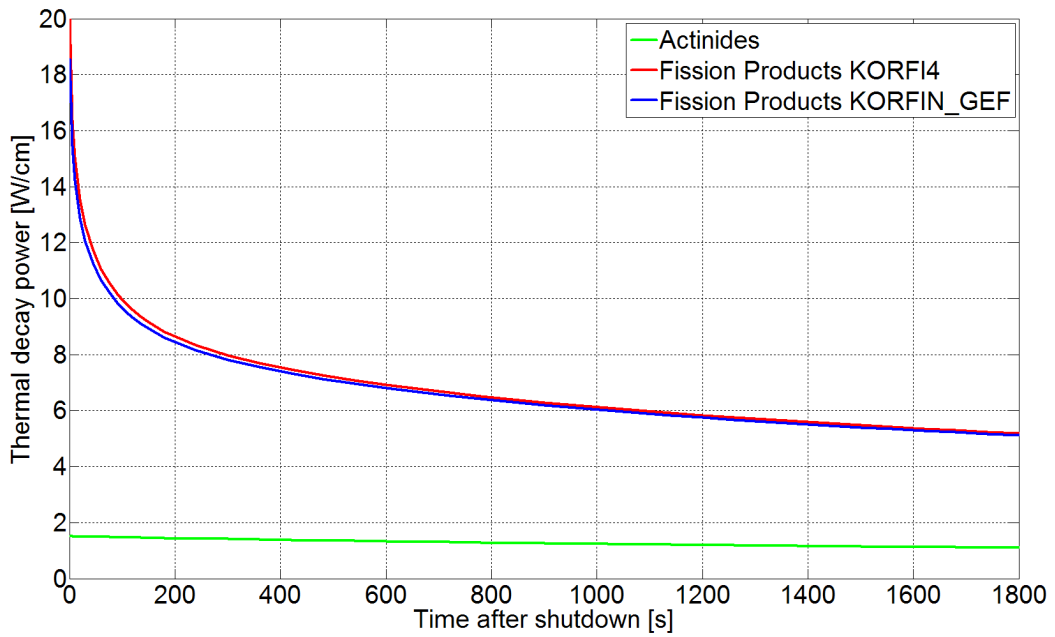
Figure 33: Thermal decay power of the SFR during the first 30 minutes after shutdown, calculated with fission yields from the KORFI4 and KORFIN_GEF libraries.
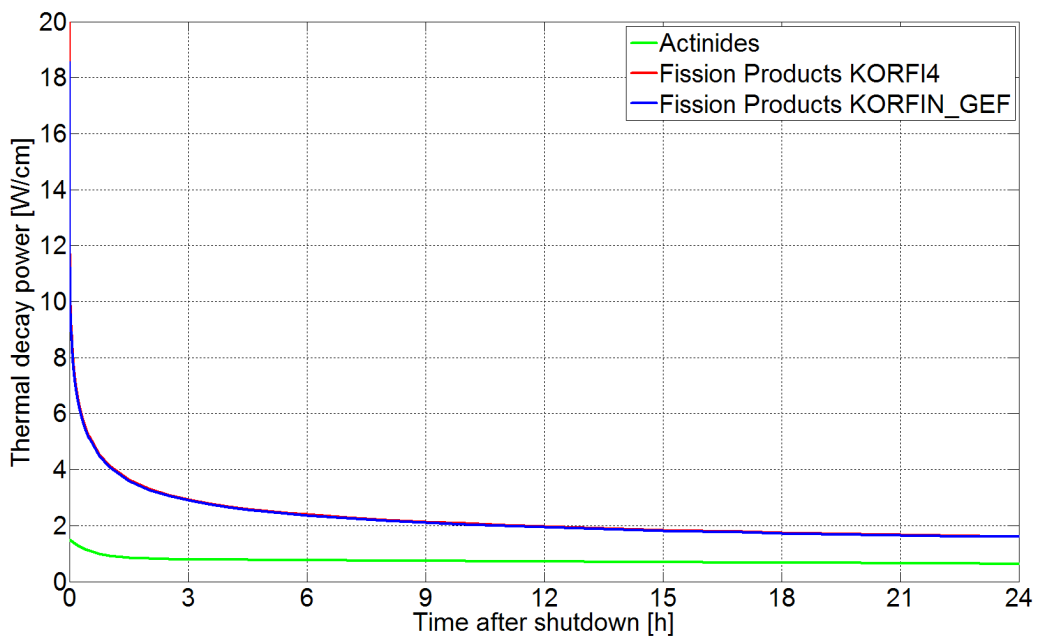
Figure 34: Thermal decay power of the SFR during the first 24 hours after shutdown, calculated with fission yields from the KORFI4 and KORFIN_GEF libraries.

4.9 Inventory of Long-term Radioactive Fission Products

4.9.1 Inventory from the SFR

Finally, the amounts of long-term radioactive fission products from the SFR have been calculated using the KORFI4 and KORFIN_GEF fission yield libraries. 21 nuclides have been selected which have half lives of more than two years and for which significant build-up is expected. Their amounts per unit of thermal energy produced by the reactor are listed in Table 14. They have been calculated for 729.6 days of operation at a power density of 335 $\frac{\text{W}}{\text{cm}}$, followed by 10 years cooling time. The final burn-up is 80.1 $\frac{\text{GWd}}{\text{t}_{\text{hm}}}$.

The results from the calculation with the KORFI4 library are compared to the calculation with the yields from KORFIN_GEF, in which ternary fission is however not included. Concerning the amount of ^{93m}Nb, it must be noted that this nuclide is a decay product of the long-lived ^{93}Zr and needs several decades to reach its equilibrium concentration.

Nuclide	Half Life	Amount			
		KORFI4		KORFIN_GEF	
	[years]	$\left[\frac{\text{mol}}{\text{TWh}}\right]$	$\left[\frac{\text{Ci}}{\text{TWh}}\right]$	$\left[\frac{\text{mol}}{\text{TWh}}\right]$	$\left[\frac{\text{Ci}}{\text{TWh}}\right]$
^{3}H	12.32	$1.599 \cdot 10^{-2}$	464.0		
^{79}Se	$2.95 \cdot 10^5$	$4.335 \cdot 10^{-2}$	$5.254 \cdot 10^{-2}$	$6.235 \cdot 10^{-2}$	$7.556 \cdot 10^{-2}$
^{85}Kr	10.776	0.1464	4857	0.1689	5602
^{90}Sr	28.79	3.527	43800	4.544	56430
^{93}Zr	$1.53 \cdot 10^6$	7.983	1.865	9.511	2.222
^{93m}Nb	16.13	$2.892 \cdot 10^{-5}$	0.6410	$3.802 \cdot 10^{-5}$	0.8428
^{99}Tc	$2.111 \cdot 10^5$	11.36	19.23	12.05	20.40
^{107}Pd	$6.5 \cdot 10^6$	5.732	0.3153	3.573	0.1965
^{113m}Cd	14.1	$8.895 \cdot 10^{-3}$	225.5	$5.951 \cdot 10^{-3}$	150.9
^{121m}Sn	43.9	$1.098 \cdot 10^{-3}$	8.939	$1.603 \cdot 10^{-3}$	13.05
^{126}Sn	$2.3 \cdot 10^5$	0.3162	0.4914	0.4054	0.6302
^{125}Sb	2.75856	$1.574 \cdot 10^{-2}$	2040	$1.696 \cdot 10^{-2}$	2199
^{129}I	$1.57 \cdot 10^7$	2.140	$4.873 \cdot 10^{-2}$	2.020	$4.601 \cdot 10^{-2}$
^{134}Cs	2.0648	$2.963 \cdot 10^{-2}$	5130	$2.185 \cdot 10^{-2}$	3784
^{135}Cs	$2.3 \cdot 10^6$	15.13	2.352	13.77	2.141
^{137}Cs	30.1671	10.24	$1.213 \cdot 10^5$	10.84	$1.285 \cdot 10^5$
^{147}Pm	2.6234	0.1981	26990	0.2127	28980
^{151}Sm	90	1.041	4136	1.051	4174
^{152}Eu	13.537	$1.457 \cdot 10^{-3}$	38.47	$1.472 \cdot 10^{-3}$	38.87
^{154}Eu	8.593	0.1020	4245	$9.902 \cdot 10^{-2}$	4119
^{155}Eu	4.7611	$8.771 \cdot 10^{-2}$	6586	0.1013	7609

Table 14: Amounts of selected long-term radioactive fission products from the SFR after 10 years of storage, final burn-up 80.1 $\frac{\text{GWd}}{\text{t}_{\text{hm}}}$. Half lives taken from [71].

4.9.2 Comparison to a LWR

To compare the characteristics of the SFR to a LWR, another burn-up calculation has been performed simulating the isotope correlation experiment (ICE) in the PWR Obrigheim in the 1970s, using the KORFI4 fission yields. In the experiment, the reactor was operated with 3.1% enriched uranium fuel. The experiment lasted for 1316.4 days with a power profile as shown in Fig. 35. A final burn-up of 30.2 $\frac{\text{GWd}}{\text{t}_{\text{hm}}}$ was reached. The amounts of the 21 nuclides after 10 more years of cooling time are given in Table 16.
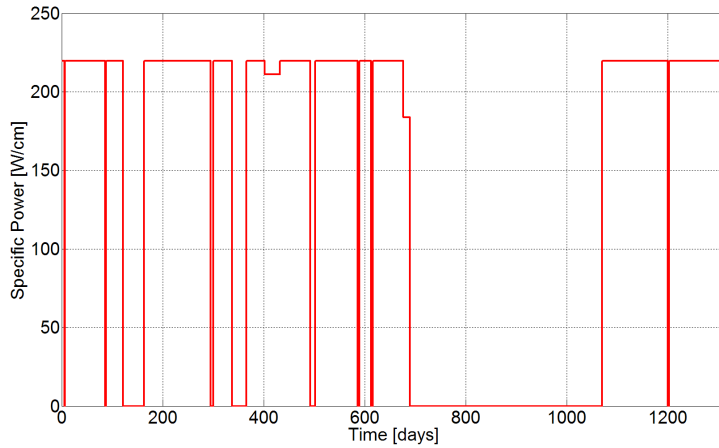
Figure 35: Power profile of the KWO ICE experiment.

Some major differences are observed between the amounts of these nuclides from the two types of reactors per unit of thermal energy production. For most of the nuclides listed in Tables 14 and 16, the differences are related to the fission yields of the main fissioning nuclides, which are ^{239}Pu in the SFR and ^{235}U in the PWR. Parent cumulative fission yields of selected nuclides are displayed in Fig. 36. Comparing the SFR to the PWR, they explain the increase of the amounts of ^{3}H, ^{107}Pd, ^{113m}Cd, ^{121m}Sn, ^{126}Sn, ^{125}Sb, ^{129}I and ^{155}Eu as well as the decrease of the amounts of ^{85}Kr, ^{90}Sr, ^{93}Zr. Considering the yields, for some other nuclides like ^{79}Se, ^{99}Tc, ^{135}Cs, ^{137}Cs and ^{147}Pm no large changes are expected.

Nevertheless, there is a large difference in the amounts of ^{135}Cs from the two reactors. This is caused by the large capture cross-section of its precursor ^{135}Xe in the PWR spectrum and its low parent independent fission yield. ^{135}Xe, which is the strongest absorber in light water reactors, has a half life of 9.14 hours. Firstly, the ratio of the production rate of ^{135}Xe to the fission rate is indicated by its parent cumulative fission yield displayed in Fig. 36, whereas the main fissioning material is ^{235}U as mentioned before. This yield has a value of 0.0661. Secondly, the ratio of the neutron capture rate of ^{135}Xe to the fission rate is given by the ratio of its one-group capture cross-section to the total one-group fission
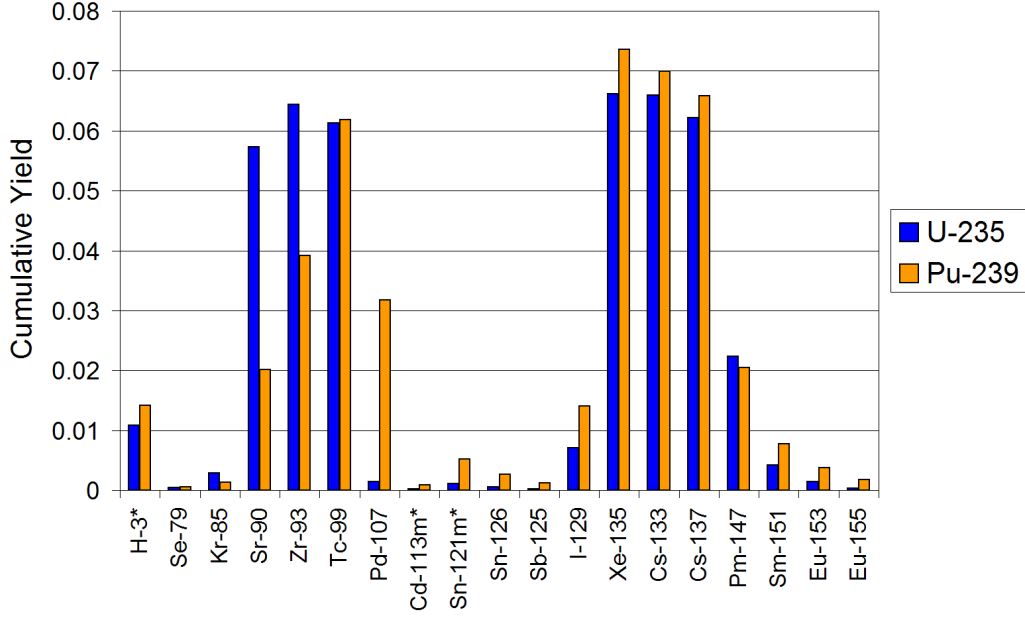
Figure 36: Parent cumulative fission yields (MT=459) of selected nuclides for the targets ^{235}U and ^{239}Pu, from JEFF-3.1.1 [36]. Nuclides with (*) enhanced by 100 for visibility.

cross-section, which is listed in Table 15 and has a value of 0.0566. From this, one can conclude that in the PWR, ^{135}Xe captures a neutron in over 80% of the cases instead of decaying to ^{135}Cs. It must be noted that this capture probability depends on the power level. At lower reactor power, i. e. lower neutron flux, the beta decay becomes more dominant. This effect, which has the benefit of reducing the amount of ^{135}Cs, is not present in the SFR. The parent independent yield of ^{135}Cs itself is very small.

Although the final burn-up of the PWR is lower, the ratios of the capture rates of the nuclides given by Table 15 to the total fission rate are much higher than in the SFR, except for ^{151}Eu. The values indicate that the amount of ^{147}Pm from the PWR is also significantly reduced by the neutron capture of this nuclide. However, the effect is more pronounced for ^{151}Sm, whose production in the PWR is almost ten times lower than in the SFR.

The nuclides ^{134}Cs, ^{152}Eu and ^{154}Eu are almost only built up by neutron capture of ^{133}Cs, ^{151}Eu and ^{153}Eu. This is due to the fact that they are shielded from the beta decay chain by the stable nuclides ^{134}Xe, ^{152}Sm and ^{154}Sm and that their parent independent fission yields are very low. Their amounts per unit energy increase with burn-up, since their build-up requires the presence of the mentioned precursors in the reactor. The amount of ^{134}Cs from the SFR is lower although the burn-up is much higher and, according to Fig. 36, the cumulative yields of ^{133}Cs from the fission of ^{235}U and ^{239}Pu are comparable. According to the values in Table 15, the neutron capture of ^{133}Cs is much less pronounced in the SFR.

Nuclide	$\dfrac{\overline{\Sigma_{c,nuclide}}}{\Sigma_{f,total}}$	
	SFR	PWR
^{133}Cs	$1.06 \cdot 10^{-2}$	$1.76 \cdot 10^{-2}$
^{135}Xe	$3.62 \cdot 10^{-6}$	$5.66 \cdot 10^{-2}$
^{147}Pm	$5.21 \cdot 10^{-3}$	$9.43 \cdot 10^{-3}$
^{151}Sm	$5.80 \cdot 10^{-3}$	$1.31 \cdot 10^{-2}$
^{151}Eu	$4.25 \cdot 10^{-5}$	$9.02 \cdot 10^{-6}$
^{153}Eu	$3.03 \cdot 10^{-3}$	$8.10 \cdot 10^{-3}$
Burn-up $\left[\frac{\text{GWd}}{\text{t}_{\text{hm}}}\right]$	80.1	30.2

Table 15: Ratios of single-nuclide capture cross-sections to the total fission cross-section at EOC before the cooling time, calculated with KORFI4 yields.

The increased production of ^{152}Eu in the SFR is obviously related to the increased amount of ^{151}Sm, which undergoes a beta decay of 90 years half life and subsequently captures a neutron. In the case of ^{154}Eu, the different cumulative yields as well as the different one-group capture cross-sections of ^{153}Eu play a role.

The comparison of the inventories from the two reactors shows that the SFR has some advantages concerning the nuclides ^{85}Kr, ^{90}Sr and ^{134}Cs. However, the production of almost all very long lived fission products is found to be higher in the SFR, which is, considering only the fission products, less favorable for the safe disposal of nuclear waste.

Nuclide	Half Life	Amount			
		KORFI4			
		PWR		SFR	
	[years]	$\left[\frac{\text{mol}}{\text{TWh}}\right]$	$\left[\frac{\text{Ci}}{\text{TWh}}\right]$	$\left[\frac{\text{mol}}{\text{TWh}}\right]$	$\left[\frac{\text{Ci}}{\text{TWh}}\right]$
^{3}H	12.32	$9.363 \cdot 10^{-3}$	271.7	$1.599 \cdot 10^{-2}$	464.0
^{79}Se	$2.95 \cdot 10^{5}$	$3.241 \cdot 10^{-2}$	$3.928 \cdot 10^{-2}$	$4.335 \cdot 10^{-2}$	$5.254 \cdot 10^{-2}$
^{85}Kr	10.776	0.1930	6403	0.1464	4857
^{90}Sr	28.79	5.949	73870	3.527	43800
^{93}Zr	$1.53 \cdot 10^{6}$	9.530	2.227	7.983	1.865
^{93m}Nb	16.13	$3.691 \cdot 10^{-5}$	0.8182	$2.892 \cdot 10^{-5}$	0.6410
^{99}Tc	$2.111 \cdot 10^{5}$	10.09	17.09	11.36	19.23
^{107}Pd	$6.5 \cdot 10^{6}$	2.465	0.1356	5.732	0.3153
^{113m}Cd	14.1	$9.090 \cdot 10^{-4}$	23.05	$8.895 \cdot 10^{-3}$	225.5
^{121m}Sn	43.9	$4.631 \cdot 10^{-5}$	0.3772	$1.098 \cdot 10^{-3}$	8.939
^{126}Sn	$2.3 \cdot 10^{5}$	0.2268	0.3525	0.3162	0.4914
^{125}Sb	2.75856	$9.971 \cdot 10^{-3}$	1292	$1.574 \cdot 10^{-2}$	2040
^{129}I	$1.57 \cdot 10^{7}$	1.520	$3.461 \cdot 10^{-2}$	2.140	$4.873 \cdot 10^{-2}$
^{134}Cs	2.0648	$3.629 \cdot 10^{-2}$	6284	$2.963 \cdot 10^{-2}$	5130
^{135}Cs	$2.3 \cdot 10^{6}$	3.166	0.4921	15.13	2.352
^{137}Cs	30.1671	8.775	$1.040 \cdot 10^{5}$	10.24	$1.213 \cdot 10^{5}$
^{147}Pm	2.6234	$8.321 \cdot 10^{-2}$	11340	0.1981	26990
^{151}Sm	90	0.1123	446.0	1.041	4136
^{152}Eu	13.537	$6.957 \cdot 10^{-5}$	1.837	$1.457 \cdot 10^{-3}$	38.47
^{154}Eu	8.593	$7.075 \cdot 10^{-2}$	2944	0.1020	4245
^{155}Eu	4.7611	$1.672 \cdot 10^{-2}$	1255	$8.771 \cdot 10^{-2}$	6586

Table 16: Amounts of selected long-term radioactive fission products from the PWR after 10 years of storage, final burn-up 30.2 $\frac{\text{GWd}}{\text{t}_{\text{hm}}}$, and from the SFR as in Table 14. Half lives taken from [71].

5 Acknowlegdements

A scientific work hardly ever results from the efforts of only one person. In this sense, I am pleased about having found all the competent persons who supported my work at KIT Campus Nord. At this point, I would like to acknowledge their efforts, which enabled me to follow my interests and to get involved into this rather exotic field of physics.

I want to give special thanks to Karl-Heinz Schmidt for answering my many E-mails and his willingness to meet me and discuss the physical aspects of the nuclear fission process. His publications and code developments contributed so much to the success of the basic physics part of this work.

I want to thank Cornelis Broeders, who allowed me much to work on my own initiative, for his assistance with the KANEXT system and my work in general, as well as for the proof-reading of my thesis.

I also want to thank Maarten Becker for his assistance with the KANEXT system, the quick solution of any computer problem and his permanent availability.

I want to thank Ron Dagan for his confidence in me, for arranging my office and for his willingness to assume the role of my co-supervisor.

I would also like to thank Alexander Konobeev for his support.

Finally, I would like to thank my other workmates for the pleasant atmosphere which I enjoyed very much during my work at our institute.

A Symbols, Abbreviations and Special Expressions

A.1 Symbols

Unless otherwise indicated, the symbols in this work denote the following quantities:

Z	proton number of the nucleus
N	neutron number of the nucleus
A	mass number of the nucleus
Δ_{SL}	Parameter in GEF which denotes the shell effect in the height of the superlong fission barrier. See section 2.1.1 for details.
E_n	incident neutron energy
E_{sc}	energy release up to the scission point
Q	Total energy release in a nuclear reaction.
ν_p	Number of prompt neutrons from the fission process.
TKE	Sum of the kinetic energies of fragments from a fission process.
TXE	Sum of the excitation energies of fragments from a fission process.
$\chi(E)$	Prompt neutron emission spectrum as a function of the outgoing energy.
S	entropy
m	nuclear mass
$\overline{Z_{scp}}(A)$	Mean fragment proton number depending on its mass number A, obtained from the scission point model.
β	Quadrupole deformation parameter. When expressing the quadrupole deformation by $R(\theta) = R_0 \cdot (1 + a_{20} Y_{20}(\theta))$, it holds $\beta = \sqrt{\frac{4\pi}{5}} \cdot a_{20}$.
k_∞	Multiplication factor between two generations of neutrons in an infinitely large reactor without leakage, which is critical if $k_\infty = 1$.
E^*	excitation energy of the nucleus
T	nuclear temperature, expressed in units of energy
CR	conversion rate

A.2 Abbreviations and Special Expressions

LDM	liquid drop model
UCD	"unchanged charge density": Indicates that a quantity is obtained assuming the $\frac{N}{Z}$ ratio of fission fragments to be equal to that of the compound nucleus.
PWR	pressurized water reactor
LWR	light water reactor
SFR	sodium-cooled fast reactor
CN	compound nucleus
BOC	begin of cycle
EOC	end of cycle
FP	fission product
charge polarization	Refers to the deviation of the $\frac{N}{Z}$ ratio of fission fragments from that of the compound nucleus.
yrast line	The line described by the minimum excitation energy for a given spin state. Below this line, there are no nuclear states.
lattice pitch	distance between the centers of neighboring fuel rods
isomeric well	Refers to any local minimum of the nuclear potential along the fission path, except the ground state and the scission point.
class-II state	An excitation state of the deformed nucleus being in its first isomeric well along the fission path.
even-odd effect	Staggering of a quantity depending on whether another discrete quantity is even or odd.
fissile	A target nucleus is called "fissile" if the excitation energy gained by the capture of a thermal neutron is higher than the fission barrier of the compound nucleus.
fertile	A "fertile" nucleus is not fissile, but becomes fissile after neutron capture. Fertile nuclides with significant abundances in nature are ^{232}Th and ^{238}U, which convert to ^{233}U and ^{239}Pu by beta decay after neutron capture.
compound nucleus	Refers to an excited, equilibrated nucleus that is formed by the capture of an incident particle.
fissioning nucleus	The nucleus which undergoes fission. In first-chance fission (n, f) it is identical to the nucleus formed by neutron capture.
conversion rate	Ratio of the production rate of fissile nuclei to their destruction rate by nuclear reactions.
pre-neutron	Indicates that the value of a quantity is the value before prompt neutrons have been emitted.
post-neutron	Indicates that the value of a quantity is the value after prompt neutrons have been emitted.

B Diagrams from EXFOR Data Analysis

This appendix contains the diagrams obtained from the analysis discussed in section 3.2.
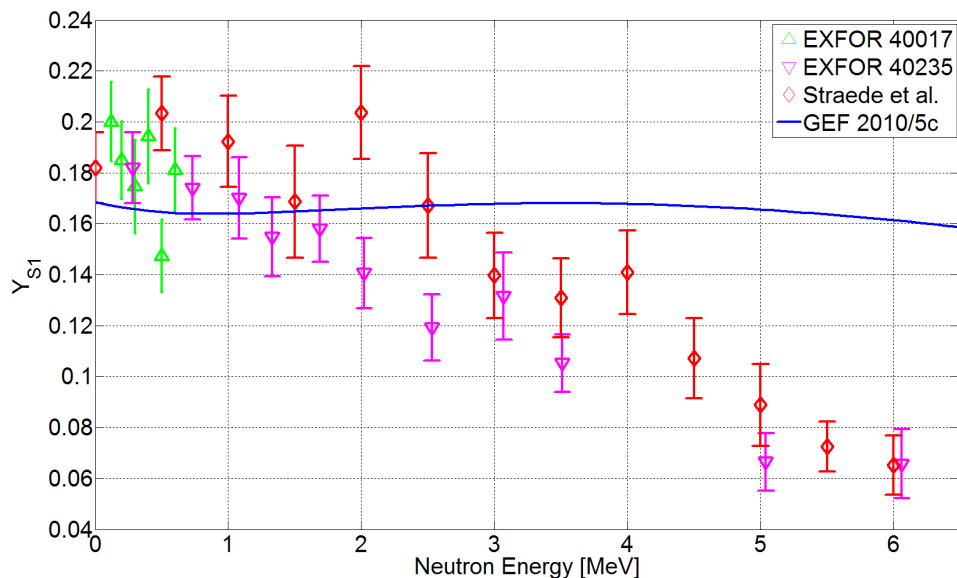
Figure B.1: S1 channel yields Y_{S1} of ^{235}U evaluated from [45, 46] in this work, compared to values of Straede et al. [47] and GEF 2010/5c.
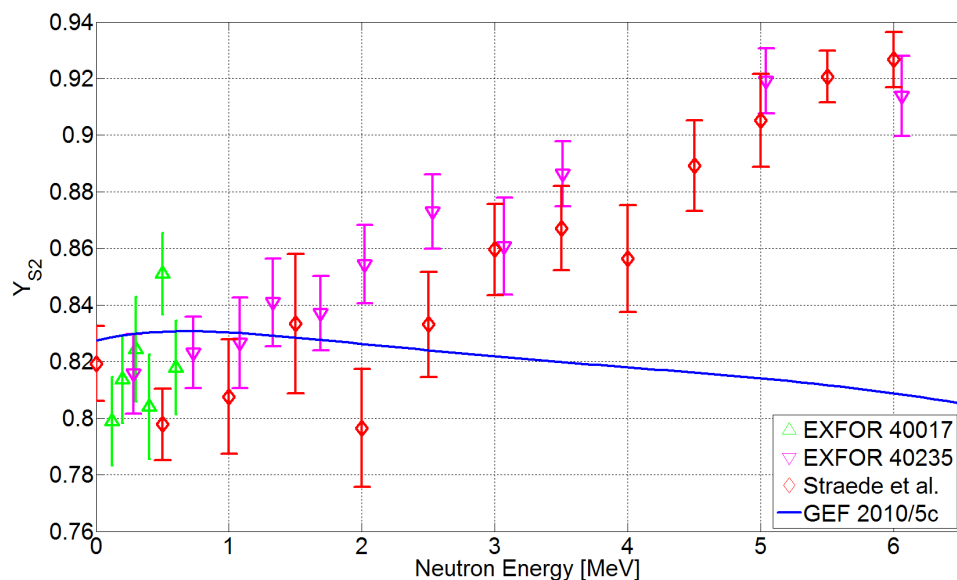
Figure B.2: S2 channel yields Y_{S2} of ^{235}U evaluated from [45, 46] in this work, compared to values of Straede et al. [47] and GEF 2010/5c.
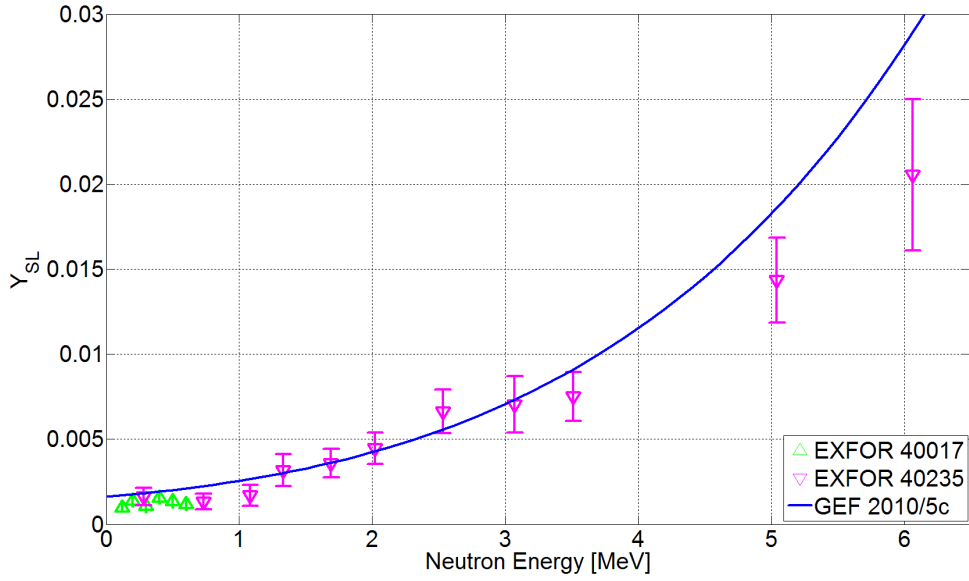
Figure B.3: SL channel yields Y_{SL} of ^{235}U evaluated from [45, 46] in this work, compared to GEF 2010/5c.
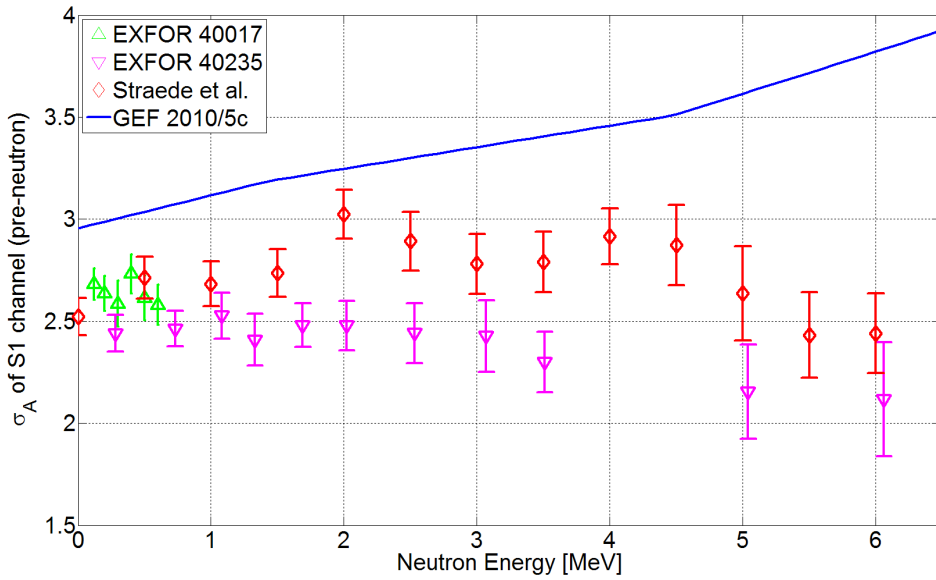
Figure B.4: S1 channel pre-neutron mass widths σ_A of ^{235}U evaluated from [45, 46] in this work, compared to values of Straede et al. [47] and GEF 2010/5c.
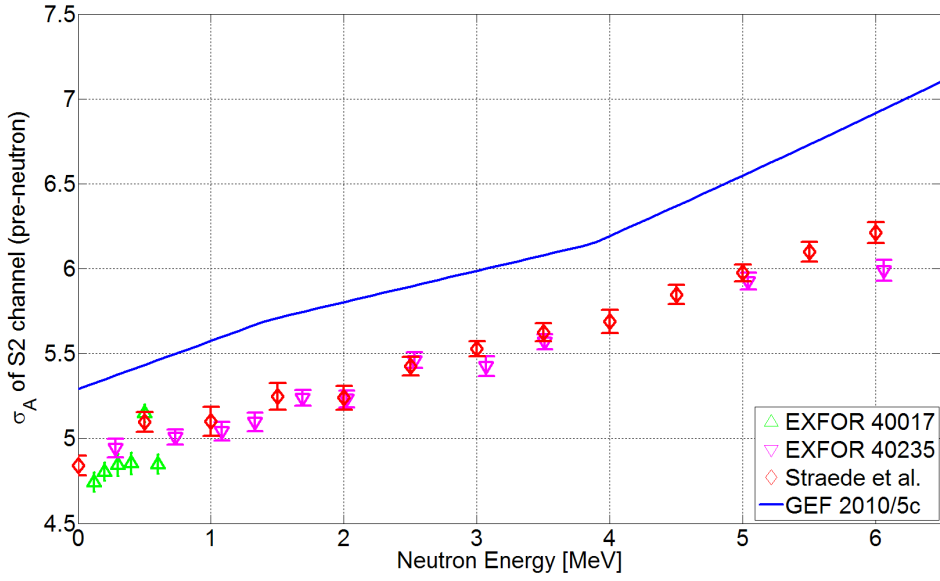
Figure B.5: S2 channel pre-neutron mass widths σ_A of ^{235}U evaluated from [45, 46] in this work, compared to values of Straede et al. [47] and GEF 2010/5c.
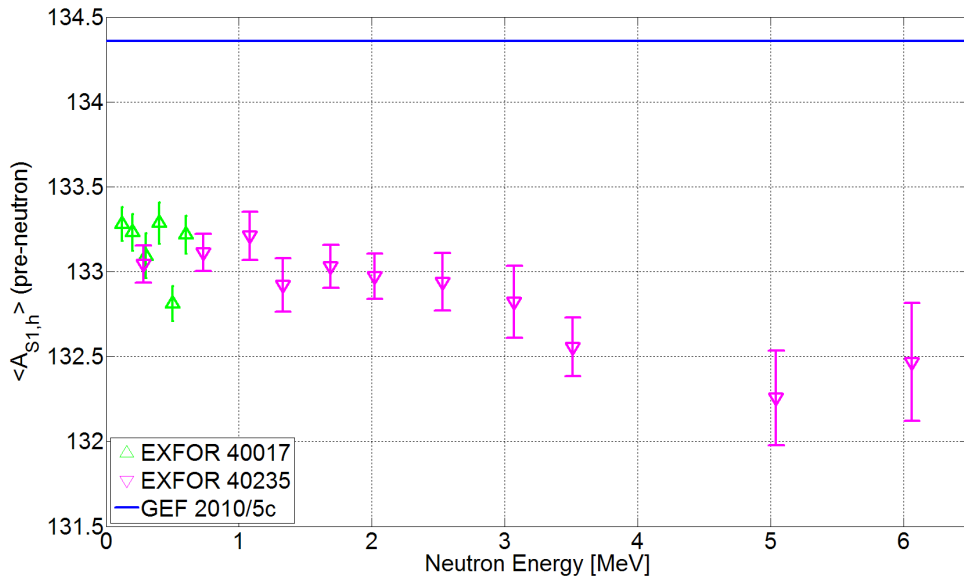
Figure B.6: S1 channel mean pre-neutron mass $\overline{A_{S1,h}}$ of the heavy fragment of ^{235}U, evaluated from [45, 46] in this work, compared to GEF 2010/5c.
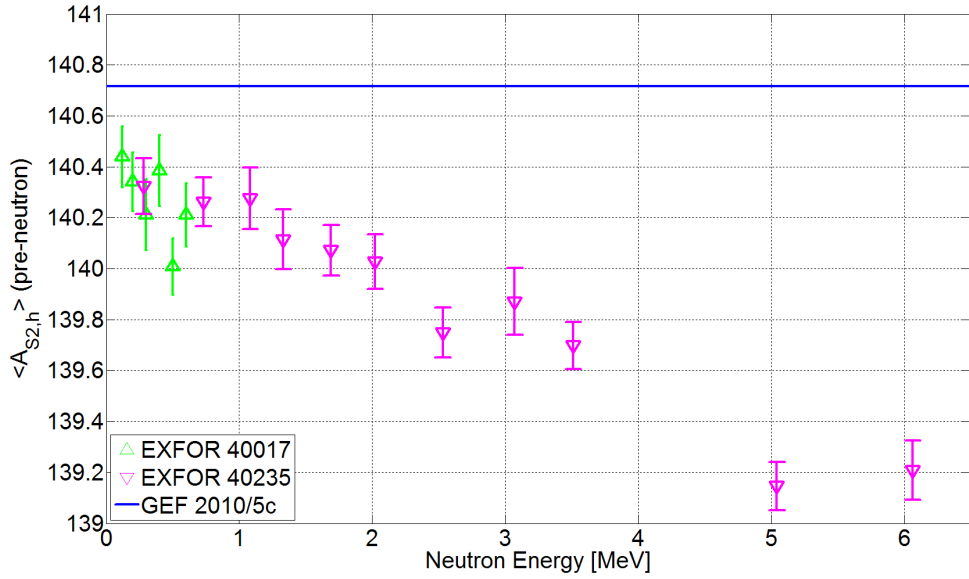
Figure B.7: S2 channel mean pre-neutron mass $\overline{A_{S2,h}}$ of the heavy fragment of ^{235}U, evaluated from [45, 46] in this work, compared to GEF 2010/5c.
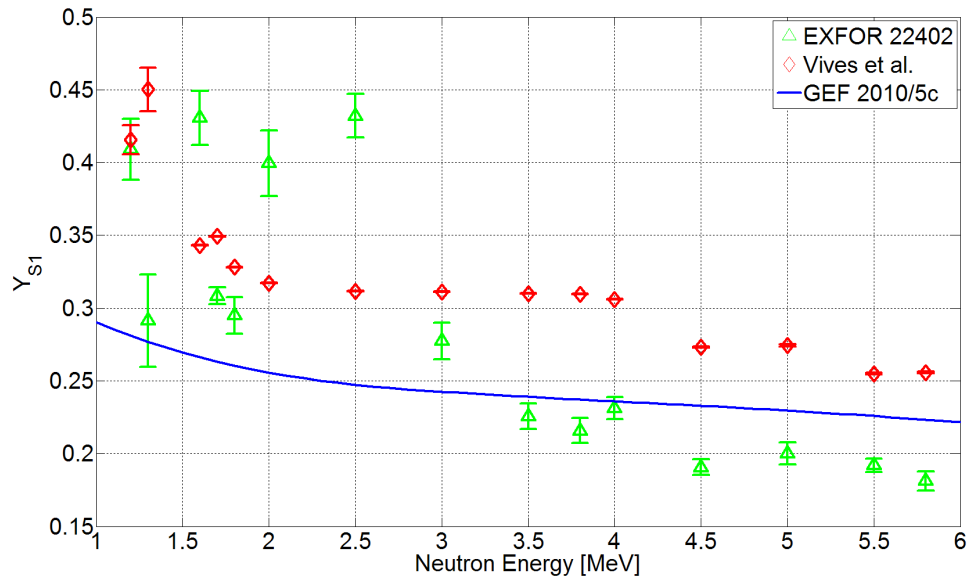
Figure B.8: S1 channel yields Y_{S1} of ^{238}U evaluated from [49] in this work (green), compared to values in the paper (red) and GEF 2010/5c.
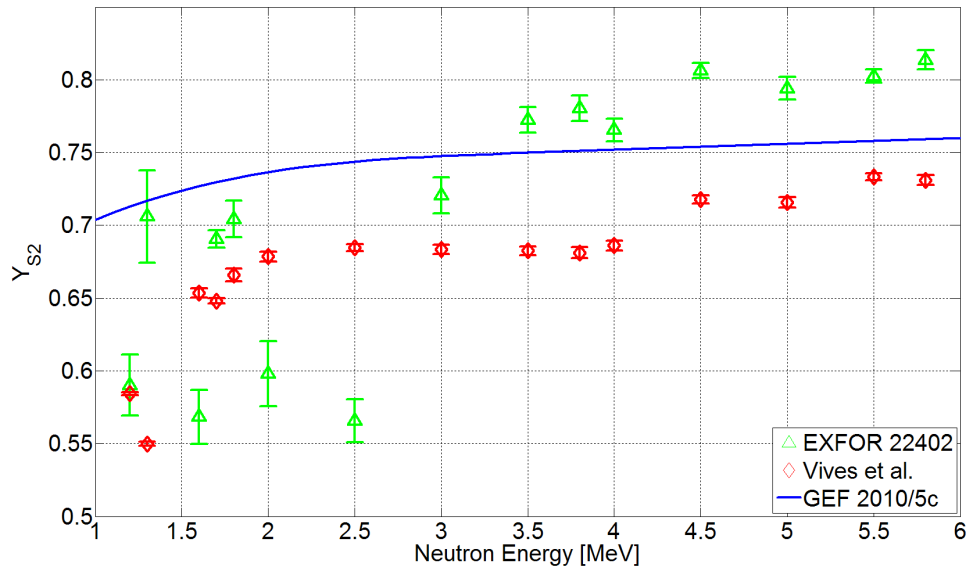
Figure B.9: S2 channel yields Y_{S2} of ^{238}U evaluated from [49] in this work (green), compared to values in the paper (red) and GEF 2010/5c.
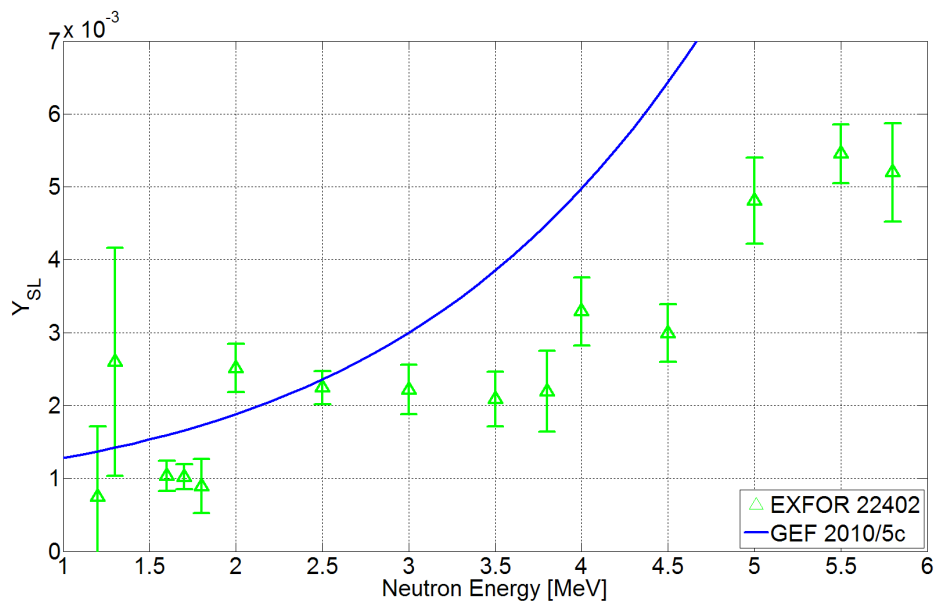
Figure B.10: SL channel yields Y_{SL} of ^{238}U evaluated from [49] in this work, compared to GEF 2010/5c.
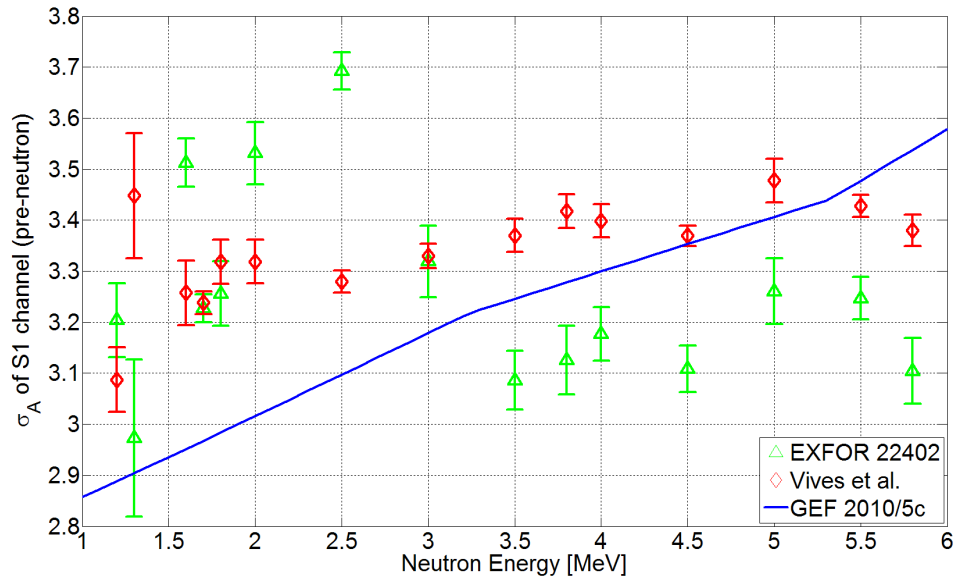
Figure B.11: S1 channel pre-neutron mass widths σ_A of ^{238}U evaluated from [49] in this work (green), compared to values in the paper (red) and GEF 2010/5c.
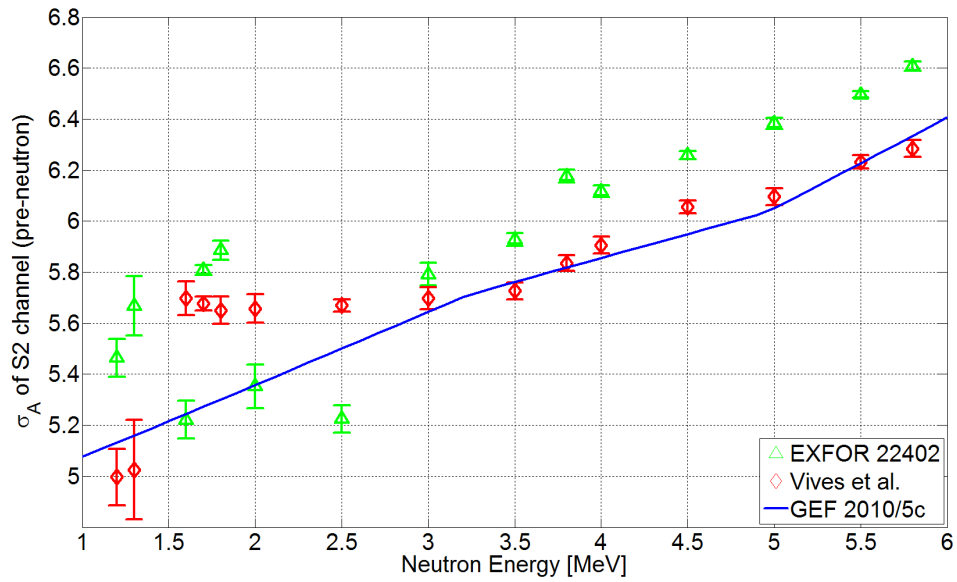
Figure B.12: S2 channel pre-neutron mass widths σ_A of ^{238}U evaluated from [49] in this work (green), compared to values in the paper (red) and GEF 2010/5c.
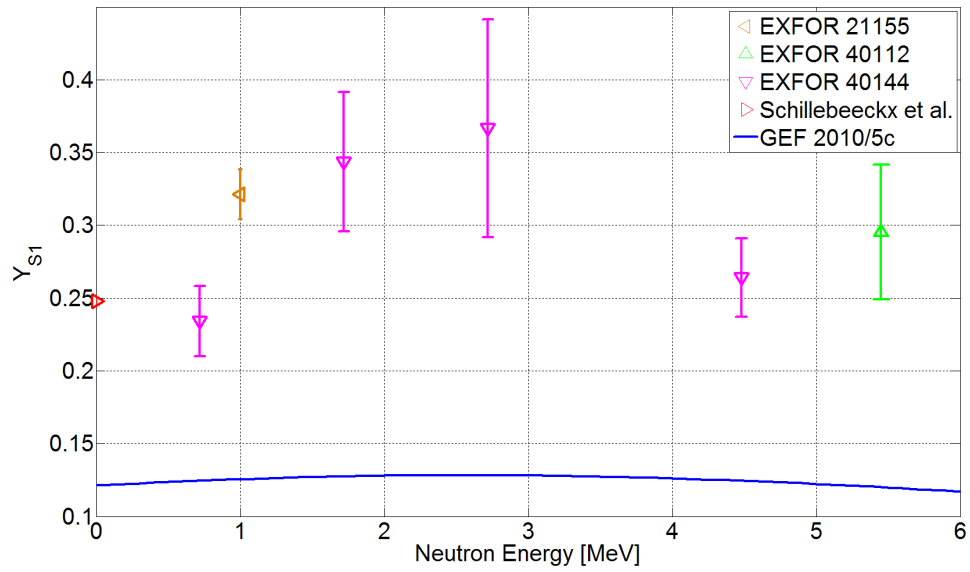
Figure B.13: S1 channel yields Y_{S1} of ^{239}Pu evaluated from [50, 51, 52] in this work and literature values from [57], compared to GEF 2010/5c.
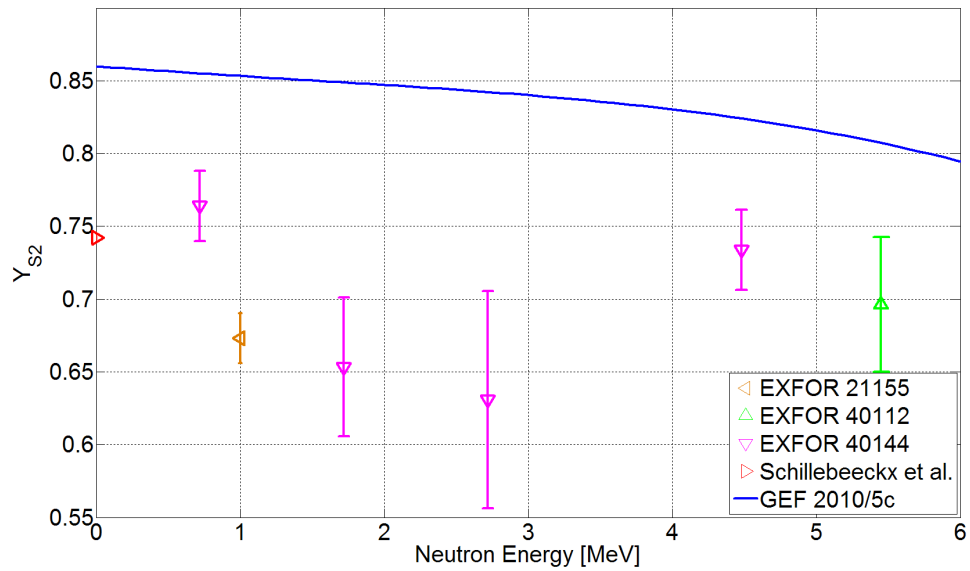
Figure B.14: S2 channel yields Y_{S2} of ^{239}Pu evaluated from [50, 51, 52] in this work and literature values from [57], compared to GEF 2010/5c.
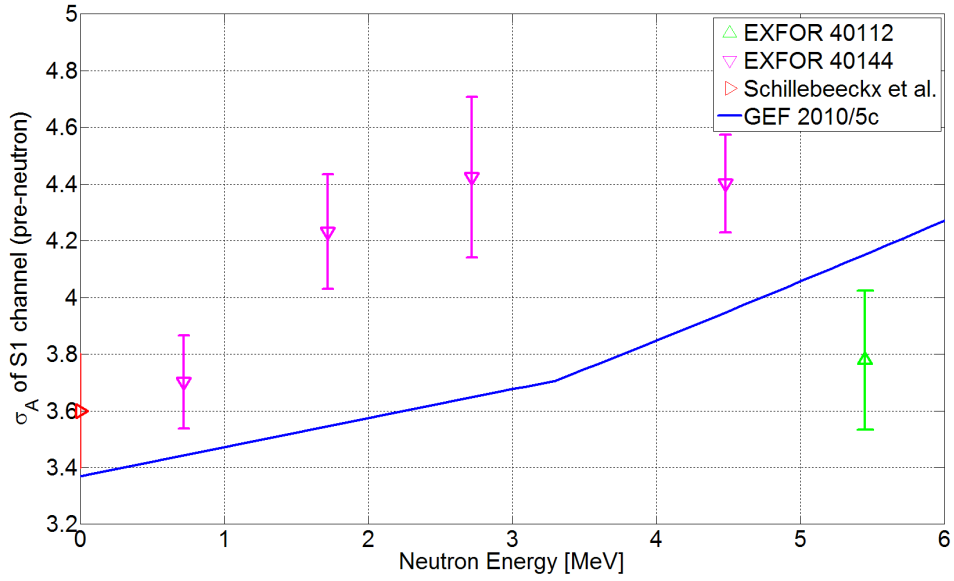
Figure B.15: S1 channel pre-neutron mass widths σ_A of ^{239}Pu evaluated from [50, 51] in this work and literature values from [57], compared to GEF 2010/5c.
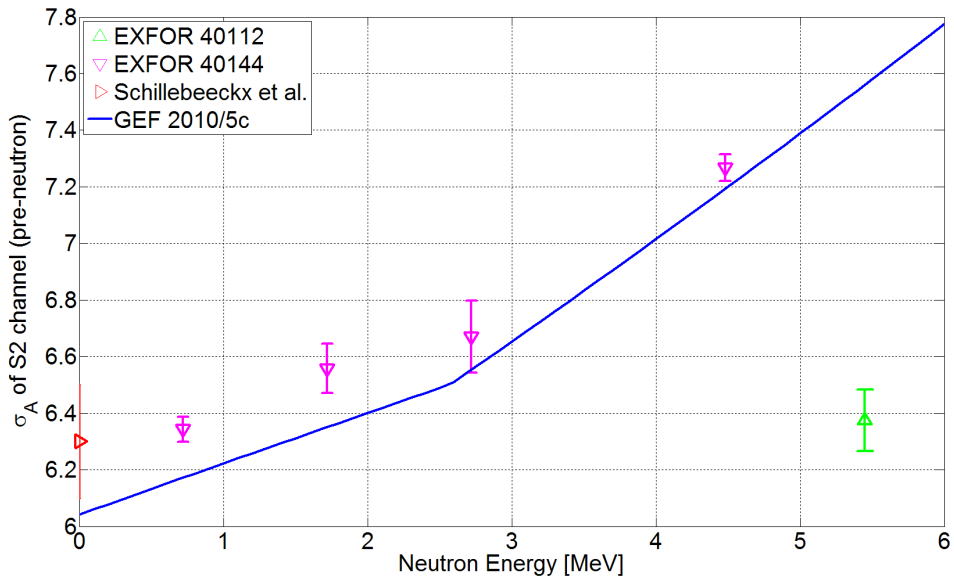
Figure B.16: S2 channel pre-neutron mass widths σ_A of ^{239}Pu evaluated from [50, 51] in this work and literature values from [57], compared to GEF 2010/5c.
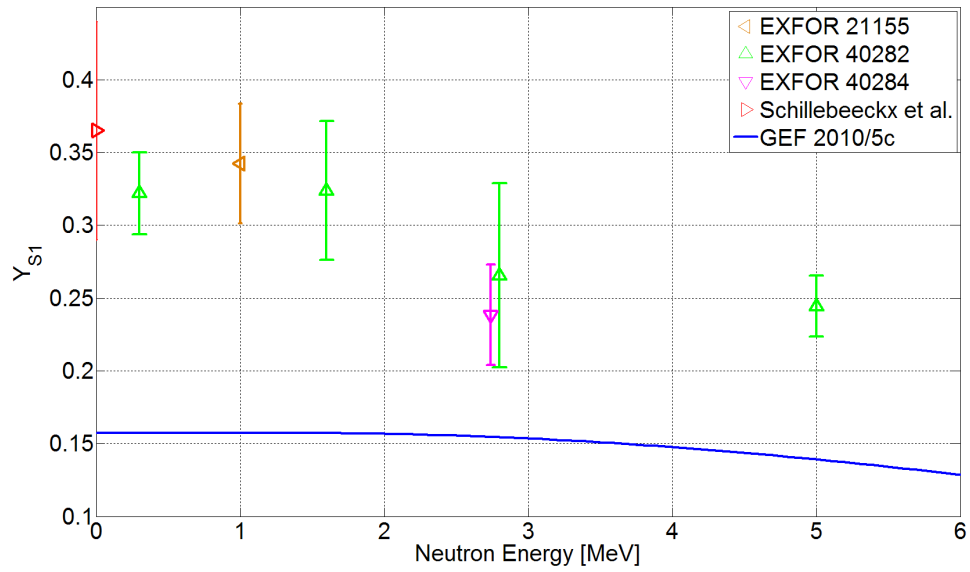
Figure B.17: S1 channel yields Y_{S1} of ^{241}Pu evaluated from [52, 53, 54] in this work and literature values from [56], compared to GEF 2010/5c.
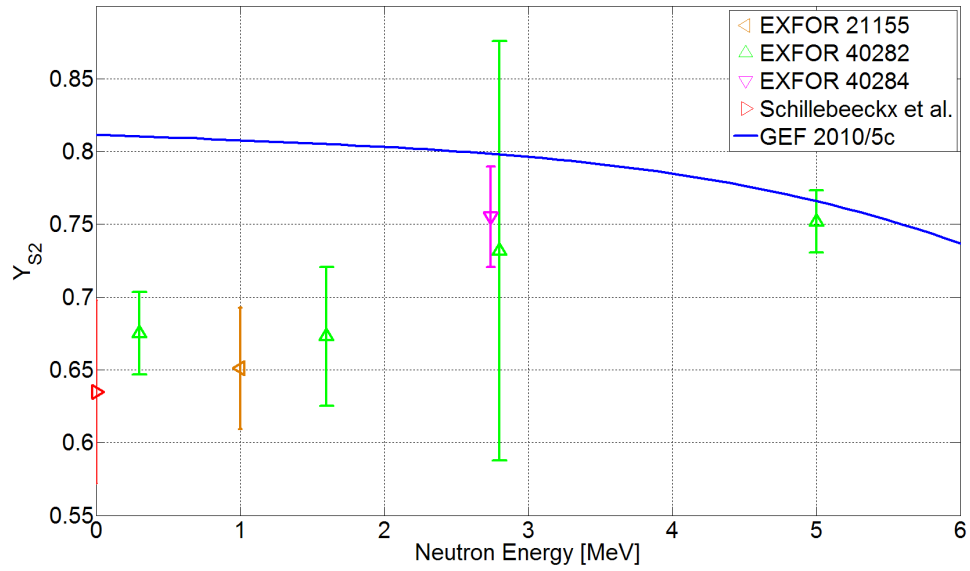
Figure B.18: S2 channel yields Y_{S2} of ^{241}Pu evaluated from [52, 53, 54] in this work and literature values from [56], compared to GEF 2010/5c.
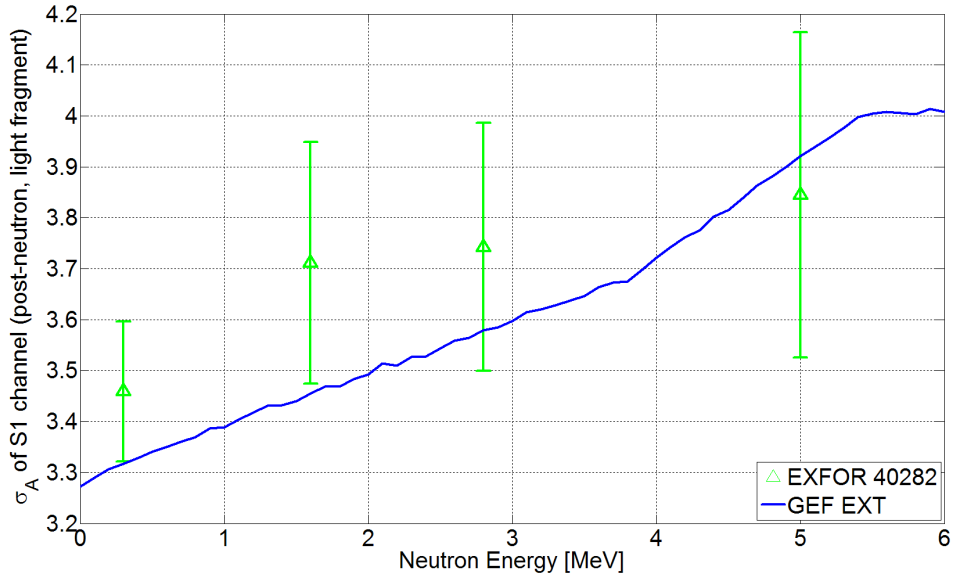
Figure B.19: S1 channel post-neutron mass widths σ_A for the light fragment of $^{241}Pu(n,f)$ evaluated from [53] in this work, compared to GEF EXT.
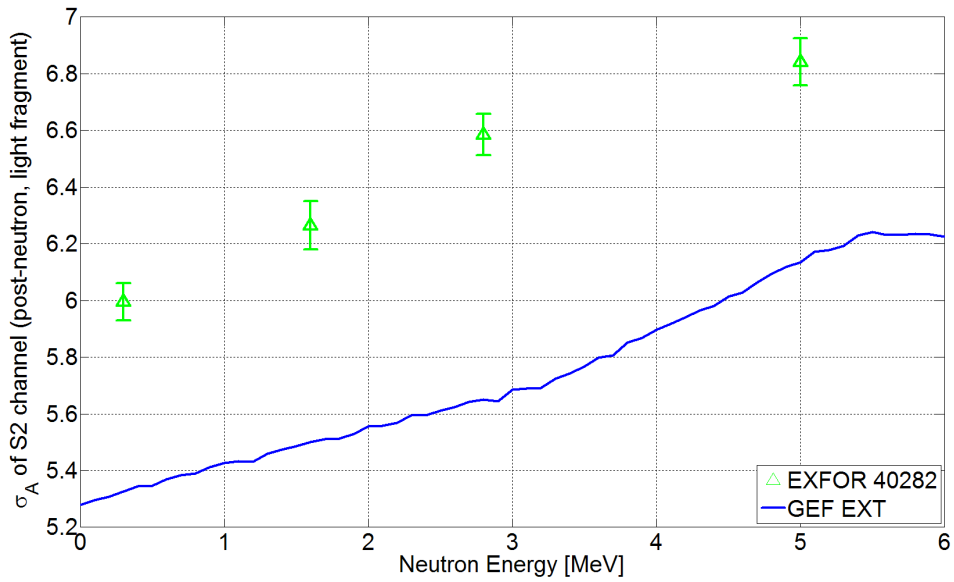
Figure B.20: S2 channel post-neutron mass widths σ_A for the light fragment of $^{241}Pu(n,f)$ evaluated from [53] in this work, compared to GEF EXT.
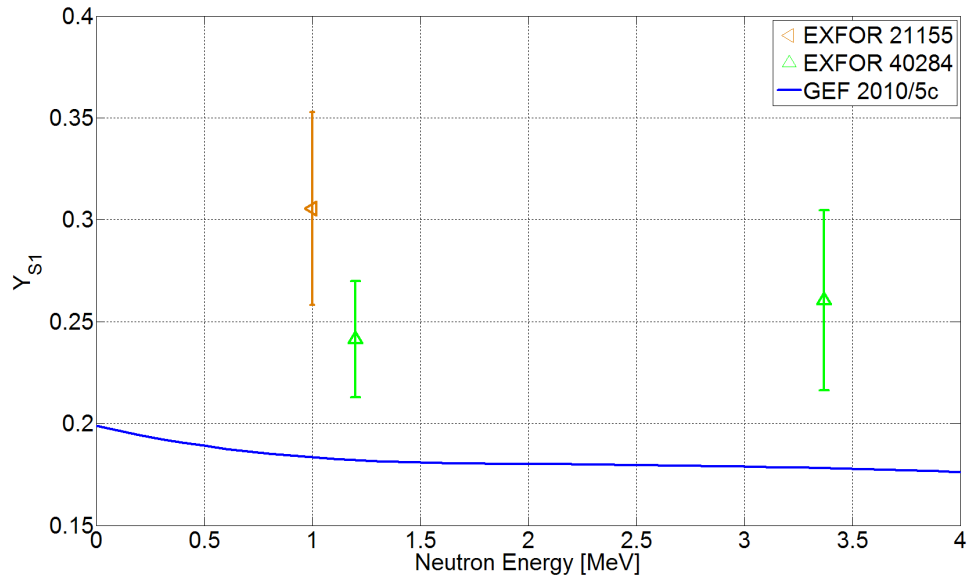
Figure B.21: S1 channel yields Y_{S1} of ^{242}Pu evaluated from [52, 54] in this work, compared to GEF 2010/5c.
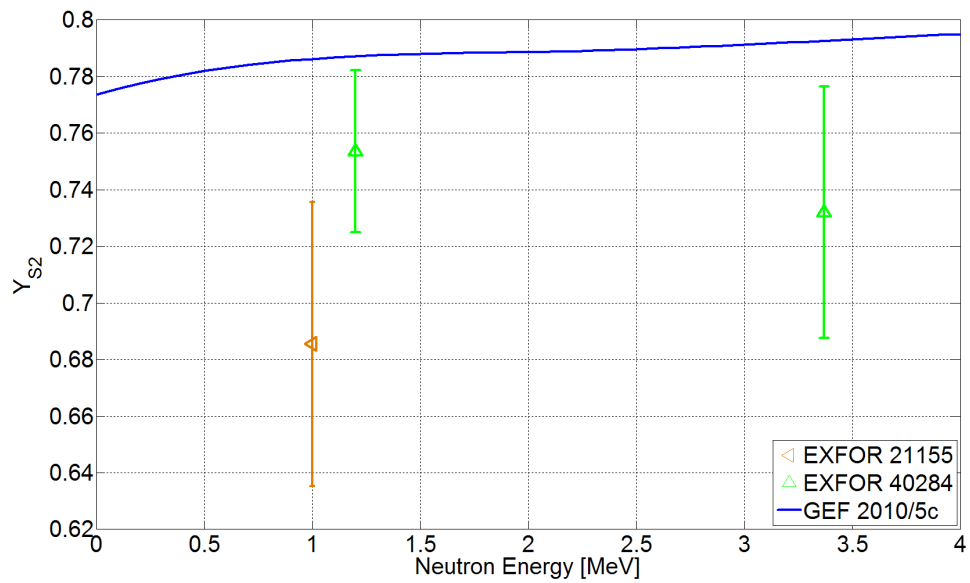
Figure B.22: S2 channel yields Y_{S2} of ^{242}Pu evaluated from [52, 54] in this work, compared to GEF 2010/5c.
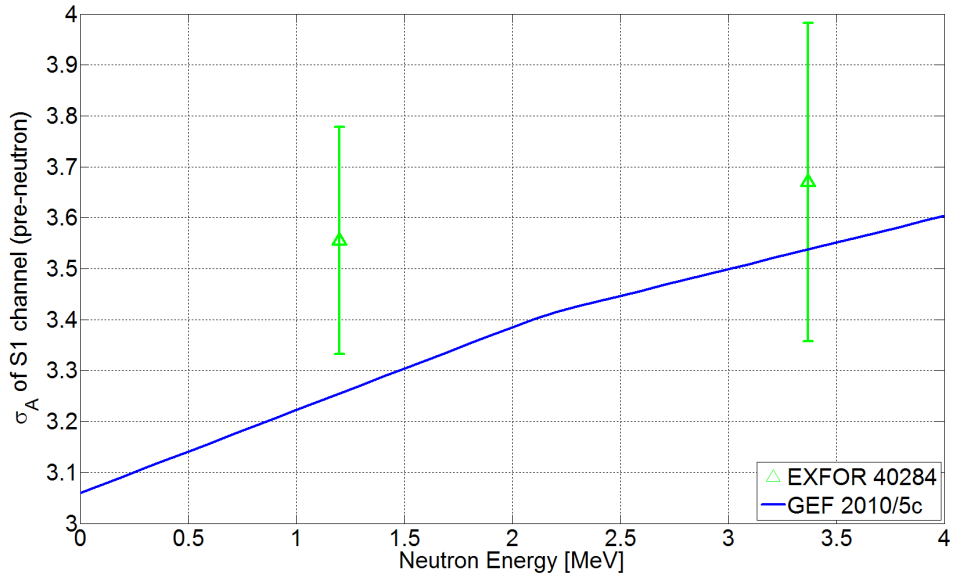
Figure B.23: S1 channel pre-neutron mass width σ_A of ^{242}Pu evaluated from [54] in this work, compared to GEF 2010/5c.
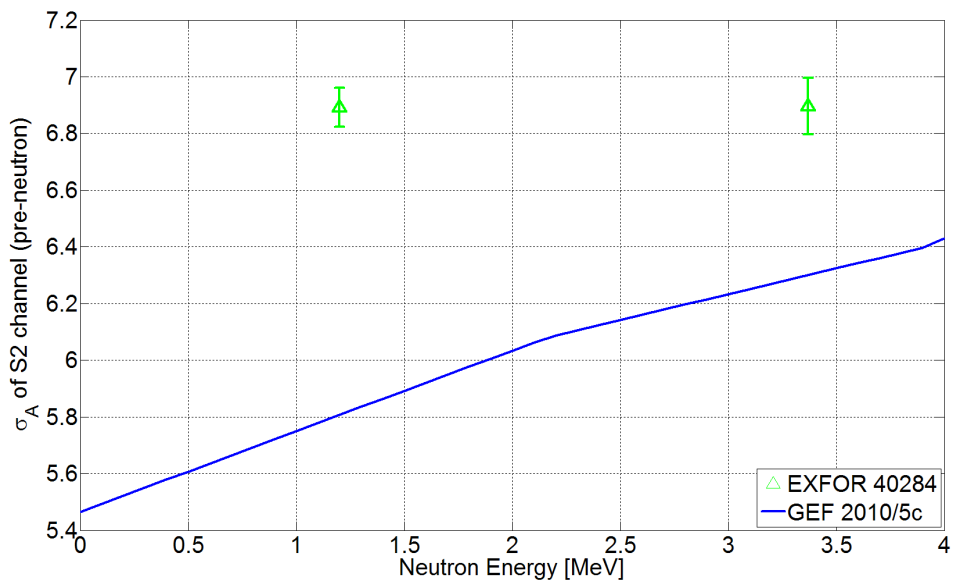
Figure B.24: S2 channel pre-neutron mass width σ_A of ^{242}Pu evaluated from [54] in this work, compared to GEF 2010/5c.

C   SFR Fission Reaction Rate Spectra

This appendix contains the additional plots being referred to in section 4.5.
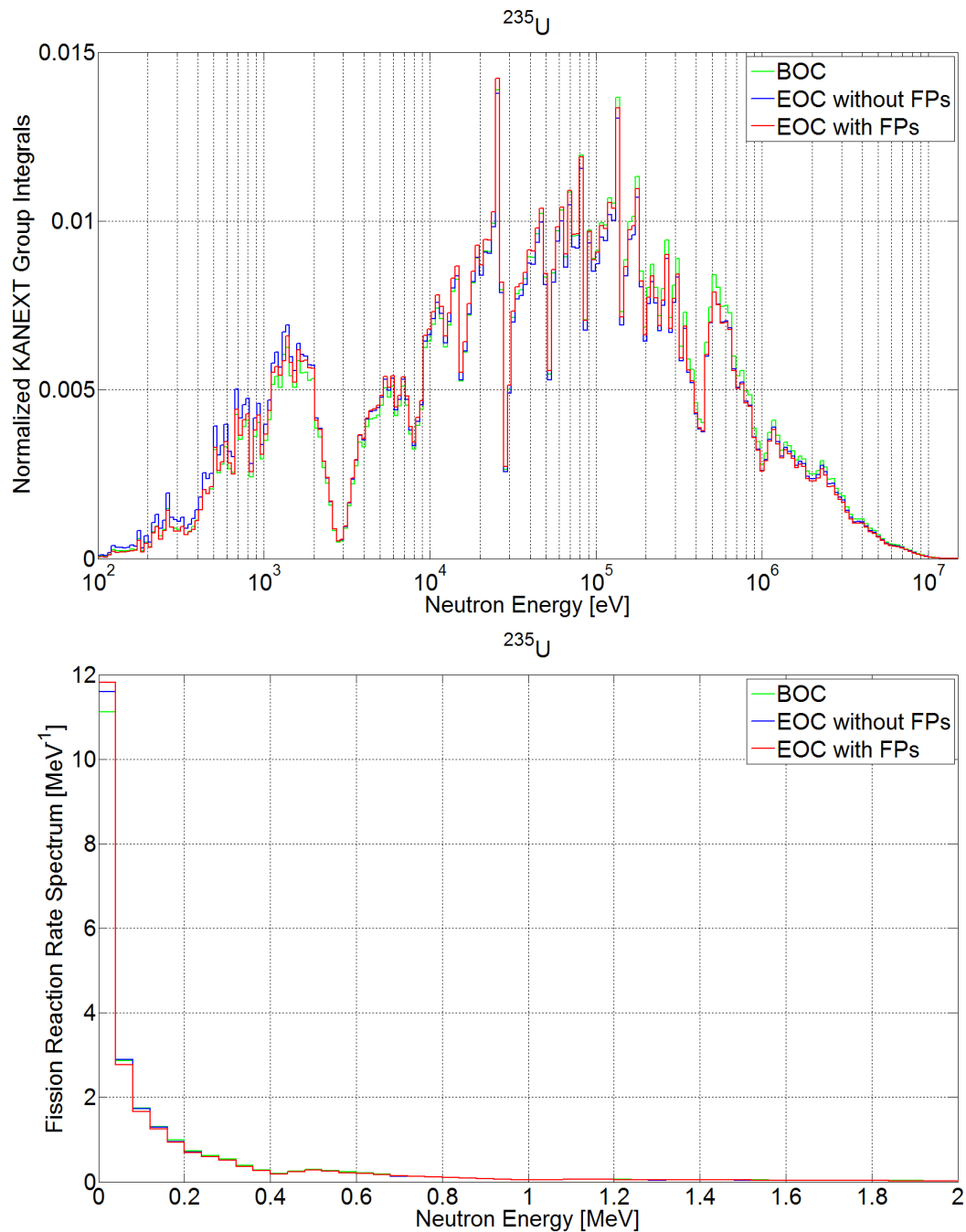
Figure C.1: Reaction rate spectrum of $^{235}U(n, f)$ expressed by the KANEXT group integrals (top) and in a linear scale per unit energy (bottom).
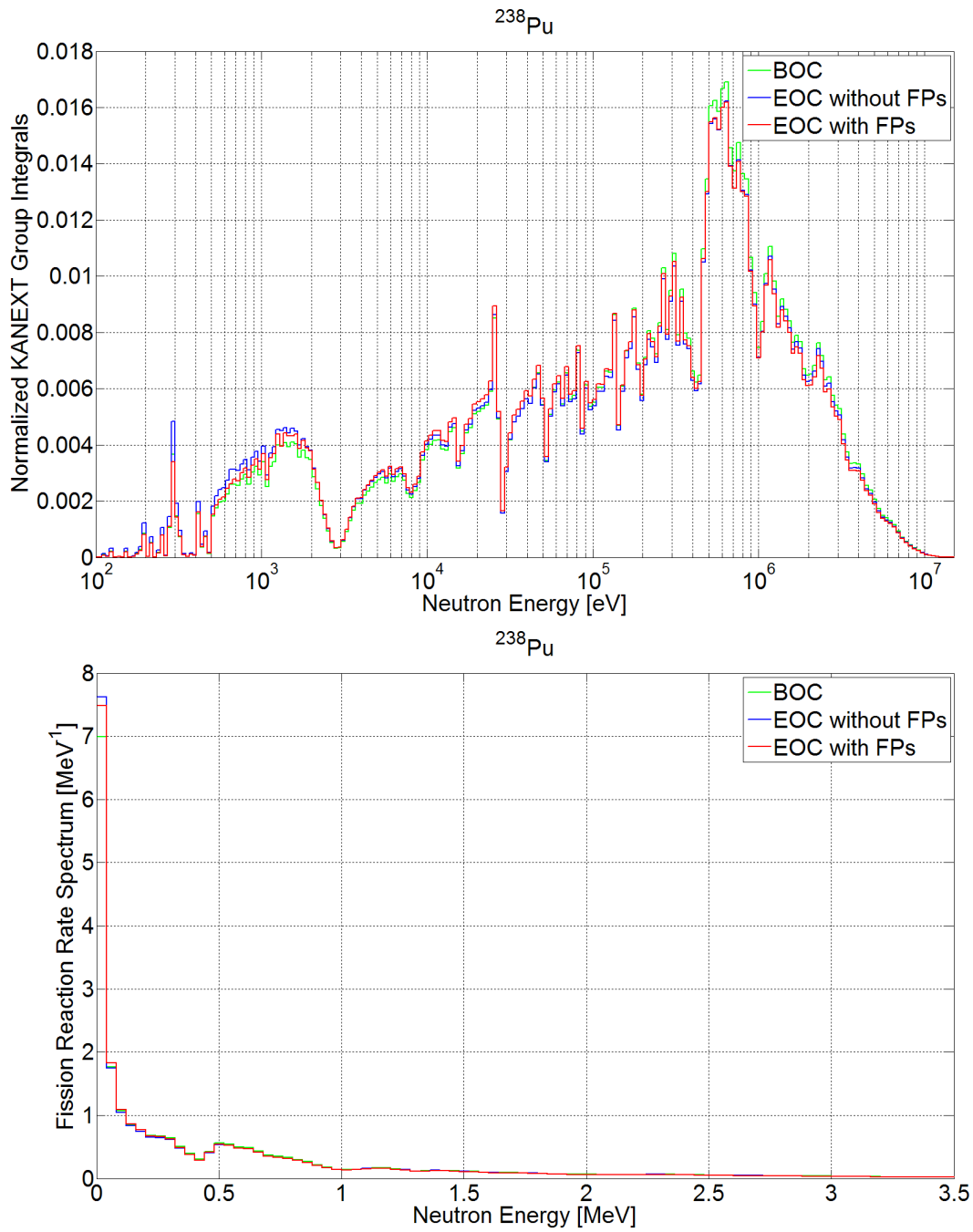
Figure C.2: Reaction rate spectrum of $^{238}Pu(n, f)$ expressed by the KANEXT group integrals (top) and in a linear scale per unit energy (bottom).
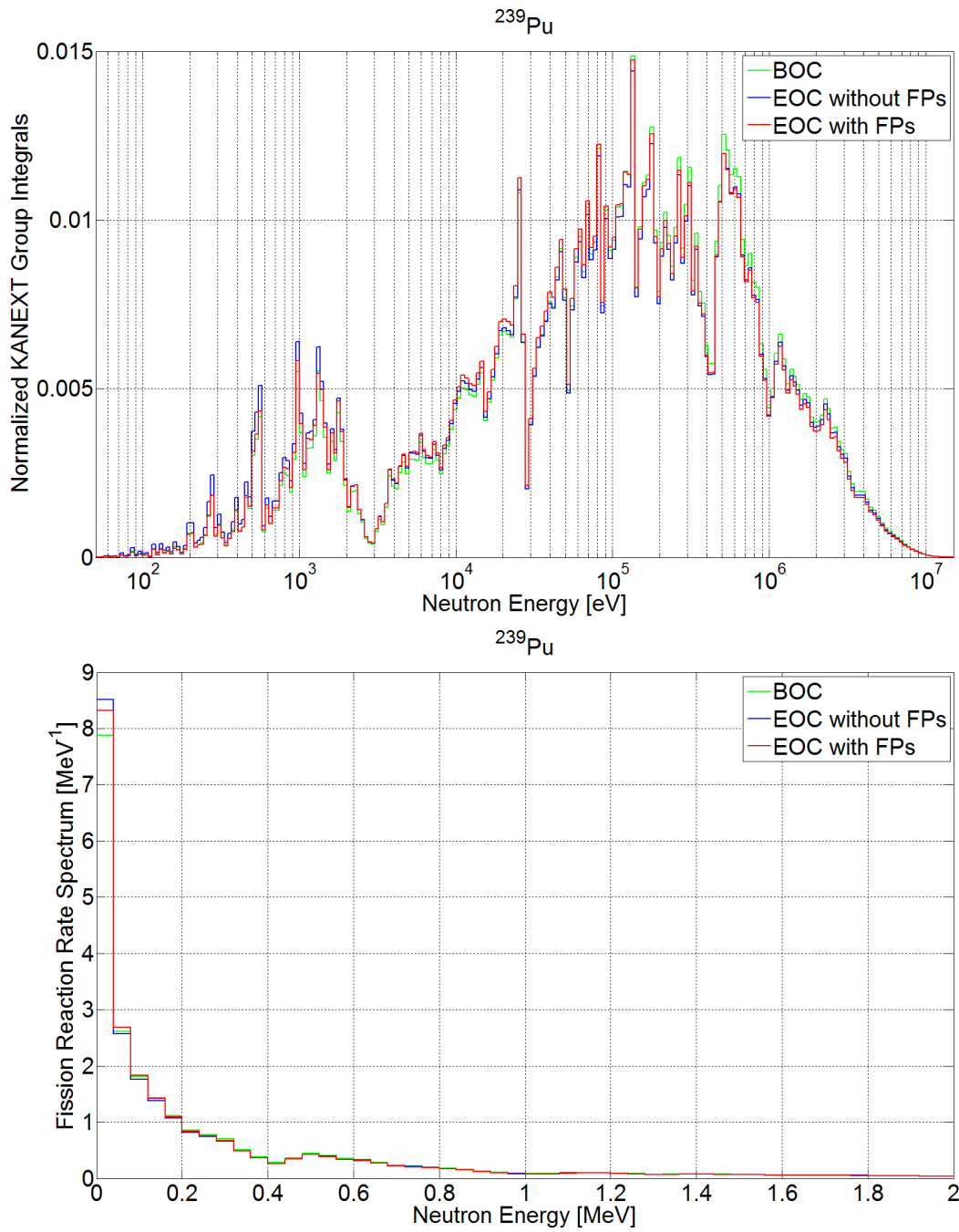
Figure C.3: Reaction rate spectrum of $^{239}Pu(n,f)$ expressed by the KANEXT group integrals (top) and in a linear scale per unit energy (bottom).
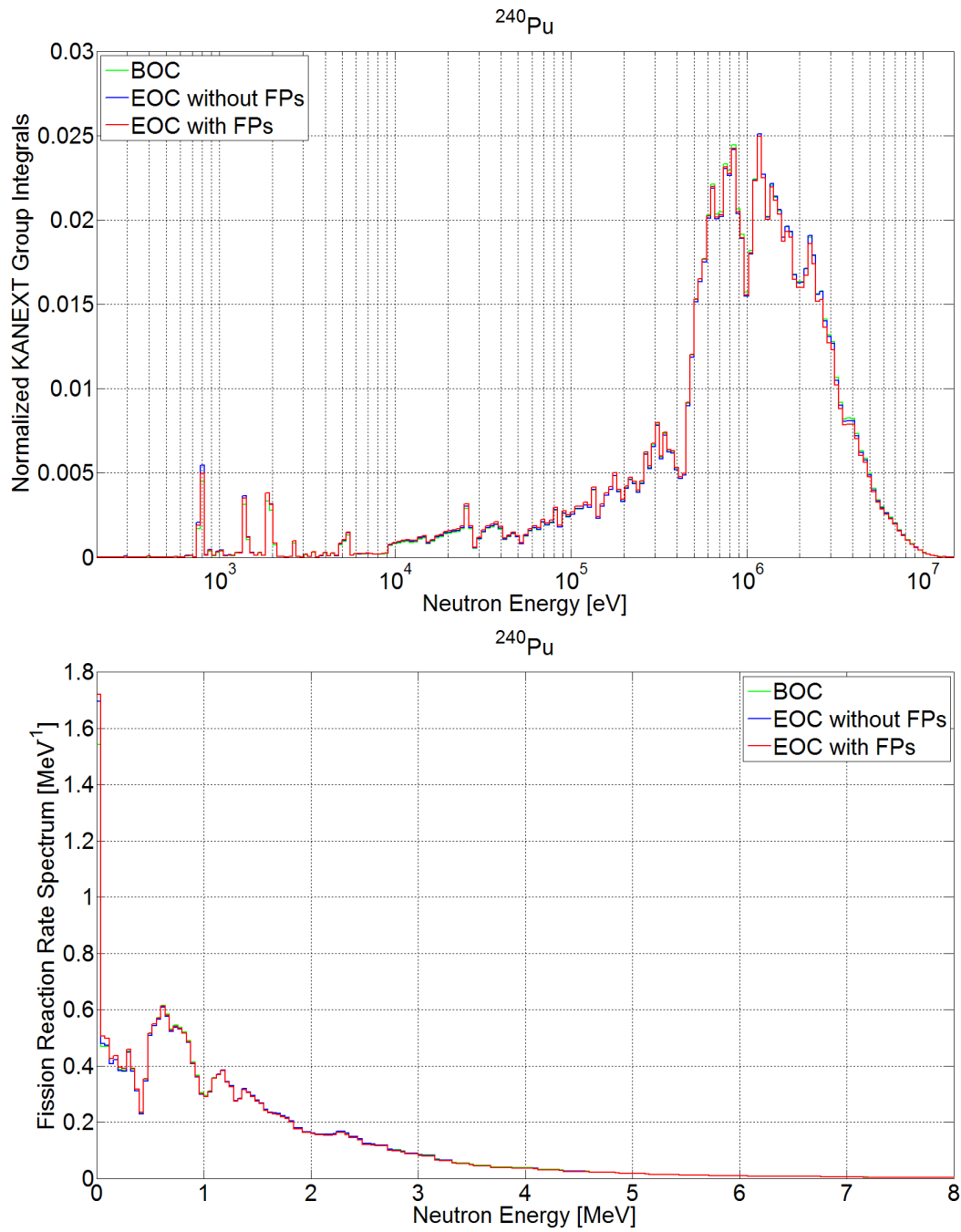
Figure C.4: Reaction rate spectrum of $^{240}Pu(n,f)$ expressed by the KANEXT group integrals (top) and in a linear scale per unit energy (bottom).
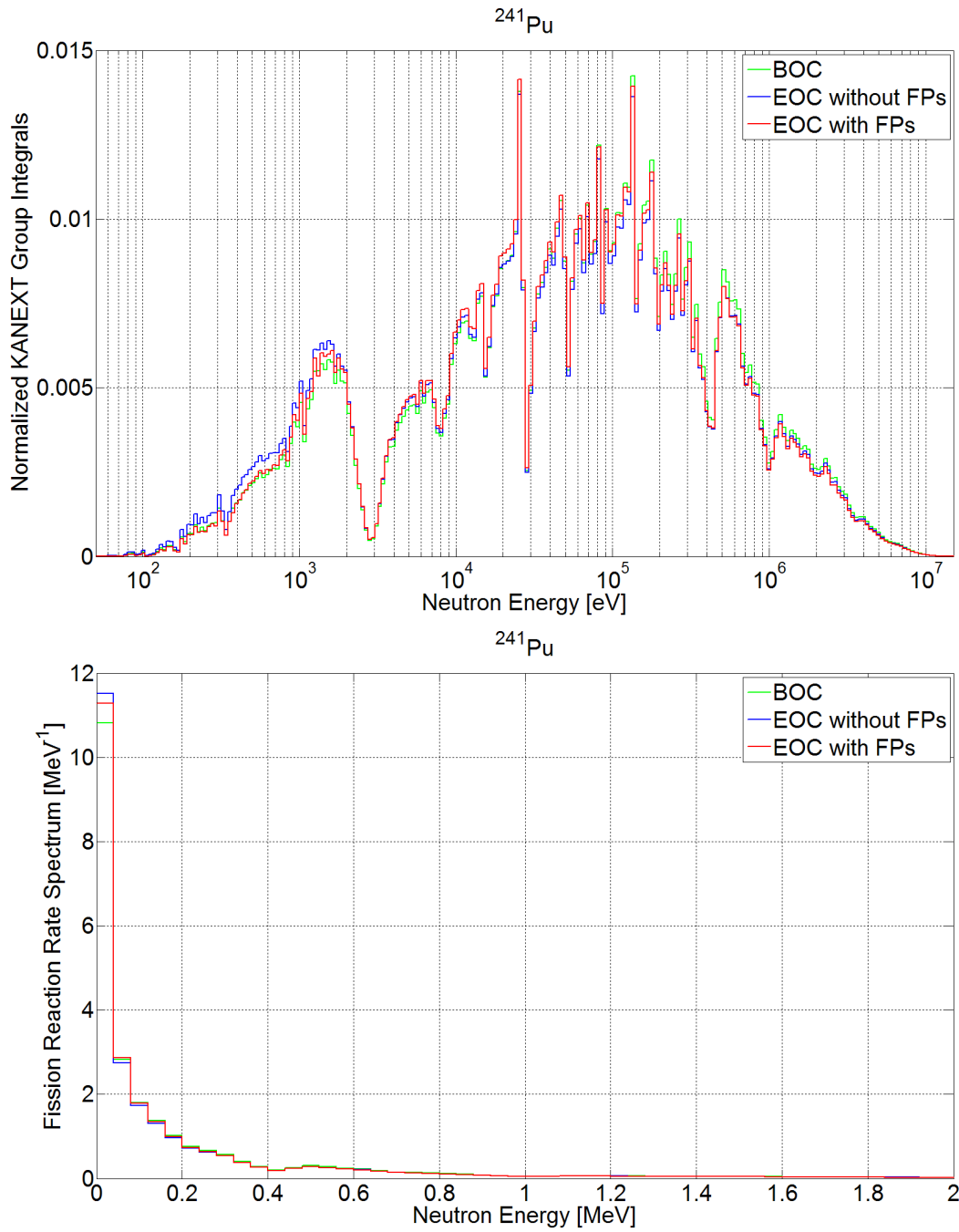
Figure C.5: Reaction rate spectrum of $^{241}Pu(n, f)$ expressed by the KANEXT group integrals (top) and in a linear scale per unit energy (bottom).
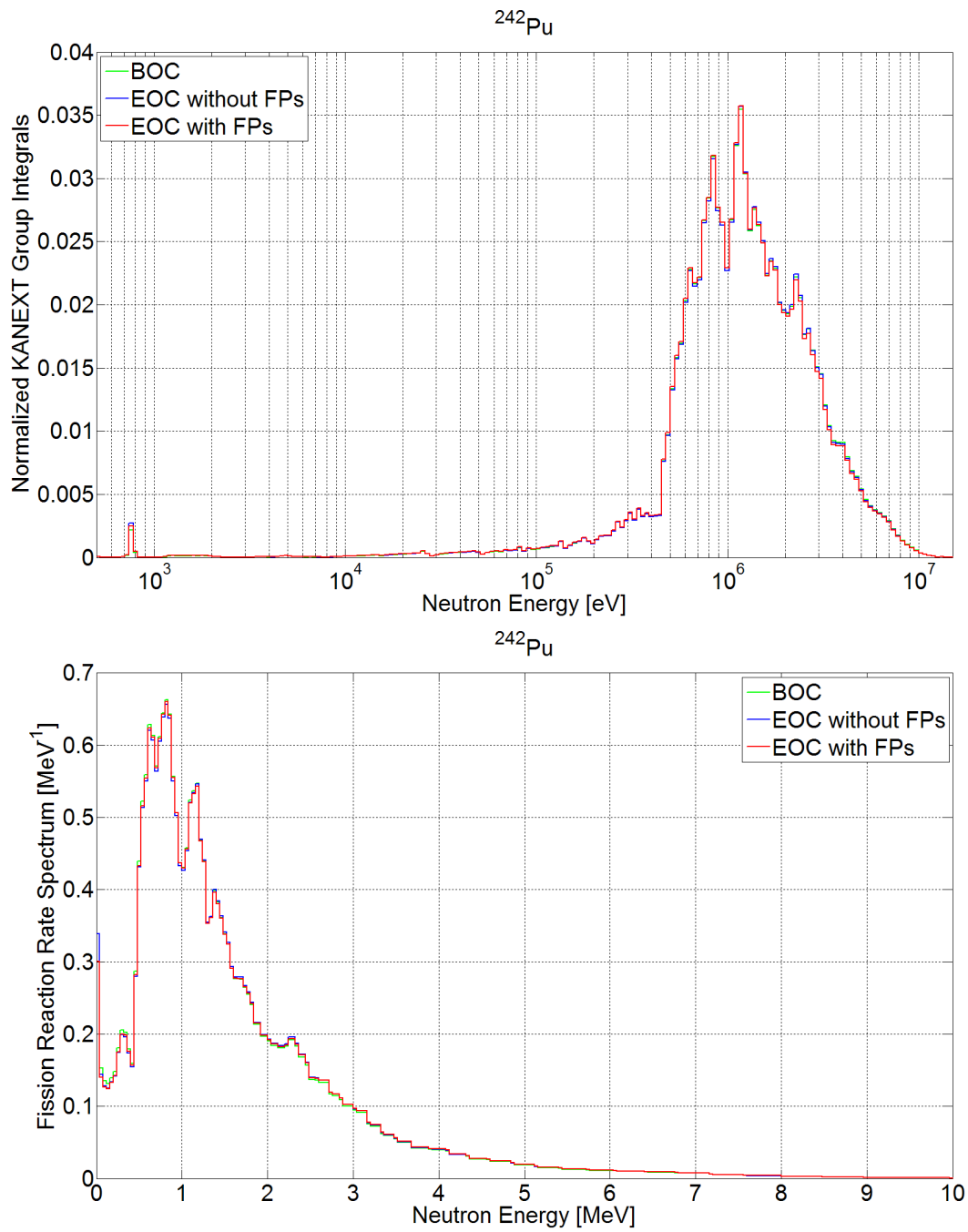
Figure C.6: Reaction rate spectrum of $^{242}Pu(n, f)$ expressed by the KANEXT group integrals (top) and in a linear scale per unit energy (bottom).

D Tables

This appendix contains the table of the absorption fractions of single fission product nuclides which is referred to in section 4.7 as well as the table of fission product yields calculated with the GEF EXT code for the SFR spectrum. The following table lists the calculated absorption fractions.

Table D.1: Absorption fractions of the top 100 fission products in the SFR at a burn-up of $80.1 \frac{\text{GWd}}{\text{t}_{\text{hm}}}$, calculated with the KORFI4 and KORFIN_GEF libraries.

Nuclide	$\overline{\sigma}_c$ [barn]	Absorption Fraction [%]			
		KORFI4		KORFIN_GEF	
		Nuclide	Cumulative	Nuclide	Cumulative
^{105}Pd	0.881	8.80	8.80	7.01	7.01
^{101}Ru	0.658	8.58	17.38	8.80	15.81
^{103}Rh	0.630	7.47	24.85	6.54	22.35
^{99}Tc	0.637	7.45	32.30	8.63	30.98
^{133}Cs	0.444	6.21	38.51	4.97	35.95
^{107}Pd	0.996	5.93	44.43	4.03	39.98
^{149}Sm	1.956	4.33	48.76	4.89	44.87
^{151}Sm	2.931	3.41	52.17	3.76	48.63
^{145}Nd	0.492	3.17	55.34	3.71	52.35
^{97}Mo	0.322	3.13	58.47	2.86	55.20
^{135}Cs	0.197	3.09	61.56	3.08	58.28
^{147}Pm	1.099	3.06	64.62	3.59	61.88
^{143}Nd	0.289	2.58	67.20	3.04	64.91
^{95}Mo	0.299	2.12	69.33	3.01	67.93
^{104}Ru	0.140	1.85	71.18	1.38	69.31
^{153}Eu	2.308	1.78	72.96	1.88	71.19
^{102}Ru	0.152	1.77	74.72	1.82	73.01
^{131}Xe	0.257	1.62	76.34	1.25	74.26
^{98}Mo	0.101	1.28	77.62	1.09	75.35
^{141}Pr	0.124	1.22	78.84	1.55	76.90
^{100}Mo	0.085	1.10	79.94	1.24	78.14
^{109}Ag	0.730	1.09	81.03	1.29	79.43
^{106}Pd	0.192	1.09	82.12	0.82	80.25
^{147}Sm	1.244	0.90	83.02	1.05	81.30
^{93}Zr	0.100	0.84	83.85	1.08	82.38
^{108}Pd	0.162	0.83	84.68	0.60	82.99
^{152}Sm	0.427	0.81	85.49	0.87	83.86
^{132}Xe	0.069	0.76	86.25	0.61	84.47
^{129}I	0.316	0.70	86.94	0.72	85.18
^{154}Eu	2.744	0.65	87.59	0.69	85.87

Nuclide	$\overline{\sigma_c}$ [barn]	Absorption Fraction [%]			
		KORFI4		KORFIN_GEF	
		Nuclide	Cumulative	Nuclide	Cumulative
^{134}Xe	0.035	0.56	88.15	0.53	86.41
^{111}Cd	0.675	0.55	88.71	0.41	86.82
^{103}Ru	0.461	0.52	89.23	0.46	87.28
^{155}Eu	1.320	0.49	89.71	0.62	87.89
^{134}Cs	0.534	0.47	90.19	0.38	88.27
^{127}I	0.563	0.47	90.66	0.51	88.78
^{148}Nd	0.138	0.46	91.12	0.51	89.29
^{142}Ce	0.043	0.45	91.57	0.56	89.84
^{106}Ru	0.084	0.41	91.98	0.30	90.14
^{139}La	0.031	0.39	92.37	0.47	90.62
^{146}Nd	0.088	0.38	92.74	0.51	91.13
^{91}Zr	0.072	0.37	93.11	0.50	91.62
^{137}Cs	0.026	0.35	93.46	0.40	92.03
^{150}Nd	0.150	0.34	93.80	0.38	92.41
^{144}Nd	0.071	0.33	94.13	0.40	92.80
^{150}Sm	0.402	0.33	94.46	0.37	93.18
^{148}Sm	0.334	0.29	94.75	0.34	93.52
^{157}Gd	1.596	0.29	95.04	0.39	93.90
^{92}Zr	0.040	0.27	95.31	0.39	94.29
^{96}Zr	0.024	0.26	95.56	0.24	94.53
^{100}Ru	0.187	0.24	95.81	0.28	94.81
^{95}Nb	0.336	0.23	96.04	0.32	95.14
^{94}Zr	0.025	0.23	96.27	0.31	95.45
^{104}Pd	0.179	0.22	96.49	0.19	95.64
^{85}Rb	0.207	0.22	96.70	0.27	95.91
^{156}Gd	0.539	0.17	96.88	0.24	96.15
^{141}Ce	0.248	0.17	97.05	0.22	96.36
^{140}Ce	0.014	0.16	97.20	0.21	96.57
^{110}Pd	0.094	0.15	97.36	0.11	96.68
^{144}Ce	0.041	0.15	97.51	0.18	96.86
^{83}Kr	0.233	0.15	97.66	0.17	97.03
^{154}Sm	0.214	0.13	97.79	0.15	97.19
^{113}Cd	0.424	0.11	97.90	0.07	97.25
^{148m}Pm	3.700	0.11	98.01	0.13	97.38
^{112}Cd	0.207	0.10	98.11	0.08	97.46
^{155}Gd	2.590	0.10	98.21	0.13	97.59
^{81}Br	0.384	0.09	98.31	0.12	97.71
^{143}Pr	0.346	0.09	98.40	0.10	97.82
^{147}Nd	0.800	0.08	98.48	0.10	97.91
^{115}In	0.579	0.07	98.55	0.05	97.96

Nuclide	$\overline{\sigma_c}$ [barn]	Absorption Fraction [%]			
		KORFI4		KORFIN_GEF	
		Nuclide	Cumulative	Nuclide	Cumulative
^{95}Zr	0.055	0.07	98.62	0.10	98.06
^{96}Mo	0.079	0.07	98.68	0.09	98.14
^{159}Tb	1.548	0.06	98.75	0.18	98.32
^{138}Ba	0.005	0.06	98.81	0.08	98.40
^{90}Sr	0.013	0.06	98.87	0.09	98.48
^{89}Y	0.017	0.06	98.93	0.08	98.56
^{125}Sb	0.288	0.06	98.99	0.07	98.63
^{84}Kr	0.054	0.06	99.04	0.07	98.70
^{130}Te	0.014	0.05	99.10	0.04	98.74
^{136}Xe	0.003	0.04	99.14	0.05	98.79
^{149}Pm	3.127	0.04	99.18	0.05	98.84
^{134}Ba	0.199	0.04	99.22	0.03	98.87
^{110}Cd	0.209	0.04	99.26	0.05	98.92
^{136}Ba	0.065	0.04	99.30	0.05	98.97
^{158}Gd	0.284	0.04	99.34	0.07	99.04
^{87}Rb	0.017	0.04	99.38	0.05	99.09
^{123}Sb	0.264	0.03	99.41	0.03	99.12
^{91}Y	0.044	0.03	99.44	0.04	99.16
^{99}Mo	0.349	0.03	99.47	0.03	99.18
^{151}Eu	4.000	0.02	99.49	0.03	99.21
^{161}Dy	1.642	0.02	99.52	0.09	99.30
^{128}Te	0.036	0.02	99.54	0.03	99.33
^{137}Ba	0.070	0.02	99.56	0.03	99.36
^{127m}Te	0.786	0.02	99.58	0.02	99.38
^{121}Sb	0.408	0.02	99.60	0.03	99.41
^{148}Pm	1.730	0.02	99.62	0.02	99.44
^{105}Rh	0.572	0.02	99.64	0.02	99.45
^{125}Te	0.358	0.02	99.66	0.02	99.47
^{119}Sn	0.179	0.02	99.68	0.01	99.49
^{131}I	0.145	0.02	99.69	0.01	99.50

The following table lists the fission product yields calculated by GEF EXT in this work for the SFR neutron flux spectrum.

Table D.2: Fission product yields calculated for the SFR neutron flux spectrum with GEF EXT in this work.

Nuclide	Target					
	^{235}U	^{238}U	^{239}Pu	^{240}Pu	^{241}Pu	^{242}Pu
	Fission Yield					
^{70}Ni	1.750E-05	1.380E-05	2.115E-05	1.390E-05	1.645E-05	1.070E-05
^{71}Ni	8.300E-06	1.000E-05	1.125E-05		1.105E-05	
^{72}Ni	1.445E-05	2.900E-05	1.140E-05	1.290E-05	1.725E-05	1.780E-05
^{71}Cu	6.500E-06		1.440E-05			
^{72}Cu	7.600E-06		1.750E-05	1.225E-05	1.480E-05	1.005E-05
^{73}Cu	1.710E-05	1.975E-05	2.380E-05	2.400E-05	2.625E-05	2.445E-05
^{74}Cu	5.700E-06	1.155E-05	1.050E-05	1.255E-05	1.390E-05	1.610E-05
^{75}Cu		1.665E-05			1.230E-05	1.505E-05
^{72}Zn	9.700E-06		2.270E-05	1.360E-05	1.015E-05	
^{73n}Zn	1.580E-05		3.245E-05	2.240E-05	1.885E-05	1.295E-05
^{74}Zn	1.008E-04	5.810E-05	1.353E-04	1.128E-04	1.083E-04	7.730E-05
^{75}Zn	8.890E-05	6.625E-05	1.062E-04	1.027E-04	1.080E-04	9.305E-05
^{76}Zn	1.966E-04	2.237E-04	1.577E-04	1.739E-04	2.170E-04	2.185E-04
^{77}Zn	6.310E-05	1.015E-04	4.570E-05	6.350E-05	8.900E-05	9.975E-05
^{77m}Zn	9.150E-06	1.310E-05			1.380E-05	1.205E-05
^{78}Zn	6.265E-05	1.623E-04	3.370E-05	4.620E-05	8.355E-05	1.094E-04
^{79}Zn	1.010E-05	2.850E-05			1.425E-05	2.155E-05
^{80}Zn		1.935E-05				1.120E-05
^{75}Ga	1.810E-05		5.235E-05	3.260E-05	2.545E-05	1.450E-05
^{76}Ga	6.295E-05	2.415E-05	1.101E-04	8.005E-05	6.705E-05	4.985E-05
^{77}Ga	1.395E-04	7.500E-05	2.004E-04	1.758E-04	1.724E-04	1.355E-04
^{78}Ga	1.534E-04	1.265E-04	1.660E-04	1.642E-04	1.827E-04	1.778E-04
^{79}Ga	1.404E-04	1.939E-04	1.308E-04	1.448E-04	1.959E-04	2.318E-04
^{80}Ga	4.255E-05	9.695E-05	4.115E-05	5.090E-05	6.945E-05	9.455E-05
^{81}Ga	2.470E-05	7.300E-05	1.715E-05	2.470E-05	3.770E-05	6.190E-05
^{82}Ga		1.190E-05				
^{76}Ge	1.405E-05		3.410E-05	1.795E-05	1.110E-05	
^{77}Ge	8.465E-05	1.090E-05	1.018E-04	5.850E-05	4.440E-05	2.340E-05
^{77m}Ge	1.465E-05		1.425E-05			
^{78}Ge	3.957E-04	8.325E-05	4.207E-04	2.924E-04	2.481E-04	1.624E-04
^{79}Ge	1.253E-04	3.545E-05	7.590E-05	5.350E-05	5.875E-05	3.890E-05
^{79m}Ge	8.188E-04	2.232E-04	5.125E-04	4.106E-04	3.834E-04	2.927E-04
^{80}Ge	1.861E-03	8.311E-04	9.986E-04	9.473E-04	1.009E-03	9.259E-04

Nuclide	Target					
	^{235}U	^{238}U	^{239}Pu	^{240}Pu	^{241}Pu	^{242}Pu
	Fission Yield					
^{81}Ge	1.180E-03	7.919E-04	4.806E-04	5.160E-04	6.118E-04	6.565E-04
^{81m}Ge	2.718E-04	1.491E-04	1.142E-04	1.054E-04	1.435E-04	1.301E-04
^{82}Ge	1.500E-03	1.476E-03	4.609E-04	5.798E-04	8.204E-04	1.026E-03
^{83}Ge	3.328E-04	5.792E-04	1.062E-04	1.417E-04	2.254E-04	3.277E-04
^{84}Ge	1.447E-04	3.682E-04	3.120E-05	5.035E-05	9.720E-05	1.672E-04
^{85}Ge	1.070E-05	6.075E-05			1.160E-05	2.470E-05
^{86}Ge		1.860E-05				
^{78}As	1.050E-05		2.690E-05			
^{79}As	5.895E-05		1.126E-04	4.950E-05	2.900E-05	1.310E-05
^{80}As	3.759E-04	5.235E-05	4.035E-04	2.179E-04	1.448E-04	7.970E-05
^{81}As	9.260E-04	2.217E-04	9.096E-04	6.022E-04	4.479E-04	3.117E-04
^{82}As	4.840E-04	1.852E-04	3.170E-04	2.154E-04	2.084E-04	1.540E-04
^{82m}As	1.462E-03	5.825E-04	9.432E-04	7.542E-04	6.489E-04	5.282E-04
^{83}As	2.223E-03	1.467E-03	1.336E-03	1.229E-03	1.264E-03	1.252E-03
^{84}As	6.047E-04	7.281E-04	3.203E-04	3.304E-04	3.931E-04	4.526E-04
^{84m}As	6.098E-04	7.236E-04	3.112E-04	3.232E-04	3.977E-04	4.599E-04
^{85}As	4.971E-04	9.066E-04	2.372E-04	3.008E-04	4.050E-04	5.667E-04
^{86}As	1.153E-04	4.155E-04	6.265E-05	8.240E-05	1.296E-04	1.922E-04
^{87}As	2.295E-05	1.289E-04	1.135E-05	1.720E-05	3.265E-05	5.610E-05
^{88}As		2.050E-05				
^{80}Se	2.355E-05		3.305E-05	1.280E-05		
^{81}Se	3.000E-05		2.630E-05	1.050E-05		
^{81m}Se	2.036E-04	1.415E-05	1.727E-04	7.585E-05	4.555E-05	1.750E-05
^{82}Se	1.066E-03	1.129E-04	8.364E-04	4.284E-04	2.826E-04	1.425E-04
^{83}Se	3.274E-03	5.296E-04	1.579E-03	1.021E-03	7.481E-04	4.163E-04
^{83m}Se	7.588E-04	1.074E-04	3.606E-04	2.052E-04	1.685E-04	8.495E-05
^{84}Se	1.027E-02	2.763E-03	4.315E-03	3.228E-03	2.754E-03	1.941E-03
^{85}Se	1.234E-02	5.345E-03	3.947E-03	3.487E-03	3.442E-03	2.819E-03
^{85m}Se		1.656E-04				
^{86}Se	1.031E-02	7.080E-03	2.975E-03	3.053E-03	3.375E-03	3.485E-03
^{87}Se	5.507E-03	6.672E-03	1.423E-03	1.685E-03	2.148E-03	2.467E-03
^{88}Se	2.130E-03	3.979E-03	4.756E-04	6.579E-04	9.483E-04	1.309E-03
^{89}Se	3.974E-04	1.432E-03	1.048E-04	1.503E-04	2.573E-04	3.948E-04
^{90}Se	7.155E-05	4.206E-04	1.550E-05	3.050E-05	5.660E-05	9.885E-05
^{91}Se		4.930E-05				1.240E-05
^{82}Br	5.400E-06		1.765E-05			
^{83}Br	7.910E-05		1.718E-04	6.470E-05	2.835E-05	1.020E-05
^{84}Br	4.196E-04	4.210E-05	5.146E-04	2.315E-04	1.268E-04	5.095E-05
^{84m}Br	4.162E-04	4.510E-05	5.210E-04	2.326E-04	1.257E-04	4.905E-05
^{85}Br	3.957E-03	6.848E-04	3.402E-03	1.920E-03	1.219E-03	6.192E-04

Nuclide	Target					
	^{235}U	^{238}U	^{239}Pu	^{240}Pu	^{241}Pu	^{242}Pu
	Fission Yield					
^{86}Br	9.277E-03	2.563E-03	5.881E-03	4.012E-03	2.979E-03	1.854E-03
^{86m}Br		8.240E-05				
^{87}Br	1.042E-02	4.977E-03	5.841E-03	4.688E-03	3.962E-03	3.044E-03
^{88}Br	1.204E-02	9.817E-03	5.662E-03	5.308E-03	5.134E-03	4.649E-03
^{89}Br	5.874E-03	7.896E-03	2.670E-03	2.888E-03	3.163E-03	3.517E-03
^{90}Br	2.233E-03	5.643E-03	1.027E-03	1.272E-03	1.608E-03	2.106E-03
^{91}Br	4.717E-04	1.913E-03	2.160E-04	3.127E-04	4.365E-04	6.796E-04
^{92}Br	6.630E-05	5.214E-04	3.685E-05	5.930E-05	9.585E-05	1.725E-04
^{93}Br	6.550E-06	9.900E-05			1.440E-05	3.040E-05
^{94}Br		1.115E-05				
^{84}Kr	1.040E-05		2.235E-05			
^{85}Kr	1.512E-04		1.859E-04	6.960E-05	3.255E-05	1.145E-05
^{85m}Kr	3.645E-05		4.345E-05	1.345E-05		
^{86}Kr	1.861E-03	1.527E-04	1.599E-03	7.566E-04	4.425E-04	1.629E-04
^{87}Kr	8.267E-03	1.081E-03	5.215E-03	2.995E-03	1.976E-03	8.958E-04
^{88}Kr	1.854E-02	4.112E-03	9.747E-03	6.711E-03	4.969E-03	2.789E-03
^{89}Kr	3.769E-02	1.392E-02	1.587E-02	1.317E-02	1.104E-02	7.556E-03
^{90}Kr	3.550E-02	2.164E-02	1.362E-02	1.311E-02	1.232E-02	1.026E-02
^{91}Kr	2.867E-02	3.006E-02	9.775E-03	1.108E-02	1.195E-02	1.193E-02
^{92}Kr	1.193E-02	2.003E-02	3.865E-03	4.946E-03	5.989E-03	7.187E-03
^{93}Kr	3.478E-03	1.072E-02	1.148E-03	1.723E-03	2.422E-03	3.422E-03
^{94}Kr	8.154E-04	4.051E-03	2.722E-04	4.495E-04	7.259E-04	1.181E-03
^{95}Kr	9.165E-05	8.671E-04	3.730E-05	6.440E-05	1.314E-04	2.463E-04
^{96}Kr	9.600E-06	1.713E-04			2.240E-05	4.520E-05
^{97}Kr		1.510E-05				
^{86m}Rb			1.430E-05			
^{87}Rb	9.145E-05		2.845E-04	1.010E-04	4.645E-05	1.370E-05
^{88}Rb	8.630E-04	7.165E-05	1.709E-03	7.584E-04	3.862E-04	1.395E-04
^{89}Rb	3.939E-03	5.120E-04	5.081E-03	2.739E-03	1.641E-03	7.337E-04
^{90}Rb	1.530E-03	3.266E-04	1.451E-03	8.563E-04	6.509E-04	3.160E-04
^{90m}Rb	1.355E-02	3.041E-03	1.292E-02	8.678E-03	5.809E-03	3.272E-03
^{91}Rb	2.366E-02	9.163E-03	1.790E-02	1.419E-02	1.115E-02	7.584E-03
^{92}Rb	3.571E-02	2.363E-02	2.271E-02	2.143E-02	1.899E-02	1.590E-02
^{93}Rb	2.112E-02	2.430E-02	1.234E-02	1.357E-02	1.365E-02	1.398E-02
^{94}Rb	1.154E-02	2.298E-02	6.496E-03	8.141E-03	9.395E-03	1.148E-02
^{95}Rb	3.279E-03	1.070E-02	1.871E-03	2.646E-03	3.392E-03	4.908E-03
^{96}Rb	3.563E-04	2.257E-03	2.321E-04	3.628E-04	5.584E-04	9.404E-04
^{96m}Rb	3.613E-04	2.178E-03	2.282E-04	3.701E-04	5.612E-04	9.418E-04
^{97}Rb	1.107E-04	1.159E-03	7.460E-05	1.398E-04	2.377E-04	4.808E-04
^{98}Rb	5.350E-06	1.148E-04			1.915E-05	4.555E-05

Nuclide	Target					
	^{235}U	^{238}U	^{239}Pu	^{240}Pu	^{241}Pu	^{242}Pu
	Fission Yield					
^{98m}Rb	5.700E-06	1.085E-04			2.175E-05	4.565E-05
^{99}Rb		2.215E-05				
^{88}Sr	5.400E-06		1.885E-05			
^{89}Sr	8.970E-05		2.177E-04	7.945E-05	3.730E-05	1.020E-05
^{90}Sr	7.600E-04	4.465E-05	1.196E-03	5.357E-04	2.956E-04	9.585E-05
^{91}Sr	4.746E-03	4.801E-04	5.699E-03	3.096E-03	1.870E-03	7.572E-04
^{92}Sr	1.502E-02	2.713E-03	1.385E-02	9.190E-03	6.411E-03	3.233E-03
^{93}Sr	4.080E-02	1.239E-02	3.035E-02	2.433E-02	1.892E-02	1.193E-02
^{94}Sr	5.285E-02	2.780E-02	3.365E-02	3.209E-02	2.830E-02	2.197E-02
^{95}Sr	5.186E-02	4.585E-02	2.902E-02	3.259E-02	3.240E-02	3.057E-02
^{96}Sr	2.864E-02	4.114E-02	1.485E-02	1.902E-02	2.124E-02	2.405E-02
^{97}Sr	1.371E-02	3.362E-02	6.720E-03	9.937E-03	1.295E-02	1.726E-02
^{98}Sr	4.110E-03	1.631E-02	1.941E-03	3.266E-03	4.768E-03	7.477E-03
^{99}Sr	7.596E-04	5.691E-03	3.794E-04	7.189E-04	1.292E-03	2.353E-03
^{100}Sr	1.220E-04	1.594E-03	6.345E-05	1.404E-04	2.832E-04	6.105E-04
^{101}Sr	7.750E-06	1.986E-04		1.085E-05	2.865E-05	6.475E-05
^{102}Sr		2.690E-05				
^{91}Y			1.985E-05	3.050E-05		
^{91m}Y	1.055E-05		8.645E-05		1.090E-05	
^{92}Y	2.198E-04	1.130E-05	9.000E-04	3.592E-04	1.734E-04	5.780E-05
^{93}Y	1.936E-04	2.005E-05	5.025E-04	1.865E-03	1.448E-04	5.150E-05
^{93m}Y	1.256E-03	1.186E-04	3.286E-03	1.470E-05	9.246E-04	3.732E-04
^{94}Y	8.572E-03	1.460E-03	1.524E-02	9.514E-03	6.168E-03	3.095E-03
^{95}Y	2.032E-02	6.132E-03	2.646E-02	2.035E-02	1.518E-02	9.585E-03
^{96}Y	1.324E-02	5.951E-03	1.395E-02	3.558E-02	1.072E-02	7.572E-03
^{96m}Y	2.390E-02	1.334E-02	2.513E-02	1.271E-04	1.920E-02	1.585E-02
^{97}Y	5.484E-03	4.817E-03	4.932E-03	2.816E-02	5.103E-03	4.337E-03
^{97m}Y	1.869E-02	1.603E-02	1.675E-02	8.330E-05	1.732E-02	1.596E-02
^{97n}Y	5.005E-03	5.297E-03	4.493E-03	2.385E-05	4.657E-03	5.422E-03
^{98}Y	4.408E-03	6.406E-03	3.580E-03	2.312E-02	4.880E-03	4.887E-03
^{98m}Y	1.856E-02	2.812E-02	1.506E-02	7.405E-05	2.033E-02	2.366E-02
^{99}Y	9.757E-03	2.511E-02	7.579E-03	1.081E-02	1.333E-02	1.792E-02
^{100}Y	1.998E-03	9.684E-03	1.593E-03	5.151E-03	3.727E-03	5.826E-03
^{100m}Y	2.015E-03	9.170E-03	1.576E-03		3.728E-03	5.826E-03
^{101}Y	6.245E-04	5.482E-03	5.196E-04	9.786E-04	1.635E-03	3.064E-03
^{102}Y	5.070E-05	9.039E-04	5.285E-05	2.144E-04	2.131E-04	4.630E-04
^{102m}Y	4.985E-05	8.657E-04	5.410E-05		2.116E-04	4.583E-04
^{103}Y	5.350E-06	1.877E-04		1.660E-05	3.565E-05	9.865E-05
^{104}Y		2.445E-05				1.245E-05
^{93}Zr	6.500E-06		4.880E-05	1.460E-05		

D-7

Nuclide	Target					
	^{235}U	^{238}U	^{239}Pu	^{240}Pu	^{241}Pu	^{242}Pu
	Fission Yield					
^{94}Zr	9.630E-05		3.828E-04	1.512E-04	7.540E-05	1.775E-05
^{95}Zr	1.128E-03	8.820E-05	2.915E-03	1.422E-03	8.153E-04	2.940E-04
^{96}Zr	6.116E-03	8.505E-04	1.098E-02	6.775E-03	4.422E-03	2.046E-03
^{97}Zr	1.944E-02	4.627E-03	2.714E-02	2.021E-02	1.458E-02	8.423E-03
^{98}Zr	2.946E-02	1.217E-02	3.315E-02	2.953E-02	2.451E-02	1.719E-02
^{99}Zr	4.228E-02	2.901E-02	4.106E-02	4.273E-02	3.950E-02	3.346E-02
^{100}Zr	3.600E-02	4.431E-02	3.146E-02	3.836E-02	4.081E-02	4.162E-02
^{101}Zr	2.280E-02	5.105E-02	1.862E-02	2.660E-02	3.272E-02	4.026E-02
^{102}Zr	7.526E-03	3.116E-02	6.067E-03	1.016E-02	1.448E-02	2.139E-02
^{103}Zr	2.083E-03	1.684E-02	1.782E-03	3.457E-03	5.858E-03	1.029E-02
^{104}Zr	3.068E-04	4.477E-03	2.796E-04	6.169E-04	1.207E-03	2.538E-03
^{105}Zr	3.820E-05	9.477E-04	3.415E-05	8.535E-05	2.058E-04	5.120E-04
^{106}Zr	7.150E-06	1.371E-04			2.400E-05	5.915E-05
^{107}Zr		3.020E-05				
^{95}Nb			1.740E-05			
^{96}Nb	2.355E-05		2.570E-04	9.105E-05	3.755E-05	1.295E-05
^{97}Nb	2.106E-04	1.565E-05	1.248E-03	6.693E-04	2.790E-04	9.500E-05
^{97m}Nb	4.840E-05		2.942E-04		6.090E-05	1.910E-05
^{98}Nb	3.943E-04	5.885E-05	1.600E-03	3.465E-03	5.121E-04	1.945E-04
^{98m}Nb	1.192E-03	1.552E-04	4.803E-03	2.235E-05	1.538E-03	6.873E-04
^{99}Nb	3.882E-03	8.302E-04	1.122E-02	9.215E-03	5.008E-03	2.729E-03
^{99m}Nb	8.970E-04	2.364E-04	2.590E-03	1.475E-05	1.165E-03	5.586E-04
^{100}Nb	2.395E-03	9.544E-04	5.451E-03	2.278E-02	3.388E-03	1.963E-03
^{100m}Nb	1.003E-02	4.009E-03	2.294E-02	1.152E-04	1.416E-02	9.527E-03
^{101}Nb	1.633E-02	1.255E-02	3.126E-02	3.083E-02	2.764E-02	2.254E-02
^{102}Nb	8.727E-03	1.240E-02	1.501E-02	3.530E-02	1.821E-02	1.826E-02
^{102m}Nb	8.689E-03	1.240E-02	1.498E-02	7.905E-05	1.820E-02	1.827E-02
^{103}Nb	8.928E-03	2.605E-02	1.493E-02	2.125E-02	2.622E-02	3.263E-02
^{104}Nb	1.921E-03	1.026E-02	3.127E-03	1.055E-02	7.554E-03	1.146E-02
^{104m}Nb	1.919E-03	1.026E-02	3.126E-03	1.630E-05	7.541E-03	1.144E-02
^{105}Nb	9.984E-04	8.500E-03	1.380E-03	2.734E-03	4.643E-03	8.606E-03
^{106}Nb	3.195E-04	3.091E-03	2.409E-04	5.514E-04	1.118E-03	2.493E-03
^{107}Nb	1.122E-04	1.082E-03	2.880E-05	6.900E-05	1.663E-04	4.189E-04
^{108}Nb	5.145E-05	5.492E-04			2.190E-05	6.145E-05
^{109}Nb	1.605E-05	2.446E-04				
^{110}Nb	6.150E-06	1.117E-04				
^{111}Nb		3.185E-05				
^{98}Mo	7.350E-06		8.645E-05	2.715E-05	1.265E-05	
^{99}Mo	8.035E-05		5.922E-04	2.357E-04	1.199E-04	3.780E-05
^{100}Mo	6.296E-04	7.155E-05	3.049E-03	1.564E-03	9.107E-04	3.532E-04

Nuclide	Target					
	^{235}U	^{238}U	^{239}Pu	^{240}Pu	^{241}Pu	^{242}Pu
	Fission Yield					
^{101}Mo	2.277E-03	4.631E-04	8.993E-03	5.695E-03	3.728E-03	1.786E-03
^{102}Mo	6.421E-03	2.685E-03	2.092E-02	1.666E-02	1.294E-02	7.860E-03
^{103}Mo	1.023E-02	7.929E-03	2.943E-02	2.870E-02	2.567E-02	1.960E-02
^{104}Mo	9.997E-03	1.591E-02	2.784E-02	3.343E-02	3.571E-02	3.437E-02
^{105}Mo	6.975E-03	2.007E-02	1.830E-02	2.648E-02	3.293E-02	3.945E-02
^{106}Mo	3.170E-03	1.557E-02	7.327E-03	1.278E-02	1.920E-02	2.856E-02
^{107}Mo	1.362E-03	9.741E-03	2.266E-03	4.655E-03	8.247E-03	1.490E-02
^{108}Mo	4.673E-04	4.441E-03	4.104E-04	9.659E-04	2.046E-03	4.418E-03
^{109}Mo	1.814E-04	2.189E-03	7.070E-05	1.802E-04	4.597E-04	1.129E-03
^{110}Mo	5.940E-05	9.714E-04	1.450E-05	3.445E-05	8.815E-05	1.973E-04
^{111}Mo	1.915E-05	3.844E-04			1.985E-05	3.560E-05
^{112}Mo	5.300E-06	1.407E-04				1.080E-05
^{113}Mo		4.235E-05				
^{100}Tc			2.690E-05			
^{101}Tc	8.250E-06		2.103E-04	7.530E-05	3.120E-05	
^{102}Tc	2.905E-05		5.814E-04	5.379E-04	1.428E-04	5.475E-05
^{102m}Tc	3.190E-05		5.799E-04		1.401E-04	5.420E-05
^{103}Tc	2.853E-04	7.530E-05	4.086E-03	2.435E-03	1.534E-03	7.284E-04
^{104}Tc	7.258E-04	4.139E-04	9.591E-03	7.241E-03	5.472E-03	3.341E-03
^{105}Tc	1.055E-03	1.338E-03	1.464E-02	1.408E-02	1.273E-02	9.856E-03
^{106}Tc	9.673E-04	2.183E-03	1.414E-02	1.685E-02	1.827E-02	1.828E-02
^{107}Tc	5.464E-04	2.067E-03	8.416E-03	1.250E-02	1.651E-02	2.086E-02
^{108}Tc	2.611E-04	1.363E-03	3.499E-03	6.079E-03	9.450E-03	1.480E-02
^{109}Tc	9.750E-05	6.588E-04	1.033E-03	2.082E-03	3.750E-03	7.017E-03
^{110}Tc	4.870E-05	3.183E-04	3.748E-04	7.589E-04	1.445E-03	2.858E-03
^{111}Tc	1.890E-05	1.354E-04	1.435E-04	2.814E-04	5.411E-04	9.894E-04
^{112}Tc	7.750E-06	6.345E-05	6.505E-05	1.257E-04	2.556E-04	4.586E-04
^{113}Tc		1.795E-05	1.995E-05	4.035E-05	8.835E-05	1.691E-04
^{114}Tc				1.785E-05	3.920E-05	8.905E-05
^{115}Tc					1.290E-05	3.100E-05
^{103}Ru			1.760E-05	2.000E-05		
^{103m}Ru			4.285E-05			
^{104}Ru	1.025E-05		4.163E-04	1.939E-04	1.071E-04	3.510E-05
^{105}Ru	3.265E-05	1.155E-05	1.534E-03	8.872E-04	5.939E-04	2.775E-04
^{106}Ru	9.310E-05	5.315E-05	4.343E-03	3.216E-03	2.537E-03	1.506E-03
^{107}Ru	1.453E-04	1.182E-04	6.624E-03	6.208E-03	5.963E-03	4.567E-03
^{108}Ru	1.630E-04	1.998E-04	7.108E-03	8.364E-03	9.677E-03	9.412E-03
^{109}Ru	1.480E-04	2.388E-04	4.715E-03	6.746E-03	9.281E-03	1.122E-02
^{110}Ru	1.169E-04	2.221E-04	2.441E-03	4.040E-03	6.550E-03	9.436E-03
^{111}Ru	1.032E-04	1.811E-04	1.155E-03	2.032E-03	3.632E-03	5.812E-03

Nuclide	Target					
	^{235}U	^{238}U	^{239}Pu	^{240}Pu	^{241}Pu	^{242}Pu
	Fission Yield					
^{112}Ru	8.235E-05	1.572E-04	5.040E-04	9.339E-04	1.781E-03	2.963E-03
^{113}Ru	2.910E-05	6.580E-05	1.093E-04	4.227E-04	4.286E-04	6.975E-04
^{113m}Ru	2.810E-05	6.085E-05	1.105E-04		4.268E-04	6.965E-04
^{114}Ru	2.405E-05	7.695E-05	7.000E-05	1.489E-04	3.292E-04	5.434E-04
^{115}Ru	8.150E-06	4.695E-05	2.415E-05	5.270E-05	1.251E-04	2.232E-04
^{116}Ru		1.710E-05		1.805E-05	4.580E-05	8.985E-05
^{117}Ru					1.400E-05	3.305E-05
^{105}Rh			1.005E-05			
^{106}Rh			2.740E-05	3.690E-05		
^{106m}Rh			6.120E-05		1.210E-05	
^{107}Rh			3.445E-04	1.893E-04	1.170E-04	5.370E-05
^{108}Rh			2.115E-04	6.031E-04	1.200E-04	6.520E-05
^{108m}Rh			6.419E-04		3.530E-04	2.241E-04
^{109}Rh	9.450E-06		1.266E-03	1.128E-03	1.127E-03	8.652E-04
^{110}Rh	1.980E-05	1.350E-05	1.212E-03	1.366E-03	1.585E-03	1.511E-03
^{110m}Rh			3.050E-05		4.455E-05	3.745E-05
^{111}Rh	3.705E-05	2.670E-05	9.197E-04	1.162E-03	1.531E-03	1.711E-03
^{112}Rh	2.785E-05	2.280E-05	2.900E-04	8.072E-04	5.633E-04	6.494E-04
^{112m}Rh	3.035E-05	2.135E-05	2.852E-04		5.537E-04	6.594E-04
^{113}Rh	6.795E-05	7.300E-05	3.290E-04	4.737E-04	6.843E-04	7.318E-04
^{114}Rh	3.055E-05	4.915E-05	1.003E-04	3.059E-04	2.265E-04	1.828E-04
^{114m}Rh	3.280E-05	4.490E-05	1.016E-04		2.266E-04	1.886E-04
^{115}Rh	4.420E-05	9.250E-05	1.019E-04	1.670E-04	2.655E-04	1.733E-04
^{116}Rh	7.750E-06	2.415E-05	1.275E-05	8.775E-05	4.215E-05	2.430E-05
^{116m}Rh	1.700E-05	5.410E-05	3.150E-05		1.023E-04	6.075E-05
^{117}Rh	8.550E-06	4.140E-05	1.235E-05	2.840E-05	5.660E-05	3.340E-05
^{118}Rh		2.190E-05			1.780E-05	1.330E-05
^{108}Pd			1.350E-05			
^{109}Pd			1.520E-05	2.375E-05		
^{109m}Pd			2.990E-05		1.140E-05	
^{110}Pd			1.226E-04	7.925E-05	6.535E-05	3.620E-05
^{111}Pd			6.770E-05	1.470E-04	4.765E-05	2.940E-05
^{111m}Pd			1.270E-04		8.770E-05	6.295E-05
^{112}Pd	1.025E-05		2.937E-04	2.676E-04	2.650E-04	1.912E-04
^{113}Pd	8.050E-06		8.955E-05	3.094E-04	9.605E-05	6.110E-05
^{113m}Pd	1.655E-05		2.156E-04		2.310E-04	1.680E-04
^{114}Pd	6.035E-05	2.715E-05	3.565E-04	3.941E-04	4.266E-04	2.708E-04
^{115}Pd	2.935E-05	2.050E-05	1.126E-04	3.876E-04	1.591E-04	6.790E-05
^{115m}Pd	5.545E-05	3.740E-05	2.154E-04		2.919E-04	1.500E-04
^{116}Pd	1.044E-04	1.127E-04	3.175E-04	4.011E-04	4.988E-04	2.066E-04

Nuclide	Target					
	^{235}U	^{238}U	^{239}Pu	^{240}Pu	^{241}Pu	^{242}Pu
	Fission Yield					
^{117}Pd	3.175E-05	4.565E-05	6.865E-05	2.902E-04	1.407E-04	4.935E-05
^{117m}Pd	5.910E-05	8.495E-05	1.293E-04		2.646E-04	1.085E-04
^{118}Pd	6.065E-05	1.304E-04	1.141E-04	1.873E-04	2.936E-04	1.213E-04
^{119}Pd	3.210E-05	9.685E-05	4.210E-05	8.630E-05	1.517E-04	7.275E-05
^{120}Pd	1.305E-05	5.650E-05	1.695E-05	3.395E-05	6.855E-05	3.595E-05
^{121}Pd		2.810E-05			2.295E-05	1.485E-05
^{122}Pd		1.160E-05				
^{112}Ag			1.200E-05			
^{113}Ag				2.090E-05		
^{113m}Ag			2.395E-05		1.110E-05	
^{114}Ag			1.165E-05	4.625E-05		
^{114m}Ag			4.730E-05		2.550E-05	1.285E-05
^{115}Ag			1.620E-05	1.028E-04	1.025E-05	
^{115m}Ag	8.900E-06		1.034E-04		7.020E-05	2.865E-05
^{116}Ag	7.400E-06		5.830E-05	1.883E-04	4.740E-05	1.345E-05
^{116m}Ag	1.645E-05		1.324E-04		1.111E-04	3.905E-05
^{117}Ag	6.650E-06		3.400E-05	2.727E-04	3.475E-05	
^{117m}Ag	4.400E-05	2.295E-05	2.253E-04		2.393E-04	7.580E-05
^{118}Ag	1.240E-05	1.130E-05	4.985E-05	3.134E-04	6.655E-05	1.805E-05
^{118m}Ag	4.970E-05	4.715E-05	2.041E-04		2.827E-04	9.115E-05
^{119}Ag	8.500E-06	1.420E-05	2.810E-05	2.790E-04	4.675E-05	1.270E-05
^{119m}Ag	5.590E-05	6.690E-05	1.764E-04		3.066E-04	1.047E-04
^{120}Ag	2.615E-05	3.760E-05	5.430E-05	2.116E-04	1.230E-04	4.455E-05
^{120m}Ag	3.225E-05	5.950E-05	8.385E-05		1.778E-04	6.925E-05
^{121}Ag	3.180E-05	8.065E-05	7.425E-05	1.172E-04	1.896E-04	8.305E-05
^{122}Ag	8.750E-06	2.750E-05	2.105E-05	6.405E-05	5.470E-05	2.650E-05
^{122m}Ag	8.300E-06	3.220E-05	1.905E-05		4.575E-05	2.785E-05
^{123}Ag	9.900E-06	3.650E-05	2.360E-05	3.185E-05	4.835E-05	3.570E-05
^{124}Ag		1.040E-05		1.680E-05	1.275E-05	1.090E-05
^{124m}Ag		1.025E-05			1.215E-05	1.295E-05
^{125}Ag		1.425E-05			1.240E-05	1.620E-05
^{116}Cd			2.635E-05	1.600E-05		
^{117}Cd			1.560E-05	4.875E-05		
^{117m}Cd			4.670E-05		2.265E-05	
^{118}Cd	1.930E-05		1.511E-04	1.332E-04	1.014E-04	2.385E-05
^{119}Cd	1.250E-05		6.675E-05	2.175E-04	5.510E-05	1.140E-05
^{119m}Cd	2.995E-05	1.060E-05	1.614E-04		1.318E-04	3.505E-05
^{120}Cd	7.935E-05	4.635E-05	3.319E-04	3.540E-04	3.722E-04	1.032E-04
^{121}Cd	2.570E-05	2.155E-05	9.045E-05	3.590E-04	1.228E-04	3.640E-05
^{121m}Cd	6.265E-05	5.590E-05	2.109E-04		2.932E-04	9.505E-05

Nuclide	Target					
	^{235}U	^{238}U	^{239}Pu	^{240}Pu	^{241}Pu	^{242}Pu
	Fission Yield					
^{122}Cd	9.845E-05	1.169E-04	2.875E-04	3.662E-04	4.501E-04	1.644E-04
^{123}Cd	2.645E-05	3.830E-05	6.510E-05	2.698E-04	1.072E-04	4.010E-05
^{123m}Cd	6.370E-05	8.710E-05	1.685E-04		2.564E-04	1.115E-04
^{124}Cd	1.072E-04	1.323E-04	2.497E-04	2.688E-04	3.337E-04	1.741E-04
^{125}Cd	3.765E-05	4.055E-05	5.655E-05	2.167E-04	8.610E-05	5.055E-05
^{125m}Cd	9.530E-05	9.755E-05	1.456E-04		1.954E-04	1.452E-04
^{126}Cd	1.528E-04	1.939E-04	1.588E-04	1.955E-04	2.651E-04	2.364E-04
^{127}Cd	9.415E-05	2.023E-04	7.160E-05	1.032E-04	1.653E-04	1.851E-04
^{128}Cd	5.675E-05	2.059E-04	3.545E-05	5.425E-05	1.108E-04	1.511E-04
^{129}Cd	5.050E-06	3.250E-05		1.475E-05	1.070E-05	1.625E-05
^{129m}Cd	1.015E-05	8.240E-05			2.805E-05	4.575E-05
^{130}Cd		7.195E-05			1.485E-05	2.605E-05
^{131}Cd		1.355E-05				
^{119}In			2.320E-05	1.940E-05		
^{120}In			2.285E-05	5.795E-05	1.260E-05	
^{120m}In			2.415E-05		1.080E-05	
^{120n}In			2.225E-05		1.160E-05	
^{121}In	1.395E-05		1.218E-04	1.338E-04	8.090E-05	2.030E-05
^{121m}In			2.570E-05		1.810E-05	
^{122}In	1.400E-05		9.125E-05	2.218E-04	7.870E-05	2.080E-05
^{122m}In	9.500E-06		6.430E-05		5.460E-05	1.505E-05
^{122n}In	9.600E-06		6.290E-05		5.450E-05	1.545E-05
^{123}In	4.915E-05	3.730E-05	2.515E-04	3.181E-04	2.532E-04	8.270E-05
^{123m}In	1.080E-05		6.005E-05		5.895E-05	1.700E-05
^{124}In	5.535E-05	4.095E-05	2.376E-04	4.002E-04	2.115E-04	7.690E-05
^{124m}In	4.770E-05	4.080E-05	2.104E-04		1.848E-04	8.740E-05
^{125}In	1.692E-04	1.254E-04	5.627E-04	5.826E-04	4.486E-04	2.322E-04
^{125m}In	4.025E-05	2.950E-05	1.322E-04		1.028E-04	4.760E-05
^{126}In	2.397E-04	1.531E-04	5.330E-04	8.679E-04	4.446E-04	2.613E-04
^{126m}In	2.139E-04	1.629E-04	4.806E-04		3.989E-04	2.755E-04
^{127}In	6.461E-04	5.483E-04	9.669E-04	1.153E-03	9.802E-04	8.040E-04
^{127m}In	1.505E-04	1.217E-04	2.246E-04		2.303E-04	1.644E-04
^{128}In	3.809E-04	4.710E-04	3.859E-04	1.221E-03	5.668E-04	5.118E-04
^{128m}In	1.546E-04	1.948E-04	1.581E-04		2.312E-04	1.985E-04
^{128n}In	4.771E-04	6.387E-04	5.010E-04		7.186E-04	7.730E-04
^{129}In	6.996E-04	1.547E-03	4.729E-04	8.640E-04	1.097E-03	1.326E-03
^{129m}In	1.637E-04	3.382E-04	1.088E-04		2.518E-04	2.684E-04
^{130}In	9.860E-05	4.941E-04	4.610E-05	4.025E-04	2.003E-04	2.866E-04
^{130m}In	1.170E-04	7.035E-04	5.295E-05		2.304E-04	4.036E-04
^{130n}In	2.007E-04	9.721E-04	9.275E-05		3.816E-04	5.718E-04

Nuclide	Target					
	^{235}U	^{238}U	^{239}Pu	^{240}Pu	^{241}Pu	^{242}Pu
	Fission Yield					
^{131}In	3.630E-05	5.326E-04	1.365E-05	1.064E-04	8.935E-05	2.079E-04
^{131m}In	3.415E-05	5.305E-04	1.280E-05		9.380E-05	2.034E-04
^{131n}In	3.370E-05	5.254E-04	1.545E-05		9.250E-05	2.006E-04
^{132}In	9.700E-06	3.420E-04		1.065E-05	3.370E-05	9.280E-05
^{133}In		5.145E-05				1.150E-05
^{133m}In		1.010E-05				
^{121}Sn				1.285E-05		
^{121m}Sn			1.235E-05			
^{122}Sn	1.265E-05	1.365E-05	6.690E-05	4.640E-05	3.280E-05	2.025E-05
^{123}Sn	2.440E-05	2.345E-05	9.950E-05	1.155E-04	6.470E-05	3.395E-05
^{123m}Sn	1.155E-05		4.490E-05		2.490E-05	1.435E-05
^{124}Sn	1.169E-04	1.147E-04	3.502E-04	2.906E-04	2.571E-04	1.433E-04
^{125}Sn	1.910E-04	1.968E-04	4.572E-04	5.282E-04	3.551E-04	2.168E-04
^{125m}Sn	7.860E-05	7.065E-05	1.905E-04		1.471E-04	7.805E-05
^{126}Sn	7.760E-04	7.306E-04	1.441E-03	1.133E-03	1.071E-03	7.159E-04
^{127}Sn	1.195E-03	1.058E-03	2.003E-03	2.172E-03	1.403E-03	1.034E-03
^{127m}Sn	4.914E-04	3.725E-04	8.331E-04		5.713E-04	3.754E-04
^{128}Sn	1.328E-03	9.599E-04	1.590E-03	4.444E-03	1.228E-03	8.646E-04
^{128m}Sn	3.076E-03	2.515E-03	3.727E-03	1.785E-05	2.880E-03	2.393E-03
^{129}Sn	2.117E-03	1.738E-03	1.891E-03	6.417E-03	1.942E-03	1.508E-03
^{129m}Sn	5.140E-03	4.352E-03	4.557E-03	2.470E-05	4.698E-03	4.233E-03
^{130}Sn	3.460E-03	3.518E-03	1.969E-03	8.267E-03	2.982E-03	2.732E-03
^{130m}Sn	8.119E-03	9.158E-03	4.574E-03	2.230E-05	6.984E-03	7.464E-03
^{131}Sn	2.630E-03	5.017E-03	1.053E-03	5.815E-03	2.595E-03	3.035E-03
^{131m}Sn	6.325E-03	1.334E-02	2.531E-03	1.260E-05	6.277E-03	8.461E-03
^{132}Sn	5.599E-03	2.389E-02	1.583E-03	3.295E-03	6.274E-03	1.032E-02
^{133}Sn	9.937E-04	9.234E-03	2.070E-04	5.417E-04	1.328E-03	2.860E-03
^{134}Sn	1.826E-04	3.499E-03	3.635E-05	1.117E-04	3.282E-04	8.510E-04
^{135}Sn	1.475E-05	7.035E-04		1.210E-05	4.630E-05	1.457E-04
^{136}Sn		1.003E-04				1.820E-05
^{123}Sb			1.605E-05	1.335E-05		
^{124}Sb			1.520E-05	3.210E-05		
^{124m}Sb			1.155E-05			
^{124n}Sb			1.580E-05			1.010E-05
^{125}Sb	3.805E-05	4.485E-05	1.146E-04	9.050E-05	7.220E-05	5.500E-05
^{126}Sb	3.205E-05	4.140E-05	9.795E-05	1.958E-04	6.030E-05	4.815E-05
^{126m}Sb	2.540E-05	2.595E-05	7.025E-05		4.480E-05	3.245E-05
^{126n}Sb	3.010E-05	3.010E-05	9.310E-05		6.010E-05	3.970E-05
^{127}Sb	2.313E-04	2.438E-04	6.890E-04	4.809E-04	3.973E-04	2.703E-04
^{128}Sb	2.090E-04	1.841E-04	7.267E-04	1.149E-03	3.098E-04	2.311E-04

Nuclide	Target					
	^{235}U	^{238}U	^{239}Pu	^{240}Pu	^{241}Pu	^{242}Pu
	Fission Yield					
^{128m}Sb	3.518E-04	2.621E-04	1.251E-03		5.164E-04	3.187E-04
^{129}Sb	1.157E-03	5.779E-04	3.225E-03	3.202E-03	1.313E-03	7.856E-04
^{129m}Sb	7.105E-04	4.034E-04	1.962E-03		7.883E-04	5.837E-04
^{130}Sb	2.797E-03	1.004E-03	5.082E-03	7.586E-03	2.818E-03	1.862E-03
^{130m}Sb	2.801E-03	1.038E-03	5.073E-03	2.370E-05	2.824E-03	1.848E-03
^{131}Sb	1.330E-02	6.018E-03	1.430E-02	1.385E-02	1.219E-02	9.604E-03
^{132}Sb	1.092E-02	9.297E-03	7.905E-03	1.727E-02	1.126E-02	1.053E-02
^{132m}Sb	8.082E-03	8.260E-03	5.861E-03	3.060E-05	8.267E-03	9.307E-03
^{133}Sb	1.850E-02	3.438E-02	8.383E-03	1.372E-02	1.919E-02	2.519E-02
^{134}Sb	1.821E-03	6.744E-03	5.999E-04	4.171E-03	2.191E-03	3.341E-03
^{134m}Sb	4.298E-03	1.761E-02	1.408E-03		5.150E-03	9.106E-03
^{135}Sb	1.436E-03	1.121E-02	4.049E-04	1.008E-03	2.134E-03	4.393E-03
^{136}Sb	3.104E-04	5.240E-03	9.145E-05	2.593E-04	6.918E-04	1.703E-03
^{137}Sb	2.750E-05	9.905E-04		2.705E-05	9.280E-05	2.785E-04
^{138}Sb		1.727E-04			1.250E-05	4.230E-05
^{139}Sb		1.255E-05				
^{126}Te			1.045E-05			
^{127}Te				1.700E-05		
^{127m}Te			2.150E-05			
^{128}Te	1.460E-05	1.080E-05	1.320E-04	6.695E-05	4.340E-05	1.555E-05
^{129}Te	1.885E-05		1.732E-04	2.425E-04	3.545E-05	1.110E-05
^{129m}Te	4.485E-05	1.370E-05	4.141E-04		8.675E-05	3.545E-05
^{130}Te	4.105E-04	5.580E-05	2.562E-03	1.120E-03	5.419E-04	1.991E-04
^{131}Te	7.102E-04	6.920E-05	2.372E-03	4.311E-03	7.126E-04	2.771E-04
^{131m}Te	1.698E-03	1.880E-04	5.724E-03	2.740E-05	1.698E-03	7.754E-04
^{132}Te	1.028E-02	1.670E-03	1.896E-02	1.318E-02	8.747E-03	4.912E-03
^{133}Te	8.401E-03	2.526E-03	9.351E-03	2.937E-02	7.328E-03	4.819E-03
^{133m}Te	2.040E-02	7.059E-03	2.252E-02	1.119E-04	1.770E-02	1.346E-02
^{134}Te	5.593E-02	3.566E-02	3.383E-02	4.171E-02	4.424E-02	4.190E-02
^{135}Te	3.767E-02	4.663E-02	1.470E-02	2.357E-02	3.080E-02	3.712E-02
^{136}Te	2.115E-02	4.571E-02	6.122E-03	1.185E-02	1.830E-02	2.672E-02
^{137}Te	8.172E-03	3.420E-02	1.949E-03	4.516E-03	8.612E-03	1.531E-02
^{138}Te	2.033E-03	1.573E-02	3.960E-04	1.117E-03	2.587E-03	5.481E-03
^{139}Te	3.096E-04	4.962E-03	5.845E-05	1.838E-04	5.483E-04	1.381E-03
^{140}Te	3.505E-05	1.070E-03		2.010E-05	8.480E-05	2.482E-04
^{141}Te		1.379E-04				3.000E-05
^{142}Te		1.250E-05				
^{129}I			1.275E-05			
^{130}I			5.820E-05	2.800E-05		
^{130m}I			2.390E-05			

Nuclide	Target					
	^{235}U	^{238}U	^{239}Pu	^{240}Pu	^{241}Pu	^{242}Pu
	Fission Yield					
^{131}I	2.350E-05		5.293E-04	1.756E-04	5.960E-05	1.740E-05
^{132}I	1.212E-04		1.470E-03	9.809E-04	2.115E-04	7.485E-05
^{132m}I	9.175E-05		1.085E-03		1.597E-04	6.635E-05
^{133}I	9.922E-04	8.755E-05	6.013E-03	4.798E-03	1.426E-03	6.249E-04
^{133m}I	6.030E-04	6.755E-05	3.660E-03	1.750E-05	8.722E-04	4.486E-04
^{134}I	5.559E-03	8.521E-04	1.535E-02	1.779E-02	6.512E-03	3.460E-03
^{134m}I	4.108E-03	7.560E-04	1.136E-02	5.125E-05	4.782E-03	3.048E-03
^{135}I	2.922E-02	9.096E-03	3.961E-02	3.610E-02	2.937E-02	2.159E-02
^{136}I	1.049E-02	5.668E-03	8.377E-03	3.299E-02	9.987E-03	8.281E-03
^{136m}I	2.451E-02	1.433E-02	1.954E-02	1.027E-04	2.333E-02	2.251E-02
^{137}I	2.949E-02	2.913E-02	1.620E-02	2.357E-02	2.801E-02	3.159E-02
^{138}I	1.992E-02	3.707E-02	8.234E-03	1.460E-02	2.085E-02	2.876E-02
^{139}I	6.865E-03	2.299E-02	2.275E-03	4.773E-03	8.036E-03	1.334E-02
^{140}I	2.013E-03	1.361E-02	6.007E-04	1.478E-03	3.081E-03	6.229E-03
^{141}I	3.163E-04	4.203E-03	9.245E-05	2.571E-04	6.431E-04	1.538E-03
^{142}I	3.535E-05	1.105E-03	1.155E-05	3.890E-05	1.171E-04	3.450E-04
^{143}I		1.460E-04			1.160E-05	3.965E-05
^{144}I		1.575E-05				
^{132}Xe			2.645E-05	1.705E-05		
^{132m}Xe			2.910E-05			
^{133}Xe			1.217E-04	1.210E-04		
^{133m}Xe	1.270E-05		2.939E-04		2.290E-05	
^{134}Xe	6.620E-05		8.364E-04	1.007E-03	1.071E-04	3.650E-05
^{134m}Xe	1.526E-04		1.954E-03		2.601E-04	9.705E-05
^{135}Xe	6.776E-04	4.785E-05	3.679E-03	6.025E-03	8.523E-04	3.344E-04
^{135m}Xe	1.636E-03	1.392E-04	8.825E-03	3.935E-05	2.057E-03	9.531E-04
^{136}Xe	1.359E-02	1.883E-03	3.310E-02	2.193E-02	1.376E-02	7.522E-03
^{137}Xe	3.030E-02	6.939E-03	3.893E-02	3.386E-02	2.627E-02	1.774E-02
^{138}Xe	4.778E-02	1.866E-02	3.795E-02	4.160E-02	3.874E-02	3.186E-02
^{139}Xe	5.084E-02	3.363E-02	2.640E-02	3.603E-02	3.982E-02	3.976E-02
^{140}Xe	3.842E-02	4.300E-02	1.421E-02	2.338E-02	3.037E-02	3.659E-02
^{141}Xe	2.006E-02	4.033E-02	5.530E-03	1.106E-02	1.718E-02	2.508E-02
^{142}Xe	7.899E-03	2.657E-02	1.677E-03	3.981E-03	7.216E-03	1.254E-02
^{143}Xe	1.654E-03	1.139E-02	3.100E-04	8.655E-04	1.992E-03	4.174E-03
^{143m}Xe		1.714E-04				
^{144}Xe	3.574E-04	4.095E-03	5.390E-05	1.750E-04	4.781E-04	1.189E-03
^{145}Xe	2.700E-05	8.468E-04		1.945E-05	6.265E-05	1.892E-04
^{146}Xe		1.324E-04				2.770E-05
^{147}Xe		1.010E-05				
^{134}Cs			2.130E-05			

Nuclide	Target					
	^{235}U	^{238}U	^{239}Pu	^{240}Pu	^{241}Pu	^{242}Pu
	Fission Yield					
^{134m}Cs			1.550E-05			
^{135}Cs			2.416E-04	1.131E-04	1.670E-05	
^{135m}Cs			1.484E-04		1.050E-05	
^{136}Cs	9.080E-05		1.849E-03	1.018E-03	2.169E-04	8.270E-05
^{136m}Cs	5.125E-05		1.074E-03		1.278E-04	5.600E-05
^{137}Cs	1.508E-03	1.328E-04	1.187E-02	5.554E-03	2.492E-03	1.154E-03
^{138}Cs	2.373E-03	2.887E-04	9.014E-03	1.331E-02	3.173E-03	1.537E-03
^{138m}Cs	3.365E-03	4.523E-04	1.279E-02	5.945E-05	4.494E-03	2.570E-03
^{139}Cs	1.388E-02	2.811E-03	2.896E-02	2.262E-02	1.585E-02	1.010E-02
^{140}Cs	2.657E-02	9.056E-03	3.294E-02	3.260E-02	2.778E-02	2.162E-02
^{141}Cs	2.715E-02	1.606E-02	2.199E-02	2.701E-02	2.751E-02	2.613E-02
^{142}Cs	2.410E-02	2.505E-02	1.373E-02	2.063E-02	2.490E-02	2.855E-02
^{143}Cs	1.133E-02	2.108E-02	5.025E-03	8.973E-03	1.282E-02	1.779E-02
^{144}Cs	2.209E-03	8.117E-03	8.380E-04	3.530E-03	3.004E-03	5.070E-03
^{144m}Cs	2.227E-03	7.533E-03	8.385E-04		2.999E-03	5.022E-03
^{145}Cs	1.065E-03	6.826E-03	3.612E-04	8.644E-04	1.749E-03	3.528E-03
^{146}Cs	1.679E-04	2.563E-03	6.215E-05	1.778E-04	4.592E-04	1.095E-03
^{147}Cs	1.920E-05	5.034E-04		2.235E-05	6.875E-05	1.919E-04
^{148}Cs		9.140E-05				2.995E-05
^{136m}Ba			1.790E-05			
^{137}Ba			9.250E-05	8.405E-05		
^{137m}Ba	5.500E-06		2.253E-04		1.395E-05	
^{138}Ba	1.386E-04		2.241E-03	7.654E-04	2.568E-04	8.755E-05
^{139}Ba	9.007E-04	5.350E-05	6.894E-03	2.976E-03	1.262E-03	5.151E-04
^{140}Ba	4.017E-03	3.412E-04	1.537E-02	8.501E-03	4.487E-03	2.125E-03
^{141}Ba	1.240E-02	1.698E-03	2.606E-02	1.849E-02	1.209E-02	6.849E-03
^{142}Ba	2.473E-02	5.541E-03	3.033E-02	2.737E-02	2.159E-02	1.464E-02
^{143}Ba	3.503E-02	1.322E-02	2.701E-02	3.043E-02	2.878E-02	2.362E-02
^{144}Ba	3.253E-02	2.108E-02	1.707E-02	2.355E-02	2.661E-02	2.652E-02
^{145}Ba	2.186E-02	2.430E-02	8.310E-03	1.389E-02	1.850E-02	2.213E-02
^{146}Ba	1.075E-02	2.033E-02	3.221E-03	6.289E-03	9.854E-03	1.412E-02
^{147}Ba	3.569E-03	1.255E-02	8.697E-04	2.058E-03	3.899E-03	6.702E-03
^{148}Ba	9.743E-04	5.606E-03	1.946E-04	5.185E-04	1.181E-03	2.387E-03
^{149}Ba	1.171E-04	1.685E-03	2.390E-05	8.365E-05	2.335E-04	5.683E-04
^{150}Ba	1.830E-05	3.667E-04		1.005E-05	3.415E-05	1.077E-04
^{151}Ba		5.365E-05				1.105E-05
^{138}La			1.820E-05			
^{139}La			1.999E-04	4.945E-05		
^{140}La	2.670E-05		9.720E-04	2.900E-04	8.225E-05	3.095E-05
^{141}La	1.780E-04	1.205E-05	3.175E-03	1.187E-03	4.187E-04	1.715E-04

Nuclide	Target					
	^{235}U	^{238}U	^{239}Pu	^{240}Pu	^{241}Pu	^{242}Pu
	Fission Yield					
^{142}La	1.036E-03	8.980E-05	8.794E-03	4.217E-03	1.963E-03	8.904E-04
^{143}La	3.021E-03	3.892E-04	1.372E-02	8.414E-03	4.804E-03	2.547E-03
^{144}La	7.382E-03	1.515E-03	1.908E-02	1.495E-02	1.051E-02	6.664E-03
^{145}La	1.044E-02	3.553E-03	1.643E-02	1.617E-02	1.389E-02	1.061E-02
^{146}La	3.741E-03	2.095E-03	4.156E-03	1.389E-02	5.139E-03	4.279E-03
^{146m}La	6.730E-03	4.192E-03	7.442E-03	3.780E-05	9.214E-03	8.930E-03
^{147}La	7.183E-03	7.494E-03	5.865E-03	8.463E-03	1.047E-02	1.171E-02
^{148}La	3.971E-03	7.604E-03	2.581E-03	4.445E-03	6.521E-03	8.826E-03
^{149}La	1.224E-03	4.450E-03	7.085E-04	1.437E-03	2.505E-03	4.095E-03
^{150}La	2.833E-04	2.182E-03	1.582E-04	3.795E-04	8.139E-04	1.588E-03
^{151}La	4.130E-05	5.731E-04	2.105E-05	6.245E-05	1.515E-04	3.640E-04
^{152}La		1.319E-04			2.480E-05	7.200E-05
^{153}La		1.750E-05				
^{141}Ce			6.630E-05	1.445E-05		
^{142}Ce	1.195E-05		3.686E-04	1.011E-04	2.655E-05	
^{143}Ce	9.775E-05		1.491E-03	4.995E-04	1.697E-04	6.225E-05
^{144}Ce	5.441E-04	2.490E-05	4.106E-03	1.773E-03	7.479E-04	3.058E-04
^{145}Ce	2.071E-03	1.585E-04	8.206E-03	4.512E-03	2.397E-03	1.107E-03
^{146}Ce	5.310E-03	6.523E-04	1.210E-02	8.439E-03	5.551E-03	2.997E-03
^{147}Ce	8.729E-03	1.832E-03	1.283E-02	1.118E-02	8.939E-03	5.791E-03
^{148}Ce	1.099E-02	3.893E-03	1.075E-02	1.158E-02	1.125E-02	8.806E-03
^{149}Ce	9.307E-03	5.976E-03	6.733E-03	8.936E-03	1.031E-02	9.916E-03
^{150}Ce	5.722E-03	6.417E-03	3.219E-03	5.043E-03	7.130E-03	8.230E-03
^{151}Ce	2.728E-03	5.542E-03	1.203E-03	2.265E-03	3.838E-03	5.444E-03
^{152}Ce	7.016E-04	2.630E-03	2.754E-04	5.835E-04	1.230E-03	2.067E-03
^{153}Ce	1.552E-04	1.179E-03	5.730E-05	1.442E-04	3.620E-04	7.567E-04
^{154}Ce	2.520E-05	2.943E-04		2.050E-05	6.560E-05	1.689E-04
^{155}Ce		6.725E-05				2.925E-05
^{143}Pr			1.725E-05			
^{144}Pr			1.005E-05	2.595E-05		
^{144m}Pr			9.820E-05			
^{145}Pr	8.750E-06		4.043E-04	1.233E-04	3.140E-05	1.205E-05
^{146}Pr	4.930E-05		1.262E-03	4.644E-04	1.512E-04	6.075E-05
^{147}Pr	1.895E-04	1.610E-05	2.677E-03	1.202E-03	5.223E-04	2.267E-04
^{148}Pr	1.186E-04	1.655E-05	9.034E-04	2.667E-03	2.934E-04	1.272E-04
^{148m}Pr	5.062E-04	5.930E-05	3.808E-03	1.640E-05	1.196E-03	6.223E-04
^{149}Pr	1.198E-03	2.424E-04	5.452E-03	3.971E-03	2.737E-03	1.646E-03
^{150}Pr	1.869E-03	6.637E-04	5.559E-03	5.062E-03	4.400E-03	3.212E-03
^{151}Pr	1.733E-03	1.076E-03	3.356E-03	3.802E-03	4.123E-03	3.762E-03
^{152}Pr	1.132E-03	1.403E-03	1.733E-03	2.422E-03	3.218E-03	3.652E-03

Nuclide	Target					
	^{235}U	^{238}U	^{239}Pu	^{240}Pu	^{241}Pu	^{242}Pu
	Fission Yield					
^{153}Pr	4.135E-04	9.870E-04	5.112E-04	8.571E-04	1.424E-03	2.008E-03
^{154}Pr	1.447E-04	6.545E-04	1.529E-04	3.130E-04	6.130E-04	1.061E-03
^{155}Pr	2.415E-05	2.308E-04	2.560E-05	6.010E-05	1.452E-04	3.010E-04
^{156}Pr		7.340E-05		1.255E-05	3.230E-05	7.935E-05
^{157}Pr		1.205E-05				1.150E-05
^{146}Nd			2.350E-05			
^{147}Nd			1.152E-04	2.895E-05		
^{148}Nd	2.120E-05		3.942E-04	1.316E-04	4.075E-05	1.490E-05
^{149}Nd	1.030E-04		1.027E-03	4.220E-04	1.751E-04	6.455E-05
^{150}Nd	3.689E-04	2.780E-05	2.208E-03	1.154E-03	6.007E-04	2.625E-04
^{151}Nd	9.172E-04	1.142E-04	3.338E-03	2.205E-03	1.505E-03	7.944E-04
^{152}Nd	1.595E-03	3.621E-04	3.719E-03	3.151E-03	2.645E-03	1.767E-03
^{153}Nd	1.640E-03	7.427E-04	2.899E-03	3.134E-03	3.385E-03	2.803E-03
^{154}Nd	1.172E-03	9.976E-04	1.558E-03	2.073E-03	2.742E-03	2.877E-03
^{155}Nd	6.519E-04	1.095E-03	7.118E-04	1.178E-03	1.902E-03	2.467E-03
^{156}Nd	2.148E-04	7.180E-04	2.108E-04	4.168E-04	8.468E-04	1.324E-03
^{157}Nd	6.060E-05	3.892E-04	4.895E-05	1.202E-04	3.077E-04	5.973E-04
^{158}Nd	8.800E-06	1.342E-04		2.355E-05	7.180E-05	1.719E-04
^{159}Nd		3.830E-05			1.280E-05	4.130E-05
^{149}Pm			1.780E-05			
^{150}Pm			7.025E-05	2.165E-05		
^{151}Pm	5.750E-06		2.368E-04	8.990E-05	2.675E-05	1.160E-05
^{152}Pm			1.197E-04	2.711E-04	2.320E-05	1.035E-05
^{152m}Pm	7.950E-06		2.307E-04		4.395E-05	1.880E-05
^{152n}Pm	1.010E-05		2.537E-04		4.850E-05	2.570E-05
^{153}Pm	6.480E-05	1.035E-05	9.666E-04	5.690E-04	3.401E-04	1.788E-04
^{154}Pm	6.085E-05	1.980E-05	6.251E-04	9.463E-04	3.675E-04	2.462E-04
^{154m}Pm	6.565E-05	1.800E-05	6.245E-04		3.734E-04	2.429E-04
^{155}Pm	1.419E-04	7.010E-05	8.918E-04	8.946E-04	8.822E-04	7.288E-04
^{156}Pm	1.261E-04	1.343E-04	6.162E-04	7.656E-04	9.716E-04	1.018E-03
^{157}Pm	6.650E-05	1.433E-04	2.371E-04	3.654E-04	5.927E-04	7.984E-04
^{158}Pm	2.480E-05	1.234E-04	8.080E-05	1.552E-04	3.086E-04	5.160E-04
^{159}Pm	6.050E-06	5.660E-05	1.715E-05	3.550E-05	9.260E-05	2.014E-04
^{160}Pm		2.390E-05			2.920E-05	6.545E-05
^{161}Pm						1.115E-05
^{152}Sm			2.515E-05			
^{153}Sm			2.495E-05	3.395E-05		
^{153m}Sm			6.310E-05			
^{154}Sm	1.605E-05		2.696E-04	1.171E-04	5.400E-05	2.235E-05
^{155}Sm	4.780E-05		5.267E-04	3.169E-04	1.899E-04	9.560E-05

Nuclide	Target					
	^{235}U	^{238}U	^{239}Pu	^{240}Pu	^{241}Pu	^{242}Pu
	Fission Yield					
^{156}Sm	8.795E-05	2.165E-05	7.196E-04	5.534E-04	4.304E-04	2.640E-04
^{157}Sm	1.310E-04	6.025E-05	7.651E-04	7.484E-04	7.699E-04	5.989E-04
^{158}Sm	1.282E-04	1.083E-04	5.097E-04	6.511E-04	8.034E-04	7.982E-04
^{159}Sm	8.680E-05	1.614E-04	3.019E-04	4.590E-04	7.484E-04	8.921E-04
^{160}Sm	4.465E-05	1.521E-04	1.086E-04	2.039E-04	4.128E-04	6.102E-04
^{161}Sm	1.670E-05	1.117E-04	3.215E-05	7.650E-05	1.872E-04	3.529E-04
^{162}Sm		4.575E-05		1.820E-05	5.350E-05	1.129E-04
^{163}Sm		1.535E-05			1.175E-05	3.320E-05
^{155}Eu			1.460E-05			
^{156}Eu			4.585E-05	2.050E-05		
^{157}Eu			9.875E-05	5.130E-05	2.650E-05	1.375E-05
^{158}Eu			1.646E-04	1.194E-04	7.940E-05	4.855E-05
^{159}Eu	7.200E-06		1.635E-04	1.539E-04	1.381E-04	1.049E-04
^{160}Eu	1.370E-05		1.394E-04	1.586E-04	1.967E-04	1.789E-04
^{161}Eu	8.200E-06	1.400E-05	6.710E-05	1.001E-04	1.575E-04	1.835E-04
^{162}Eu	5.650E-06	1.675E-05	2.890E-05	5.100E-05	1.030E-04	1.517E-04
^{163}Eu		1.150E-05		1.770E-05	3.775E-05	6.525E-05
^{164}Eu					1.260E-05	2.340E-05
^{158}Gd			1.985E-05			
^{159}Gd			5.570E-05	3.185E-05	1.480E-05	
^{160}Gd	5.250E-06		9.650E-05	7.040E-05	5.605E-05	2.665E-05
^{161}Gd	1.155E-05		1.373E-04	1.250E-04	1.163E-04	7.515E-05
^{162}Gd	1.120E-05		1.124E-04	1.287E-04	1.473E-04	1.281E-04
^{163}Gd	1.235E-05	1.770E-05	8.240E-05	1.078E-04	1.604E-04	1.698E-04
^{164}Gd	7.550E-06	1.945E-05	3.490E-05	5.545E-05	1.046E-04	1.339E-04
^{165}Gd		1.575E-05	1.175E-05	2.340E-05	5.555E-05	8.665E-05
^{166}Gd					1.550E-05	2.865E-05
^{162}Tb			1.230E-05			
^{163}Tb			1.850E-05	1.425E-05	1.020E-05	
^{164}Tb			2.025E-05	1.905E-05	1.845E-05	1.520E-05
^{165}Tb			1.265E-05	1.485E-05	2.050E-05	1.880E-05
^{166}Tb					1.590E-05	1.960E-05
^{165}Dy			1.215E-05			
^{166}Dy			1.505E-05	1.215E-05	1.320E-05	
^{167}Dy			1.155E-05	1.130E-05	1.615E-05	1.440E-05
^{168}Dy					1.305E-05	1.195E-05

References

[1] K.-H. Schmidt, B. Jurado, *General fission-model code GEF for fragment distributions*, newest versions available at **http://www.khs-erzhausen.de/40376.html**

[2] W. Demtröder, *Experimentalphysik 3 - Atome, Moleküle und Festkörper*, **Springer-Verlag, Heidelberg, Germany, ISBN 3-540-21473-9, (2005)**

[3] C. Wagemans, *The Nuclear Fission Process*, **CRC Press, Boca Raton, Florida, USA, ISBN 0-8493-5434-X, (1991)**

[4] K.-H. Schmidt, A. Kelic, M. V. Ricciardi, *Experimental evidence for the separability of compound-nucleus and fragment properties in fission*, **Europhys. Lett. 83 (2008), No. 3, Art. 32001**

[5] K.-H. Schmidt, **private communication**

[6] E. G. Ryabov et al., *Application of a temperature-dependent liquid drop model to dynamical Langevin calculations of fission-fragment distributions of excited nuclei*, **Phys. Rev. C, Vol. 78, No. 4 (2008), Art. 044614**

[7] U. Brosa, S. Grossmann, A. Müller, *Nuclear scission*, **Phys. Rep. 197, No. 4 (1990), p. 167**

[8] T. von Egidy, D. Bucurescu, *Systematics of nuclear level density parameters*, **Phys. Rev. C, Vol. 72, No. 4 (2005), Art. 044311**

[9] T. von Egidy, D. Bucurescu, *Erratum: Systematics of nuclear level density parameters*, **Phys. Rev. C, Vol. 73, No. 4 (2006), Art. 049901**

[10] B. Povh, K. Rith, C. Scholz, F. Zetsche, *Teilchen und Kerne*, **Springer-Verlag, Heidelberg, Germany, ISBN 978-3-540-68075-8, (2009)**

[11] A. Kelic, M. V. Ricciardi, K.-H. Schmidt, *ABLA07 - towards a complete description of the decay channels of a nuclear system from spontaneous fission to multifragmentation*, **http://arxiv.org/pdf/0906.4193v1**

[12] P. Möller, A. Iwamoto, D. G. Madland, *Structure of Fission Potential-Energy Surfaces in Complete, Multi-Million-Grid-Point Five-Dimensional Deformation Spaces*, **http://t2.lanl.gov/publications/kumatori2000/kumatori00col.ps.gz**

[13] B. D. Wilkins, E. P. Steinberg, R. R. Chasman, *Scission-point model of nuclear fission based on deformed-shell effects*, **Phys. Rev. C, Vol. 14, No. 5 (1976), p. 1832**

[14] C. Böckstiegel et al., *Nuclear-fission studies with relativistic secondary beams: Analysis of fission channels*, **Nucl. Phys. A 802 (2008), p. 12**

[15] K.-H. Schmidt, B. Jurado, *Semi-empirical model for fission*, interim report of an EF-NUDAT research project, contract No. FP6-036434 (2009)

[16] K.-H. Schmidt et al., *Relativistic radioactive beams: A new access to nuclear-fission studies*, **Nucl. Phys. A 665 (2000), p. 221**

[17] S. I. Mulgin, V. N. Okolovich, S. V. Zhdanova, *Observation of new channel in the proton-induced low-energy fission of nuclei from ^{233}Pa to ^{245}Bk*, **Phys. Lett. B 462 (1999), p. 29**

[18] P. Siegler, F.-J. Hambsch, S. Oberstedt, J. P. Theobald, *Fission modes in the compound nucleus ^{238}Np*, **Nucl. Phys. A 594 (1995), p. 45**

[19] A. J. Koning, S. Hilaire, M. Duijvestijn, *TALYS-1.2 User Manual*, **http://www.talys.eu/fileadmin/talys/user/docs/talys1.2.pdf**

[20] IAEA Reference Input Parameter Library 3, *Empirical Fission Barriers*, **http://www-nds.iaea.org/RIPL-3/fission/empirical-barriers.dat**

[21] BNL National Nuclear Data Center, **http://www.nndc.bnl.gov/chart/getdataset.jsp?nucleus=236U&unc=nds** **http://www.nndc.bnl.gov/chart/getdataset.jsp?nucleus=238U&unc=nds**

[22] F.-J. Hambsch, H.-H. Knitter, C. Budtz-Jørgensen, J. P. Theobald, *Fission mode fluctuations in the resonances of $^{235}U(n, f)$*, **Nucl. Phys. A 491 (1989), p. 56**

[23] K.-H. Schmidt, B. Jurado, *Entropy-driven excitation-energy sorting in superfluid fission dynamics*, **Phys. Rev. Lett. 104, No. 21 (2010), Art. 212501**

[24] R. G. Stokstad, *The Use of Statistical Models in Heavy-Ion Reaction Studies*, contribution to D. A. Bromley, *Treatise on Heavy-Ion Science, Vol. 3*, **Plenum Press, New York, USA, ISBN 0-306-41573-9, (1985)**

[25] K.-H. Schmidt, B. Jurado, *General model description of fission observables*, final report of an EFNUDAT research project, contract No. FP6-036434, **http://www.khs-erzhausen.de/media/3728f8ae67fefafffff804dffffffef.pdf** (2010)

[26] W. Lang, H.-G. Clerc, H. Wohlfarth, H. Schrader, K.-H. Schmidt, *Nuclear charge and mass yields for $^{235}U(n_{th}, f)$ as a function of the kinetic energy of the fission products*, **Nucl. Phys. A 345 (1980), p. 34**

[27] J. Benlliure, A. Grewe, M. de Jong, K.-H. Schmidt, S. Zhdanov, *Calculated nuclide production yields in relativistic collisions of fissile nuclei*, **Nucl. Phys. A 628 (1998), p. 458**

[28] B. L. Tracy et al., *Rb and Cs Isotopic Cross Sections from 40-60-MeV-Proton Fission of ^{238}U, ^{232}Th and ^{235}U*, **Phys. Rev. C, Vol. 5, No. 1 (1972), p. 222**

[29] K.-H. Schmidt, B. Jurado, *New insight into superfluid nuclear dynamics from the even-odd effect in fission*, **http://arxiv.org/pdf/1007.0741v1**

[30] E. Gadioli, P. E. Hodgson, *Pre-Equilibrium Nuclear Reactions*, **Oxford University Press, Oxford, Great Britain, ISBN 0-19-851734-3, (1992)**

[31] A. Konobeev, **private communication**

[32] H. Naik, S. P. Dange, R. J. Singh, A. V. R. Reddy, *Single-particle spin effect on fission fragment angular momentum*, **Europ. Phys. J. A 31 (2007), p. 195**

[33] M. Zielinska-Pfabé, K. Dietrich, *Angular momentum distribution of fission fragments as a result of bending modes at the scission point*, **Phys. Lett. B 49 (1974), p. 123**

[34] I. N. Mikhailov, P. Quentin, *On the spin of fission fragments, an orientation pumping mechanism*, **Phys. Lett. B 462 (1999), p. 7**

[35] L. Bonneau, P. Quentin, I. N. Mikhailov, *Scission configurations and their implication in fission-fragment angular momenta*, **Phys. Rev. C, Vol. 75, No. 6 (2007), Art. 064313**

[36] Neutron induced fission yields from the JEFF-3.1.1 evaluated nuclear data library, ENDF file available at **http://www.oecd-nea.org/dbforms/data/eva/evatapes/jeff_31/JEFF311/JEFF-311FY**

[37] W. D. Myers, W. J. Swiatecki, *Thomas-Fermi fission barriers*, **Phys. Rev. C, Vol. 60, No. 1 (1999), Art. 014606**

[38] *The 2003 Atomic Mass Evaluation*, **http://www.nndc.bnl.gov/amdc/masstables/Ame2003/mass.mas03 http://www.nndc.bnl.gov/amdc/masstables/Ame2003/Ame2003.errata**

[39] *Janis, Java-based Nuclear Data Display Program*, developed by the OECD Nuclear Energy Agency, available at **http://www.oecd-nea.org/janis/download.html**

[40] M. Herman, A. Trkov, *ENDF-6 Formats Manual*, BNL-XXXXX-2009 (2009), **http://www-nds.iaea.org/ndspub/documents/endf/endf102/endf102.pdf**

[41] J.-O. Denschlag et al., *Fission Product Yield Data for the Transmutation of Minor Actinide Nuclear Waste*, **IAEA STI/PUB/1286 (2008), http://www-nds.iaea.org/publications/tecdocs/sti-pub-1286.pdf**

[42] M. A. Kellett, O. Bersillon, R. W. Mills, *The JEFF-3.1/-3.1.1 radioactive decay data and fission yields sub-libraries*, JEFF Report 20, **NEA No. 6287 (2009)**

[43] *Compilation and evaluation of fission yield nuclear data,*
IAEA-TECDOC-1168 (2000),
http://www-pub.iaea.org/MTCD/publications/PDF/te_1168_prn.pdf

[44] *ROOT*, an object-oriented data analysis framework developed at CERN, available at
http://root.cern.ch/drupal/content/downloading-root

[45] P. P. Djachenko, B. D. Kuzminov, A. Lajtai, *Kinetic energy of fragments at the fission of ^{235}U by neutrons in the energy range 0 - 0.6 MeV*, **EXFOR 40017**,
http://www-nds.iaea.org/exfor/servlet/X4sGetSubent?plus=1&sub=40017

[46] P. P. Djachenko, B. D. Kuzminov, M. Z. Tarasko, *Energy and mass distribution of fragments at the fission of ^{235}U by monoenergetic neutrons in the energy interval 0 - 15.5 MeV*, **EXFOR 40235**,
http://www-nds.iaea.org/exfor/servlet/X4sGetSubent?plus=1&sub=40235

[47] C. Straede, C. Budtz-Jørgensen, H.-H. Knitter, $^{235}U(n,f)$ *fragment mass-, kinetic energy- and angular distributions for incident neutron energies between thermal and 6 MeV*, **Nucl. Phys. A 462 (1987), p. 85**

[48] U. Brosa, H.-H. Knitter, T.-S. Fan et al., *Systematics of fission-channel probabilities*, **Phys. Rev. C, Vol. 59, No. 2 (1999), p. 767**

[49] F. Vives, F.-J. Hamsch, H. Bax, S. Oberstedt, *Investigation of the fission fragment properties of the reaction $^{238}U(n,f)$ at incident neutron energies up to 5.8 MeV*, **Nucl. Phys. A 662 (2000), p. 63**, **EXFOR 22402**,
http://www-nds.iaea.org/exfor/servlet/X4sGetSubent?plus=1&sub=22402

[50] N. I. Akimov, V. G. Vorobyeva, V. N. Kabenin, N. P. Kolosov, B. D. Kuzminov, A. I. Sergachev, L. D. Smirenkina, M. Z. Tarasko, *Effect of excitation energy on yields and kinetic energies of fragments at the fission of ^{239}Pu by neutrons*, **EXFOR 40144**,
http://www-nds.iaea.org/exfor/servlet/X4sGetSubent?plus=1&sub=40144

[51] V. M. Surin, A. I. Sergachev, N. I. Rezchikov, B. D. Kuzminov, *Yields and kinetic energies of fragments at the fission of ^{233}U and ^{239}Pu by 5.5 and 15 MeV neutrons*, **EXFOR 40112**,
http://www-nds.iaea.org/exfor/servlet/X4sGetSubent?plus=1&sub=40112

[52] L. Koch, *Systematics of fast cumulative fission yields*, **EXFOR 21155**,
http://www-nds.iaea.org/exfor/servlet/X4sGetSubent?plus=1&sub=21155

[53] V. G. Vorobyeva, N. P. Djachenko, N. P. Kolosov, B. D. Kuzminov, A. I. Sergachev, V. M. Surin, *Yields and kinetic energies of fragments from fission of the ^{241}Pu nuclei induced by fast neutrons*, **EXFOR 40282**,
http://www-nds.iaea.org/exfor/servlet/X4sGetSubent?plus=1&sub=40282

[54] V. G. Vorobyeva, N. D. Djachenko, B. D. Kuzminov, A. I. Sergachev, V. M. Surin, *Mass yields and kinetic energy of fragments for fission of plutonium isotopes*, **EXFOR 40284**, **http://www-nds.iaea.org/exfor/servlet/X4sGetSubent?plus=1&sub=40284**

[55] C. Schmitt et al., *Fission yields at different fission product kinetic energies for thermal-neutron-induced fission of ^{239}Pu*, **Nucl. Phys. A 430 (1984), p. 21**

[56] P. Schillebeeckx, C. Wagemans, P. Geltenbort, F. Gönnenwein, A. Oed, *Investigation of mass, charge and energy of $^{241}Pu(n_{th}, f)$ fragments with the Cosi-Fan-Tutte spectrometer*, **Nucl. Phys. A 580 (1994), p. 15**

[57] P. Schillebeeckx, C. Wagemans, A. J. Deruytter, R. Barthélémy, *Comparative study of the fragments' mass and energy characteristics in the spontaneous fission of ^{238}Pu, ^{240}Pu and ^{242}Pu and in the thermal-neutron-induced fission of ^{239}Pu*, **Nucl. Phys. A 545 (1992), p. 623**

[58] S. Pommé et al., *Excitation energy dependence of charge odd-even effects in the fission of ^{238}U close to the fission barrier*, **Nucl. Phys. A 560 (1993), p. 689**

[59] A. Ponomarev et al., *Evaluation of some neutron physics parameters and reactivity coefficients for sodium cooled fast reactors*, **International Congress on Advances in NPPs, San Diego, California, June 13-17, 2010**

[60] M. Becker, S. Van Criekingen, C. H. M. Broeders, *Short description of the export version of KANEXT*, **KANEXT documentation (2010)**

[61] C. H. M. Broeders, *Entwicklungsarbeiten für die neutronenphysikalische Auslegung von Fortschrittlichen Druckwasserreaktoren (FDWR) mit kompakten Dreiecksgittern in hexagonalen Brennelementen*, PhD thesis, **KfK 5072 (1992), http://inrwww.fzk.de/kfk5072.pdf**

[62] L. Send, *Investigations for fuel recycling in LWRs*, **master's thesis (2005), http://inrwww.fzk.de/students_work/thesis_send.pdf**

[63] C. H. M. Broeders, Y. Cao, Y. Gohar, *MCNPX Monte Carlo burn-up simulations of the isotope correlation experiments in the NPP Obrigheim*, **Annals of Nuclear Energy 37, Issue 10, p. 1321 (2010)**

[64] MCNPX authors, *MCNPX*, **(2009)**

[65] C. H. M. Broeders, *A personal review on history, status and outlook for the future of KAPROS/KANEXT*, **http://inrwww.fzk.de/home/kapros.php**

[66] M. J. Bell, *ORIGEN - The ORNL isotope generation and depletion code*, **Oak Ridge National Laboratory, ORNL-4628 (1973)**

[67] U. Fischer, H. W. Wiese, *Verbesserte konsistente Berechnung des nuklearen Inventars abgebrannter DWR-Brennstoffe auf der Basis von Zell-Abbrand-Verfahren mit KORIGEN*, **Kernforschungszentrum Karlsruhe, KfK 3014 (1983)**

[68] E. Stein, E. Wiegner, C. Broeders, *Kurzbeschreibung des KAPROS-Moduls BURNUP zur numerischen Lösung der Abbrandgleichungen*, internal technical report, **Kernforschungszentrum Karlsruhe, INR (1982)**

[69] K. Wirtz, *Grundlagen der Reaktortechnik, Teil II - Reaktortheorie*, lecture notes, **Lehrstuhl für physikalische Grundlagen der Reaktortechnik, TH Karlsruhe (1966)**

[70] C. H. M. Broeders, **private communication**

[71] G. Audi, O. Bersillon, J. Blachot, A. H. Wapstra, *The NUBASE evaluation of nuclear and decay properties*, **Nucl. Phys. A 729 (2003), p. 3**, **http://www.nndc.bnl.gov/amdc/nubase/nubtab03.asc**